Elastic and Inelastic Scattering of Neutrons from Neon and Argon: Impact on Neutrinoless Double-Beta Decay and Dark Matter Experimental Programs

Sean Patrick MacMullin

A dissertation submitted to the faculty of the University of North Carolina at Chapel Hill in partial fulfillment of the requirements for the degree of Doctor of Philosophy in the Department of Physics and Astronomy.

Chapel Hill
2013

Approved by:

Reyco Henning

John Wilkerson

Werner Tornow

Jonathan Engel

Rene Lopez

Abstract

SEAN PATRICK MACMULLIN: Elastic and Inelastic Scattering of Neutrons from Neon and Argon: Impact on Neutrinoless Double-Beta Decay and Dark Matter Experimental Programs.
(Under the direction of Reyco Henning.)

In underground physics experiments, such as neutrinoless double-beta decay and dark matter searches, fast neutrons may be the dominant and potentially irreducible source of background. Experimental data for the elastic and inelastic scattering cross sections of neutrons from argon and neon, which are target and shielding materials of interest to the dark matter and neutrinoless double-beta decay communities, were previously unavailable. Unmeasured neutron scattering cross sections are often accounted for incorrectly in Monte-Carlo simulations.

Elastic scattering cross sections were measured at the Triangle Universities Nuclear Laboratory (TUNL) using the neutron time-of-flight technique. Angular distributions for neon were measured at 5.0 and 8.0 MeV. One full angular distribution was measured for argon at 6.0 MeV. The cross-section data were compared to calculations using a global optical model. Data were also fit using the spherical optical model. These model fits were used to predict the elastic scattering cross section at unmeasured energies and also provide a benchmark where the global optical models are not well constrained.

Partial γ-ray production cross sections for $(n, xn\gamma)$ reactions in natural argon and neon were measured using the broad spectrum neutron beam at the Los Alamos Neutron Science Center (LANSCE). Neutron energies were determined using time of flight and resulting γ rays from neutron-induced reactions were detected using the GErmanium Array for Neutron Induced Excitations (GEANIE). Partial γ-ray production cross sections for six transitions in ^{40}Ar, two transitions in ^{39}Ar and the first excited state transitions is ^{20}Ne and ^{22}Ne were measured from threshold to a neutron energy where the γ-ray yield dropped below the detection sensitivity. Measured $(n, xn\gamma)$ cross sections were compared with calculations using the TALYS and CoH$_3$ nuclear reaction codes. These new measurements will help to identify potential backgrounds in neutrinoless double-beta decay and dark matter experiments that use argon or neon. The measurements will also aid in the identification of neutron interactions in these experiments through the detection of γ rays produced by $(n, xn\gamma)$ reactions.

To Mildred S. MacMullin (a.k.a. “Grammy”), the first scientist I ever met.

Acknowledgments

I would like to thank a number of people who contributed to the success of this work. First, thank you to Dr. Werner Tornow and Dr. Calvin Howell for the opportunity to perform measurements at TUNL and for spending a tremendous amount of time helping with experimental setup, taking shifts, and ensuring the overall success of the experiments. Thank you also to Dr. Mary Kidd, Dr. Alex Couture and Michael Brown for taking shifts and contributing to data analysis. I would also like to acknowledge the TUNL technical staff including Richard O'Quinn, Bret Carlin, Chris Westerfeldt, John Dunham, Paul Carter and Patrick Mulkey.

I would like to thank Dr. Steve Elliott and Dr. Keith Rielage for the opportunity to work at LANL and to participate in the LANSCE measurements. Additional thanks to Dr. Mitzi Boswell, Dr. Vince Guiseppe and Ben LaRoque for help with the LANSCE proposals and data analysis. I would also like to acknowledge Dr. Matt Devlin, Dr. Nik Fotiades, Dr. Ron Nelson and Dr. John O'Donnell for hardware, data acquisition and analysis support for the LANSCE measurements.

On a more personal note, I would like to thank all of the members of the ENPA group at UNC for providing a fun and stimulating work environment. Special thanks to my fiancé, Jacquie Strain, and to my Mother and Father for unconditional support, encouragement and inspiration.

Finally, I would like to thank Dr. Reyco Henning and Dr. John Wilkerson for the opportunity to be a member of the Majorana Collaboration over the past five years and for their contributions to this project. None of this work would have been possible without them.

Table of Contents

List of Figures

List of Tables

Chapter 1

Background and Motivation

1.1 Dark Matter

Dark matter is a type of matter that accounts for about one quarter of the mass-energy in the universe. Unlike the matter made up of protons, neutrons and electrons, dark matter neither emits nor absorbs detectible amounts of electromagnetic radiation. Because it is not visible, its existence must be inferred from its gravitational interaction and influence on the observed large-scale structure of the universe. This section will describe the current evidence for dark matter, candidates for dark matter, and the current status of experimental techniques for its direct detection.

1.1.1 Dark Matter on Galactic Scales

The existence of dark matter was first postulated by Zwicky in 1933 [Zwi33], who calculated that the gravitational mass of galactic clusters must be much greater than expected from their luminosity. Since then, the existence of dark matter has been verified in a variety of different ways, the first of which was from the measurements of galactic rotation curves (see Fig. 1.1 for example). The rotational velocity for an object in a stable Keplerian orbit is

$$v(r) = \sqrt{\frac{GM(r)}{r}}, \tag{1.1}$$

where $M(r)$ is the mass inside the orbit at a particular radius r. Therefore, for r outside the visible part of the galaxy, the rotational velocity should scale as $v(r) \propto 1/\sqrt{r}$. It was observed however, that the rotational velocity was greater than expected if mass tracks light. In most galaxies, it was found that v becomes approximately constant to measurable values of r. This implies that there is a halo comprised of non-luminous matter with $M(r) \propto r$ and mass density $\rho(r) \propto 1/r^2$.

Dynamical evidence for dark matter can be inferred from motion of galaxies relative to one another, which was found to be slower than Hubble's law would predict. These "peculiar velocities" allow for estimates of galactic masses based on the assumption that gravitational interactions are responsible for their motions. Analyses of peculiar velocities indicated that the total matter density of the Universe must be greater than the value that is permitted by the standard model of Big-Bang nucleosynthesis [Lid99]. The conclusion is that not only is the Universe composed of dark matter, but at least some of it takes a non-baryonic form.

Observations of x-rays from hot gas in galaxy clusters provide more evidence for dark matter. X-ray maps show that within galaxy clusters, there is more matter in the gas than in all of the galaxies put together. After accounting for the hot gas as well as the possibility of stars too faint to detect or with insufficient material to initiate nuclear burning, it can be determined that clusters contain mostly dark matter [Lid99].

One particularly interesting example is the bullet cluster shown in Fig. 1.2. The Magellan Telescopes mapped the location of the mass in the bullet cluster through weak gravitational lensing [Clo06]. This map was compared with the x-ray images of

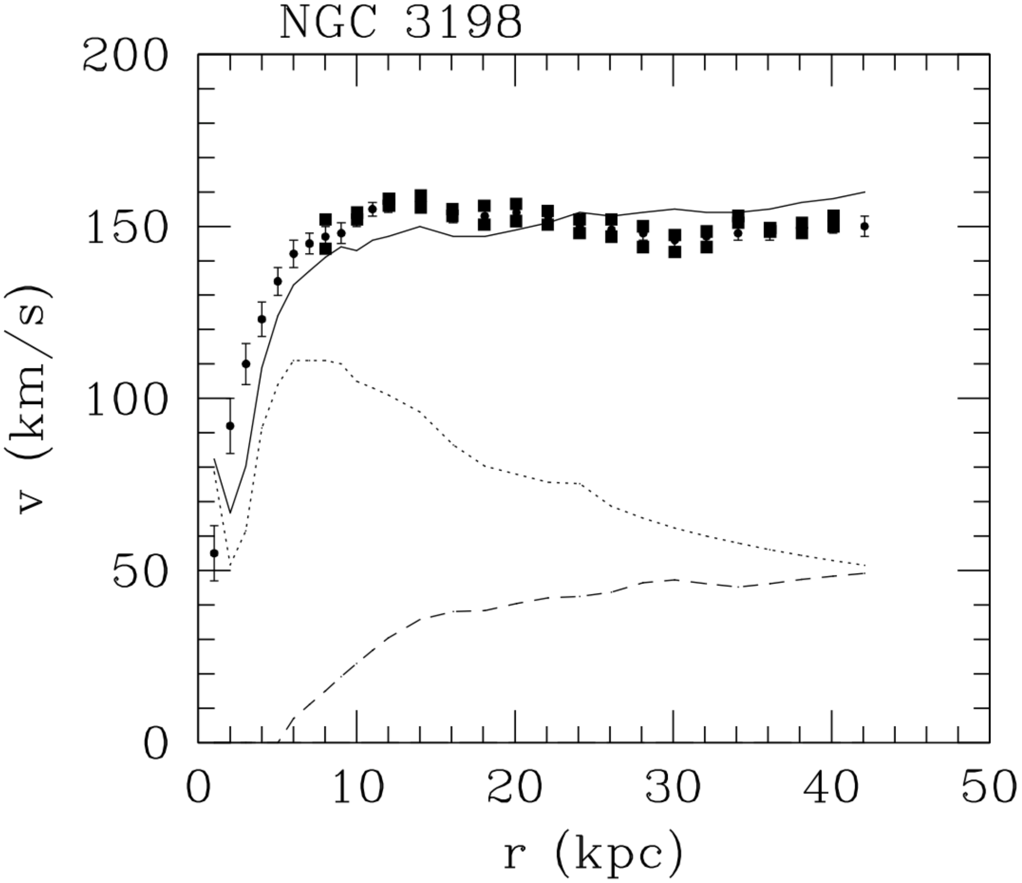

Figure 1.1: Galactic rotation curve for NGC 3198. The solid line represents the rotational velocity of the galaxy as a function of distance from the center. The dotted line represents the inferred contribution from matter in the disc and the dashed line represents the contribution from matter in the dark halo. Image from Ref. [Bot02].

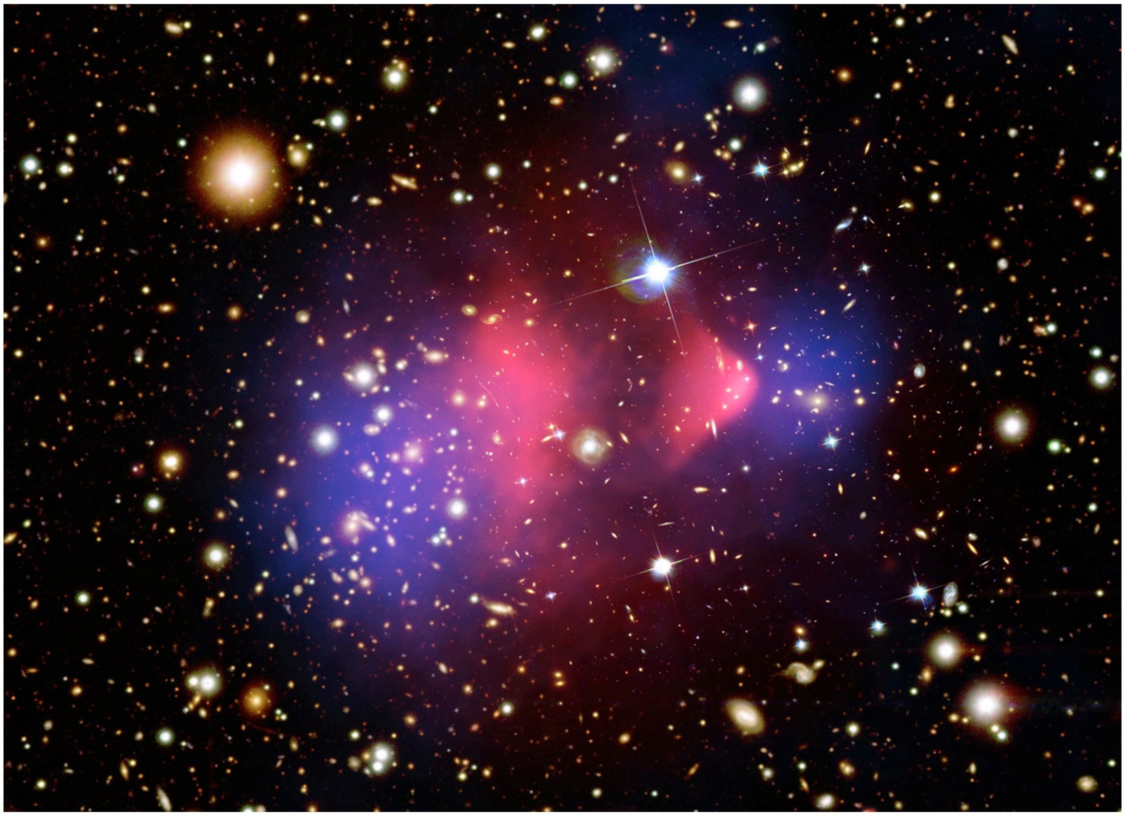

Figure 1.2: Composite image of the matter in the bullet cluster. The dark matter (blue) trails the luminous matter (red) following the collision of two galaxy clusters. Composite image from NASA [NAS06].

the luminous matter taken from the Chandra X-ray Observatory [Mar05]. The resulting structure shows two clusters of galaxies passing through one another. One possible interpretation is that the luminous matter, shown in red, interacts with luminous matter in the other cluster, slowing it down, whereas the dark matter, shown in blue, passes directly through. The result is that each galaxy cluster is separated into two components; the luminous matter trailing the dark matter.

1.1.2 Modern Cosmology

Modern cosmology has been successful in describing many areas of observational astronomy and particle physics. In particular, the ΛCDM model describes a Universe that contains a cosmological constant, Λ, as well as cold dark matter (CDM). This model, which contains only a few parameters, can describe many features of the Universe today, including the cosmic microwave background (CMB) [Hu97], the large-scale structure of the Universe, the light-element abundances, and the accelerating expansion of the Universe [Lid99].

The model contains density parameters, Ω_i, which determine the abundance of a specific substance in the Universe of species i, and are given as

$$\Omega_i \equiv \frac{\rho_i}{\rho_c}, \tag{1.2}$$

where ρ_i is the density of species i and ρ_c is the *critical density*, given in terms of an expansion parameter (the Hubble constant, $H_0 = 100\ h$ km s^{-1} Mpc^{-1}, where $h = 0.72 \pm 0.03$ [Ber12]) as

$$\rho_c = \frac{3H_0^2}{8\pi G}. \tag{1.3}$$

To show how these parameters fit into the model, we start with Einstein's theory of general relativity, which states how the presence of matter curves space-time. The Friedmann equation, a simple form of Einstein's equations [Ein16] is given as

$$H_0^2 = \frac{8\pi G}{3}\rho - \frac{k}{a^2}, \tag{1.4}$$

where ρ is the energy density, which can have a number of different subcomponents, k is the curvature constant, and a is a scale factor. Following Ref. [Bah99], we will consider a model which contains matter, m, curvature, k, and a cosmological constant, Λ. The cosmological constant can be thought of as the energy density of empty space, or "dark energy". It is speculated to be responsible for the observed acceleration of the Universe against the attractive effects of gravity. The contributions of each term to the right hand side of Eqn. 1.4 are given by

$$\Omega_m = 8\pi G\rho_m/3H_0^2, \tag{1.5}$$

$$\Omega_\Lambda = 8\pi G\rho_\Lambda/3H_0^2, \tag{1.6}$$

$$\Omega_k = -k/(aH_0)^2. \tag{1.7}$$

Dividing both sides of Eqn. 1.4 by H_0^2 gives the sum rule:

$$1 = \Omega_m + \Omega_k + \Omega_\Lambda. \tag{1.8}$$

Inflationary theory [Gut81] and analysis of the CMB [Hin09] appear to suggest the universe is flat ($\Omega_k = 0$). The ΛCDM model contains four basic parameters: $\Omega_m = 1/3$, $\Omega_\Lambda = 2/3$, $\Omega_k = 0$, and H_0. The mass-energy breakdown according to the current ΛCDM model is a mixture of $\sim$ 70% dark energy, $\sim$ 25% dark matter and $\sim$ 5% normal matter (electrons, protons, neutrons and neutrinos) [Lid99].

Quantitative information on the total amount of matter in the universe may be extracted from analysis of the CMB, large-scale structure, and other observations. The CMB spectrum is described by a blackbody function with $T = 2.725$ K. Temperature angular anisotropies in the CMB at the 10^{-5} level were first discovered with the COBE satellite [Smo92]. These data were improved upon by NASA's Wilkinson Microwave Anisotropy Probe (WMAP) [Ben03, Hin09] and several ground-based measurements [Fow10, Hou12].

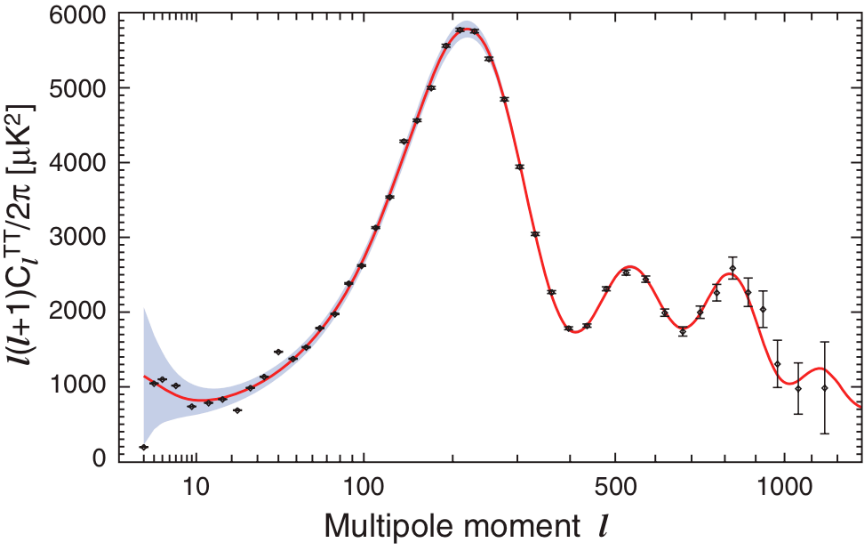

Figure 1.3: The observed power spectrum of CMB anisotropies from WMAP. From Ref.[Lar11].

The observed anisotropies put stringent constraints on various cosmological parameters, including dark matter. The temperature anisotropies are expanded as

$$\frac{\Delta T}{T}(\theta\phi) = \sum_{l=2}^{+\infty}\sum_{m=-l}^{+l} a_{lm}Y_{lm}(\theta\phi), \tag{1.9}$$

where $Y_{lm}(\theta\phi)$ are the spherical harmonics. The variance C_l of a_{lm} is given by

$$C_l \equiv \left\langle |a_{lm}|^2 \right\rangle \equiv \frac{1}{2l+1}\sum_{m=-l}^{l}|a_{lm}|^2 \,. \tag{1.10}$$

The information in the CMB maps is usually compressed in a power spectrum, which gives the behavior of ΔT as a function of l (see Fig. 1.3).

The monopole term a_{00} determines the mean CMB temperature, $T = 2.725$ K. The higher order multipoles represent perturbations in the density of the early universe. The first peak's position, centered around $l = 200$, is sensitive to curvature, and is in good agreement with a flat Universe [Hin09]. The series of peaks in the power spectrum, owing to the fluctuating density of matter caused by acoustic waves that existed in the early Universe [Eis05], is sensitive to the energy density ratio of dark matter to radiation in the Universe [Hu96a, Hu96b, Hu12]. A standard set of cosmological parameters obtained using the CMB data can be found in Ref.[Ber12]. The total matter density is $\Omega_m h^2 = 0.133 \pm 0.066$ and the baryon density is $\Omega_b h^2 = 0.0227 \pm 0.0006$. The measurement of $\Omega_b h^2$ using the CMB data is in good agreement with the observed light element abundances and the standard model of Big-Bang nucleosynthesis [Lid99].

1.1.3 Dark Matter Properties

Because $\Omega_b << 1$, it is clear that baryons cannot account for all of the mass-energy in the Universe. In fact, using the parameters from the CMB, one finds that non-baryonic matter constitutes the majority of the matter density in the Universe with a density of $\Omega_{nbm} h^2 = 0.110 \pm 0.006$ [Ber12]. Additionally, the optically luminous matter density is $\Omega_{lum} h^{-1} \approx 0.0024$ [Fuk04], so the baryon density is much greater than the luminous matter density. This implies that most of the baryons in the Universe are optically dark, probably in the form of a diffuse intergalactic medium [Cen99]. It is possible, however, that some of the baryonic matter could contribute to dark matter. Popular candidates for baryonic dark matter include MAssive Compact Halo Objects (MACHOs) [Pac86, Gri91] or cold molecular gas clouds [DeP95]. Because the total matter density is $\Omega_m \sim 0.3$, we can conclude that most matter in the Universe is not only optically dark, but is also non-baryonic. The analysis of structure formation in the universe suggests that dark matter should also be "cold" (non-relativistic) [Ber10]. This is consistent with the upper bound on the possible contribution from light neutrinos.

Because neither baryons nor neutrinos can be all of the dark matter, it is necessary to postulate new kinds of particles not currently found within the Standard Model, assuming that the general relativistic principles underlying the cosmological models are correct. Candidates for non-baryonic cold dark matter must also satisfy several conditions: (a) they must be stable on cosmological timescales, otherwise they would have decayed, (b) they must interact weakly or not at all with electromagnetic radiation, otherwise they would not be optically dark, (c) they must interact weakly or not at all with “normal” matter, (d) they must yield the correct relic density.

1.1.4 Weakly Interacting Massive Particles

When considering the criteria for a non-baryonic cold dark matter candidate, a well-motivated theoretical and experimental choice appears to be a Weakly Interacting Massive Particle (WIMP), denoted by χ. The fact that annihilation cross sections on the weak scale lead to the correct relic abundance, sometimes referred to as the “WIMP miracle”, was first noticed in the late 1970s [Hut77, Lee77]. This first proposed WIMP, a massive neutrino, is currently not well-motivated by particle physics because it requires a large mass splitting between the three known neutrinos [Pri88].

Among the proposed WIMP candidates, the currently best motivated choice appears to be the lightest superparticle (LSP) in supersymmetric (SUSY) models [Mar11, Jun96]. SUSY models describe a complete symmetry between fermions and bosons and have many interesting features that make them attractive. Specifically, SUSY solves divergence problems in calculating certain Standard Model interactions, such as the Higgs mass correction. It also provides a framework to unify particle physics and gravity, and may explain the origin of the large differences between the electroweak scale, $v = (\sqrt{2}G_F)^{1/2} \approx 246$ GeV and the Planck scale, $M_p \approx 10^{19}$ GeV [Dim81, Sus84, Ber12]. If the SUSY solution is correct, supersymmetric particles could be observed with the next generation of particle accelerators, such as the Large Hadron Collider (LHC) [CER12]. A subset of supersymmetric theories, the Minimal Supersymmetric Standard Model (MSSM) contains the smallest amount of additional information to fully describe all of the fields in the Standard Model within a SUSY framework [Hab85, Ber12]. Many

MSSM models contain a conserved multiplicative quantum number, called R-parity, defined as

$$R \equiv (-1)^{3B+L+2s}, \tag{1.11}$$

where B is the baryon number, L is the lepton number and s is the spin. All of the Standard Model particles have $R = 1$ and all superparticles have $R = -1$. As a consequence of R-parity conservation, superparticles can only decay into an odd number of superparticles and the LSP can only be destroyed by pair annihilation. Because dark matter has no electromagnetic interactions, a WIMP LSP must have no charge, ruling out several candidates. The stability of the LSP makes it an excellent WIMP candidate, since they would have been produced copiously during the Big Bang and would still be present today.

It is possible that the dark matter is not a WIMP, nor does it need to be one specific type of particle. Further discussion on some of the more exotic forms of dark matter can be found in Refs.[Ber05, Ber00] and references therein. One particularly interesting non-WIMP candidate for dark matter is the axion, which was postulated to solve the "strong *CP*" problem in quantum chromodynamics (QCD) [Pec77b, Pec77a]. Even though axions would be light, they would still be classified as cold dark matter because they would be produced non-thermally [Ber12]. Although the axion is a perfectly viable dark matter candidate, we will restrict our further discussion mainly to the WIMP.

1.1.5 Methods for WIMP Detection

In some detectors for nuclear physics experiments, such as scintillators, particle detection is accomplished by the transfer of energy to electrons in a detector. Whereas charged particles and photons may interact directly with the atomic electrons, other neutral particles are detected using a secondary interaction. For example, neutrons are often detected by the transfer of kinetic energy to a nucleus, which can then produce ionization. Dark matter particles are difficult to detect because they are both neutral and weakly interacting. Methods for detecting WIMP dark matter can be classified as "direct" or "indirect". Direct methods are those in which all interactions take place in a terrestrial apparatus. These methods and experiments will be discussed in detail in the following sections. Indirect methods are those in which the primary interaction happens outside the Earth and produces observable particles that can be detected. For example, positrons may be created through WIMP annihilation in the Milky Way [Jun96]. Both PAMELA [Adr09] and the Fermi Large Area Telescope [Abd09] have observed an excess of high-energy positrons compared to conventional astrophysical models [Mos98]. Although these observations are interesting, they cannot rule out astrophysical sources such as pulsars [Ato95] as a source of the observed excess.

Particle colliders may also be used to look for supersymmetric dark matter. Specifically, the Large Hadron Collider (LHC) is a proton-proton collider that has two large, general purpose experiments called ATLAS [Aad08] and CMS [Ado08], which are being used to search for physics beyond the Standard Model. Energetic collisions at the LHC may produce a variety of supersymmetric particles. Squarks and gluinos, which are the superpartners of the Standard Model quarks and gluons will be produced according to their masses and strong couplings. Considering a model in which R-parity is conserved, they will each cascade to the LSP, which will escape the detector. The LSP can be therefore be characterized by the "missing energy" in the event. The disadvantage of such searches is that the signatures are model dependent [Ber10].

1.1.6 Direct Detection of WIMP Dark Matter

The basics of a direct WIMP search are very simple in principle. WIMPs are gravitationally bound inside galaxies and are constantly passing through the Earth. The direct detection of WIMPs is possible by searching for the nuclear recoil from a putative WIMP-nucleus scatter. For WIMP masses in the 10 GeV to 1 TeV range, the nuclear recoil energy will be less than about 100 keV. Because any particle can scatter from an atomic nucleus, fast neutrons can also deposit energy in these detectors. These scattered neutrons are indistinguishable from WIMPs and are therefore potentially the most dangerous source of background. However, it is interesting to note that the ultimate sensitivity of direct detection experiments to WIMPs in this mass range will be limited by coherent nuclear scattering from solar neutrinos.

The shape of the nuclear recoil spectrum depends on the WIMP velocity distribution, which is usually taken to be a Maxwellian distribution with an average of 220 km/s. The differential energy spectrum is expected to be a featureless and smoothly decreasing exponential function [Lew96]. The expected rate in a direct detection experiment is given approximately by Ref.[Ber05] as

$$R \approx \sum_i N_i \frac{\rho_\chi}{m_\chi} \left\langle \sigma_{i\chi} \right\rangle . \tag{1.12}$$

This rate depends on the number of nuclei in the detector, N_i, of species i from which a WIMP could scatter, the local WIMP density ρ_χ, the WIMP mass m_χ and the WIMP-nucleus interaction cross section $\langle \sigma_{i\chi} \rangle$. Based on galactic modeling, Ref.[Kam98] estimated the local dark matter density to be $\rho_{\mathrm{DM}}^{\mathrm{local}} \approx 0.3$ GeV cm^{-3}. This essentially leaves the mass and cross section of the WIMP as unknowns. For this reason, the experimental observable, which is the scattering rate as a function of nuclear recoil energy, is usually expressed as a contour in the WIMP cross section - WIMP mass plane. At low WIMP masses, the sensitivity decreases due to experimental energy thresholds. At high WIMP masses, the sensitivity decreases because the rate is proportional to $1/m_\chi$. From these considerations, direct detection experiments will be more sensitive to WIMP masses close to the target nuclear mass. See Fig. 1.5.

The WIMP scattering cross section also depends on the nature of the couplings. WIMP scattering is usually discussed in the context of spin-dependent (SD) and spin-independent (SI) couplings. Because SD interactions depend on a nuclear spin factor $J(J+1)$ rather than the number of nucleons, little is gained from using a heavier target. On the other hand, SI cross sections scale approximately as the square of the nuclear mass number A. It is therefore preferable to use higher-mass nuclei as targets for these types of experiments.

1.1.7 Direct Detection Experiments

There are many direct dark matter detection experiments that use of a variety of different technologies including detection via ionization, scintillation, phonons, or some combination. A selection of current direct dark matter detection experiments is illustrated in Fig. 1.4. For detailed descriptions of these experiments, the reader is referred to Refs.[Ber12, Ber10] and references therein. Fig. 1.5 shows a selection of current experimental results along with selected theoretical predictions and next generation experiment's projected sensitivities.

There are currently several experiments that have claimed a result consistent with WIMPs. The DAMA collaboration operated up to 250 kg of NaI(Tl) detectors at the Laboratori Nazionali del Gran Sasso (LNGS), near L'Aquila, Italy. They search for an annual modulation in their signal as a consequence of the Earth's rotation around the Sun with respect to the solar system's rotation around the galaxy. A higher WIMP flux is expected around June 2, when the two velocities are in the same direction, and a smaller flux around December 2, when the two velocities are in opposite directions. They have reported an observed annual modulation of their signal with the expected period and phase at an 8.9 σ level. The red regions in the plot show two possible explanations of the data, one with $m_\chi \approx 50$ GeV and one for a lower WIMP mass of

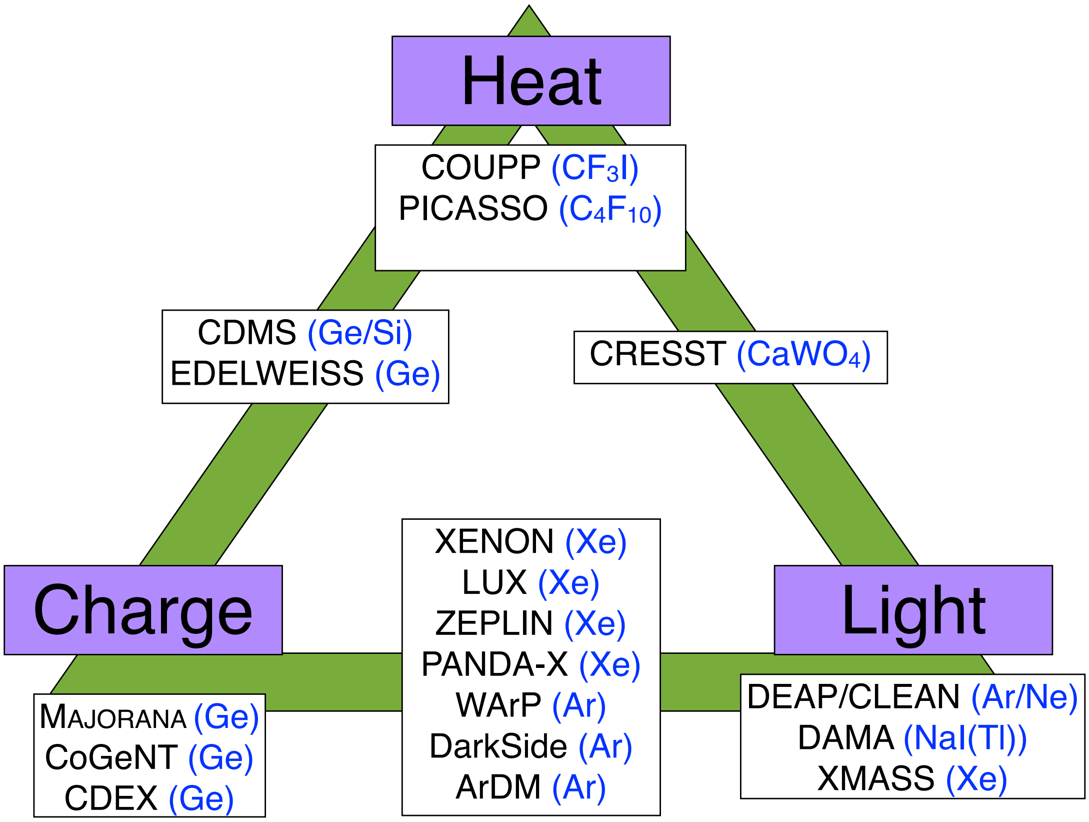

Figure 1.4: Selection of current dark matter direct detection experiments and detection technologies. The detector target materials are listed in blue following the experiment name. Experiments shown between categories uses a hybrid of those detection techniques.

about 6 to 10 GeV. The dark red regions correspond to the DAMA data if there was a significant ion channeling effect [Ber07].

The CRESST experiment [Ang11] uses both the phonon and scintillation signal from cryogenic $CaWO_4$. A recent analysis of their data showed an excess compatible with WIMPs, although their signal is present in a large background. The green regions in Fig. 1.5 show the results of a maximum likelihood analysis which provides two possible solutions at the 4 σ level corresponding to WIMP masses of about 12 and 25 GeV.

There is considerable tension with these results and the compatibility with the null observations from several other experiments. The CDMS [Coo10] and XENON100 [Apr11] experiments, along with the 2010 CoGeNT analysis [Aal11] seem to rule out both the CRESST and DAMA results. The next generation of WIMP dark matter direct detection experiments should provide significant insight into this problem. Projected sensitivities of these experiments will probe cross sections as low as 10^{-47} cm^2 for WIMP masses on the 10 to 1000 GeV range, testing many of the SUSY model predictions. A selection of future experiment's projected sensitivities are shown as dashed curves in Fig. 1.5. Experiments with very low energy thresholds such as the MAJORANA DEMONSTRATOR (Section 1.2.5) will be sensitive to lighter WIMP masses.

1.1.8 Noble Liquids for WIMP Detection

Of particular relevance to this dissertation, several of the current and next generation large-scale detectors designed to search for WIMP dark matter will make use of large volumes of liquified noble gas (LNe, LAr, LXe). Noble liquids are excellent scintillators and have a large ionization yield in response to the passage of radiation. In addition, the relative low cost and ease of scalability make them attractive target materials for WIMP searches. These experiments will search for the scintillation light, and in some cases, the ionization charges generated from the recoiling nucleus after a putative

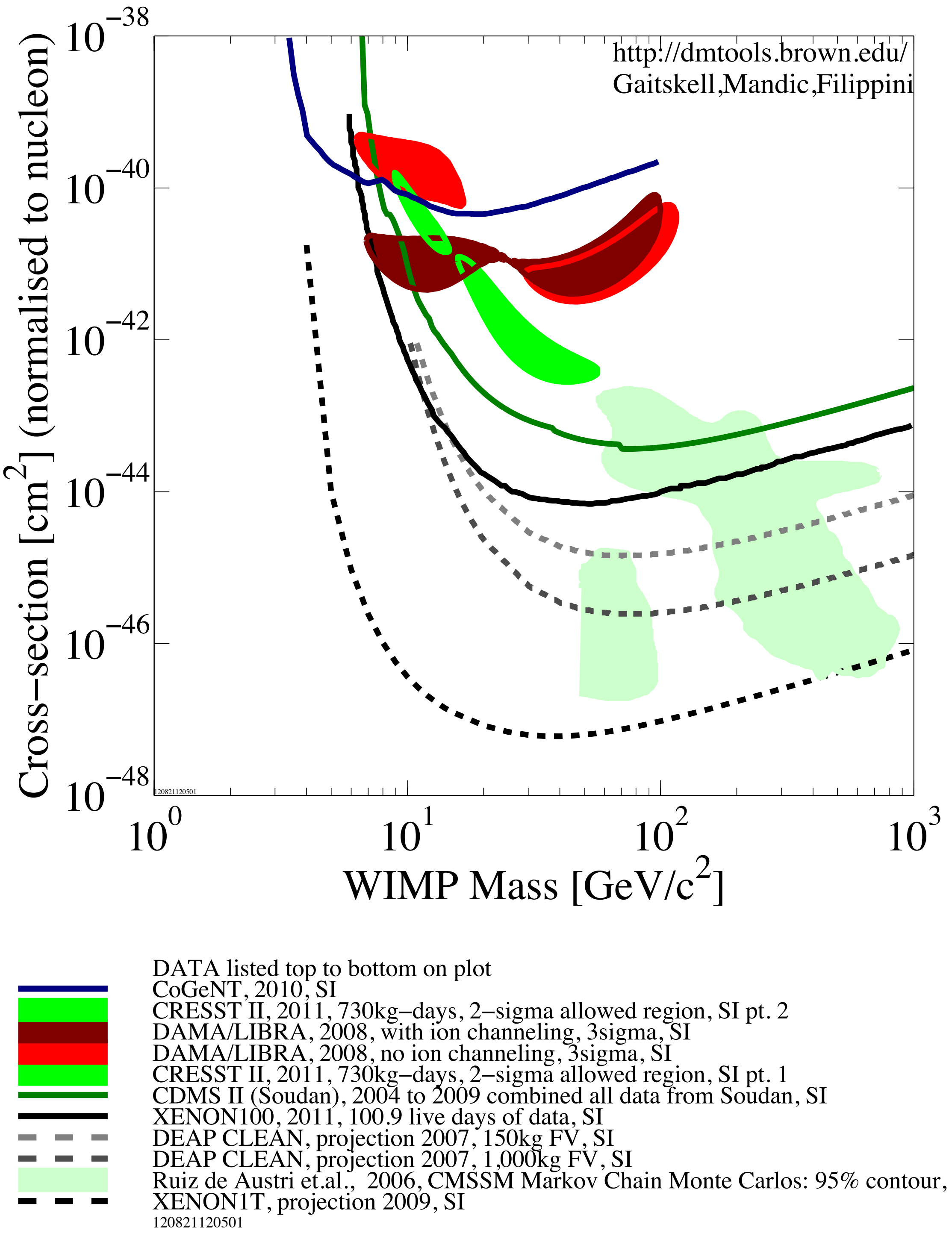

Figure 1.5: Selected current experimental results for SI dark matter interactions. Solid lines indicate exclusion limits determined from experiments. The red and green filled regions are the allowed regions from experiments who have claimed positive signals. Dashed curves are next generation experiment's projected sensitivities. The light green filled region is a theoretical prediction using a Constrained Minimal Supersymmetric Standard Model (CMSSM) [dA06], which allows fewer free parameters than other MSSM models [Kan94].

Table 1.1: Some relevant physical properties of Ne, Ar and Xe. Excimer lifetimes from Refs.[Lip08, Nik08, Hit83].

Property	Ne	Ar	Xe
Atomic number	10	18	54
Mean atomic mass	20.2	40.0	131.3
Boiling point T_b at 1 atm (K)	27.1	87.3	165.0
Liquid density at T_b (g/cm^3)	1.12	1.40	2.94
Scintillation wavelength (nm)	78	128	178
Singlet lifetime (ns)	$< 18.2 \pm 0.2$	7.0 ± 1.0	4.3 ± 0.6
Triplet lifetime (ns)	14900 ± 300	1600 ± 100	22.0 ± 2.0

WIMP-nucleus scatter.

Scintillation light is generated in noble gases as a result of Ne, Ar or Xe atoms, denoted by R, interacting with ionizing radiation where an excited dimer R_2^* is formed [Kub77, Apr05]. The scintillation light has two decay components due to de-excitation of the singlet and triplet states of the excimer $\mathrm{R}_2^* \rightarrow 2\mathrm{R} + h\nu$, where $h\nu$ denotes a vacuum-ultraviolet (VUV) photon emitted in the process. Whereas the scintillation pulse shape from nuclear recoils shows both a fast and a slow component from the de-excitation of singlet and triplet states, respectively, an electronic recoil produces only a slow component [Hit83]. The difference in the scintillation response to different types of radiation becomes the basis for pulse shape discrimination (PSD). This is most effective in LAr and LNe where the time separation between the two decay components is large. Some of the relevant physical properties of Ne, Ar and Xe are shown in Table 1.1.

Noble gas detectors for dark matter searches may be divided roughly into two classes: those that use both the scintillation and ionization channels and those that use the scintillation channel only. The breakdown of these experiments including their detector target material can be seen in Fig. 1.4.

Time Projection Chambers (TPCs) make use of both the ionization and scintillation signal. An event within the liquid volume of the TPC will create both ionization electrons and prompt scintillation light, referred to as $S1$. The ionization electrons drift under the influence of an external electric field into a gas volume where they produce a second scintillation signal proportional to the ionization yield [Dol70, Bol99, Bol06], referred to as $S2$. The ratio $S2/S1$ will be higher for an electronic recoil which produces a greater ionization yield than for a nuclear recoil. Because WIMPs or neutrons produce nuclear recoils, whereas β and γ rays produce electronic recoils, this becomes the basis for background discrimination. An ArTPC has the advantage over a XeTPC in that PSD may be used in addition to $S2/S1$. The disadvantages of the ArTPC are the lower mass number and because the scintillation wavelength is small compared to Xe, a wavelength shifter must be used for the efficient detection by commercial photomultiplier tubes (PMTs).

The DEAP/CLEAN Experimental Program

Single phase noble liquid detectors search for WIMPs using the scintillation channel only. The Dark matter Experiment with Argon and Pulse shape discrimination (DEAP) and proposed Cryogenic Low Energy Astrophysics with Noble gases (CLEAN) experiments are based on LAr and LNe detectors for dark matter and *pp* solar neutrino detection [Bou04]. Both materials have excellent scintillation light yields, are transparent to their own scintillation light, and allow pulse shape discrimination to separate electronic and nuclear recoils [Lip08, Nik08]. The MiniCLEAN detector is a 500 kg (∼100 kg fiducial mass) prototype to be built at SNOLAB, located in Sudbury, Ontario, which will operate interchangeably with LAr and LNe [McK07]. The experiment will first run with LAr to be followed by operation with LNe. Because the WIMP scattering cross section scales as A^2, the event rate of a potential signal can be compared between the different phases to verify a potential WIMP signal. The detector will consist of a spherical acrylic vessel, filled with purified LAr or LNe. The center

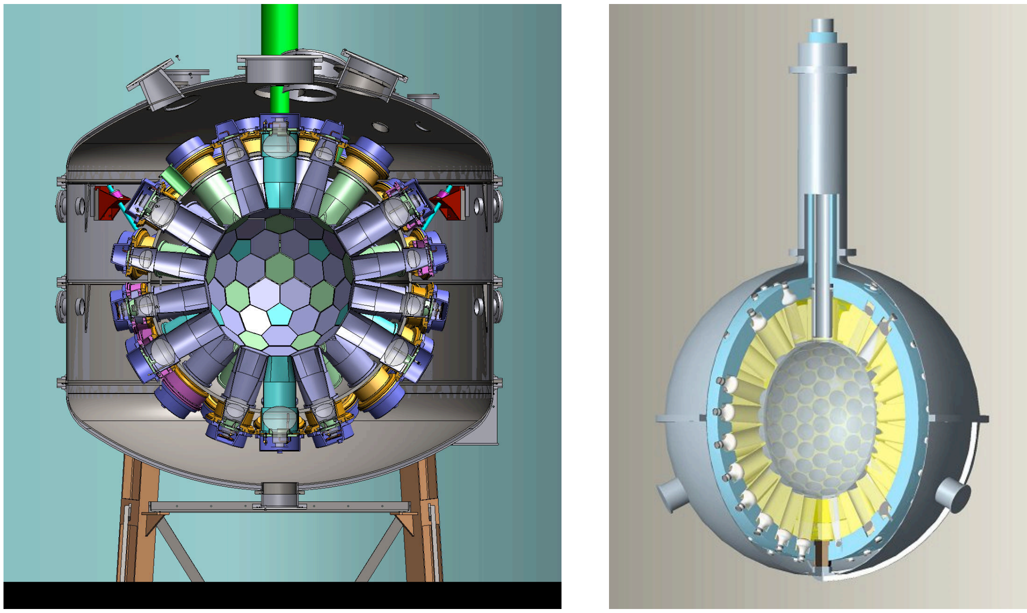

Figure 1.6: Schematic view of the MiniCLEAN (left) and DEAP-3600 (right) detectors. The MiniCLEAN inner target has a diameter of about 45 cm. The DEAP-3600 inner target will be about twice the diameter of MiniCLEAN to accommodate a larger fiducial mass. Figures from the DEAP/CLEAN collaboration (`deapclean.org`).

of the detector will be viewed by 92 PMTs immersed in the cryogenic liquid. The primary scintillation light will be absorbed by a tetra-phenyl butadiene (TPB) wavelength shifter, reemitted in the visible range, and will be transported to the PMTs via acrylic lightguides. Additionally, a 3600 kg LAr detector, called DEAP-3600, is being deployed at SNOLAB [Bou08]. The detector will have a fiducial mass of approximately 1000 kg viewed by 266 PMTs. A schematic view of the MiniCLEAN and DEAP-3600 detectors is shown in Fig. 1.6. The longer-term goal for the DEAP/CLEAN collaboration is to build a 100-ton-scale LNe detector called CLEAN [McK05].

1.2 Neutrino Masses and Mixings

1.2.1 Neutrino History

Early physics experiments had shown that α particles were emitted at well-defined energies, but physicists were puzzled when they found that β particles were emitted with a continuous energy distribution. A new particle was first postulated by Pauli in a letter to the attendees of a physics conference in Tübingen, Germany in 1930 as a "desperate remedy" to conserve energy and angular momentum in the β-decay process [ETH]. This new particle would be electrically neutral to conserve charge, and would have spin $\frac{1}{2}$ to conserve angular momentum. It also must not interact strongly with matter so that it would not be detected along with the electron. Later, in a letter to Fred Reines, Fermi called this particle the *neutrino*. Nuclear beta decay can be written as

$$ {}^{A}_{Z}X_{N} \rightarrow {}^{A}_{Z+1} X_{N-1} + e^{-} + \bar{\nu}_{e}, \tag{1.13}$$

where the neutrino $\bar{\nu}_e$ is actually an anti-neutrino so the final state contains a lepton anti-lepton pair. Following Pauli's neutrino hypothesis, Fermi developed the formal theory of β decay in 1934 [Fer34], which has since evolved into the standard model of electroweak interactions.

The neutrino remained elusive for more than two decades before it was discovered in 1956 by Reines and Cowan using anti-neutrinos produced from a nuclear reactor [Rei53, Cow56]. Less than ten years later, a new discovery was made at Brookhaven National Laboratory (BNL) showing the neutrinos produced with muons were different than neutrinos produced with electrons [Dan62]. Following this discovery, these neutrinos were referred to as "electron-neutrinos" (ν_e) and "muon-neutrinos" (ν_μ). In 1989, measurements of the partial widths of the Z^0 from the Large Electron-Positron Collider

(LEP) at CERN showed that there were three families of light, weakly-interacting neutrinos [DeC89]. In 2000, the DoNuT Experiment at Fermilab confirmed the existence of a "tau-neutrino"(ν_τ) [Kod02].

1.2.2 Neutrino Masses and Mixings

During the 1950s and 1960s, attempts to observe neutrinos from the sun were pioneered by Davis and Bahcall [Bah64, Dav64]. The famous Homestake neutrino experiment detected solar neutrinos in 1968 with a flux of only about one third of what was predicted from solar models [Cle98]. This discrepancy was known as the "solar neutrino problem". A proposed solution to this problem was that neutrinos can change in flavor on macroscopic length scales provided that they have mass and their states of definite mass (ν_1,ν_2,ν_3) are not the same as their flavor states (ν_e,ν_μ,ν_τ). This difference between flavor and mass eigenstates lead to the phenomenon of neutrino oscillations. In this scenario, the three known neutrino flavor eigenstates can be connected with the mass eigenstates through the Pontecorvo-Maki-Nakagawa-Sakata (PMNS) matrix $U_{\alpha i}$ as [Pon68, Mak62]

$$|\nu_\alpha\rangle = \sum_i U_{\alpha i} \, |\nu_i\rangle \, , \tag{1.14}$$

where $|\nu_\alpha\rangle$ represents a neutrino with definite flavor, α, and $|\nu_i\rangle$ represents a neutrino with definite mass, i.

Considering a hypothetical two-neutrino scenario, the mixing can be described by a 2 × 2 matrix, given by

$$U_{2\nu} = \begin{pmatrix} \cos\theta & \sin\theta \\ -\sin\theta & \cos\theta \end{pmatrix} . \tag{1.15}$$

Using this matrix, the probability of a neutrino in flavor state α to be found later in flavor state β can be calculated to be [Bil78]

$$P_{\alpha\beta} = \sin^2(2\theta)\sin^2\left(1.27\frac{(m_i^2 - m_j^2)L}{E}\right), \tag{1.16}$$

which describes periodic neutrino oscillations. The angle θ determines the amplitude of the oscillation, i.e. the amount of mixing between flavor states α and β. The quantity L is the distance the neutrino has traveled in km, E is the neutrino energy in GeV, and $m_{i,j}$ are the neutrino masses in eV. The quantity $m_i^2 - m_j^2$ determines the frequency of the oscillation.

Extending this to the three-neutrino scenario, a common parameterization of the mixing matrix motivated by experimental observables is given by

$$\begin{aligned} U &= \begin{bmatrix} U_{e1} & U_{e2} & U_{e3} \\ U_{\mu1} & U_{\mu2} & U_{\mu3} \\ U_{\tau1} & U_{\tau2} & U_{\tau3} \end{bmatrix} \\ &= \begin{bmatrix} 1 & 0 & 0 \\ 0 & c_{23} & s_{23} \\ 0 & -s_{23} & c_{23} \end{bmatrix} \begin{bmatrix} c_{13} & 0 & s_{13}e^{-i\delta} \\ 0 & 1 & 0 \\ -s_{13}e^{-i\delta} & 0 & c_{13} \end{bmatrix} \begin{bmatrix} c_{12} & s_{12} & 0 \\ -s_{12} & c_{12} & 0 \\ 0 & 0 & 1 \end{bmatrix} \begin{bmatrix} e^{i\alpha_1/2} & 0 & 0 \\ 0 & e^{i\alpha_2/2} & 0 \\ 0 & 0 & 1 \end{bmatrix}, \end{aligned} \tag{1.17}$$

where $s_{ij} \equiv \sin(\theta_{ij})$ and $c_{ij} \equiv \cos(\theta_{ij})$. The mixing matrix can be described by three angles and one complex phase, δ, which is non-zero only if neutrino oscillations violate CP symmetry. The phases α_1 and α_2 affect only Majorana particles [Avi08] (see Section 1.2.3). Although the probabilities $P_{\alpha\beta}$ in the real three-neutrino scenario may depend on all of the observable parameters that characterize U, the approximate two-neutrino probability (Eqn. 1.16) works for many experimental situations [Cam08].

While neutrino oscillations indicate that neutrinos have mass, the experiments are sensitive only to the absolute value of the differences in the squares of the neutrino masses, $\Delta m_{ij}^2 \equiv |m_i^2 - m_j^2|$. However, a lower limit on the absolute value of the neutrino mass scale $m_{\text{scale}} = \sqrt{\Delta m^2}$ can be determined. Neutrino oscillations were first discovered in atmospheric neutrinos by the Super-Kamiokande collaboration in 1998 [Fuk98]. These results can be interpreted as nearly maximal mixing between the ν_μ and ν_τ neutrinos. This mixing, known as atmospheric mixing, gives one of the angles in the PMNS matrix, θ_{23}. This angle has since been constrained further by searches for ν_μ disappearance in accelerator-produced ν_μ beams, specifically by the K2K [Ahn06] and MINOS [Ada12] experiments. The corresponding Δm^2 implies a neutrino mass scale of about 50 meV. Results from the Sudbury Neutrino Observatory (SNO) provided a direct solution to the "solar neutrino problem" discussed above by showing v_e's produced in the sun underwent flavor change affected by solar matter [Ahm01, Wol78]. The solar mixing angle, θ_{12}, and associated mass splitting was determined from SNO [Aha08] and KamLAND [Abe08] data. The third mixing angle, θ_{13}, was recently measured by the Daya Bay [An12] and RENO [Ahn12] experiments.

Although many neutrino oscillation experiments over the past several decades have convincingly shown neutrinos to have mass, there is still much to be learned about the nature of neutrino masses. The mass splitting $\Delta m_{21}^2 \equiv \Delta m_{\text{sol}}^2$ is referred to as "solar mixing" and $|\Delta m_{31}^2| \approx |\Delta m_{32}^2| \equiv |\Delta m_{\text{atm}}^2|$ is referred to as "atmospheric mixing". The sign of Δm_{sol}^2 is known from matter effects [Wol78] but it is currently unknown whether m_3 is the heaviest or lightest mass eigenstate. The former is referred to as the "normal" hierarchy and the later is referred to as the "inverted" hierarchy. It is also not known whether all m_i are of similar magnitude as $\sqrt{\Delta m_{ij}^2}$ or all $m_i >> \sqrt{\Delta m_{ij}^2}$; the latter is referred to as the "degenerate" pattern. The current best values for the mixing angles and mass splittings taken from a global analysis of oscillation data are shown in

Table 1.2.

Table 1.2: The best-fit experimental values for neutrino mixing angles and mass splittings, derived from a global fit of the current neutrino oscillation data [Ber12].

Parameter	value ($\pm 1\sigma$)
$\Delta m^2_{\rm sol}$ [$\times 10^{-5}$eV^2]	$7.58^{+0.22}_{-0.26}$
$\lvert\Delta m^2_{\rm atm}\rvert$ [$\times 10^{-3}$eV^2]	$2.35^{+0.12}_{-0.09}$
$\sin^2\theta_{12}$	$0.312^{+0.018}_{-0.015}$
$\sin^2\theta_{23}$	$0.42^{+0.08}_{-0.03}$
$\sin^2\theta_{13}$	$0.025^{+0.007}_{-0.008}$

There is another very important implication of neutrino masses. Neutrinos are separated from anti-neutrinos because of the chiral nature of the weak interaction. Chirality is the Lorentz invariant analog of helicity, which is defined as the spin projection on the momentum vector. The weak interaction has a definite preferred handedness [Wu57]. Only the left-handed (LH) component of the neutrino field interacts, whereas the right-handed component has no weak interactions. Similarly, for anti-neutrinos, only the RH component interacts. In a massless neutrino scenario, the chirality coincides with the helicity, and is always conserved [Cam08]. This means that the LH neutrino is always different from a RH anti-neutrino (Dirac neutrinos). However, if the neutrino is massive, it is possible for the LH neutrino to develop a RH component. A neutrino and an anti-neutrino with both a RH and LH component might be identical particles, as recognized by Majorana in 1937 [Maj37]. The only practical way to search for the Majorana nature of the neutrino is through neutrinoless double-beta decay ($\beta\beta(0\nu)$) [Rac37].

1.2.3 Double-Beta Decay

Double-beta decay is a rare transition that can proceed in many even-even nuclei. Two-neutrino double beta decay ($\beta\beta(2\nu)$) is a second-order weak process predicted within the Standard Model. It can be written as

$$^A_ZX_N \rightarrow ^A_{Z+2} X_{N-2} + 2e^- + 2\bar{\nu}_e. \tag{1.18}$$

The rate for $\beta\beta(2\nu)$ is given by

$$(T^{2\nu}_{1/2})^{-1} = G_{2\nu}(Q_{\beta\beta}, Z)|M_{2\nu}|^2 \tag{1.19}$$

where $G_{2\nu}(Q_{\beta\beta}, Z)$ is a four-body phase space factor and $M_{2\nu}$ is a nuclear matrix element that describes the physics of the reaction. This reaction conserves both electric charge and lepton number. Early estimates of the $\beta\beta(2\nu)$ decay rate were greater than 10^{20} y [GM35]. Double-beta decay was first observed in 1987 with the isotope ^{82}Se [Ell87]. Of the 35 naturally occurring isotopes capable of undergoing double-beta decay, $\beta\beta(2\nu)$ has currently been observed in twelve [Ber12].

On the other hand, neutrinoless double-beta decay ($\beta\beta(0\nu)$) can only occur if neutrinos are Majorana particles. The process can be mediated by the exchange of light Majorana neutrinos. However, even if this were not the case, the successful observation of a $\beta\beta(0\nu)$ decay would show that the neutrino is a Majorana fermion [Sch82]. Neutrinoless double-beta decay may be written as

$$^A_ZX_N \rightarrow ^A_{Z+2} X_{N-2} + 2e^-, \tag{1.20}$$

where there are only two electrons and no final-state neutrinos. Within a nucleus, a β decay produces a RH anti-neutrino $\bar{\nu}_e$. The $\bar{\nu}_e$ develops a LH component, which is nothing but the LH component of the neutrino ν_e, and is captured by a nearby neutron through the reaction $\nu_e + n \rightarrow p + e^-$ [Cam08]. This reaction violates lepton number, and is thus forbidden in standard electroweak theory. If we assume light Majorana neutrino exchange, the rate for $\beta\beta(0\nu)$ may be written as

$$(T^{0\nu}_{1/2})^{-1} = G_{0\nu}(Q_{\beta\beta}, Z)|M_{0\nu}|^2 m^2_{\beta\beta}, \tag{1.21}$$

where $m_{\beta\beta}$ effective Majorana mass of the electron neutrino. Using the notation of Eqn. 1.17, $m_{\beta\beta}$ is given by

$$m_{\beta\beta} \equiv \left|\sum_i m_i U^2_{ei}\right| = \left|c^2_{13}c^2_{12}m_1 + c^2_{13}s^2_{12}m_2e^{i2\alpha_1} + s^2_{13}m_3e^{i2\alpha_2}\right|, \tag{1.22}$$

where the m_i's are the masses of the three light neutrinos and α_1 and α_2 are the Majorana phases. In general, any values for the Majorana phases are possible, leading to potential cancellations in the sum, see Fig. 1.7.

Nuclear structure calculations are required to determine $m_{\beta\beta}$ from the $\beta\beta(0\nu)$ decay rate. The quantity $G_{0\nu}(Q_{\beta\beta}, Z)$ is a calculable two-body phase space factor, which includes a Z-dependent Fermi function [Fer34, Boe92]. The quantity $M_{0\nu}$ is a nuclear matrix element. Averaging over all published matrix elements for any given double-beta decay isotope results in a factor of ~ 3 uncertainty [Ber12], although imposing the requirement that the $\beta\beta(2\nu)$ is correctly reproduced may reduce the spread in $M_{0\nu}$ [Šim08]. The accuracy to which the neutrino mass can be determined from the $\beta\beta(0\nu)$ rate will ultimately be determined by the uncertainty in the nuclear matrix elements, the values of the unknown phases, and the experimental sensitivity.

Complimentary to $\beta\beta(0\nu)$, the endpoint of the electron spectrum in traditional β decay is sensitive to the effective electron neutrino mass,

$$m^2_\beta = \sum_i |U_{ei}|^2 m^2_i = c^2_{13}c^2_{12}m^2_1 + c^2_{13}s^2_{12}m^2_2 + s^2_{13}m^2_3. \tag{1.23}$$

Fig. 1.7 shows the allowed regions for $m_{\beta\beta}$ and the lightest neutrino mass for the normal and inverted hierarchies. The contours are shown for the maximum and minimum

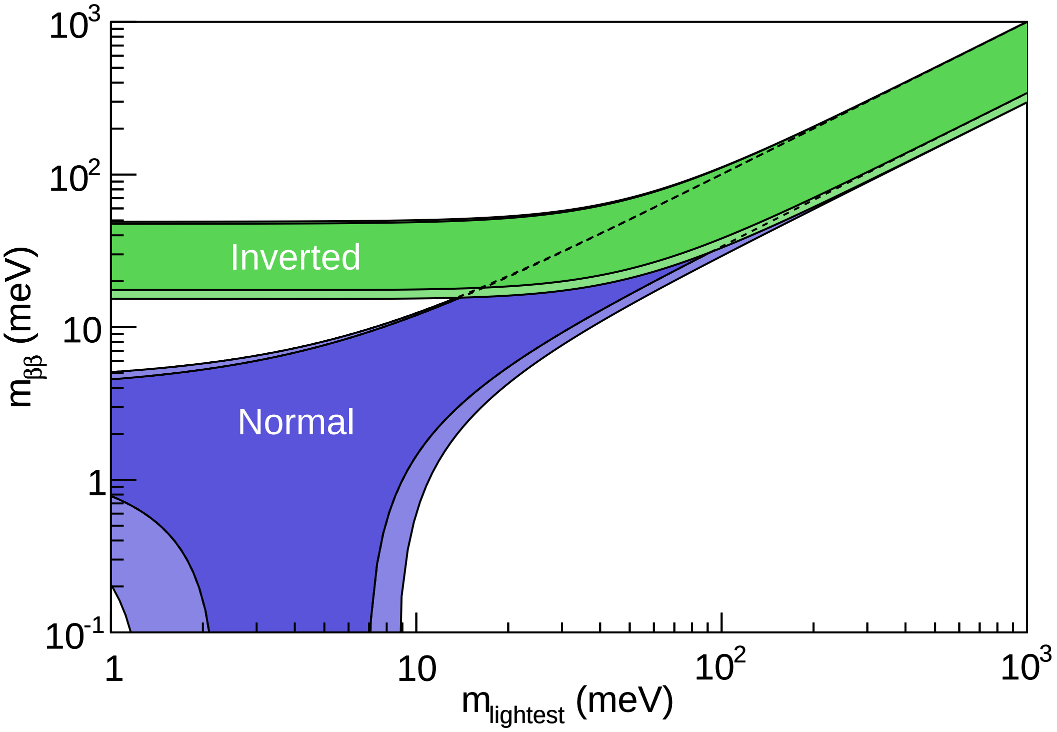

Figure 1.7: Allowed regions for $m_{\beta\beta}$ and the lightest neutrino mass for the normal and inverted hierarchies. The contours are shown for the maximum and minimum allowed values and for the 1σ best fit values for the oscillation parameters in Table 1.2. Plot generated using code written by A. Schubert.

allowed values and for the 1σ best fit values for the oscillation parameters in Table 1.2. Whereas $\beta\beta(0\nu)$ are sensitive to $m_{\beta\beta}$ (Eqn. 1.22), tritium β-decay experiments, such as KATRIN [Wol10], are sensitive to m_β (Eqn. 1.23), hence a limit on the lightest neutrino mass. Additionally, current cosmological models predict the cosmic neutrino background (CνB) [Han06] number density, n_ν, which is related to the neutrino energy density of the Universe, $\Omega_\nu = n_\nu(m_1 + m_2 + m_3)/\rho_{crit}$ [Cam08]. Cosmological data put an upper limit Ω_ν, and thus on the sum of the neutrino masses [Ber12].

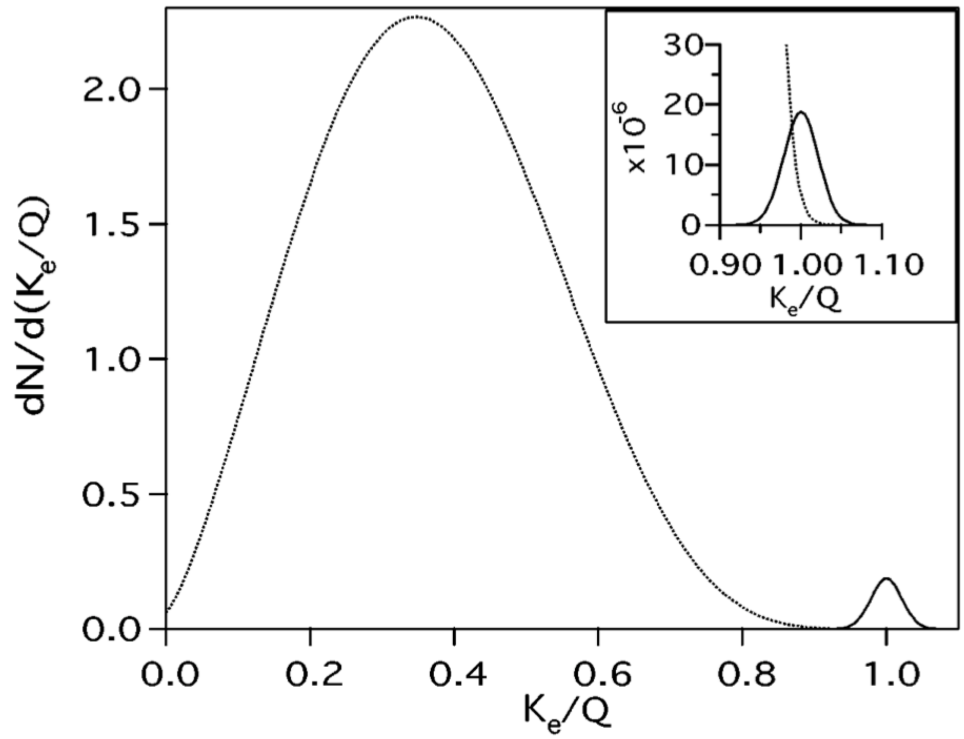

Figure 1.8: Illustration of the $\beta\beta(2\nu)$ (dotted curve) and $\beta\beta(0\nu)$ (solid curve) electron energy spectra. The $\beta\beta(2\nu)$ spectrum is normalized to 1 and the $\beta\beta(0\nu)$ spectrum is normalized to 10^2 (10^6 in the inset). Spectra are convolved with a 5% energy resolution. Image from Ref. [Ell02].

1.2.4 Experimental Aspects

The experimental detection of double-beta decay is accomplished through the observation of the electron sum energy spectra, which is dependent on the phase space of the outgoing light particles. Fig. 1.8 illustrates this for both $\beta\beta(2\nu)$ and $\beta\beta(0\nu)$. The 2ν decay mode is similar to a single β-decay spectrum, where the summed kinetic energy of the two electrons, K_e, displays a continuous energy spectrum spectrum up to the Q-value of the decay. In contrast, in the 0ν decay mode the two electrons carry all of the available kinetic energy. Thus, the experimental signature of $\beta\beta(0\nu)$ is a single peak at the Q-value of the decay.

For the best sensitivity to $m_{\beta\beta}$, a detector must maximize the $\beta\beta(0\nu)$ signal and minimize other sources of background. For a background-limited experiment, the sensitivity is to $m_{\beta\beta}$ is given explicitly as [Moe91]

$$m_{\beta\beta} = (2.50 \times 10^{-8}\mathrm{eV}) \left[\frac{W}{fx\epsilon G^{0\nu} \left|M^{0\nu}\right|^2}\right]^{1/2} \left[\frac{b\Delta E}{MT}\right]^{1/4}, \tag{1.24}$$

where W is the molecular weight of the source material, f is the isotopic abundance, x is the number of double-beta decay candidate atoms per molecule, ϵ is the detector efficiency, b is the number of background counts per kg·year·keV, ΔE is the energy window in keV, M is the mass of isotope in kilograms, T is the live time of the experiment in years, and $G^{0\nu}$ and $M^{0\nu}$ are the phase space factors and nuclear matrix elements from Eqn. 1.21, respectively. It can be seen from Eqn. 1.24 that in order to build a successful experiment to begin to probe the $m_{\beta\beta}$ regions shown in Fig. 1.7, one needs a large, efficient source mass, good energy resolution, and extremely low levels of backgrounds. In fact, $\beta\beta(0\nu)$ experiments are searching for one of the rarest signals ever to be detected; their success requires large, shielded detectors, extremely radio-pure construction materials and operation in deep underground laboratories.

1.2.5 Double-Beta Decay Experimental Programs

Because of the large uncertainties in the nuclear matrix elements and technical challenges, it is the consensus of the double-beta decay community that measurements of $\beta\beta(0\nu)$ in at least three isotopes is warranted [Avi08]. Each isotope has its own experimental advantages and disadvantages in regards to Q-value, isotopic abundance, and its performance as a radiation detector. A list of current experimental efforts can be found in Table 1.3. Of particular relevance to the measurements in this dissertation are the current experimental efforts to measure $\beta\beta(0\nu)$ in ^{76}Ge.

Table 1.3: Current and proposed $\beta\beta 0\nu$ experiments. Details on these experiments may be found in Refs.[Avi08, Ber12] and references therein.

$\beta\beta$ isotope	Experiment	Technique	Isotope natural abundance (%)	Q-value (MeV)
^{116}Cd/^{130}Te	COBRA	CZT semiconductor detectors	7.49 / 33.8	2.805 / 2.533
^{130}Te	COURICINO/CUORE	TeO_2 bolometers	33.8	2.533
^{136}Xe	EXO	Enriched LXe TPC	8.9	2.479
^{136}Xe	KamLAND-Zen	LXe scintillator	8.9	2.479
^{136}Xe	NEXT	Enriched high-pressure gas TPC	8.9	2.479
^{76}Ge	MAJORANA/GERDA	Enriched Ge semiconductors	7.8	2.039
^{100}Mo	MOON	Enriched Mo foils/scintillator	9.6	3.034
^{150}Nd	SNO+	Nd loaded liquid scintillator	5.6	3.367
^{82}Se	SuperNEMO	Enriched Se foils/tracking	8.8	2.996

The Majorana and GERDA Experiments

The MAJORANA [Sch11a, Phi12, Agu11b] and GERmanium Detector Array (GERDA) [Sch05, Car12] experiments are searching for $\beta\beta(0\nu)$ in ^{76}Ge. Germanium can be made into high-purity Ge-diode radiation detectors that will serves as both source and detector. High-purity germanium (HPGe) detectors offer excellent energy resolution and can be enriched in the double-beta decay isotope from 7.44% to greater than 86%. Ge-based experiments have established the best limits on $\beta\beta(0\nu)$ [Aal02, Bau99]. One analysis of the data in Ref. [Bau99] claims evidence for $\beta\beta(0\nu)$ with a half-life of $2.23 \pm 0.44 \times 10^{25}$ y [KK06]. The EXO-200 experiment has recently published limits for $\beta\beta(0\nu)$ in ^{136}Xe that rule out this claimed discovery for all but a few nuclear matrix element calculations [Aug12].

The MAJORANA collaboration is currently conducting an R&D experiment through a demonstrator module consisting of arrays of HPGe detectors deployed in low-background electroformed copper cryostats. The cryostats will be surrounded by a graded passive shield consisting of copper, lead, an active muon veto, and a layer of hydrogenous material to eliminate external backgrounds. The MAJORANA DEMONSTRATOR will be located at the 4850' level of the Sanford Underground Research Facility (SURF), in Lead, SD. The experiment will be fielded with two individual cryostats, containing about 40 kg of HPGe detectors, of which about 30 kg will be enriched to $> 86\%$ ^{76}Ge. Assuming a background of 10^{-3} counts/(keV kg y), after about 100 kg-years of exposure, the MAJORANA DEMONSTRATOR should significantly improve the lower limits on the decay lifetime from the current level of about 2×10^{25} y to about 2×10^{26} y. Assuming a matrix element calculated using the Quasiparticle Random Phase Approximation (QRPA), this corresponds to an upper limit of 90 meV on the effective Majorana electron-neutrino mass [Agu11b]. Backgrounds for the MAJORANA DEMONSTRATOR will be the lower by a factor of about 10^2 with respect to its precursor experiments [KK04].

The GERDA experiment is located in Hall A of the Laboratori Nazionali del Gran Sasso (LNGS), near L'Aquila, Italy. The first phase will use 15 kg of existing enriched detectors from the previous Heidelberg-Moscow [Bau99] and IGEX [Aal02] experiments. The goal for the first phase is to test the claimed signal in Ref. [KK06] with a background of less than 10^{-2} counts/(keV kg y). The second phase will add about 20 kg of additional enriched detectors with a background goal of 10^{-3} counts/(keV kg y). Instead of the compact lead and copper shield used by MAJORANA, the GERDA detectors are submerged directly in a cryostat filled with liquid argon. One key motivation for the work in this thesis is to evaluate neutron shielding properties and γ-ray production from neutron-induced reactions in this shielding material. The liquid argon approach has the potential to significantly reduce backgrounds, but is technically more challenging and riskier. The MAJORANA and GERDA collaborations are preparing to join for a single international tonne-scale Ge-based experiment using the best technologies developed by each collaboration.

1.3 Backgrounds

Current experiments searching for rare interactions such as neutrinoless double-beta decay ($\beta\beta(0\nu)$) and dark matter anticipate event rates in their region of interest to be as low as a few per ton of detector per year. For these experiments to reach the necessary sensitivity, background mitigation is crucial. This section discusses some of the common backgrounds in these types of experiments, with a specific focus on backgrounds caused by fast neutrons. The neutron scattering experiments described in Chapters 3–6 are motivated by the lack of measured cross sections for reactions responsible for these backgrounds. We discuss how these measurements are included in Monte-Carlo simulations used to estimate backgrounds and guide detector design for these rare-event searches.

Although the sources of backgrounds vary from experiment to experiment, they can be roughly divided into two categories: (1) radionuclides from environmental uranium, thorium and potassium which decay with γ-ray emission and may also produce neutrons through (α, n) reactions, and (2) cosmic rays, which can activate materials or produce fast neutrons underground via spallation reactions in rock and shielding materials.

1.3.1 Gamma Rays

The γ radiation from which these experiments must be shielded comes primarily from the decay of primordial ^{238}U, ^{232}Th, ^{40}K and their daughters. Higher concentrations of environmental uranium and thorium require thicker shielding and cause higher levels of radon and neutrons from (α, n) reactions. The presence of isotopes from these decay chains in construction materials results in wide range of radioactivity inside the detectors. Careful material selection or production, and screening is required to ensure acceptable radioactivity levels in detector and shield components. The ^{238}U and ^{232}Th decay chains are shown in Figs. A.1 and A.2.

A particular problem for these experiments is radon; an intermediate decay member of both the uranium and thorium decay series that readily diffuses into the air. The isotope ^{222}Rn, which is produced in the ^{238}U decay series, is by far the strongest source of airborne radioactivity. The daughter isotopes of ^{222}Rn are originally positively charged and may attach to aerosols or plate out on surfaces. The most important of these isotopes to consider is ^{210}Pb, whose 22.2-year half-life is by far the longest among the radon daughters, which makes it a persistent background during the lifetime of any experiment. ^{210}Pb β decays with the emission of a soft β and 46.5-keV γ ray. The decay of the daughter isotope ^{210}Bi produces a 1.16-MeV β and the daughter isotope ^{210}Po produces a 5.3-MeV α particle. All of these decays can be problematic for low background experiments if they occur in or near the detector material. Cleaning procedures such as acid etching or polishing are used in an attempt to remove this surface contamination [Hop08].

1.3.2 Cosmic Rays

Primary hadronic cosmic rays consist of about 90% protons, 9% α particles and 1% other nuclei. Secondary particles including neutrons, electrons, neutrinos, muons and pions are produced through interactions of primary cosmic-ray particles with the Earth's atmosphere. At the surface of the Earth, muons are the most numerous secondary particles. It is because of these backgrounds that it becomes necessary to construct experiments in deep underground laboratories. Only muons and neutrinos are relevant to underground experiments. Secondary neutrons, electrons, protons and photons are absorbed by the overburden within a few tens of meters, but muons can penetrate through miles of rock. Muons that reach underground experiments may produce tertiary photons, electrons and hadrons. Muon-induced neutron backgrounds are discussed further in Section 1.3.3.

Cosmogenic Activation

Secondary cosmic-ray particles can produce backgrounds not only through direct interactions near or inside a detector, but also indirectly though the production of radionuclides. In underground experiments, cosmogenic backgrounds may be produced through exposure of detector materials to the hadronic component of cosmic rays on the surface of the Earth during production, transportation or storage. For argon, ^{39}Ar may be produced via the $(n, 2n)$ reaction, ^{41}Ar may be produced via neutron capture on ^{40}Ar, ^{42}Ar may be produced via the $(\alpha, 2p)$ reaction, and ^{38,39}Cl may be produced via spallation reactions. The isotopes ^{40}Cl and ^{38}Cl can be produced in argon underground through muon capture and spallation reactions. For natural xenon, the cosmogenic isotopies with the largest production rates are ^{121m}Te, ^{123m}Te. ^{127m}Te and ^{109}Cd [Mei09b]. For other target and shield materials of interest such as Ge, Cu and stainless steel, these cosmogenic isotopes can include ^{54}Mn, ^{57,58,60}Co, ^{65}Zn, ^{67}Ga and ^{68}Ge.

1.3.3 Fast Neutrons

Muon-induced neutrons are produced through several processes including spallation and muon capture reactions. The muon-induced neutron flux is strongly depth dependent as the vertical muon intensity decreases with depth. Primary spallation neutrons themselves interact to produce secondary neutrons, which quickly become dominant at larger depths and can compose up to 75% of the high-energy flux at deep sites [For04]. Fast neutrons may also be produced via α particles from decays of uranium and thorium in the detector and surrounding materials that undergo (α, n) reactions on elements in surrounding rock or shielding. Fission neutrons from uranium and thorium may also contribute to the neutron flux, but the dominant production mechanism is usually (α, n) [For04]. Fig. 1.9 illustrates how the neutron fluxes change as a function of depth in meters of water equivalent (m.w.e.) shielding. The data for this plot was taken from Ref. [Heu95]. The flux of neutrons produced by muons in a typical lead shield is shown along with the flux of neutrons from (α, n) reactions for uranium and thorium concentrations typical in the continental upper crust (36 Bq ^{238}U kg^{-1} and 44 Bq ^{232}Th kg^{-1}). Muon-induced neutrons are dominant until about 100 m.w.e, where (α, n)-derived neutrons become more important.

The neutron energy spectra for muon-induced neutrons and (α, n)-derived neutrons are quite different. The (α, n) spectrum cuts off sharply around 10 MeV whereas the muon-induced spectrum extends out to several hundred MeV. The lower energy

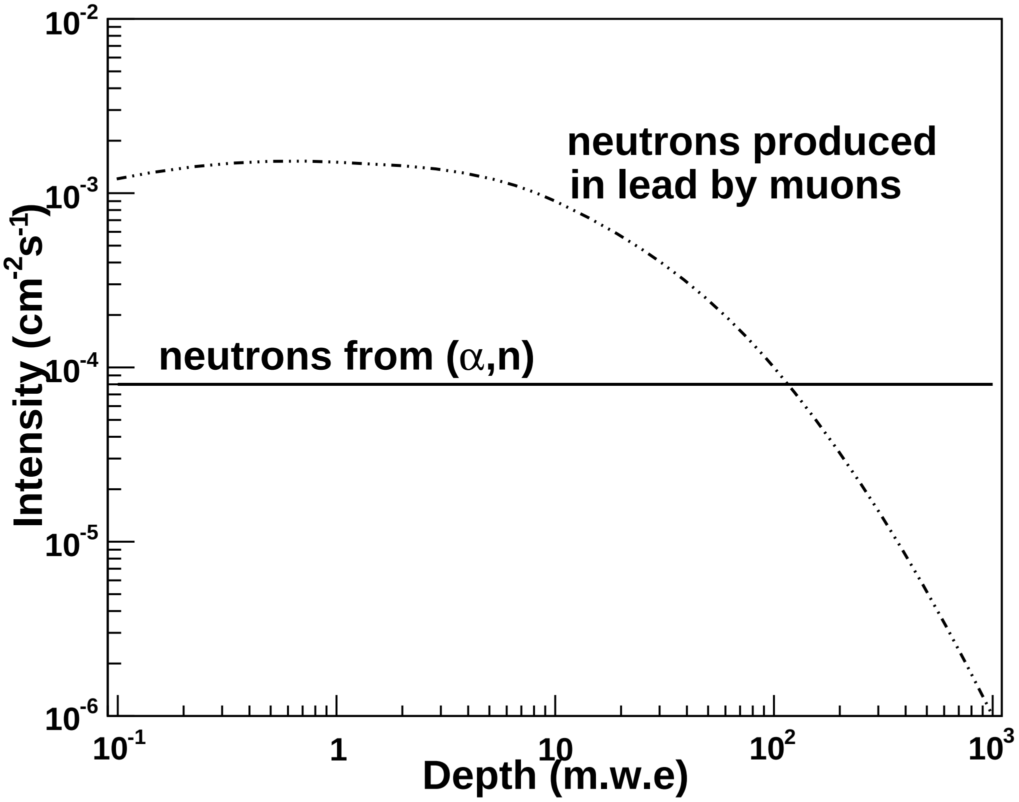

Figure 1.9: Muon-induced neutron and (α, n)-derived neutron fluxes as a function of depth. The flux of neutrons produced by muons in a typical lead shield is shown along with the flux of neutrons from (α, n) reactions for uranium and thorium concentrations typical in the continental upper crust (36 Bq ^{238}U kg^{-1} and 44 Bq ^{232}Th kg^{-1}). Data for this plot was taken from Ref.[Heu95].

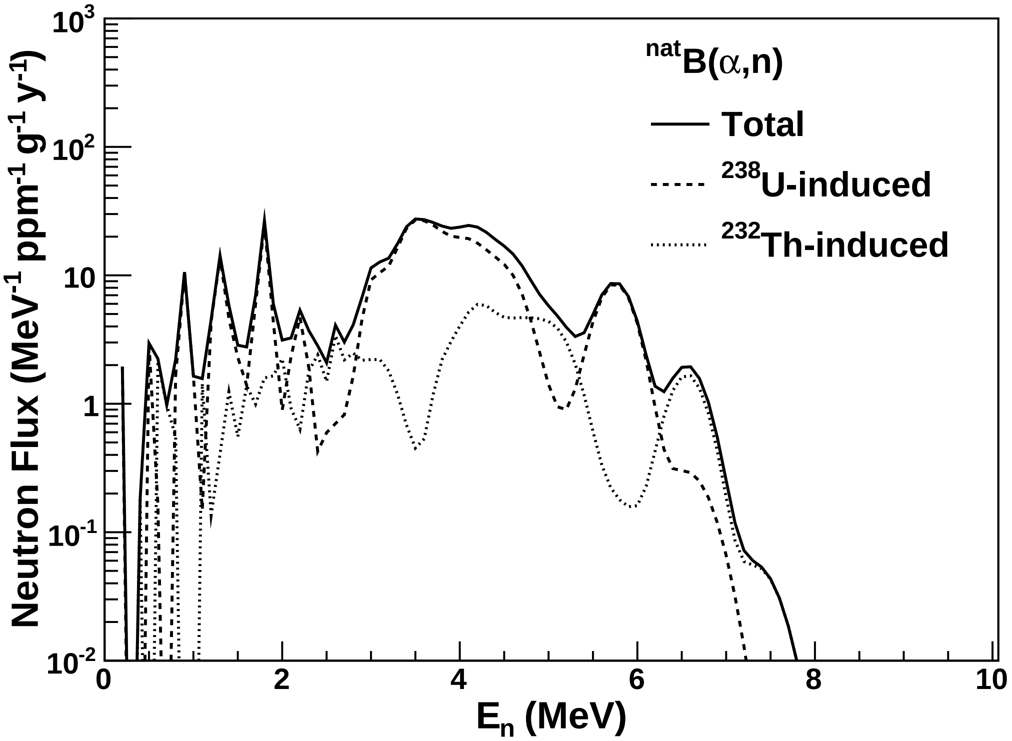

Figure 1.10: The ${}^{\mathrm{nat}}\mathrm{B}(\alpha, n)$-derived neutron yields for α particles in the ^{238}U and ^{232}Th decay series. On the y-axis, "ppm" refers to the fractional mass of ^{238}U or ^{232}Th, and "g" refers to the mass of ${}^{\mathrm{nat}}$B in the material. Calculations were performed using Ref. [Mei09a].

neutrons can be efficiently absorbed using hydrogenous material, however, the high-energy portion of the muon-induced neutron flux persists.

Because the (α, n)-derived neutrons that originate from inside a detector are typically not moderated, they usually become the dominant source of neutrons in a shielded underground experiment. One particular site of these reactions is in borosilicate PMT glass since the ${}^{11}\mathrm{B}(\alpha, n){}^{14}\mathrm{N}$ cross section is considerably larger than (α, n) cross sections in other typical detector and shielding materials. Ref. [Mei09a] provides a prescription for calculating the (α, n)-derived neutron yields for alpha particles from the ^{238}U and ^{232}Th decay series using the (α, n) cross sections for any combination of elements. The ${}^{\mathrm{nat}}\mathrm{B}(\alpha, n)$-derived neutron yield is shown in Fig. 1.10.

1.4 Neutron Cross Sections for Dark Matter and Double-Beta Decay Experiments

Level diagrams up to 3.5 MeV in ^{40}Ar, which is the most abundant natural isotope in argon (99.6%), and 5.8 MeV in ^{20}Ne, which is the most abundant natural isotope in neon (90.5%), are shown in Fig. 1.11. For neutrons with energies of just a few MeV, there are already many open channels for inelastic scattering. As the nucleus de-excites to the ground state, one or more prompt γ rays may be produced. For dark matter and $\beta\beta(0\nu)$ experiments, at very low background levels, backgrounds which were previously unimportant must be considered. Because the underground muon-induced neutron energy spectrum extends to several GeV, backgrounds from γ rays produced in neutron-induced reactions ($(n, xn\gamma)$, where x is the number of neutrons in the final state) will be a concern for next-generation $\beta\beta(0\nu)$ experiments [Mei06]. It is therefore necessary to understand the $(n, xn\gamma)$ cross sections for potential detector and shielding components as a function of neutron energy. Cross sections for $(n, xn\gamma)$ reactions in shielding and cryogenic materials of interest to $\beta\beta(0\nu)$ community, such as Pb, Cu and Ar were unknown until recently. Measurements are crucial as the depth requirement for a tonne-scale ^{76}Ge experiment may be driven by the magnitude of muon-induced backgrounds [Agu11a]. The inclusion of measured $(n, xn\gamma)$ cross sections over a wide energy range in Monte-Carlo codes will help in predicting γ-ray backgrounds in $\beta\beta(0\nu)$ experiments. The portion of this work to measure partial γ-ray production cross sections in argon and neon is a continuation of previous experiments which measured $(n, xn\gamma)$ reactions in lead [Gui09] and copper [Bos10].

The lack of elastic scattering cross-section measurements for neutrons in neon and argon poses a problem for background estimates, performed primarily via Monte-Carlo calculations. Both total and differential cross sections for elastic scattering are important for dark matter experiments, as the rate of multiple scattering inside the detector's

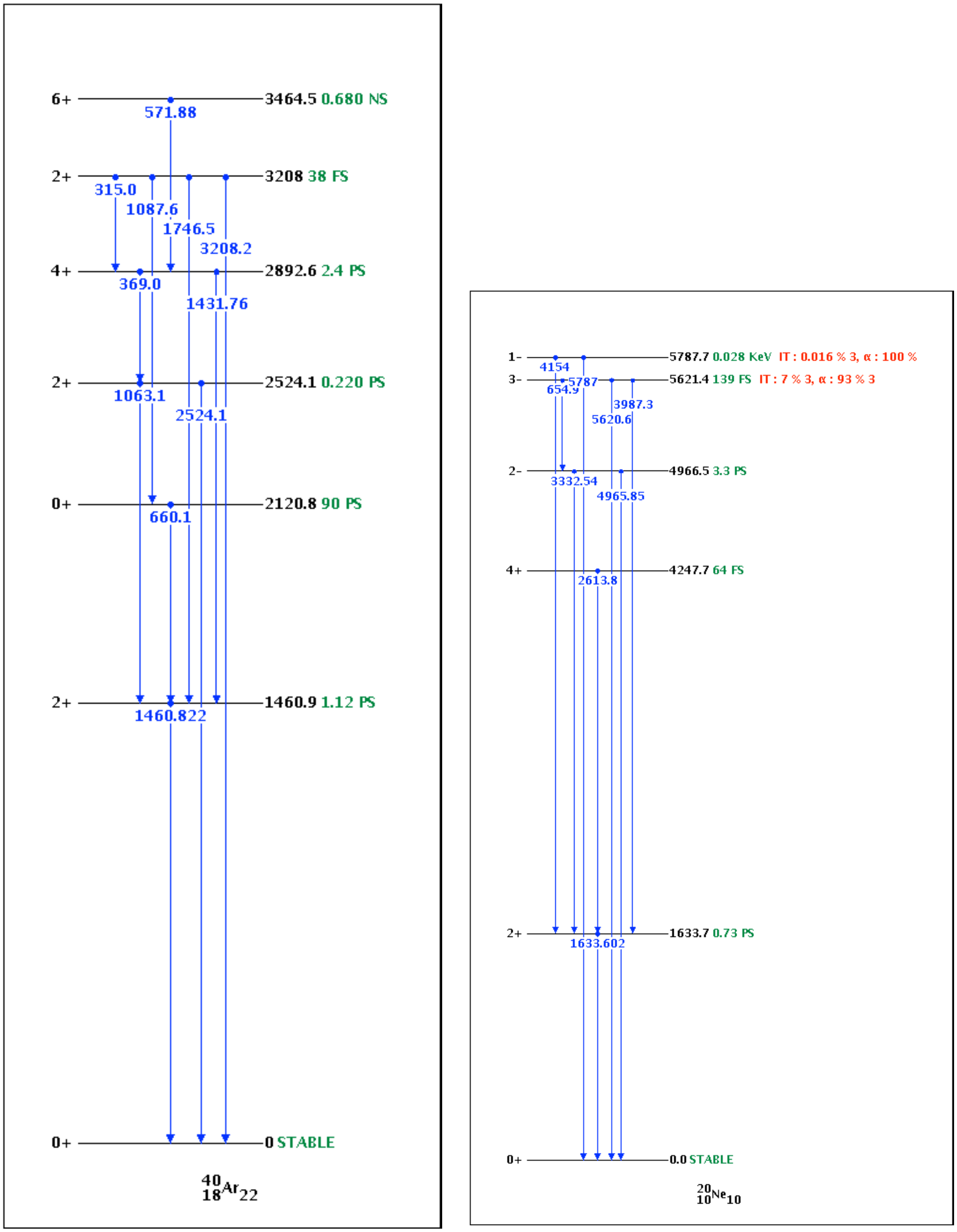

Figure 1.11: Level diagrams for ^{20}Ne and ^{40}Ar, the most abundant of the natural isotopes. Level energies and γ-ray energies are in keV. Level lifetimes are shown in green. Diagrams from `nndc.bnl.gov`.

sensitive volume is determined by the angular differential cross section. Neutrons that multiple scatter can be cut using event-reconstruction techniques, but calibrations and Monte-Carlo simulations using known cross sections are required to determine the efficiency of this analysis cut. Cross sections will be used as inputs to quantitative estimates of neutron backgrounds in these experiments. New measurements will also provide a useful benchmark for optical model (see Section 2.2) parameters in a nuclear mass where the model is not well constrained.

For noble liquid dark matter detectors, the knowledge of both elastic and inelastic neutron scattering cross sections is crucial in predicting the neutron backgrounds. Although neutron elastic scattering can mimic a WIMP signal, experiments may be able to discriminate against inelastic scattering if one or more coincident γ rays are produced. In addition to using neutron inelastic scattering as an active veto, if the rate of inelastic scattering in the detector's sensitive volume can be measured, the background from neutron elastic scattering may be estimated if both the elastic and γ-ray production cross sections are known. These cross sections, combined with the elastic scattering cross sections will help to predict a component of the neutron backgrounds in liquid argon and neon-based dark matter detectors which may be quantified during offline analysis.

1.5 Previous Measurements

Neutron cross-section measurements in Ne, Ar and Xe have been primarily confined to slow and thermal neutrons. Previous measurements for total, inelastic (γ production) and elastic scattering cross sections are shown in Fig. 1.12. Measurements and analyses presented in this work are also included in the figure. It is obvious that cross sections relevant to dark matter and $\beta\beta(0\nu)$ experiments were largely unmeasured. In some cases, nuclear models may be used to approximate these cross sections, however, experimental data are still necessary to constrain phenomenological models.

Total neutron cross sections for Ne, Ar and Xe were measured from 120 keV to 6.2 MeV and from 12.1 to 19.8 MeV by Vaughn et al. [Vau60]. The authors performed a simple transmission experiment where protons or deuterons were created from a Van de Graaff accelerator and neutrons were produced using standard source reactions. Neutrons that scattered from gas-filled stainless-steel cylinders were detected by either a ^{6}LiI or plastic phosphor detector coupled to a PMT. The total neutron cross section was measured for ^{20,22}Ne from 1.9 to 3.5 MeV by Sikkema et al. [Sik57, Sik58]. In this experiment, neutrons were created using a $D + D$ generator and nuclear recoils were measured in a neon multiple-wire proportional counter. These measurements provided a useful estimate for the magnitude of the previously unmeasured elastic scattering cross sections.

Cross sections and angular distributions for $^{40}\mathrm{Ar}(n, n'\gamma)^{40}\mathrm{Ar}$ have been measured at $E_n = 3.5$ MeV for the first few excited states in ^{40}Ar by Mathur and Morgan [Mat65]. Neutrons were produced via the $^{2}\mathrm{H}(d, n)^{3}\mathrm{He}$ source reaction using deuterons from a Van de Graaff accelerator. Gamma rays from neutron-induced excitations in a liquid-argon-filled polyethylene target were detected using a crystal scintillator detector. Data from Ref. [Mat65] are compared to the cross sections measured in this work in Chapter 6.

For elastic scattering, there is one measurement available for argon [Bea67]. In this experiment, 14.0-MeV neutrons were produced via the $^{3}\mathrm{H}(d, n)^{4}\mathrm{He}$ reaction using a 150-keV deuteron beam from a Cockcroft-Walton accelerator. Neutrons that scattered from a liquid-argon target were measured using a plastic scintillator detector and the cross section was determined using the time-of-flight technique. These data were used explicitly in the cross-section analysis presented in Chapter 4. The elastic scattering cross section for $^{\mathrm{nat}}$Ne was measured from 0.8 to 1.9 MeV, with the purpose of determining resonances in neon [Coh59]. Elastic scattering cross sections for neon for

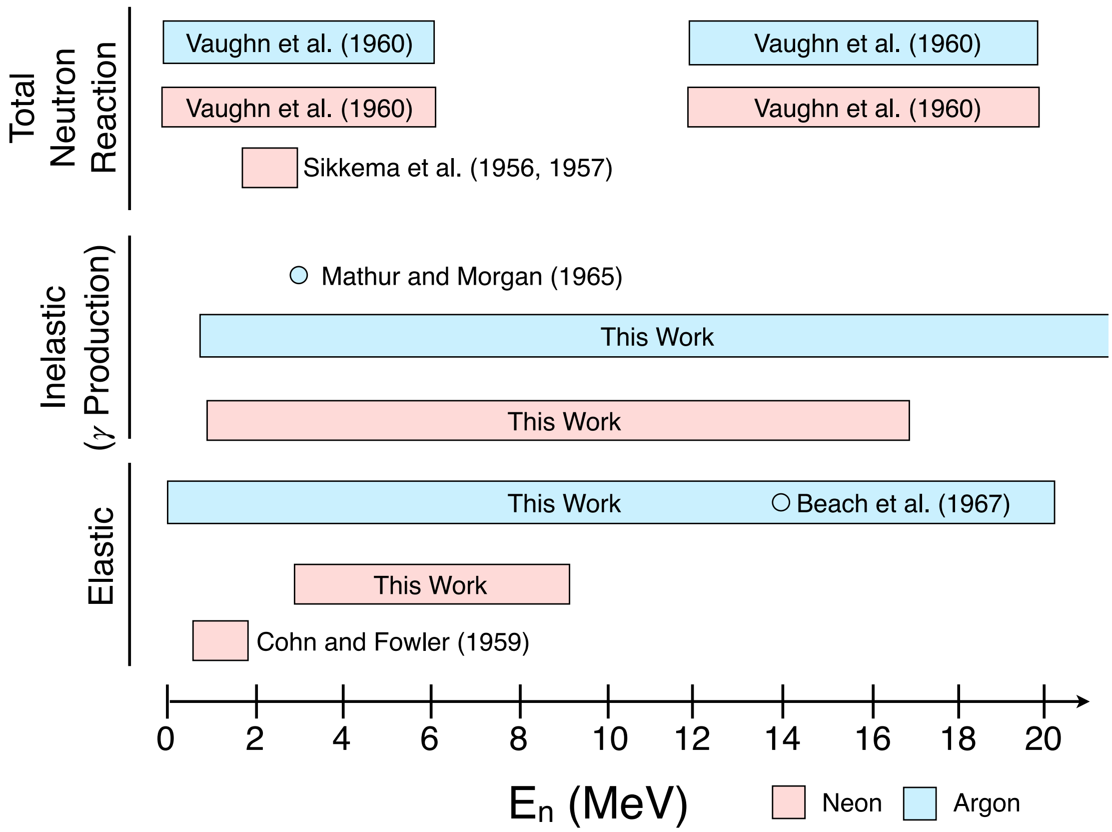

Figure 1.12: Previous measurements of neutron cross sections for argon and neon below 20 MeV (see text for references). Boxes correspond to measurements in the given energy range and circles correspond to a measurement at a single energy. Measurements and analyses presented in this work are also included. The 14.0-MeV elastic scattering point for argon overlaps with this work because the measurement was explicitly used in the analysis. Measurements of slow and thermal neutrons are not included.

neutron energies above 1.9 MeV were previously unmeasured.

Chapter 2

Theory of the Experiment

When a neutron collides with a nucleus, two main processes may occur: direct and compound nucleus reactions. The incident neutron may be elastically scattered in a direct process, where the neutron loses no energy apart from the recoil energy imparted to the target nucleus. In the direct process, it is assumed that the projectile interacts with the nucleus without exciting any internal degrees of freedom. Direct reactions take place on the timescale of 10^{-22} s, or roughly the time it takes for the incoming neutron to traverse the nucleus. In low-energy collisions ($E < 10$ MeV) the incident neutron may also be absorbed to form a compound nucleus. The subsequent decay of the compound nucleus may proceed through a variety of different channels, including a decay back to a neutron and the original target nucleus. Although indistinguishable by experiment, compound nucleus reactions are longer by several orders of magnitude ($\approx 10^{-14}$ s) [Won98]. Because there is no Coulomb barrier for neutral particles, the emission of neutrons in compound nucleus reactions is more favorable than protons or α particles. If the incident neutron energy is high enough, the re-emitted neutrons may leave the residual nucleus in an excited state, resulting in inelastic neutron scattering.

2.1 The Compound Nucleus

Many nuclear reactions take place by capturing a particle to form a compound nucleus, which subsequently decays by particle emission. The compound nucleus exists long enough so that it reaches thermodynamic equilibrium, and the energy of the captured particle is shared statistically among all nucleons in the compound nucleus. Particles are then emitted through a number of possible decay channels. All memory of the formation of the compound system is lost; the process of compound nucleus formation is completely independent of the decay process. This is referred to as the Bohr Independence Hypothesis [Boh36]. In other words, the decay of the compound nucleus is determined entirely by its energy, angular momentum and parity, but not by the way it was formed [Hod87]. The compound nucleus may re-emit the incident particle. This process is called compound elastic scattering, or compound inelastic scattering, depending on whether the residual nucleus is left in an excited state. The probability of compound elastic or inelastic scattering is greatest when there are few other reaction channels open, typically for low (<10 MeV) energies.

The scattering cross section for an entrance channel α and an exit channel β is given using the notation of Marmier and Sheldon [Mar71] as

$$\sigma_{\alpha\beta} = \frac{\pi}{k_\alpha^2} \left| \delta_{\alpha\beta} - U_{\alpha\beta} \right|^2 , \tag{2.1}$$

where $U_{\alpha\beta}$ are the unitary collision matrix elements used to derive the formal theory of nuclear reactions and k is the wave number. If resonances are present, $U_{\alpha\beta}(E)$ will fluctuate rapidly with energy. In this case it is useful to separate the matrix elements into two parts:

$$
\begin{aligned}
U_{\alpha\beta} &= \bar{U}_{\alpha\beta} + \tilde{U}_{\alpha\beta} \\
\bar{U}_{\alpha\beta} &= \langle U_{\alpha\beta} \rangle = \text{constant} \\
\tilde{U}_{\alpha\beta} &\neq \text{constant but } \left\langle \tilde{U}_{\alpha\beta} \right\rangle \equiv 0
\end{aligned}
\tag{2.2}
$$

Physically, we can associate $\bar{U}_{\alpha\beta}$, which is constant over a given energy interval, with the direct reaction (D). $\tilde{U}_{\alpha\beta}$ varies over the given energy interval, but averages to zero. This is the compound nucleus (CN) contribution. Thus we can write the cross section averaged over an energy interval as

$$
\begin{aligned}
\langle \sigma_{\alpha\beta} \rangle &= \frac{\pi}{k_\alpha^2} \left\langle \left| \delta_{\alpha\beta} - U_{\alpha\beta} \right|^2 \right\rangle \\
\langle \sigma_{\alpha\beta} \rangle &= \frac{\pi}{k_\alpha^2} \left| \delta_{\alpha\beta} - \bar{U}_{\alpha\beta} \right|^2 + \frac{\pi}{k_\alpha^2} \left\langle \left| \tilde{U}_{\alpha\beta} \right|^2 \right\rangle \\
&= \sigma_{\alpha\beta}^{(D)} + \sigma_{\alpha\beta}^{(CN)}.
\end{aligned}
\tag{2.3}
$$

It can be seen from Eqn. 2.3 that the direct and compound nucleus reactions for a particular reaction channel add incoherently so that they may be evaluated separately for comparison to experimental data. The direct reaction may be evaluated using the optical model, discussed in Section 2.2. The compound nucleus reaction can be evaluated using Hauser-Feshbach theory, discussed in Section 2.3, along with other statistical models.

2.2 The Optical Model of Elastic Scattering

The elastic scattering process is currently computationally intractable from first principles as it depends on the interaction between the incident particle and each of the target nucleons as well as nucleon-nucleon interactions. For an approximate solution to this problem, we turn to the optical model.

The optical model has been known to provide an excellent phenomenological description of nucleon-nucleus elastic scattering for medium mass and heavy nuclei ($A > 24$) over a wide energy range ($E < 200$ MeV) [Hod63]. Dave and Gould [Dav83] have also shown good agreement using the optical model for light ($A < 16$) $1-p$ shell nuclei from 7 to 15 MeV. The optical model attempts to describe the complex process of elastic scattering by using an analogy of light reflecting from a cloudy crystal ball. The optical potential consists of a real term, $V(r)$, to describe the elastic scattering (reflection), and an imaginary term, $W(r)$, to describe non-elastic processes which reduces the incident flux (absorption), where r is the distance between the incident neutron and center of the target nucleus.

The potential is separated into E-dependent potential well depths and r-dependent radial parts. The general form of the potential is

$$\begin{aligned} U_{\text{opt}}(E_n, r) = -V_v(E_n) f(r, r_v, a_v) - iW_v(E_n) f(r, r_v, a_v) + \\ 4ia_i W_d(E_n) \frac{d}{dr} f(r, r_d, a_d) + \\ V_{\text{s.o.}}(E_n) \left(\frac{\hbar}{m_\pi c}\right)^2 \frac{\vec{\sigma}\cdot\vec{l}}{r} \frac{d}{dr} f(r, r_{\text{s.o.}}, a_{\text{s.o.}}) + iW_{\text{s.o.}}(E_n) \left(\frac{\hbar}{m_\pi c}\right)^2 \frac{\vec{\sigma}\cdot\vec{l}}{r} \frac{d}{dr} f(r, r_{\text{s.o.}}, a_{\text{s.o.}}) + V_C(r), \end{aligned} \tag{2.4}$$

where E is the laboratory energy in MeV and r_i, a_i are the radii and surface diffuseness parameters in fm, respectively. $V_{v,s.o.}$ and $W_{v,d,s.o.}$ are the real and imaginary components for the "volume-central" (v), "surface-central" (d) and "spin-orbit" (s.o.)

potentials. Whereas the potential well depths depend only on energy, the radial parts depend on the geometrical parameters (r_i, a_i). The geometrical parameters depend on the mass number A, and vary from nucleus to nucleus. The real and imaginary components share the same energy independent terms. It is further assumed that the geometry-dependent parameters are the same for each pair (V_i, W_i). This will allow for optical-model parameter searches to vary as few parameters as possible and still obtain a good fit to data.

The Woods-Saxon potential [Woo54], given by

$$f(r, r_j, a_j) = (1 + \exp[(r - R_j)/a_j])^{-1}, \tag{2.5}$$

where $j = v, d$,s.o and $R_j = r_j A^{1/3}$, is used to describe the shape of the volume-central part of the optical potential. This form is desirable because it has properties characteristic of the strong nuclear force. It is attractive, nucleons near the surface experience a large force toward the center, and it is short-range, the force rapidly approaches zero as $r \to \infty$. Because it is thought that absorption takes places near the surface [Lem59], the shape of the surface-central potential is taken to be the derivative of the Woods-Saxon potential. The potential will peak at the surface and fall to zero within a few fm. The r-dependent real central potentials from Eqn. 2.4 are shown in Fig. 2.1 using the parameters from Ref. [Kon03] for ^{40}Ar.

Early calculations using the optical model used only the central potentials. The polarizations of the scattered nucleons are accounted for using the spin-orbit term [Hod63]. The quantities $\vec{l}$ and $\vec{\sigma}$ in the spin-orbit potential are the orbital angular momentum and the Pauli spin matrices, respectively. The term $V_C(r)$ is the Coulomb potential for charged-particle scattering, given in terms of the Coulomb radius, R_C. Although it does not contribute for neutron scattering it is included here for completeness:

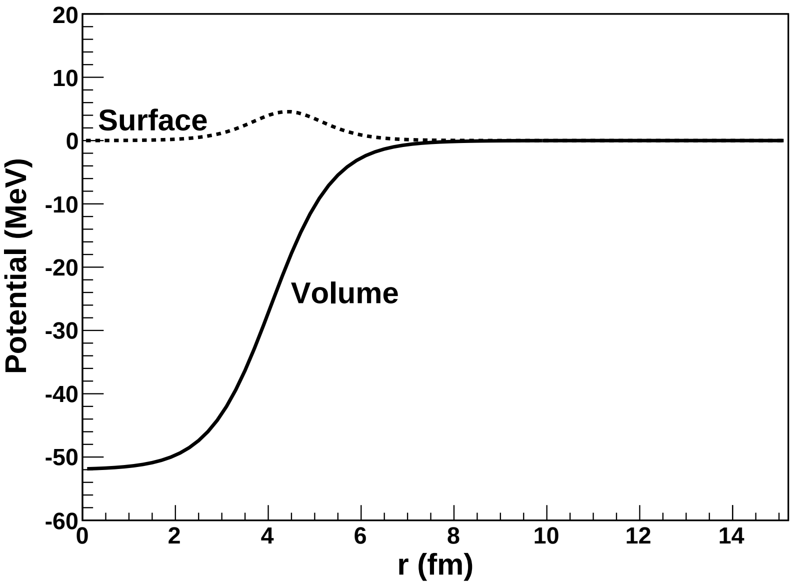

Figure 2.1: The r-dependent real central potentials potentials using the parameters from Ref. [Kon03] for ^{40}Ar.

$$\begin{aligned} V_C(r) &= \tfrac{Zze^2}{2R_C}(3 - \tfrac{r^2}{R_C^2}) \quad && r \leq R_C \\ V_C(r) &= \tfrac{Zze^2}{r} && r \geq R_C \end{aligned} \tag{2.6}$$

The goal of a good optical-model potential is to describe E-dependent potential well depths by smooth functions with as few parameters as possible. The functional forms for these potential well depths depend on $(E - E_f)$ where E_f is the Fermi energy in MeV, defined as the energy halfway between the last occupied and first unoccupied shell of the nucleus. For neutrons, the Fermi energy is given by

$$E_f = -\frac{1}{2}[S_n(Z, N) + S_n(Z, N + 1)], \tag{2.7}$$

where S_n is the neutron separation energy for a nucleus with proton number Z and neutron number N. Following Ref.[Kon03], the functional form of the potential well depths are given as:

$$
\begin{gathered}
V_v(E_n) = v_1[1 - v_2(E - E_f) + v_3(E - E_f)^2 - v_4(E - E_f)^3] \qquad (2.8) \\
W_v(E_n) = w_1 \tfrac{(E-E_f)^2}{(E-E_f)^2+(w_2)^2} \\
W_d(E_n) = d_1 \tfrac{(E-E_f)^2}{(E-E_f)^2+(d_3)^2} \exp[-d_2(E - E_f)] \\
V_{(s.o)}(E_n) = v_{so1} \exp[-v_{so2}(E - E_f)] \\
W_{(s.o)}(E_n) = w_{so1} \tfrac{(E-E_f)^2}{(E-E_f)^2+(w_{so2})^2}
\end{gathered}
$$

where the v_i, w_i, d_i are parameters which may be adjusted to fit experimental data.

Over a broad energy range, a polynomial dependence on $V_v(E_n)$ is the best choice. Over a narrow energy range, a linear dependence is a reasonable assumption. At low energies, the absorption is dominated by the surface term, $W_d(E_n)$. The volume term, $W_v(E_n)$, can be ignored until about 10 MeV and begins to dominate the surface term at about 40 MeV. The Brown–Rho [Bro81] function is used for $W_v(E_n)$. $W_d(E_n)$ uses a Brown–Rho function multiplied by an exponential function. These forms, which were determined empirically from fits to neutron scattering data for ^{90}Zr, were first used in Ref. [Del89]. To obtain a homogeneous notation for the whole potential, the spin-orbit term is assigned to have a $(E - E_f)$-dependence and $V_{s.o}(E_n)$ and $W_{s.o.}(E_n)$ are described by an exponential function and a Brown–Rho function, respectively.

Koning and Delaroche [Kon03] also define a set of parameters used for specific nuclei referred to as the neutron local optical-model potential. For the ^{40}Ar local potential, the E-dependence on the potential well depths is illustrated in Fig. 2.2.

A global neutron optical-model potential, varying smoothly with the mass number A is also defined. The global model has been mostly successful in describing neutron reactions on medium-mass and heavy nuclei ($A > 24$) for incident neutron energies up to about 200 MeV. Therefore, we expect that the global potential will work reasonably well for argon. Although neon is slightly outside the mass range of the global potential, it provides a starting point for parameters when attempting to fit experimental cross sections. The parameters used to describe the Koning-Delaroche neutron global optical-model potential are found in Table 2.1. We compare these models to real data and use them as starting points for fits constrained by the data (see Section 4.5).

Table 2.1: Neutron global optical-model parameters from Ref. [Kon03] used to describe the optical-model potential in Eqns. 2.4 – 2.9.

v_1	$59.30 - 21.0(N-Z)/A - 0.024A$	MeV
v_2	$0.007228 - 1.48 \times 10^{-6}A$	MeV^{-1}
v_3	$1.994 \times 10^{-5} - 2.0 \times 10^{-8}A$	MeV^{-2}
v_4	7×10^{-9}	MeV^{-3}
w_1	$12.195 + 0.0167A$	MeV
w_2	$73.55 + 0.0795A$	MeV
d_1	$16.0 - 16.0(N-Z)/A$	MeV
d_2	$0.0180 + 0.003802/(1 + \exp[(A-156)/8])$	MeV^{-1}
d_3	11.5	MeV
v_{so1}	$5.992 + 0.0030A$	MeV
v_{so2}	0.0040	MeV^{-1}
w_{so1}	-3.1	MeV
w_{so2}	160	MeV

2.3 Hauser-Feshbach Theory

The expression for the compound nucleus reaction in Eqn. 2.3 may be rewritten as the product of the cross section for formation of the compound nucleus into state α (σ_α) and the probability of the compound nucleus decaying through channel β (P_β):

$$\sigma_{\alpha\beta}^{(CN)} = \frac{\pi}{k_\alpha^2} \left\langle \left| \tilde{U}_{\alpha\beta} \right|^2 \right\rangle = \sigma_\alpha P_\beta \tag{2.9}$$

The cross section for CN formation of a particular channel α is given by the sum over

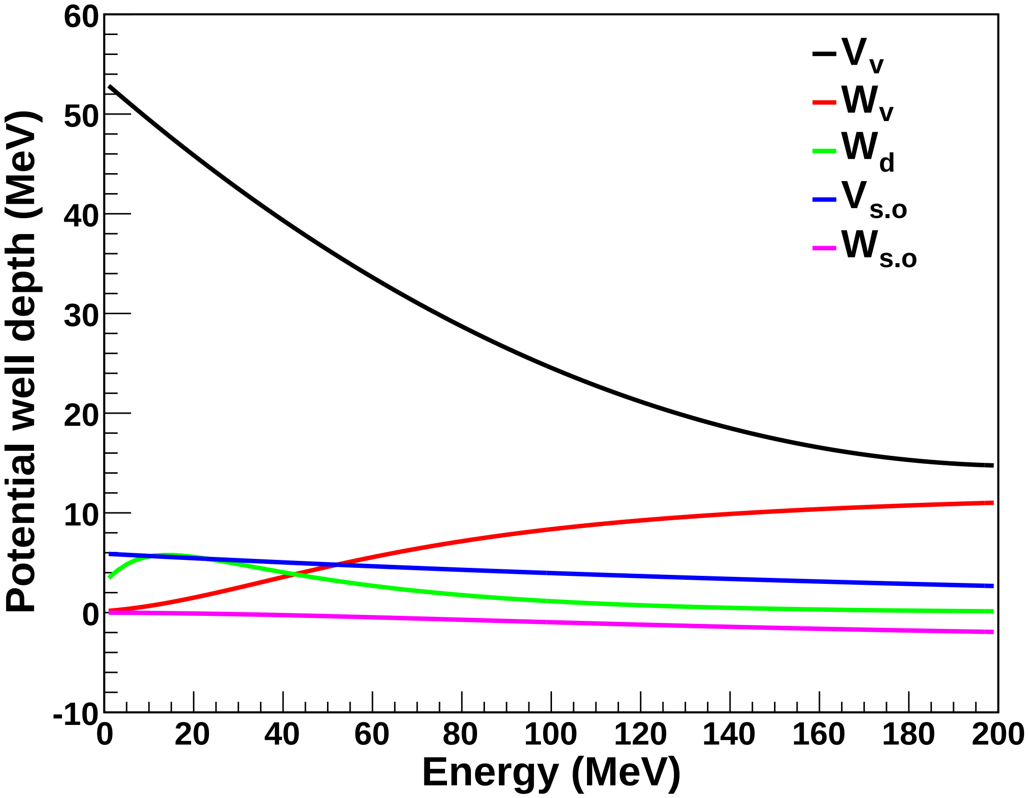

Figure 2.2: The functional form of the potential well depths in Equation 2.9 for $0 < E_n < 200$ MeV. Numerical values for the parameters are from the neutron optical model potential for ^{40}Ar from Ref. [Kon03].

all exit channels β as

$$\sigma_{\alpha}^{(CN)} = \frac{\pi}{k_{\alpha}^{2}} \sum_{\beta} \left\langle \left| \tilde{U}_{\alpha\beta} \right|^{2} \right\rangle . \tag{2.10}$$

Because flux is conserved, i.e. the matrix U is required to be unitary, and the probability of formation must equal the sum of the probabilities for each exit channel, we can rewrite the CN formation cross section as

$$\sigma_{\alpha}^{(CN)} = \frac{\pi}{k_{\alpha}^{2}} \left(1 - \sum_{\beta} \left| \bar{U}_{\alpha\beta} \right|^{2} \right) . \tag{2.11}$$

We have now expressed the cross section for compound nucleus formation in terms of the direct reaction matrix elements $\bar{U}_{\alpha\beta}$. This implies the cross section for both the direct and compound nucleus reactions can be computed using the optical model. With this in mind, we now define the direct reaction matrix elements in terms of particle transmission coefficients as

$$T_{\alpha} \equiv 1 - \sum_{\beta} \left\langle \left| \bar{U}_{\alpha\beta} \right|^{2} \right\rangle . \tag{2.12}$$

Thus,

$$\sigma_{\alpha}^{(CN)} = \frac{\pi}{k_{\alpha}^{2}} T_{\alpha}, \tag{2.13}$$

where T_{α} depends on energy and quantum numbers of the channel α. We can write the CN cross section in terms of the transmission coefficients as

$$\sigma_{\alpha\beta}^{(CN)} = \frac{\pi}{k_{\alpha}^{2}} T_{\alpha} P_{\beta}, \tag{2.14}$$

Because the sum of the probabilities of decay of the compound nucleus over all channels

β must be unity, P_β can be expressed as a ratio of transmission coefficients,

$$P_\beta = \frac{T_\beta}{\sum_\gamma T_\gamma}, \tag{2.15}$$

where the sum of transmission coefficients, $\sum_\gamma T_\gamma$, is over all possible outgoing channels. Thus, from Eqn. 2.14, we arrive at the simplest form of the Hauser-Feshbach formula [Hau52]:

$$\sigma_{\alpha\beta} = \frac{\pi}{k_\alpha^2} \frac{T_\alpha T_\beta}{\sum_\gamma T_\gamma} \tag{2.16}$$

This expression gives the cross section for a compound nucleus reaction for spinless particles from a single entrance channel α to a single outgoing channel β. The channel labels α, β and γ serve to characterize their quantum descriptions. If the interacting particles have spin, the expression must include the appropriate weighting factors and is subject to angular momentum coupling rules. In this case, the cross section may be written as [Hod71]

$$\sigma_{\alpha\beta} = \frac{\pi}{k_\alpha^2} \sum_{J, j_\alpha, l_\alpha} \left[\frac{2J+1}{(2I+1)(2s_\alpha+1)} \right] \frac{T_{l_\alpha j_\alpha}(E_\alpha) T_{l_\beta j_\beta}(E_\beta)}{\sum_{l_\gamma, j_\gamma, E_\gamma} T_{l_\gamma j_\gamma}(E_\gamma)}. \tag{2.17}$$

The quantities s_α, s_β are the spin of the incident and exiting particle, respectively. The quantities l_α, l_β are the orbital angular momentum in the incident and outgoing channel, respectively. The incident channel α is specified by the spin of the target nucleus, denoted by I, and the quantities s_α, l_α and j_α, where the channel spin $\vec{j} = \vec{s} + \vec{I}$. These couple to give the the spin of the compound nucleus, J. The differential cross section averaged over the angular-momentum states is given as [Hod71]

$$
\begin{aligned}
\sigma_{\alpha\beta}(\theta) = \frac{\pi}{k_\alpha^2} \sum_{J^\pi, j_\alpha, l_\alpha, j_\beta, l_\beta} & \frac{2l_\alpha + 1}{(2I+1)(2s_\alpha+1)} \\
\times A_J(j_\alpha, l_\alpha, j_\beta, l_\beta; \theta) & \frac{T^{J^\pi}_{l_\alpha j_\alpha} T^{J^\pi}_{l_\beta j_\beta}}{\sum_{\gamma l_\gamma j_\gamma} T^{J^\pi}_{l_\gamma j_\gamma}},
\end{aligned}
\tag{2.18}
$$

where the angular information is contained in the function

$$
\begin{aligned}
A_J(j_\alpha, l_\alpha, j_\beta, l_\beta; \theta) = \frac{(2l_\beta+1)(2J+1)^2}{4\pi} \\
\times \left| \sum_L C^{L l_\alpha l_\alpha}_{000} C^{L l_\beta l_\beta}_{000} W(J J l_\alpha l_\alpha; L j_\alpha) W(J J l_\beta l_\beta; L j_\beta) P_L(\cos(\theta)) \right|,
\end{aligned}
\tag{2.19}
$$

given in terms of Clebsch-Gordan, Racah W-coefficients [Rac42], and Legendre polynomials where θ is the scattering angle in the center-of-mass frame. The sum over L is defined by $0 \leq L \leq \min(2l_\alpha, 2l_\beta, 2J)$. The full derivation of Eqn. 2.18 can be found in Ref. [Hod71]. It is important to note several features of this equation. First, since L is even, the cross section is symmetric about 90°. Additionally, if $l_\alpha = 0$, $l_\beta = 0$, $J = 0$ or $\frac{1}{2}$, then $L = 0$ and the compound nucleus cross section is isotropic, i.e. $A_J(j_\alpha, l_\alpha, j_\beta, l_\beta; \theta)$ is independent of θ. Because the transmission coefficients may be determined from an optical-model analysis, the compound nucleus cross section $\sigma_{\alpha\beta}(\theta)$ may then be calculated if all of the spins corresponding to all energetically available final states are known.

2.3.1 Nuclear Level Densities

At moderate neutron energies, where only a few nuclear levels may be excited, the cross section depends on the incident neutron energy E_n, the energy of the excited level

E_x, the angular momentum of the excited level and the parity change of the excited levels. As neutron energy increases more nuclear levels become available. In this case, instead of treating the levels separately, a statistical model is applied to determine the density of states. There are many different models for calculating level densities ranging from phenomenological analytical expressions to tabulated level densities derived from microscopic models. To set the notation for the calculation of these level densities, we provide some general definitions. The "level density" $\rho(E_x, J, \pi)$ is the number of nuclear levels per unit energy around an excitation energy E_x, for a certain spin J and parity π. The "total level density" $\rho^{tot}(E_x)$ corresponds to the total number of nuclear levels per unit energy around E_x and is obtained by summing the level density over spin and parity. The "total state density" $\omega^{tot}(E_x)$ includes $2J+1$ states for each level:

$$\omega^{tot}(E_x) = \sum_J \sum_\pi (2J+1)\rho(E_x, J, \pi). \tag{2.20}$$

Analytical expressions for level densities are usually factorized into a parity distribution $P(E_x, J, \pi)$ and a spin distribution $R(E_x, J)$ as:

$$\rho(E_x, J, \pi) = P(E_x, J, \pi) R(E_x, J) \rho^{tot}(E_x). \tag{2.21}$$

Most level density models assume parity equipartition, i.e.

$$P(E_x, J, \pi) = \frac{1}{2}. \tag{2.22}$$

The Fermi gas spin distribution, given by Ref. [Eri60] as

$$R_F(E_x, J) = \frac{2J+1}{2\sigma^2} \exp\left[-\frac{(J+\frac{1}{2})^2}{2\sigma^2}\right], \tag{2.23}$$

was used for the calculations in this work. The quantity σ^2 is the spin cut-off parameter, representing the width of the angular momentum distribution.

The known levels in the residual nucleus may be treated individually and all other channels are written as integrals over the excitation energy of the residual nuclei using averaged transmission coefficients. We therefore write the denominator in Eqn. 2.18 as [Tow67]

$$\sum_{l_\gamma,j_\gamma} T^{J^\pi}_{l_\gamma,j_\gamma} = \sum_{l_\gamma,j_\gamma}{}' T^{J^\pi}_{l_\gamma,j_\gamma} + \sum_{l_\gamma,j_\gamma} \int \rho(E_x, J, \pi) T^{J^\pi}_{l_\gamma,j_\gamma}(E_x) dE_x, \tag{2.24}$$

where $\rho_J(E_x)$ is the density of states of spin J and the $\sum'$ indicates the sum, which is usually taken over only a few excited states in the residual nuclei. The separation between the two terms is usually taken at excitation energies where the spins of the levels are no longer known and the level spacing is close enough where level-density models are sufficiently accurate.

The Constant Temperature Model

The Constant Temperature Model (CTM), proposed by Gilbert and Cameron [Gil65] is used at low excitation energies. The CTM is based on the fact that the cumulative number of discrete levels, to a certain excitation energy, $N(E_x)$ can be produced by an exponential law for the first few levels. This is called the constant temperature law, given by

$$N_{CTM}(E_x) = \exp(\frac{E_x - E_0}{T}), \tag{2.25}$$

where E_0 is the pairing energy and T is the nuclear temperature that are adjusted to fit the experimental data for discrete levels. The CTM total level density is given by

$$\rho^{tot}_{CTM}(E_x) = \frac{dN(E_x)}{dE_x} = \frac{1}{T}\exp(\frac{E_x - E_0}{T}). \tag{2.26}$$

The Fermi Gas Model

The Fermi Gas Model [Eri60] of calculating level densities is based on the assumption of equal level spacing:

$$\begin{aligned} \omega_F^{tot}(E_x) &= \frac{\sqrt{\pi}}{12}\frac{\exp[2\sqrt{aU}]}{a^{1/4}U^{5/4}} \\ U &\equiv E_x - \Delta \end{aligned} \tag{2.27}$$

where the level-density parameter a and pairing energy Δ are treated as free parameters. The level-density parameter depends slightly on the excitation energy. The total Fermi gas level density is related to the total Fermi gas state density as

$$\rho_F^{tot}(E_x) = \frac{\omega_F^{tot}(E_x)}{\sqrt{2\pi}\sigma}. \tag{2.28}$$

The level densities for ^{20}Ne and ^{40}Ar is shown in Fig. 2.3. The calculation was done using TALYS [Kon08]. The code can use up to 30 discrete levels if they are known. This corresponds $E_x = 10.3$ MeV for ^{20}Ne and $E_x = 4.7$ MeV for ^{40}Ar. Beyond the first 30 levels the constant temperature model was used up to a matching energy, E_M, at which point the Fermi gas model was used. The value of E_M was chosen where $\rho_{CTM}(E_x)$ and $\rho_F(E_x)$, along with their derivatives, were identical. The default TALYS values, shown in Table 2.2 were used for E_0, T, σ, a, Δ and E_M.

Table 2.2: Default TALYS parameters used in the calculations of level densities for argon and neon.

	E_0 (MeV)	T (MeV)	σ	a (MeV)	Δ (MeV)	E_M (MeV)
^{20}Ne	0.867	2.667	2.402	3.026	5.367	24.3
^{40}Ar	-0.939	1.365	2.045	6.730	1.922	10.5

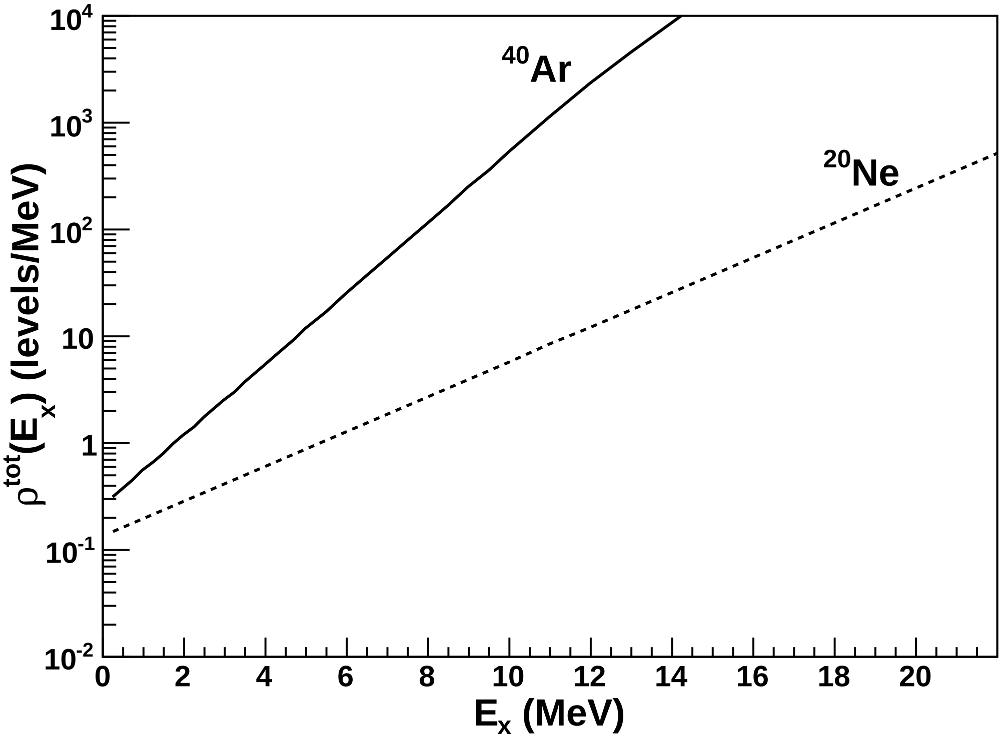

Figure 2.3: The level densities for ^{20}Ne and ^{40}Ar calculated using the constant temperature and Fermi gas models.

2.3.2 Width Fluctuation Corrections

We have thus far assumed the Bohr independence hypothesis and therefore have excluded effects from correlations between incoming and outgoing channels, such as between incident and outgoing waves is in the elastic channel. These effects are accounted for with a multiplicative factor $W_{\alpha\beta}$ called the width fluctuation correction factor (WFCF):

$$\sigma_{\alpha\beta} \rightarrow \sigma_{\alpha\beta} W_{\alpha\beta} \tag{2.29}$$

There are several approaches for determining the WFCF, namely, the Hofmann-Richert-Tepel-Weidenmüller (HRTW) [Hof75, Tep74, Hof80], Moldauer [Mol76, Mol80], and Gaussian orthogonal ensemble (GOE) [Ver85] approaches. The GOE approach involves an exact expression, whereas the HRTW and Moldauer approaches are approximations. In practice, the GOE approach may require too much computation time to be used extensively for cross-section calculations. In a comparison of these approaches [Hil03] it was determined that Moldauer's WFCF is the best choice to use in reaction models for practical applications.

The WFCF enhances the compound nucleus cross section calculated directly using Hauser-Feshbach theory. The compound nucleus cross section is larger at low energies when fewer reaction channels are open and is negligible compared to the direct reaction above about 10 MeV. A compound nucleus cross section for elastic scattering of 5.0-MeV neutrons from ^{20}Ne and ^{40}Ar is shown in Fig. 2.4. The calculation was done using TALYS [Kon08]. The optical model from Ref. [Kon03] was used for the transmission coefficients in the Hauser-Feshbach calculation. The same level density models as described above were used in this calculation.

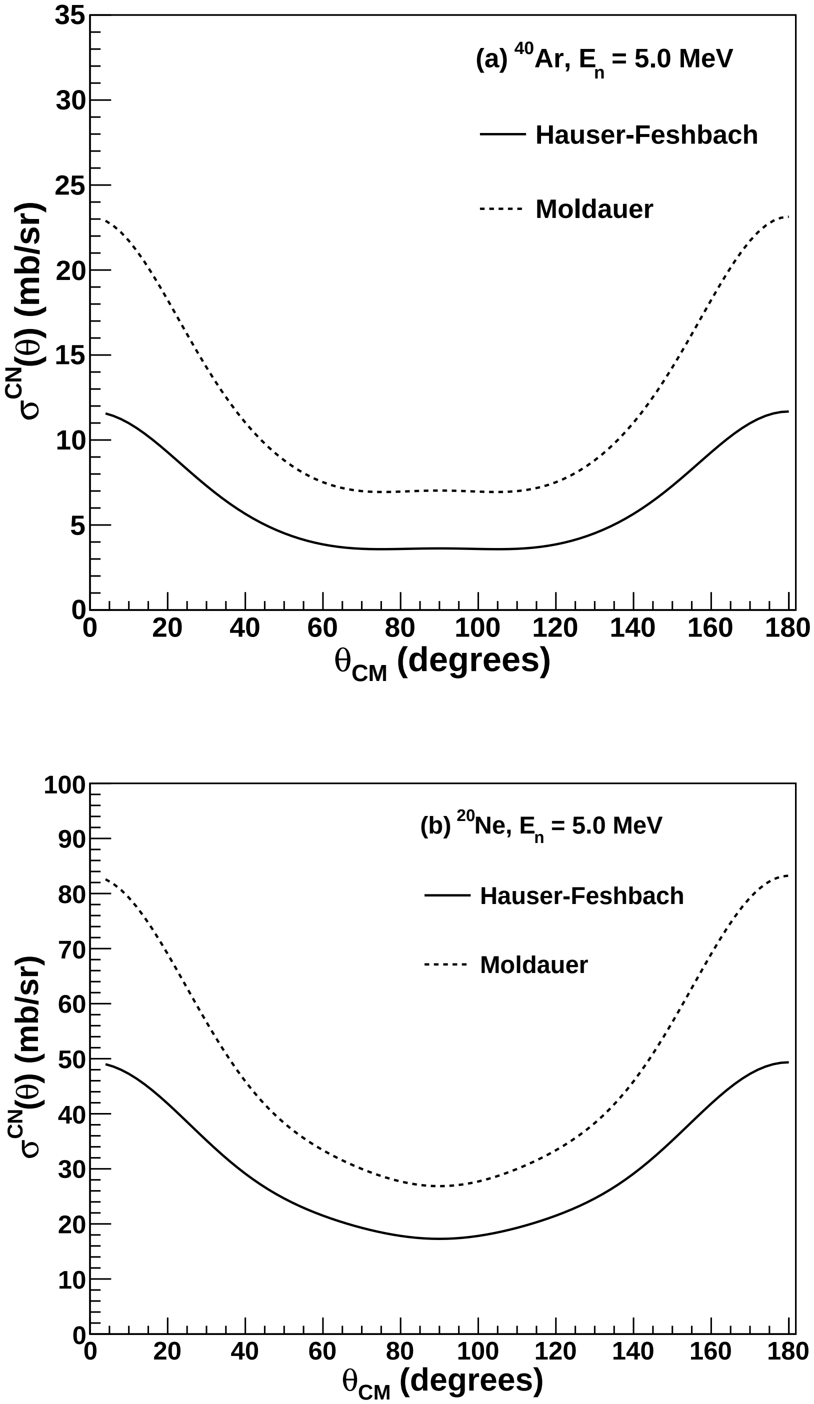

Figure 2.4: Compound elastic cross sections for ^{20}Ne and ^{40}Ar at $E_n = 5.0$ MeV. The solid curves represent a pure Hauser-Feshbach calculation. The dashed curves include the Moldauer WFCF.

2.4 Gamma-ray Emission

Neutron inelastic scattering reactions become possible when the neutron has enough energy to leave the nucleus in an excited state. In this case, the nucleus may be deexcited with the emission of electromagnetic radiation in the form of γ rays. Because nuclei contain moving charges, the emission of γ rays from a nucleus may be studied using electromagnetic theory. Classically, electromagnetic radiation may be expanded in terms of multipole moments. The γ-radiation from a nuclear decay may be classified by multipole expansions in terms of the nucleus' angular momentum L and parity π. The total angular momentum L is a combination of the orbital angular momentum and spin. For a photon, the spin is 1. The multipole order is 2^L, where $L = 0$ for a monopole, $L = 1$ for a dipole, $L = 2$ for a quadrupole, etc. Each multipole may be separated by its parity. "Electric" transitions have a parity of (-1^L) whereas "magnetic" transitions have a parity of (-1^{L+1}). The names electric and magnetic are given because the electric multipoles are connected with the charge distribution and the magnetic multipoles are connected with the current density.

When a nucleus decays from an initial state, characterized by an angular momentum J_i and parity π_i to a final state characterized by an angular momentum J_f and parity π_f, and must satisfy

$$|J_i - J_f| \leq L \leq J_i + J_f. \tag{2.30}$$

The transitions are subject to the following selection rules: (a) if there is no parity change between states ($\pi_i = \pi_f$), the photon must have even parity and may be associated with even electric or odd magnetic multipoles, (b) if there is a parity change between states ($\pi_i = -\pi_f$), the photon must have odd parity and may be associated with odd electric or even magnetic multipoles, (c) because the photon always carries away one unit of angular momentum, transitions between two $J = 0$ states is forbidden for γ-ray transitions.

Under the assumption that the radiation results from the transition of a single proton between nuclear levels, Weisskopf [Wei51] estimated the transition rates λ for electric and magnetic transitions, denoted by E and M, of multipolarity L to be [Kra88]

$$\lambda(EL) \approx \frac{8\pi(L+1)}{L[(2L+1)!!]^2}\frac{e^2}{4\pi\epsilon_0\hbar c}\left(\frac{E_\gamma}{\hbar c}\right)^{2L+1}\left(\frac{3}{L+3}\right)^2 cR^{2L} \tag{2.31}$$

$$\begin{aligned}\lambda(ML) \approx \frac{8\pi(L+1)}{L[(2L+1)!!]^2}\left(\mu_p - \frac{1}{L+1}\right)^2\left(\frac{\hbar}{m_p c}\right)^2\left(\frac{e^2}{4\pi\epsilon_0\hbar c}\right) \\ \times\left(\frac{E_\gamma}{\hbar c}\right)^{2L+1}\left(\frac{3}{L+2}\right)^2 cR^{2L-2},\end{aligned} \tag{2.32}$$

where λ is in s^{-1} and E_γ is in MeV, and R is the nuclear radius in fm. The Weisskopf estimates are not meant to be true theoretical calculations, but instead provide a reasonable comparison of transition rates for certain multipoles. Estimates for lower multipole orders are given in Table 2.3. It is important to note two important conclusions from the Weisskopf transition probability estimates: (1) The lower multipolarities are dominant. The transition probability for a given multipolarity is suppressed by about 10^{-5} compared to the next lowest order. (2) For a given multipole order, the electric transition is more likely than the magnetic transition by more than an order of magnitude.

Table 2.3: Weisskopf estimates [Wei51] for electric and magnetic transition rates for lower multipole orders. The transition rate λ is in s^{-1} and E_γ is in MeV.

$\lambda(E1)$	$=$	$1.0 \times 10^{14} A^{2/3} E^3$	$\lambda(M1)$	$=$	$5.6 \times 10^{13} E^3$
$\lambda(E2)$	$=$	$7.3 \times 10^{7} A^{4/3} E^5$	$\lambda(M2)$	$=$	$3.5 \times 10^{7} A^{2/3} E^5$
$\lambda(E3)$	$=$	$34 A^2 E^7$	$\lambda(M3)$	$=$	$16 A^{3/4} E^7$
$\lambda(E4)$	$=$	$1.1 \times 10^{-5} A^{8/3} E^9$	$\lambda(M4)$	$=$	$4.5 \times 10^{-6} A^2 E^9$

2.4.1 Strength Functions

The γ-ray production cross section in compound nucleus reactions may calculated using a similar statistical calculation as for the particle decay channels. The γ-ray transmission coefficients are similar to the particle transmission coefficients determined from the optical model. They enter the Hauser-Feshbach model for the description of the γ-ray emission in nuclear reactions. The γ-ray transmission coefficient is given as

$$T_{XL}(E_\gamma) = 2\pi f_{XL}(E_\gamma) E_\gamma^{2L+1}, \tag{2.33}$$

where X and L are the type and multipolarity of the transition, respectively. The quantity $f_{XL}(E_\gamma)$ is the γ-ray strength function. Several different models for the γ-ray strength function can be used to calculate the transmission coefficients [Kop90]. The Brink-Axel strength function is given by [Bri57, Axe62]

$$f_{XL}(E_\gamma) = \frac{1}{(2L+1)\pi^2\hbar^2c^2} \frac{\sigma_{XL} E_\gamma \Gamma_{XL}^2}{(E_\gamma^2 - E_{XL}^2)^2 + E_\gamma^2 E_{XL}^2}, \tag{2.34}$$

where a Lorentzian form describes the shape of the giant dipole resonance (GDR). The quantities Γ_{XL}, σ_{XL} and E_{XL} are the strength, width and energy of the multipole's associated GDR in photoabsorption, respectively. This form has provided a successful description of data except for in the case of E1 transitions. For E1 transitions, Ref.[Kop90] suggests a generalized Lorentzian form,

$$f_{E1}(E_\gamma, T) = \frac{1}{3\pi^2\hbar^2c^2} \left[\frac{E_\gamma \tilde{\Gamma}_{E1}(E_\gamma)}{(E_\gamma^2 - E_{E1}^2)^2 + E_\gamma^2 \tilde{\Gamma}_{E1}(E_\gamma)^2} + \frac{0.7\Gamma_{E1} 4\pi^2 T^2}{E_{E1}^3} \right] \sigma_{E1}\Gamma_{E1}, \tag{2.35}$$

where the damping width $\tilde{\Gamma}(E_\gamma)$ is given by

$$\tilde{\Gamma}(E_\gamma) = \Gamma_{E1}\frac{E_\gamma^2 + 4\pi^2 T^2}{E_{E1}^2}, \tag{2.36}$$

and the nuclear temperature T is given as

$$T = \sqrt{\frac{E_n + S_n - \Delta - E_\gamma}{a(S_n)}}, \tag{2.37}$$

where S_n is the neutron separation energy, E_n is the incident neutron energy, Δ is the pairing correction and a is the level density parameter at S_n (same as in Section 2.3.1). The GDR parameters for each isotope may be found in Ref. [Cap09]. The calculation of these parameters are based on a fit of the theoretical photoabsorption cross sections to the experimental data for 121 nuclides from ^{12}C through ^{239}Pu. We used nuclear reaction codes to calculate γ-ray production cross sections based on these γ-ray transmission coefficients and a Hauser-Feshbach statistical calculation to compare to our data for argon and neon (see Section 6.5).

2.4.2 Angular Distribution

The spin direction of excited states formed in nuclear reactions are oriented with respect to the projectile. That is, the incident beam partially aligns the nuclear spins in a plane orthogonal to the beam direction. The z-axis is usually taken to be along the direction of the beam, so that the z-component of $\vec{l}$ is zero and the z-component of $\vec{j}$ is m. For a given spin state $\vec{j}$, the magnetic sub-states m $(m = -j, ..., j)$ will not be occupied with a uniform distribution. What is measured experimentally is not a state with a defined m, but an ensemble where the population can be dealt with statistically. The population of sub-states is taken to be a Gaussian distribution, given by Ref. [Mor76] as

$$P(m) = \frac{e^{\frac{-m^2}{2\sigma^2}}}{\sum_{m'=-j}^{j} {}^{\frac{-m'^2}{2\sigma^2}}}. \tag{2.38}$$

σ is a measure of the width of the m distribution, or degree of alignment of the nuclear spin ($\sigma = 0$ for a fully aligned state and $\sigma \to \infty$ for no alignment). The angular distribution of emitted photons from a nuclear de-excitation may be expanded in terms of Legendre Polynomials as

$$W(\theta) = \sum_{k=\text{even}} A_k P_k(\cos(\theta)), \tag{2.39}$$

where the k can only be even due to parity conservation and $k_{\text{max}} < 2j_i$, where j_i is the angular momentum of the excited state. In the above expression

$$A_k(j_i, \lambda_1, \lambda_2, j_f) = \rho_k(j_i)\frac{1}{1+\delta^2}[F_k(j_f, \lambda_1, \lambda_1, j_i) + 2\delta F_k(j_f, \lambda_1, \lambda_2, j_i) + \delta^2 F_k(j_f, \lambda_2, \lambda_2, j_i)], \tag{2.40}$$

where j_i is the angular momentum of the excited state, j_f is the angular momentum of the final state, λ_1 and λ_2 are the multipolarities of the two most dominant multipoles (dipole ($\lambda = 2$) versus quadrupole ($\lambda = 3$), etc.), and δ is the mixing ratio between λ_1 and λ_2, given by reduced transition matrix elements as

$$\delta = \frac{\langle j_f || \lambda_2 || j_i \rangle}{\langle j_f || \lambda_1 || j_i \rangle}, \tag{2.41}$$

or other words,

$$\delta^2 = \frac{\text{intensity of } \lambda_2}{\text{intensity of } \lambda_1}. \tag{2.42}$$

The F_k's are the Ferentz-Rosenzweig coefficients given in terms of Clebsch-Gordan and

Racah W-coefficients [Rac42, Bie52] by Ref.[Fer55] to be

$$\begin{aligned} F_k(\lambda_1, \lambda_2, j_f, j_i) = (-1)^{j_f - j_i - 1} &\sqrt{(2j_i+1)(2\lambda_1+1)(2\lambda_2+1)} \\ &\times \langle \lambda_1 1 \lambda_2 (-1) | k0 \rangle \, W(\lambda_1 \lambda_2 j_i j_i; k j_f). \end{aligned} \tag{2.43}$$

The statistical tensor, ρ_k, which includes the m sub-state population, is given by

$$\rho_k(j_i) = \sqrt{(2j_i+1)} \sum_{m=-j_i}^{j_i} (-1)^{j_i - m} \langle j_i m j_i (-m) | k0 \rangle \, P(m). \tag{2.44}$$

The angular distribution of γ rays for any transition where the spin and parity of the initial and final states is known may be calculated if the quantity $P(m)$ is known. In our case, the calculated angular distribution presented here was used to extrapolate our data for cases where a full angular distribution could not be measured. The calculation of σ in the expression for $P(m)$ (Eqn. 2.38), hence the angular distribution correction for the specific γ-ray transitions measured in this work is discussed in Section 6.4.6.

2.4.3 Internal Conversion

Internal conversion is an electromagnetic process that competes with γ-ray emission. Internal conversion occurs when the multipole fields in a nucleus interact with the atomic electrons and result in an emission of an electron rather than a γ ray. The emission of an electron should not be confused with β decay, as the ejected electron was not from a nuclear decay but rather an existing electron in the atom. The rate of internal conversion may be quantified by the ratio of electron emission to γ-ray emission. It is important to note several features of the internal conversion rate: (1) It increases as Z^3 making the process more important for heavy nuclei. (2) It decreases rapidly with increased transition energy, and the γ-ray emission process increases rapidly with increasing transition energy. (3) It increases rapidly as the multipole order increases. (4) It provides a channel for $L = 0$ transitions, which are forbidden for γ-ray emission. For both argon and neon, the internal conversion process is negligible compared to γ-ray emission [Hag68].

Chapter 3

Experimental Facilities at Triangle Universities Nuclear Laboratory

The technical details of the experimental facility used to measure neutron elastic scattering cross sections will be described in this chapter. Neutron elastic scattering cross sections from $^{\mathrm{nat}}$Ne and $^{\mathrm{nat}}$Ar were measured using the time-of-flight spectrometer at the Triangle Universities Nuclear Laboratory (TUNL). TUNL is located on the west campus of Duke University, and is jointly operated by Duke University, University of North Carolina and North Carolina State University. The measurements in this work were done using the 10 MV tandem Van de Graaff accelerator. A floor plan of the TUNL accelerator and target areas is provided in Fig. 3.1.

3.1 Neutron beam production

Fast neutrons were produced via the $^{2}\mathrm{H}(d,n)^{3}\mathrm{He}$ reaction by accelerating a beam of pulsed deuterons and bombarding a small gas cell filled with deuterium. The following sections describe the ion beam production, pulsing, transport and neutron beam production.

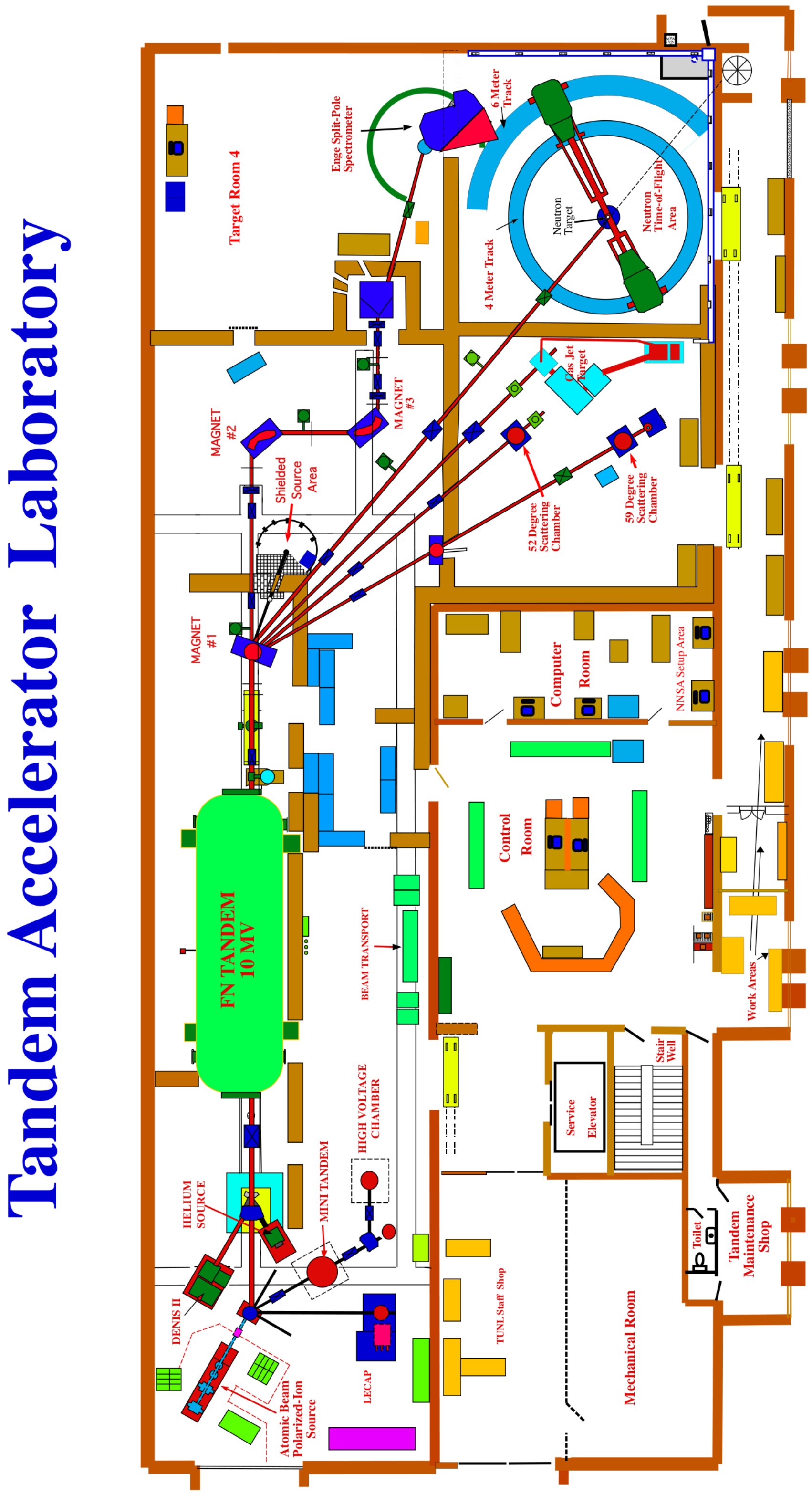

Figure 3.1: TUNL floorplan

3.1.1 Negative Ion Source

A beam of negatively charged deuterium ions was produced using the Direct Extraction Negative Ion Source (DENIS II) that is located in the low-energy bay of the tandem accelerator laboratory at TUNL. Ions were extracted from the source head, which was held at -50 kV, and were accelerated toward ground potential, resulting in a 50 keV continuous negative ion beam. A schematic of DENIS II is shown in Fig. 3.2.

The filament was composed of nickel mesh coated with a carbonate. The filament material was chosen because it has a low work function with respect to the thermionic emission of electrons. In order to create and maintain an arc discharge between the filament and the anode, the region around the filament was evacuated to about 10^{-2} torr and a small amount of gas (usually D_2 or H_2) was injected into the system. The filament current was then raised to between about 30 and 70 A until an arc was struck between the filament and anode. The arc was constrained by a solenoidal magnetic field created by the source magnet, which was maintained at around 1 A.

Electrons from the arc were accelerated through an intermediate electrode, which provided mechanical constriction of the arc, toward the anode. During this acceleration the electrons collide with molecules in the gas creating positive and negative ions through the reaction $e^- + \mathrm{H}_2 \rightarrow \mathrm{H}^- + \mathrm{H}^+ + e^-$, for example. The choice of gas injected into the system determines the species of the resulting beam. For example, we used D_2 gas to create a deuterium ion beam. In practice, to create a deuterium beam, a small amount of hydrogen was mixed with the deuterium to keep the deuteron current low enough to inject into the tandem.

Ions were drawn through the anode aperture into a second high-vacuum ($\sim 10^{-6}$ torr) region due to the large pressure gradient. The core plasma consists of mainly positive ions with negative ions forming a less dense halo around the core. For this reason, the anode aperture was offset slightly from the center so that negative ions from

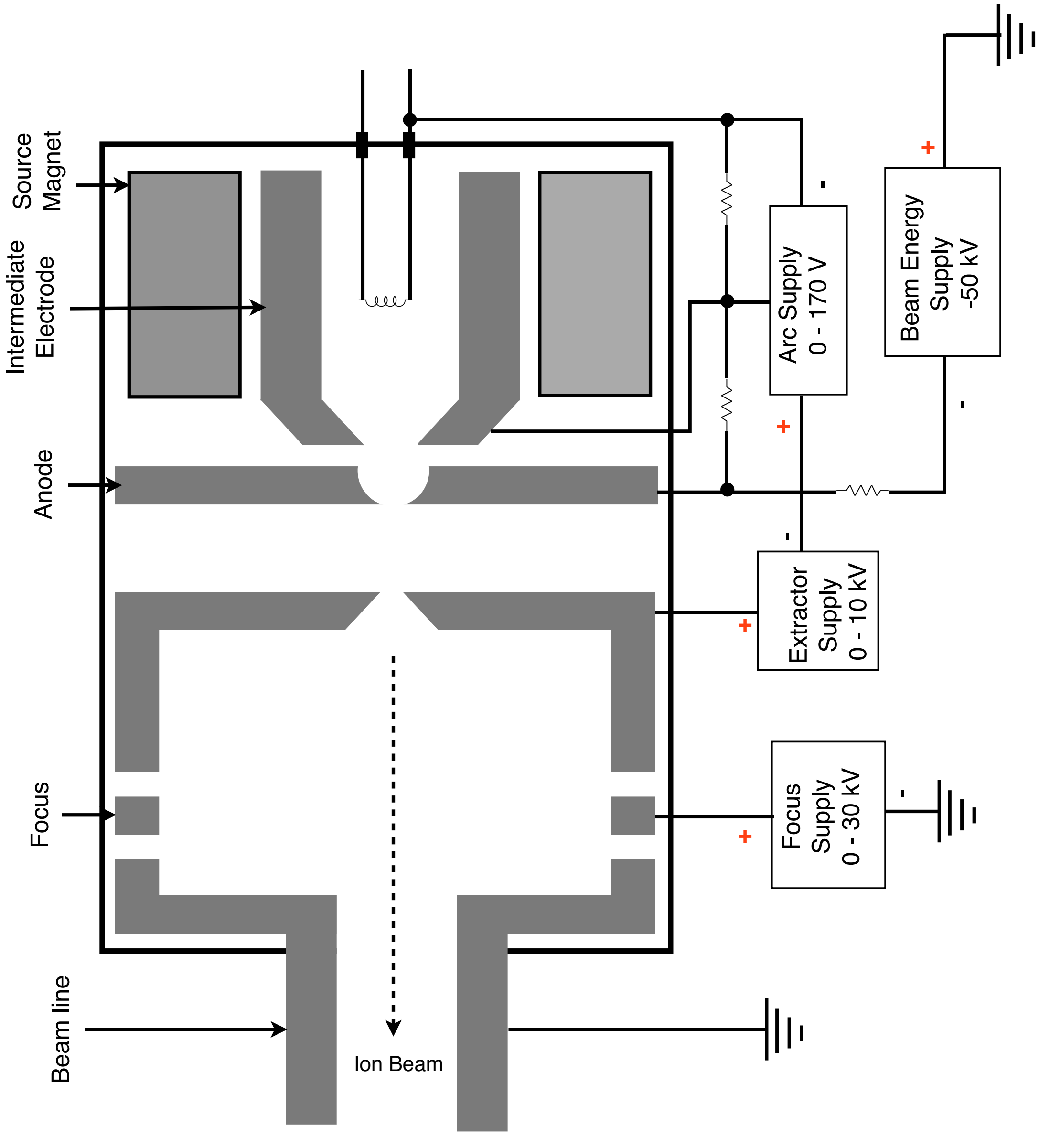

Figure 3.2: Direct Extraction Negative Ion Source (DENIS II)

the halo were selected. From the second plasma that forms on the high-vacuum side of the anode, negative ions were selected using an extractor, which was held at about 7–8 kV so that a large potential difference existed between the extractor and anode. The extracted negative ions were focused using a focusing magnet and accelerated to 50 keV toward the tandem accelerator.

3.1.2 Low-Energy Beam Transport

The low-energy side of the tandem accelerator was designed to transport beams from various ion sources to the accelerator. The ion beam from DENIS was first bent through an inflection magnet, selecting D^- from any other negative ions that may have been present in the beam, and provided initial steering of the beam toward the accelerator. The beam may then be optionally pulsed by a chopping and bunching system described in Section 3.1.3. The beam was steered and focused by magnetic steerers, a quadrupole magnet, an Einzel lens and a gridded lens. Each section of the accelerator beam line was kept under high vacuum ($< 10^{-6}$ torr) to ensure minimal kinematic losses during ion acceleration and transport.

3.1.3 Beam Pulsing

Many physics experiments require beams consisting of short pulses or a small spread in energy of the beam. An excellent discussion of accelerator beam pulsing and bunching can be found in Ref.[Wie07]. The traditional method for pulsing beams is to sweep the beam across an aperture using a time-varying electric field followed by compression of the resulting beam packets with a longitudinal sinusoidal voltage [Lef62]. The TUNL chopping and bunching system consists of two electrostatic choppers and a single double-drift buncher [Wen80]. With typical DC beam currents at about 30 μA, we were able to produce about 3 μA of pulsed deuterium beam at a rate of 2.5 MHz and

2 ns width.

The main chopper consists of two parallel plates. A sinusoidal voltage of 2.5 MHz was applied to the plates resulting in an oscillating electric field that sweeps away ions which do not pass through the plates at the zero-crossing ($V = 0$) times. This results in pulses that have a frequency of 5 MHz because there are two zero-crossings per 400-ns period. Two sets of movable slits ensure that only ions with minimal angular deflection from the chopper pass through. The main chopper reduces the DC beam current by about 80%. A second auxiliary chopper is oriented at 90° with respect to the plates of the main chopper. A variable-frequency square-wave voltage phased to the main chopper was applied to the plates of the auxiliary chopper. The frequency of the auxiliary chopper was chosen to select one out of every two pulses from the main chopper, resulting in a 2.5 MHz repetition rate, which was ideal for our neutron time of flight setup, at the cost of an additional 50% in the DC beam current. Using this chopping scheme, one can expect about 10% of the net initial DC beam current in a usable pulsed beam.

The double-drift buncher [Mil76] is a cylindrical tube consisting of a long middle section with two short segments on either end. The end segments are at ground potential and the middle section is an rf cavity with a drift space on either side. The double-drift buncher earns its name because the beam is bunched as it traverses each gap. The length of the middle section of the buncher was set so that the distance traveled by the particles is one-half of an rf cycle. The ion velocity distribution is distorted into a sinusoidal distribution. Depending on the phase of the electric field at the time a particle passes through the buncher, it may be accelerated or decelerated. The phase was timed with the chopper such that the front edge of the beam pulse was decelerated while the back edge was accelerated, resulting in a compression of the beam pulse.

3.1.4 The 10 MV Tandem Van de Graaff

Upon exiting the pulsing and bunching system, the 50 keV negative ion beam was accelerated by the 10 MV FN Tandem Van de Graaff accelerator. Negative ions were accelerated through an evacuated tube which runs through a large steel tank. Central to the tank is a terminal electrode which was maintained at a large positive voltage using two charging chains. The tank is filled with insulating sulfur hexafluoride (SF_6) gas to prevent electrical discharges from the terminal. The attractive force felt by the negative ions accelerates them toward the terminal where they collide with a thin ($\approx 3\mu$g/cm) carbon foil. The foil strips electrons from the negative ions turning them into positive ions. A second acceleration is provided by the terminal to the now-positive ions. It is from these two accelerations that the tandem accelerator earns its name. The energy of the positive ion beam as it exits the accelerator is $T + 50\text{keV} + QT$ where T is the terminal voltage and Q is the charge state of the ion. A schematic of a Tandem Van de Graaff accelerator is shown in Fig. 3.3.

The terminal was charged using a Pelletron charging system [Nat12]. Two chains (referred to as the high-energy (HE) chain and low-energy (LE) chain) comprise metal pellets connected by insulating nylon links. The chain links are charged via a negatively-charged inductor electrode. The positively-charged links are driven mechanically toward the terminal. Chains pass through a suppressor electrode so they do not arc as charge is inductively transferred to the terminal via the terminal pulley. Charging currents of 100 - 200 μA per chain are delivered to the terminal.

The terminal voltage was measured with a generating voltmeter (GVM). Two capacitive pick-off (CPO) units measure the capacitance variation due to movement of the terminal. The signal from the CPO units are used to correct the GVM measurement of the terminal voltage. In order to maintain a stable terminal voltage, charge may be extracted by moveable corona needles. A variable resistor connected to the needles

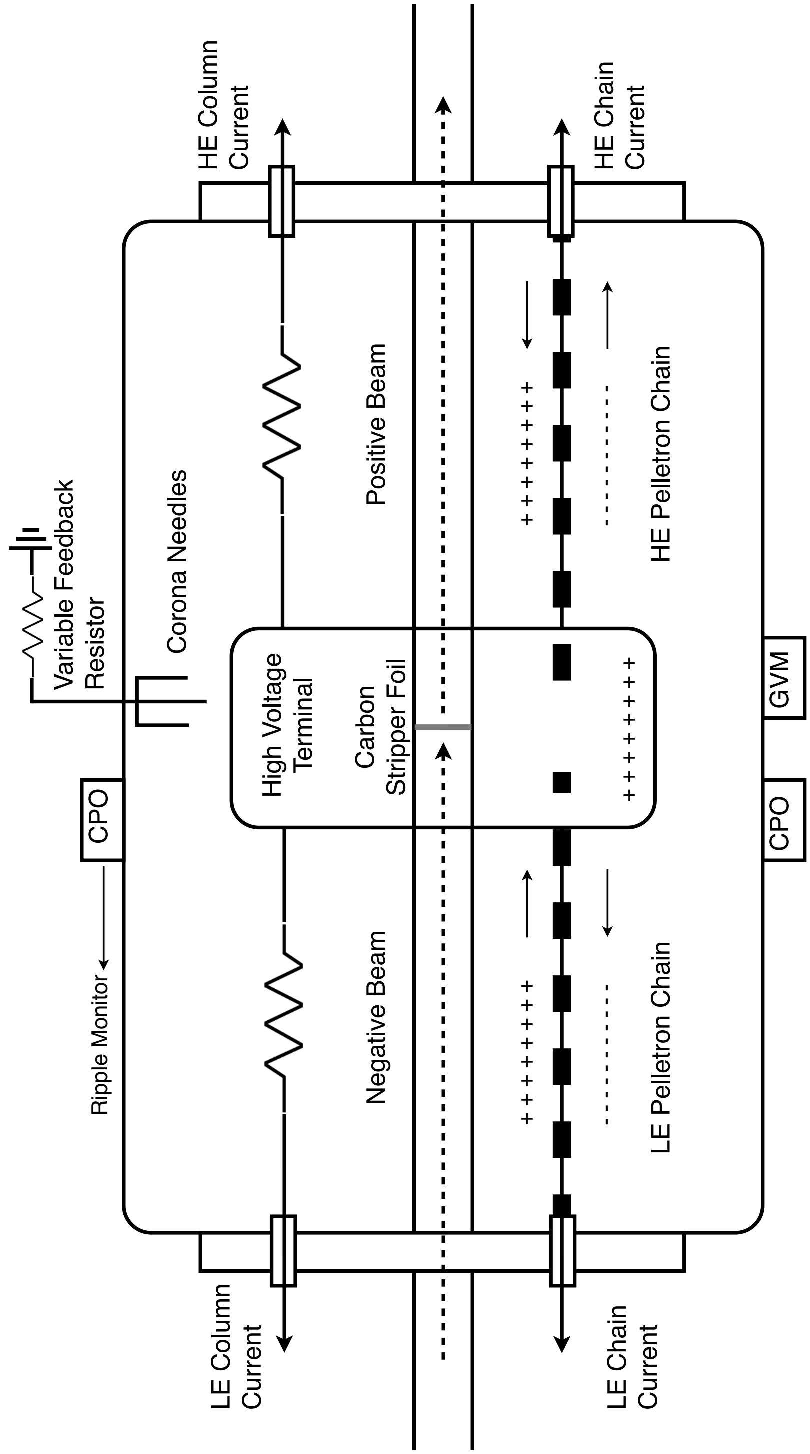

Figure 3.3: Tandem Van de Graaff accelerator schematic (adapted from Ref.[Ins12]).

may be adjusted to increase or decrease the charge removed from the terminal so that a constant terminal voltage may be obtained. The signal that provides feedback to the variable resistor is generated from a stabilizer circuit. When the stabilizer circuit is set to *GVM mode*, the output of the GVM is compared to a reference value which is set by the experimenter. The error signal created from the difference of these two values provides the feedback to the variable resistor connected to the corona needles, adjusting the terminal voltage measured by the GVM until the GVM signal and reference value agree. A second mode of the stabilizer circuit is described in the Section 3.1.5.

3.1.5 High Energy Beam Transport

After passing through a quadrupole focusing magnet upon exiting the tandem, the accelerated positive ion beam passes through the 20–70° analyzing magnet, labeled as "Magnet #1" in Fig. 3.1, where the beam is deflected into one of a number of possible experimental areas. The beam line used for the experiment described in this work was at 38° with respect to the tandem. The magnetic field of the analyzing magnet was adjusted such that only beam with the energy desired for the experiment was able to complete the 38° bend. A pair of symmetric metal slits were situated just beyond the analyzing magnet. When the field is properly adjusted, the beam will pass directly through the slits. The slits were set to intercept a small part of the beam on either side so that a well-tuned beam will strike both slits evenly. This allows for another mode of operation of the terminal stabilizer circuit described in Section 3.1.4. *Slit mode*, which was used during experimental runs, generates an error signal when the current read from the slits is not properly balanced due to variations in the terminal voltage. This error signal is then used to adjust the variable resistance in the corona needle assembly.

Once the mono-energetic beam passed through the 20-70° analyzing magnet, it was steered and focused by three additional quadrupole magnets and three magnetic steerers before it reached the deuterium gas cell in the neutron time-of-flight area.

3.1.6 Deuterium Gas Cells

The pulsed deuterium beam was used to produce pulsed neutron beams ranging in energy from about 4–15 MeV via the $^{2}\mathrm{H}(d,n)^{3}\mathrm{He}$ reaction [Hut07]. This source reaction is desired for our experiment because of the large cross section for the production of forward-angle neutrons [Dro78]. The Q-value of the source reaction is 3.26 MeV, which allows for good energy separation between neutrons produced from deuteron breakups (2.2 MeV threshold) on the beam stop.

The deuteron beam was incident on a deuterium gas cell at the end of the beam line, shown schematically in Fig. 3.4. The gas cell was 3.15 cm long and 1.0 cm in diameter. The deuterium pressure in the gas cell can be varied to allow for different neutron energy spreads. Because lowering the gas pressure decreases the probability of interaction and energy loss in the gas, both the energy spread and neutron flux are decreased. Selected gas-cell pressures and neutron energy spreads can be found in Table 3.1.

The beam entered the cell through a 6.35-μm thick Havar® foil [Hav], which separates the deuterium gas from the evacuated beam line. The deuterium beam was stopped at the end of the gas cell by a small piece of tantalum. The gas cell was electrically isolated from the beam line so that charge accumulated on the beam stop could be collected and measured with a beam-current integrator (BCI) that generates a pulse per fixed amount of charge, which can be counted by a scaler.

Beam Current

We attempted to perform experimental runs at a beam current of about 1 μA. There are many factors which can affect the beam current on target, including the choice of beam

Table 3.1: Deuterium gas cell pressures and neutron energy spreads for neutron energies of 4 to 10 MeV. The gas cell was 3.15-cm long and 1.0-cm diameter with a 6.35 μm Havar$^{®}$ foil.

Neutron energy at center of cell (MeV)	Gas cell pressure (atm)	Deuteron energy before foil (MeV)	Deuteron energy at cell center (MeV)	Deuteron energy loss in foil (MeV)	Average neutron energy loss in gas (MeV)
4.0	2.0	1.978	0.883	0.795	0.709
5.0	4.0	2.776	1.774	0.637	0.803
6.0	4.0	3.544	2.735	0.540	0.562
7.0	4.0	4.410	3.733	0.464	0.436
8.0	7.8	5.488	4.751	0.398	0.699
9.0	7.8	6.429	5.783	0.356	0.594
10.0	7.8	7.399	6.823	0.322	0.518

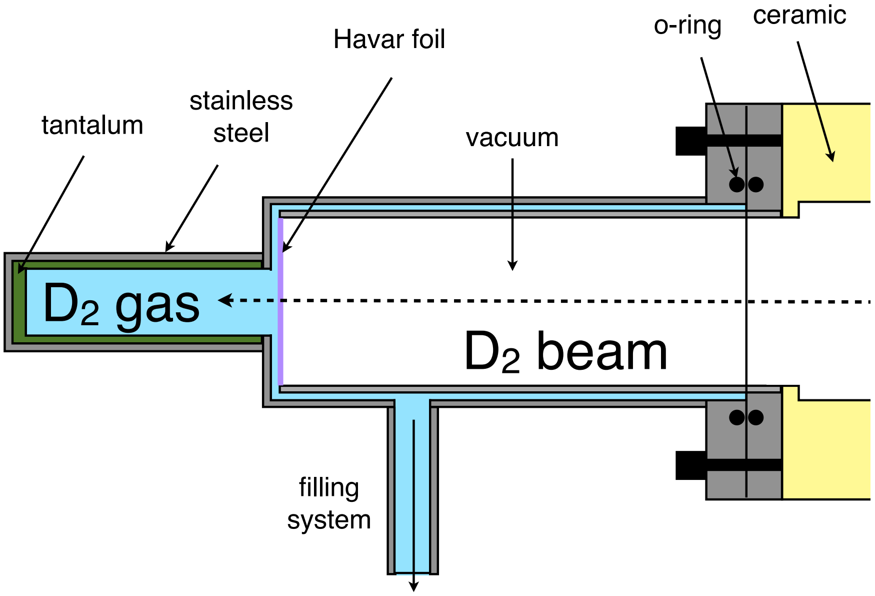

Figure 3.4: The deuterium gas cell where the ^{2}H$(d,n)^3$He source reaction takes place. Drawing not to scale.

energy, performance of the ion source, transmission of the beam through the tandem, and steering and focusing the beam to target. The intensity of the initial beam was reduced by about 50% during acceleration through the tandem. An additional 20-30% was lost as the beam was steered and focused to target. This resulted in beam currents ranging from about 0.5 - 1.5 μA on target for the experimental runs.

3.2 Neutron Scattering Targets

The neutrons emerging from the source reaction at around zero degrees were scattered from steel spheres filled with argon or neon. Descriptions of the gas sample can be found in Table 3.2. The scattering data were normalized to $n-p$ scattering using a small cylindrical polyethylene $(C_2H_4)_n$ target. Backgrounds due to neutron scattering from carbon were subtracted using a carbon target which was made to have the same number of carbon atoms as the polyethylene. Descriptions of the polyethylene and carbon normalization samples can be found in Table 3.3.

The gas target cell is described fully in Ref.[Rup09]. The cell was a 21.0-mm diameter stainless steel sphere with 0.5-mm wall thickness. The cell was filled with 99.999% natural neon or natural argon using a coupling device connected to a high-pressure filling station at TUNL. First, air was pumped from the filling system and gas cell with a roughing pump. Gas was introduced into the filling system and cell from a gas bottle. The bottle and gas cell were then valved off and the filling lines were cooled with liquid nitrogen, reducing the pressure. Gas from the bottle was introduced into the filling system, which was at a lower pressure than the gas in the bottle after cooling the system. The gas bottle was then valved off and the filling system was raised back to room temperature, resulting in a higher gas pressure in the filling system. The gas in the filling system was then introduced into the cell. This procedure of cooling, filling and heating the system was repeated 2–3 times. The cell was operated at about 170 atm, corresponding to a steel-to-gas ratio of about 4-to-1 by mass. This was well below the maximum pressure rating of 550 atm. The achievable pressure was limited by the ability to condense the gas in the cell at the filling station. The number of nuclei in the cell was determined by measuring the mass before and after filling to 0.01 mg accuracy. The pressure in the cell was stable, with no measurable difference during the experimental runs, sometimes up to 48 hours. Following the neon experiment, we determined that the gas pressure was stable over longer periods. The argon gas cell was filled only once at the beginning of the experiment and the same cell was used throughout.

3.3 Neutron Time-of-Flight Spectrometer

The neutron time-of-flight spectrometer comprises two liquid scintillator detectors. One detector was placed to the left and one was placed to the right of the beam axis, about

Table 3.2: Description of the gas targets. The uncertainty in the number of sample nuclei was approximately 0.2%.

Sample	Isotopic composition (% of nuclei)			Diameter (cm)	Number of sample nuclei
Neon	^{20}Ne	^{21}Ne	^{22}Ne	2.05	1.45–1.94$\times 10^{22}$
	90.48	9.25	0.27		
Argon	^{40}Ar	^{36}Ar	^{38}Ar	2.05	2.389×10^{22}
	99.6	0.34	0.07		

Table 3.3: Description of the polyethylene and carbon scattering targets

Sample	Isotopic composition (% of nuclei)		Diameter (cm)	Height (cm)	Number of sample nuclei
Polyethylene	^{1}H	^{12}C	1.43	2.28	$(2.923 \pm 0.003)\times 10^{23}$ hydrogen
$(C_2H_4)_n$	$\sim$66	$\sim$33			$(1.461 \pm 0.002)\times 10^{23}$ carbon
Carbon	^{12}C	^{13}C	0.95	2.38	$(1.463 \pm 0.002)\times 10^{23}$
	99.0	1.0			

four meters and six meters from the gas target cell, respectively. The detector on the four-meter track was filled with NE-218 liquid scintillator and the detector on the six-meter track was filled with NE-213 liquid scintillator (Nuclear Enterprise Ltd., Edinburgh, UK). Each liquid scintillator detector was optically coupled to a photomultiplier tube (PMT). Liquid scintillator detectors are ideal for this type of measurement because of their n-γ pulse-shape-discrimination (PSD) capabilities, described further in Section 3.3.2. These detectors are referred to as the "four-meter" and "six-meter" detectors. Technical details on the neutron detectors can be found in Table 3.4. The original publication describing the time-of-flight facility only describes the four-meter detector [Gla74]. The six-meter detector was first described in Ref.[Gle80]. The two neutron detectors and shielding were mounted to a steel carriage and move around the central scattering target on tracks. The angular range of the spectrometer is 20–155° with better than 0.5° accuracy. The neutron time-of-flight spectrometer is shown schematically in Fig. 3.5. A photograph of the scattering targets mounted in the beam

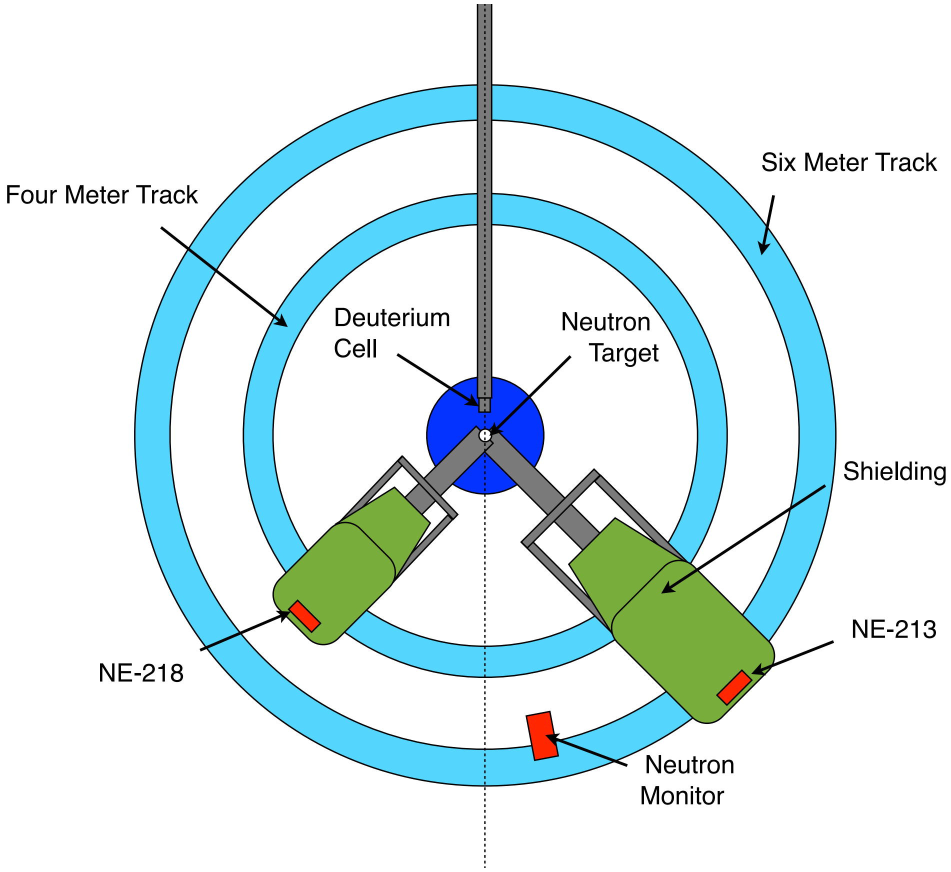

Figure 3.5: The TUNL time-of-flight setup. The target is located 10 cm from the end of the beam line where the neutron production cell is located. The two neutron detectors move on a four-meter and six-meter track around the neutron target. Figure not to scale.

line is shown in Fig. 3.6.

A third liquid scintillator detector, referred to as the "floor monitor" was placed behind the six-meter track at about 10° with respect to the beam axis. This detector was unshielded and had a direct line-of-sight to the neutron production cell behind the scattering target. This detector was used to monitor the direct neutron and γ-ray spectra and normalize the yields from the four- and six-meter detectors. A second monitor detector was installed on the ceiling of the time-of-flight area and used during the argon experimental runs. This detector, referred to as the "ceiling monitor", viewed the source reaction at 50° from the horizontal. The detector also had a copper collimator

Table 3.4: Properties of the TUNL time-of-flight liquid scintillator detectors. Both detectors are right cylinders. Densities and hydrogen/carbon ratios are taken from Ref.[Ang79].

Detector	Type	Radius (cm)	Thickness (cm)	Density (g/cm^3)	N_H (hydrogen atoms/cm^3)	N_C (carbon atoms /cm^3)	hydrogen/carbon ratio
six-meter	NE-213	6.35	5.08	0.874	4.82×10^{22}	3.98×10^{22}	1.213
four-meter	NE-218	4.45	5.08	0.879	5.10×10^{22}	3.99×10^{22}	1.28

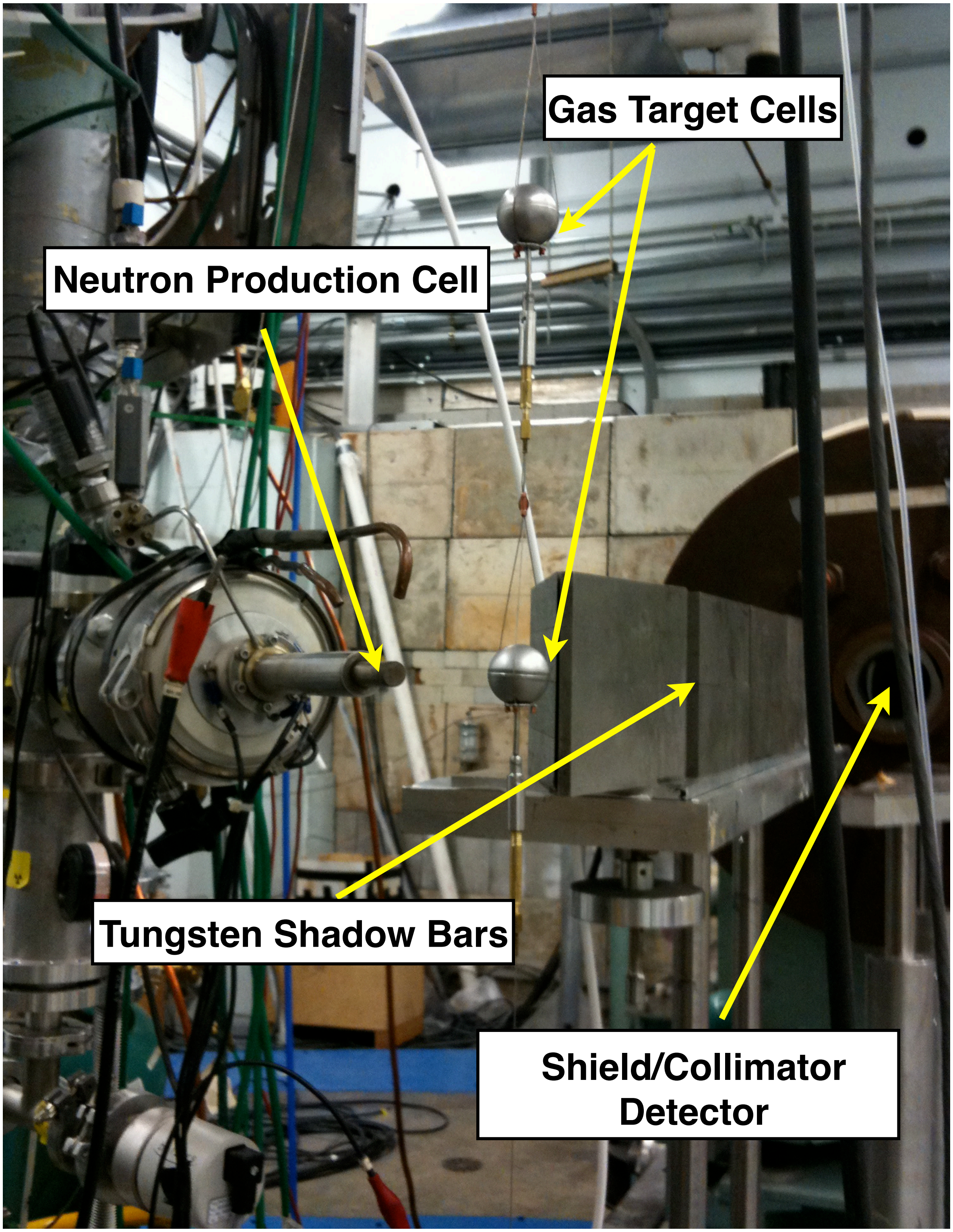

Figure 3.6: The scattering targets mounted in the NTOF beam line, the neutron production cell, and six-meter detector.

which allowed a direct line-of-sight to the neutron production cell and no line-of-sight to the scattering target.

3.3.1 Shielding

Each of the detectors is surrounded by a massive shield and collimators. A pre-shield is made from rings of lead and copper to shield from γ-rays. The primary neutron shield is made of paraffin mixed with lithium carbonate. The collimator is a double-truncated cone designed to shield neutrons scattered from the air around the sample. The double-cone serves to minimize neutron scattering from the walls of the collimator. A schematic of a detector and shielding is shown in Fig. 3.7.

Despite the forward-angle preference for neutrons created in the source reaction, the neutron detectors had to be shielded from a direct line-of-sight to the neutron production cell by placing massive tungsten blocks on a stand close to the target cell. These "shadow bars" were placed so that the scattering target had a direct line-of-sight to the neutron detectors while the neutron production cell was fully shielded. The shadow bars were also placed so that scattering from the shadow bars themselves was minimized.

3.3.2 Electronics and Data Acquisition

A beam pick-off (BPO) signal was generated using a capacitive pick-off unit located in the beam line just before the deuterium gas cell. As a beam bunch passed through the capacitor, a charge pulse was generated and sent to a pre-amplifier. The signal was then sent to the TUNL control room and through a zero-crossing module. The resulting bi-polar charge pulse was used to mark the creation of each neutron pulse, serving as the "start signal" in the neutron time-of-flight measurement. It was also counted by a scaler in the TUNL control room to verify the correct repetition rate.

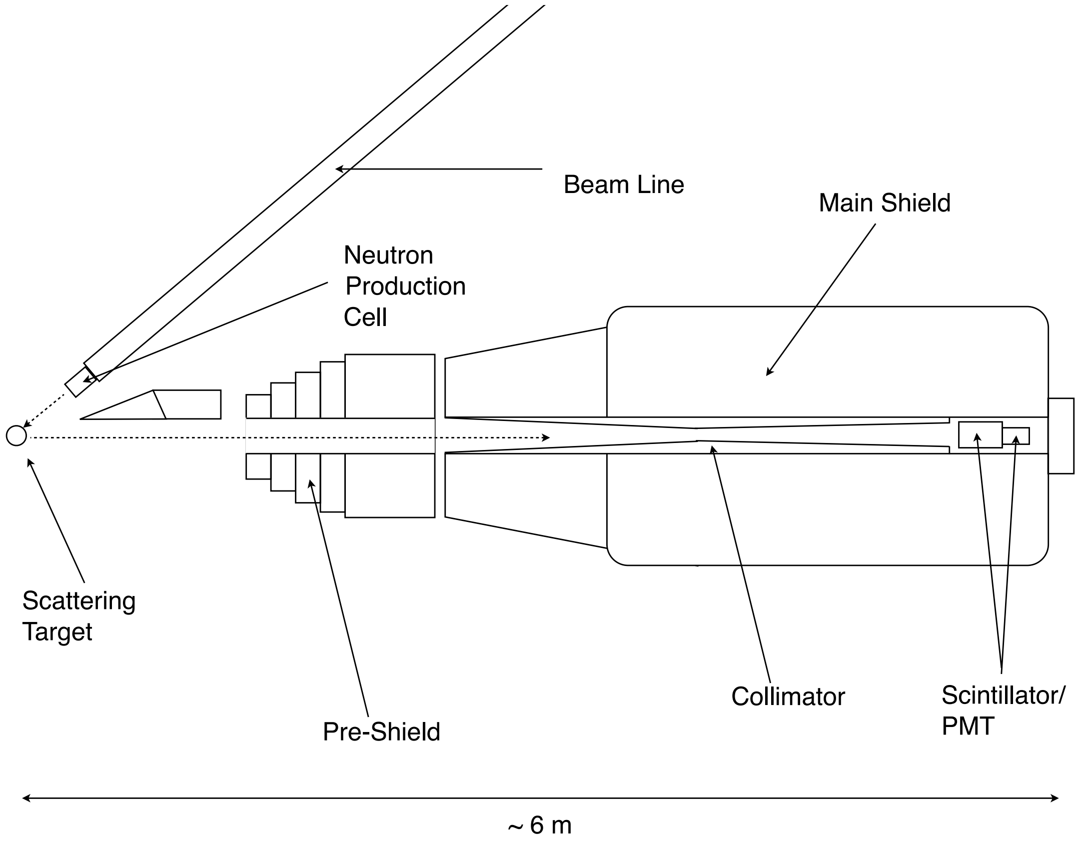

Figure 3.7: Schematic of a neutron time-of-flight detector and shielding. The path of the scattered neutrons is indicated by the dashed line. The 6-m scale is approximate.

Using an oscilloscope, the signal width and zero crossing location was also continuously monitored for quality since the chopper settings, particularly the amplitude of the main chopper and phasing of the auxiliary chopper could affect the pick-off signal and time resolution of the spectrometer.

The PMT anode signals from each detector (four-meter, six-meter, floor monitor, ceiling monitor) and the beam pick-off signal were carried from the neutron time-of-flight area to the TUNL control room via low-loss 50 Ω cables. The signals were processed using standard Nuclear Instrumentation Modules (NIM) and Verse Module Eurocard (VME) electronics. A block diagram of the TUNL time-of-flight electronics and data acquisition can be found in Fig. 3.8.

The signals from the neutron detectors were processed identically. The PMT anode signals were sent to a Mesytec MPD-4 n-γ discriminator [Mes]. Because liquid scintillator detectors are sensitive to both neutrons and γ rays, it was necessary to discriminate against γ rays to reduce backgrounds. This was accomplished using pulse-shape-discrimination (PSD) techniques. Gamma rays interact directly with atomic electrons in the scintillator and neutrons interact with protons via $n-p$ scattering. Because the photon emission decay rate in the scintillator is shorter for electrons, which are low-ionizing, than for recoiling protons, which are high-ionizing, the decay time of the resulting PMT signal is shorter for γ-ray interactions than it is for neutron interactions.

The MPD-4 module outputs an analog pulse at a constant fraction of the trailing edge of the PMT pulse, yielding a slightly smaller signal for a γ ray than for a neutron-induced signal. This signal was digitized by a CAEN V785 14-bit peak-sensing analog-to-digital converter (ADC). The PMT anode signal was also sent to the ADC so that a neutron energy spectrum was obtained. A third output gate signal from the MPD-4 module and the BPO signal were sent to a CAEN 775 14-bit time-to-digital converter

(TDC). The TDC effectively measured the time difference between the BPO signal and a signal in one of the detectors, thus measuring the neutron time-of-flight. To reduce dead time, the TDC was operated in “common start” mode, in which any detector’s gate signal could provide the start signal for the TDC. The stop signal was provided by the beam pick-off signal from the following beam pulse. The TAC range on the TDC was set to 0–400 ns resulting in a time conversion of 0.088 ns/channel in the TDC spectra.

A DAQ trigger circuit was employed in order to measure the dead time associated with the computer readout and electronics. The “ADC busy” signal was raised for 8 μs following an ADC hit while the module converted the pulse height into a digital signal. About 200 ns following the ADC conversion, the “ADC data ready” (drdy) signal was raised. This signal triggered a separate VME-based trigger module for about 25 μs as the event was read from the buffer. The combination of these signals ($\sim$ 32 μs) is referred to as the “DAQ busy” signal. A 60 Hz clock was counted by a scaler directly and after being vetoed by the DAQ busy signal. The dead time was measured by the dividing the vetoed scaler counts by the raw scaler counts. Measured dead-times were usually less than 3%.

The signals from the ADC, TDC and scaler modules were read out to a PC through a single board computer (SBC) in the VME crate. The subsequent online visualization and analysis was performed using code based on the CODA DAQ software framework. Offline analysis was performed using the ROOT data-analysis framework [Bru97].

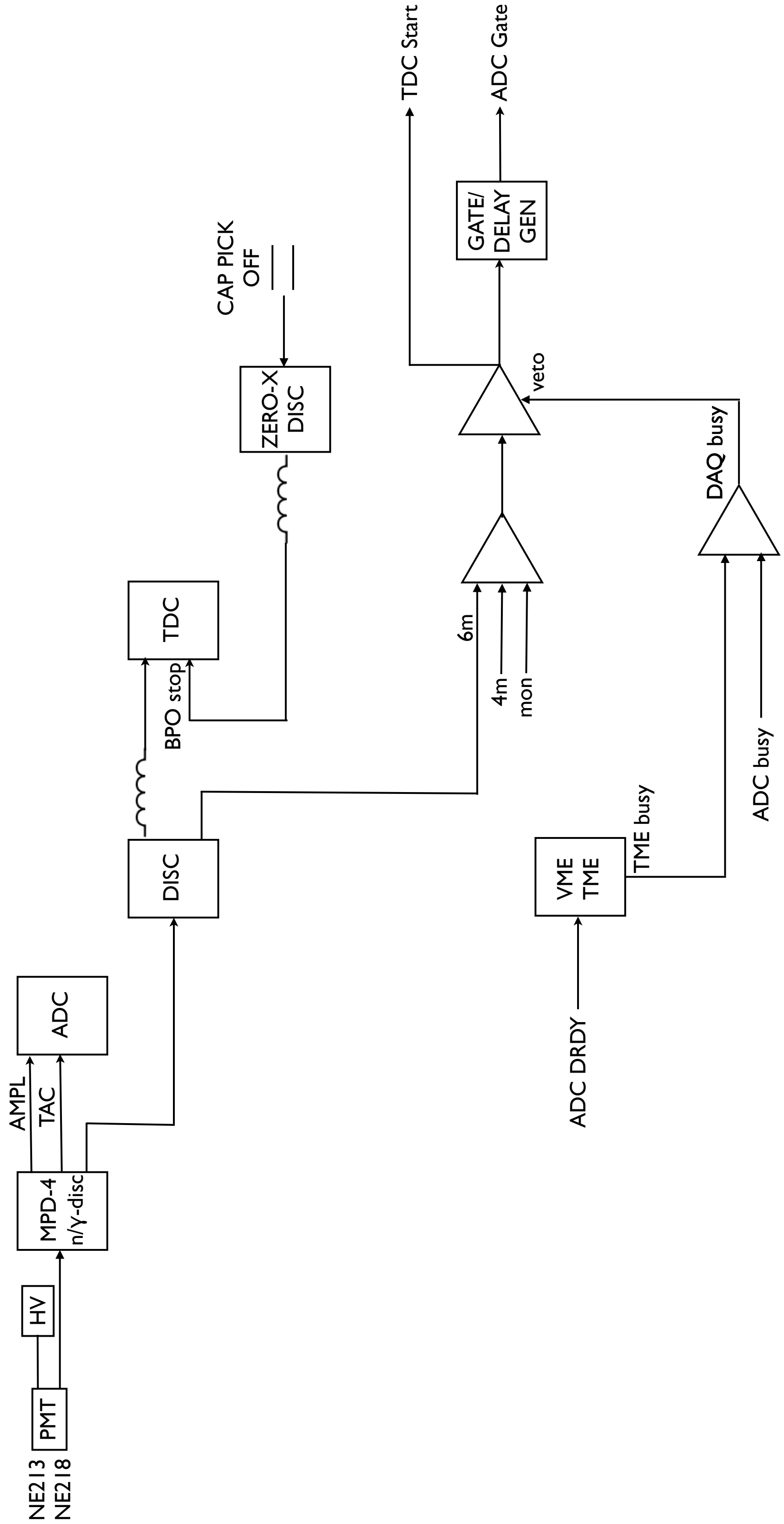

Figure 3.8: Schematic of the TUNL time-of-flight data acquisition and electronics.

Chapter 4

TUNL Experimental Data, Analysis and Results

This chapter describes the data analysis and results for the differential elastic scattering cross sections of neutrons from argon at 6.0 MeV and neon at 5.0 and 8.0 MeV. Cross-section data were obtained using the neutron time-of-flight (TOF) technique described in Chapter 3. Data were fit using the spherical optical model, which was described in Section 2.2. Measurements were performed between August 2009 and August 2011 and represent about 1200 hours of beam time.

4.1 Experimental procedure

To determine the differential cross section, neutron TOF spectra were accumulated for neutrons scattering from target cells filled with argon or neon at the TUNL neutron time-of-flight (NTOF) facility. The scattering samples were suspended from steel wires located 10.0 cm from the end of the neutron production cell. This arrangement allowed a filled cell (SAMPLE IN) and an empty cell (SAMPLE OUT) to be moved in and out of the beam without changing the horizontal alignment. The center of the sample was aligned with the beam axis so that the neutron beam would illuminate the sample symmetrically with respect to its center. After sufficient statistics were acquired for SAMPLE IN, SAMPLE OUT data were collected. Because of the large number of nuclei in the stainless steel sphere compared to sample nuclei, it was sometimes necessary to run for about 12 hours for each SAMPLE IN and SAMPLE OUT to acquire enough statistics. SAMPLE IN and SAMPLE OUT spectra were acquired for each angle in roughly 10° steps from 20–155°. For most angles, the four-meter and six-meter detectors were placed at symmetric angles with respect to the beam axis so that count rates and spectra could be checked for systematic errors as data were acquired. This arrangement was not possible for about 75–95° because the shadow bars could not be placed to avoid scattering from the opposite shadow bar into the detector. These angles were measured in asymmetric pairs.

Data were taken periodically with the polyethylene (SAMPLE IN) and carbon (SAMPLE OUT) scattering samples, which were mounted to the steel wires in the same manner as the gas target cells. Thirty minutes of running with these samples was sufficient to achieve a statistical uncertainty of 1%. Both the four-meter and six-meter detectors were placed at 36° for this measurement. This angle was determined based on the neutron energies used, so that the hydrogen elastic peak in the TOF spectrum fell between the carbon elastic and inelastic peaks, shown in Fig. 4.6a.

4.2 Data Reduction

4.2.1 Threshold and Pulse Shape Discrimination Cuts

Both an energy threshold and a PSD cut were placed on each TOF spectrum to reduce backgrounds. The threshold cut was used primarily to remove low-energy neutrons. The placement of this cut was determined using a strong ^{137}Cs source, which produces a single 662-keV γ ray. The cut was placed at 1×Cs for the 8.0-MeV data and 1/2×Cs for the 5.0- and 6.0-MeV data. A threshold of 1×Cs corresponds to the Compton edge (447 keVee) from a backscattered 662-keV γ ray.

It is important to understand the relationship between the energy deposited in the scintillator and the light produced. This depends on the type of particle depositing energy and the type of scintillator material. To determine the neutron energy that corresponds to a particular fraction-of-Cs threshold, the light output response for both recoiling protons and electrons must be understood. For both the four-meter and six meter detectors, a 1×Cs threshold corresponds to a 2.2-MeV neutron that transferred all of its kinetic energy to a proton in the scintillator. A 1/2×Cs threshold corresponds to a neutron energy of about 1.4 MeV. The determination of the light output response for our scintillators is discussed in Section 4.3.1.

Fig. 4.1 shows a ^{137}Cs spectrum for the four-meter detector. The 1×Cs threshold was determined from the position of the Compton edge. Because of the finite energy resolution of the detector, the endpoint of the spectrum is distorted. The position of the Compton edge was therefore chosen as the point halfway between the peak and endpoint in the spectrum. The 1/2×Cs threshold was determined from the 1×Cs value, adjusted for the ADC pedestal. Special "pedestal" runs were taken before each experiment to record the ADC value when there was no PMT hit. The hardware threshold was then set higher than the pedestal value in order to minimize dead time. Fine adjustments in the ADC threshold and gain were adjusted for each detector using the MPD-4 n-γ discriminator module discussed in Section 3.3.2. Course changes to the ADC gain were made by raising or lowering the high voltage on the PMT.

The neutrons in the TOF spectrum were separated from the γ rays using a PSD cut. Fig. 4.2 shows a PSD spectrum for the four-meter detector. A clear separation can be seen between the neutrons and γ rays. Low-energy neutrons were also eliminated using the energy threshold cut shown in the figure. The threshold cut also discriminates most of the events where the pulse height is too small to perform an adequate PSD cut.

The effect of the threshold and PSD cuts can be seen in Fig. 4.3. An un-cut TOF

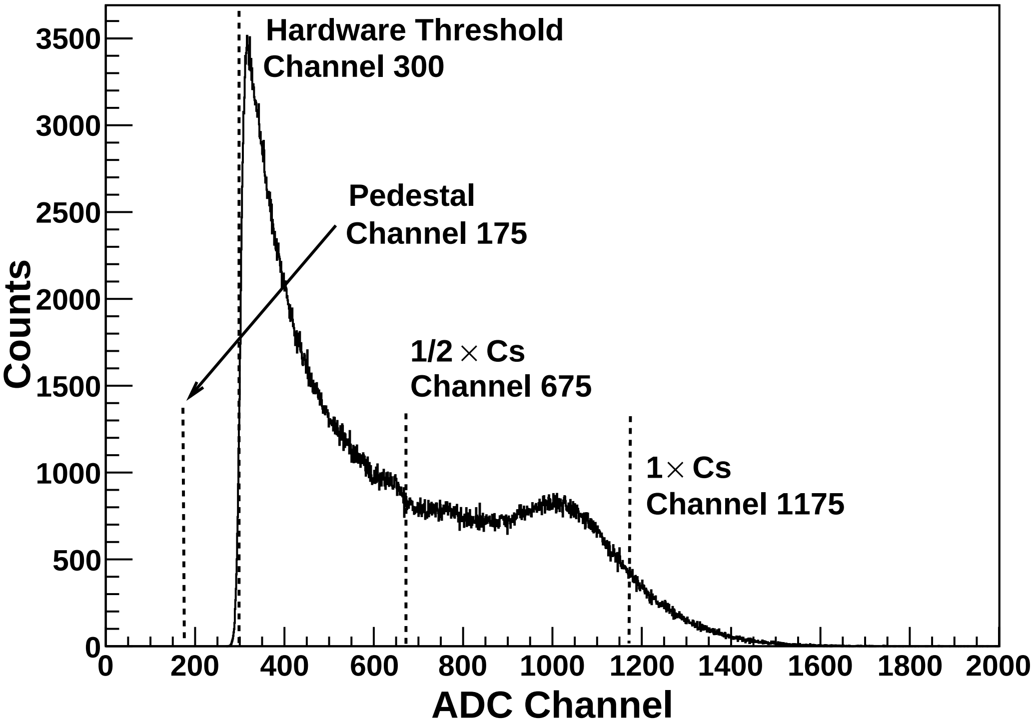

Figure 4.1: A ^{137}Cs spectrum for the four-meter detector. See text for discussion of the figure.

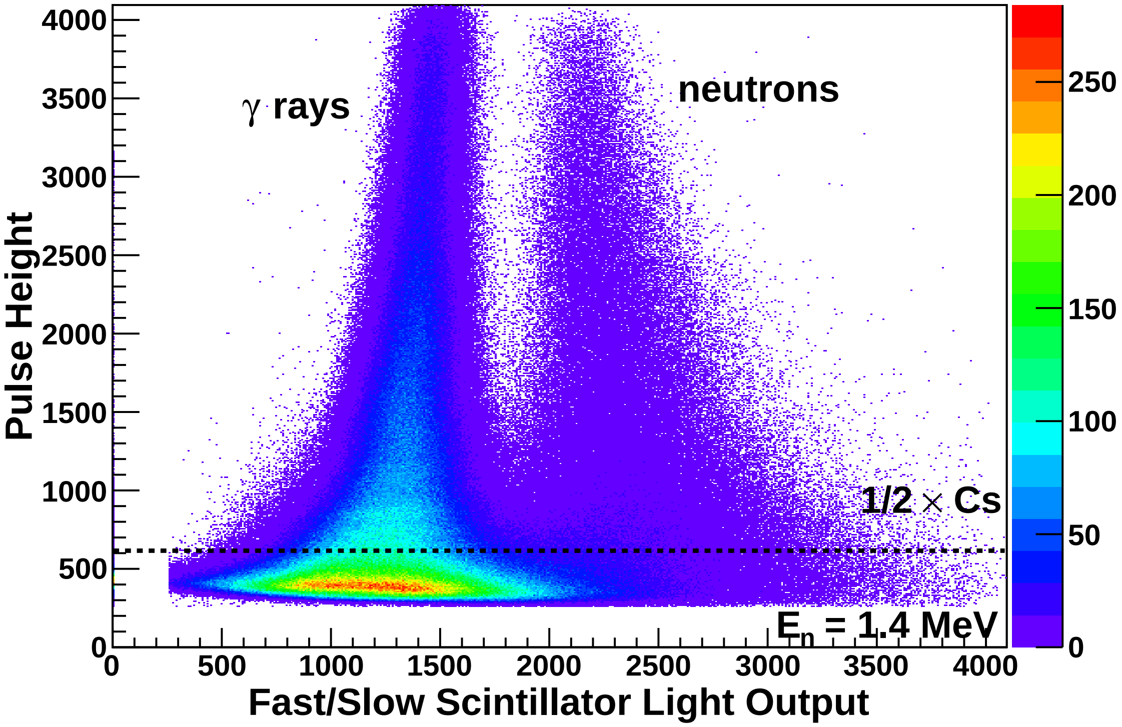

Figure 4.2: A PSD spectrum for the four-meter detector showing the pulse-height output from the PMT versus the fast/slow component of the scintillator light output. This allows γ-ray and neutron interactions in the scintillator to be separated. An energy threshold cut for 1/2×Cs (E_n = 1.4 MeV) is also shown.

spectrum taken with the four-meter detector using the neon gas cell target is compared with the same spectrum after threshold and PSD cuts. Because of how the TDC was triggered with respect to the detector and beam pick-off signals, time of flight increases with decreasing channel number. The large time-correlated γ-ray background, which is mostly due to neutron-induced excitations of nuclei in the tantalum beam stop is eliminated in the cut spectrum. Elastic and inelastic scattering of neutrons from the neon sample and the stainless steel sphere become more prominent after low-energy neutrons and γ rays from room backgrounds are eliminated. The time resolution of the spectrometer as determined from the γ-ray peak was about 4 ns full width at half maximum (FWHM).

4.2.2 Monitor Spectra

To normalize the SAMPLE IN and SAMPLE OUT spectra, neutron spectra were also acquired for the floor monitor and ceiling monitor described in Chapter 3. Because the floor monitor was able to view both the scattering sample and neutron production cell, it was not the optimal choice for normalization because the neutron spectrum depends slightly on whether the measurement was SAMPLE IN or SAMPLE OUT. Another concern was that when the four-meter and six-meter detectors were placed at small angles, close to the floor monitor, neutrons could undergo a small-angle scatter from the detector shield and be counted in the neutron spectrum. The ceiling monitor is a better choice since it is out of the horizontal plane and is collimated to ensure that it only views the neutron production cell and not the scattering sample. However, it was determined from the data that the choice of which monitor to use made no difference in the yields for this experimental setup. Another choice for normalization was to use the BCI scaler. The results from the BCI normalization were consistent with both the floor monitor and ceiling monitor within statistical uncertainty, about 0.2%.

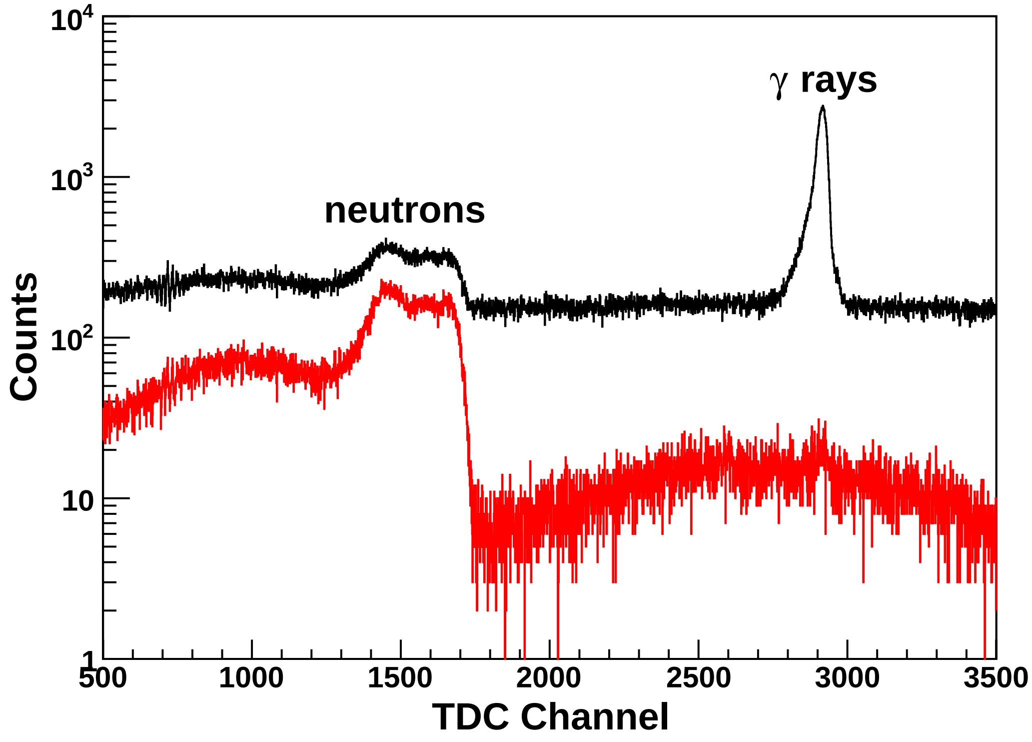

Figure 4.3: A TDC spectrum with no cuts (black) and with both the PSD and threshold cut (red). Gamma rays and low-energy neutrons are removed with the PSD and threshold cuts leaving a peak from from elastic and inelastic scattering in neon and the target cell as well as background of "room-return" neutrons. Time of flight increases with decreasing channel number. The TDC has a gain of 0.088 ns/channel.

A sample floor monitor TOF spectrum is shown in Fig. 4.4. The large peak around channel 2175 corresponds to the mono-energetic neutrons produced in the ^{2}H$(d, n)^3$He reaction in the deuterium gas cell. To determine the ^{2}H$(d, n)^3$He neutron yield, this peak was integrated between limits chosen to contain the whole peak. A background was subtracted by integrating a linear function between the two peak limits. The choice of integration window for the peak was not critical as long as it was unchanged during the analysis of data for a particular angle.

Care must be taken when filling the deuterium gas cell to minimize contamination. Neutrons produced in the ^{12}C$(d, n)^{13}$N reaction due to carbon contamination in the gas cell can produce backgrounds in the TOF spectrum. In order to minimize carbon contamination, the deuterium gas cell was evacuated and filled with deuterium gas that passed through a liquid-nitrogen cold trap. These carbon backgrounds will appear in the TOF spectra about 5 MeV down from the ^{2}H$(d, n)^3$He neutrons. Although these neutrons are well-separated in time from the elastic scattering peak, they may produce backgrounds for the inelastic peaks.

4.2.3 Neutron Time-of-Flight Yields

Difference Spectra

With the monitor yields determined, the normalized TOF spectra for the scattering samples could be obtained and the TOF yields could be determined. The SAMPLE OUT TOF spectrum was normalized to the SAMPLE IN TOF spectrum. The two spectra were subtracted bin-by-bin to determine the difference yields. The difference spectrum was obtained using

$$\text{DIFF} = \text{SAMPLE IN} - \text{SAMPLE OUT}\frac{\text{MON IN}}{\text{MON OUT}}, \tag{4.1}$$

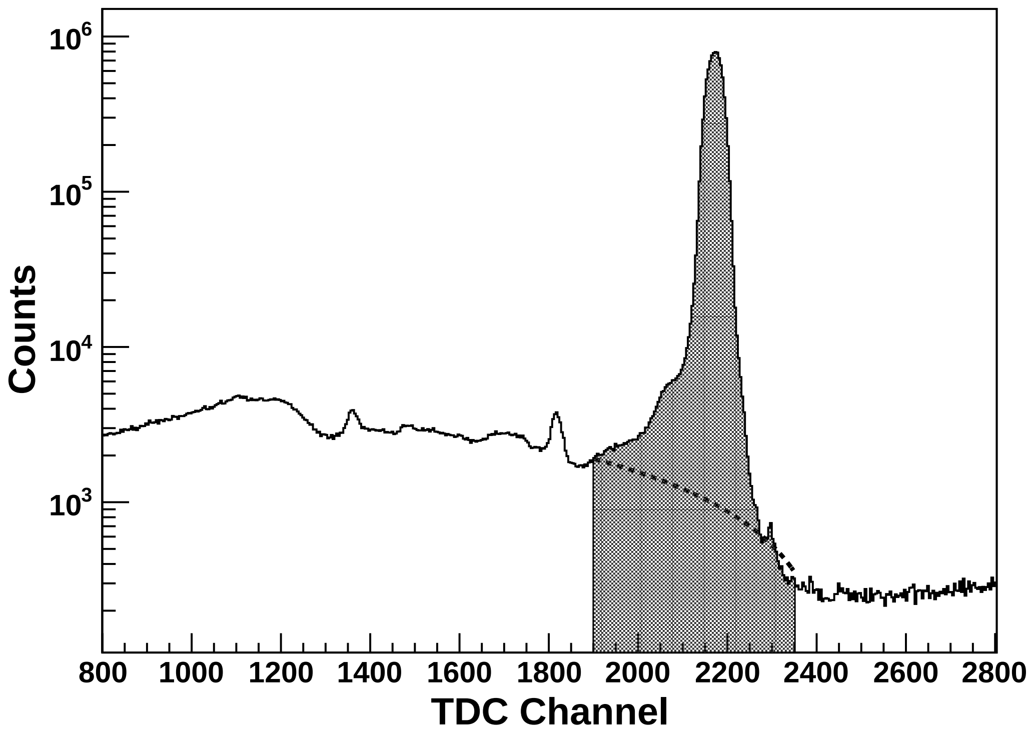

Figure 4.4: Floor monitor TOF spectrum at $E_n = 8.0$ MeV cut for PSD and a threshold of 1×Cs. The neutron peak is shown as the shaded region. The other peaks in the spectrum are are from carbon contamination in the deuterium gas cell, see text for further details. The deuterium gas cell was pressurized to 7.8 atm. Time of flight increases with decreasing channel number. The TDC has a gain of 0.088 ns/channel.

where DIFF is the number of counts in the difference bin, SAMPLE IN and SAMPLE OUT are the number of counts in the SAMPLE IN and SAMPLE OUT bins, respectively, and MON IN and MON OUT are the neutron yields from the SAMPLE IN and SAMPLE OUT monitor spectra, respectively. All spectra were corrected for dead time.

Fig. 4.5a shows an example TOF spectrum for SAMPLE IN and SAMPLE OUT normalized to the neutron monitor using the target cell filled with neon at $\theta_{CM} = 102°$ at $E_n = 8.0$ MeV. Fig. 4.5b shows the difference spectrum. The elastic scattering peak from ^{20}Ne can be seen on the right. Peaks from the 2^+ first excited state ($E_x = 1634$ keV) and 4^+ ($E_x = 4248$ keV) second excited state are visible to the left of the elastic peak.

Fig. 4.6a shows an example TOF spectrum for polyethylene and carbon normalization samples at $\theta_{CM} = 36\ °$ at $E_n = 8.0$ MeV. The SAMPLE IN refers to the polyethylene and the SAMPLE OUT refers to the carbon. Fig. 4.6b shows the difference spectrum where only the peak from $n - p$ scattering is visible.

Calculation of Yields

The TOF yields were obtained by integrating the elastic neutron peak in the difference spectrum. The elastic peak was fit with a Gaussian function. The integration window was chosen to be $\pm 3\sigma$ of the mean of the fitted Gaussian. Because the first excited states are relatively high for argon and neon ($E_x = 1.46$ MeV for ^{40}Ar and $E_x = 1.62$ MeV for ^{20}Ne) the inelastic peaks were well-separated in time of flight from the elastic peaks. Fig. 4.7 shows a TOF difference spectrum for the four-meter detector using neon at $\theta_{CM} = 102°$ as an example.

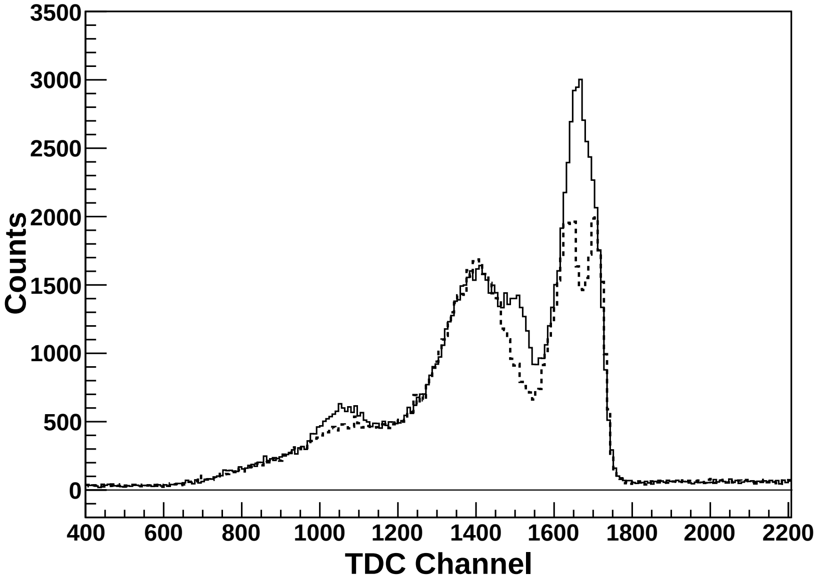

(a) The solid curve corresponds to the SAMPLE IN measurement (scattering cell and neon). The dashed curve corresponds to the SAMPLE OUT measurement (scattering cell only).

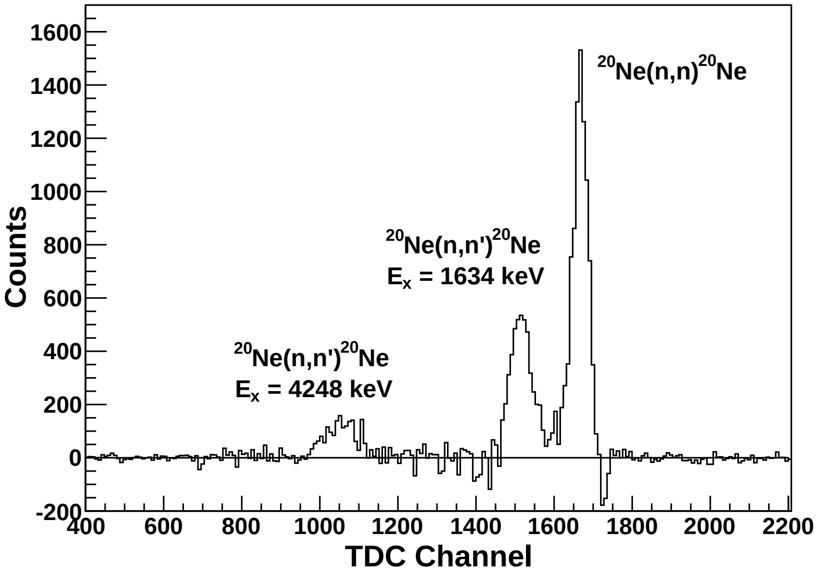

(b) The difference between SAMPLE IN and SAMPLE OUT. Peaks from both elastic scattering and inelastic scattering are visible.

Figure 4.5: Normalized SAMPLE IN, SAMPLE OUT and DIFF TOF spectra for the six-meter detector. The sample is neon at $\theta_{CM} = 102^\circ$ at $E_n = 8.0$ MeV. The dip to the right of the elastic peak is due to changes in the timing resolution from beam instabilities during the course of an experimental run. Time of flight increases with decreasing channel number. The TDC has a gain of 0.088 ns/channel.

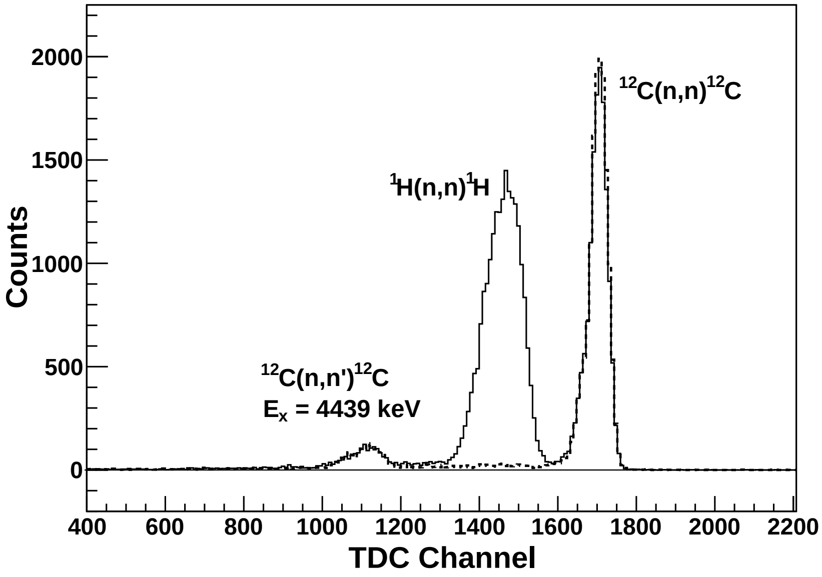

(a) The solid curve corresponds to the SAMPLE IN measurement (polyethylene). The dashed curve corresponds to the SAMPLE OUT measurement (carbon).

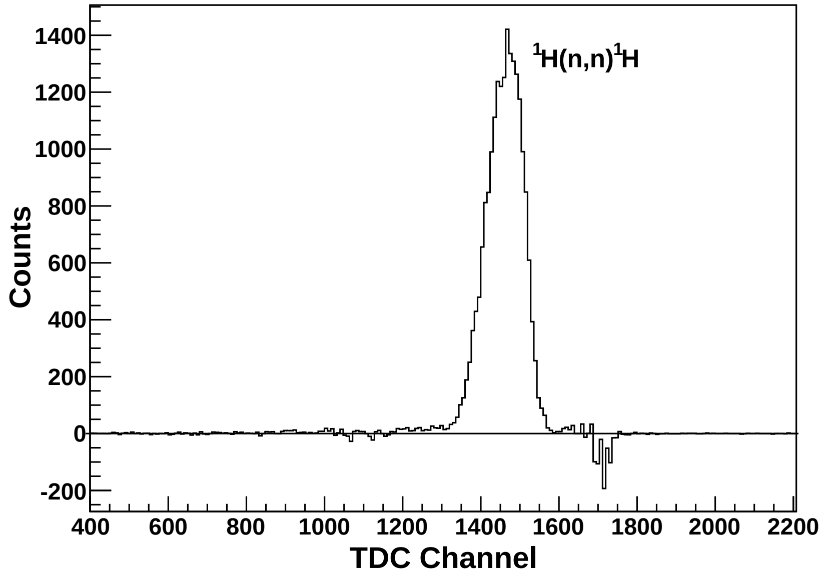

(b) The difference between the polyetyhlene and carbon spectra where only the peak from $n-p$ scattering is visible.

Figure 4.6: Normalized SAMPLE IN, SAMPLE OUT and DIFF TOF spectra for the six-meter detector using the polyethylene and carbon targets. The spectrum was measured at $\theta_{CM} = 36$ ° at $E_n = 8.0$ MeV. Time of flight increases with decreasing channel number. The TDC has a gain of 0.088 ns/channel.

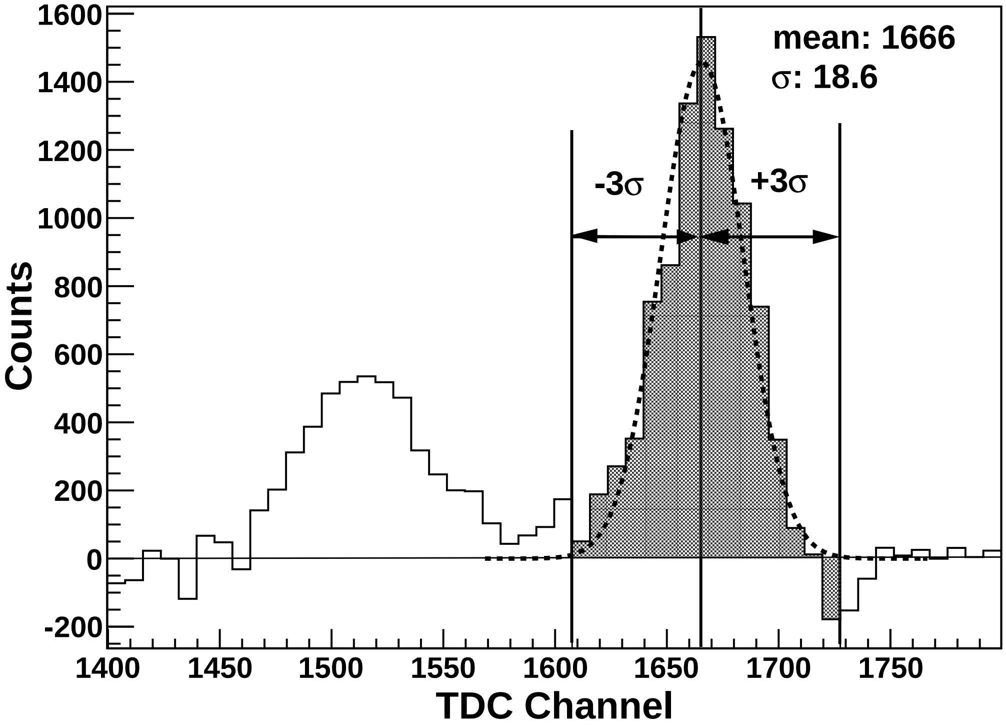

Figure 4.7: TOF difference spectrum for neon at $\theta_{CM} = 102°$. The elastic peak was fit with a Gaussian function and the window of integration was chosen to be $\pm 3\sigma$ of the mean of the fitted Gaussian.

4.3 Data Normalization

The differential cross sections for elastic scattering from argon and neon were calculated relative to the $n-p$ scattering cross section, which is well known. For each angle at a given neutron energy, a differential elastic scattering cross section was obtained using

$$\frac{d\sigma}{d\Omega}(E_n,\theta_s) = \frac{Y_s(\theta_s)}{Y_p(\theta_p)}\frac{A_p(\theta_p)}{A_s(\theta_s)}\frac{\epsilon_p}{\epsilon_s}\frac{n_p}{n_s}\frac{d\sigma_p}{d\Omega}(E_n,\theta_p), \tag{4.2}$$

where θ_s and θ_p are the angles, relative to the beam axis, of the scattering sample and polyethylene normalization sample, respectively. $Y_s(\theta_s)$ and $Y_p(\theta_p)$ are the time-of-flight yields of the scattering sample and hydrogen in the polyethylene normalized to the neutron monitor detector. $A_s(\theta_s)$ and $A_p(\theta_p)$ account for attenuation and multiple scattering in the scattering sample and polyethylene are described further in Section 4.3.2. The quantities ϵ_s and ϵ_p are the detection efficiencies of a neutron scattered elastically from a sample nucleus and a hydrogen atom in the polyethylene, respectively. The determination of the efficiencies is described in Section 4.3.1. The quantities n_s and n_p and are the number target nuclei in the scattering sample and the number of hydrogen atoms in the polyethylene. These values can be found in Tables 3.2 and 3.3. The $n-p$ cross section $\sigma(E_n,\theta_p)$ is known well up to about 350 MeV. The cross sections used in this experiment, shown in Table 4.1, were obtained from the Nijmegen partial-wave analysis of $N-N$ scattering data [Sto93, nn-12].

4.3.1 Detector Efficiencies

The detector efficiency depends on the relationship between the energy deposited in the scintillator and the light produced. Neutrons produce light via $n-p$ scattering in the scintillator material. Although scattering is isotropic for neutron energies less than about 10 MeV, the light-output (L.O.) function is not directly proportional to the

Table 4.1: Selected $n-p$ scattering cross sections used for data normalization. Cross sections were obtained from the Nijmegen partial-wave analysis of $N-N$ scattering data [Sto93, nn-12].

Lab angle	$n-p$ cross section (mb/sr)				
(degrees)	4.0 MeV	5.0 MeV	6.0 MeV	7.0 MeV	8.0 MeV
30.0	523	448	391	347	311
32.0	513	439	384	340	305
34.0	501	430	375	333	299
36.0	490	420	367	325	292
38.0	478	409	358	317	285
40.0	465	398	348	309	277

deposited energy, but rather [Kno00]

$$\text{L.O.} = kE_n^{3/2}, \tag{4.3}$$

where the proportionality constant k depends on the dimensions and properties of the liquid scintillator, specifically the density and hydrogen-to-carbon ratio. The L.O. response for various liquid scintillators has been studied by many authors (ex. [Pyw06, Nak01, Sas02, Ang79, Mas70, Cec79]). Combining the scintillator L.O. non-linearity with the recoil energy distribution for neutrons on protons, and using the fact that a neutron can impart up to all of its kinetic energy to a proton during a collision, one can construct a reasonable scintillator response function for neutron energy deposits in the liquid scintillator. In order to create a more realistic response function, carbon scattering in the liquid scintillator must be also be accounted for. Because the scintillation efficiency is low for high dE/dx particles, the carbon recoils do not contribute much to the scintillator response. Neutrons can however lose some energy following a scatter from ^{12}C and then scatter from a proton. Because of the mass difference the neutron cannot impart all of its energy to the ^{12}C, but will lose between 0 and 28% of its initial energy. This results in a decrease from $0.72E_n$ to E_n in the recoil energy distribution for neutrons with energy E_n. Lastly, the finite resolution of a detector will distort the response function in the vicinity of E_n.

If the scintillator response function is known for each E_n, it is straightforward to construct a detector efficiency curve. For a given neutron energy, the total area under the differential proton energy spectrum, which represents the scintillator response, is proportional to the number of $n-p$ scatters at that energy. This can either be simulated in detail, calculated approximately, or measured experimentally. For neutron scattering experiments, it is also common to use an energy threshold, which removes low-energy recoil protons from the differential energy spectrum at a set discrimination level. As a standard, the energy threshold is usually stated in terms of a fraction of the ^{137}Cs Compton edge, as described in Section 4.2.1.

Detector efficiencies at various thresholds were measured for both the four-meter and six-meter detectors by Ref.[Ped86]. Because there was no measurement of the efficiency at 1/2×Cs for the six-meter detector, the neutron response and detector efficiency was also simulated using the code NEFF7 [Die82]. The simulation code was written for NE-213 liquid scintillators and was modified for the NE-218 detector by changing the scintillator density and hydrogen-to-carbon ratio (Table 3.4).

For comparison to the experimental data and simulations, the efficiency was also calculated using the expression given by [Dro72]:

$$\epsilon(E_n) = \Big(1 - \frac{B}{E_n}\Big)\Big(1 - e^{-\rho_H \cdot t \cdot \sigma_n(E_n)}\Big)\Big(1 + \frac{B}{E'}\Big(1 - e^{-0.5 \cdot \rho_H \cdot t \cdot \sigma_n(E'_n)}\Big)\Big). \tag{4.4}$$

The first term is related to the light output. The neutron energy is E_n and B is the bias (threshold energy). The quantity B was determined for NE-213 by fitting the data from Ref.[Pyw06] to Equation 4.3. The best fit was for $k = 0.15$, where the L.O. was in MeV electron equivalent (MeVee) and E_n was in MeV. Using this, a threshold of 1×Cs (0.477 MeVee) corresponds to $B = 2.16$ MeV and a threshold of 1/2×Cs (0.234

MeVee) corresponds to $B = 1.36$ MeV. The second term accounts for a single $n - p$ scatter. The quantity ρ_H is the hydrogen density in the scintillator. The quantity t is the thickness of the scintillator, which was 5.04 cm for both the four-meter and six-meter detectors. The quantity $\sigma_n(E_n)$ is the total $n - p$ scattering cross section. To a very good approximation, this is given as [Kno00]

$$\sigma_n(E_n) = \frac{4.83}{\sqrt{E_n}} - 0.578, \tag{4.5}$$

where the cross section is in barns and E_n is in MeV. The third term in Equation 4.4 accounts for multiple $n - p$ scattering, which contributes when the light output of the first scatter plus the light output from the second scatter is greater than the bias energy. E'_n is the initial energy minus half the bias energy, giving the effective neutron energy after a single scatter. The term $0.5 \cdot \rho_H \cdot t$ is an approximation for the areal density for a second scatter. All first scatters resulting in a pulse hight much less than B must be small-angle scatters.

The efficiency curves for the four-meter and six-meter detectors are shown in Fig. 4.8 for energy thresholds of 1×Cs and 1/2×Cs from 0 to 20 MeV. There is good agreement between the data of Ref.[Ped86] and the NEFF7 simulation, which was used to determine the efficiencies for the cross-section analysis. The calculation from the method outlined in Ref.[Dro72] appears to be valid to about 10 MeV, which is also noted in the reference. The disagreement above 10 MeV is due to the fact that ^{12}C reactions are ignored in the calculation.

4.3.2 Finite Geometry and Multiple Scattering Corrections

Although the total number of argon or neon sample nuclei was low, hence effects of attenuation in the target are small, multiple scattering was still a concern because there were many more nuclei in the steel sphere than argon or neon nuclei. Two main cases

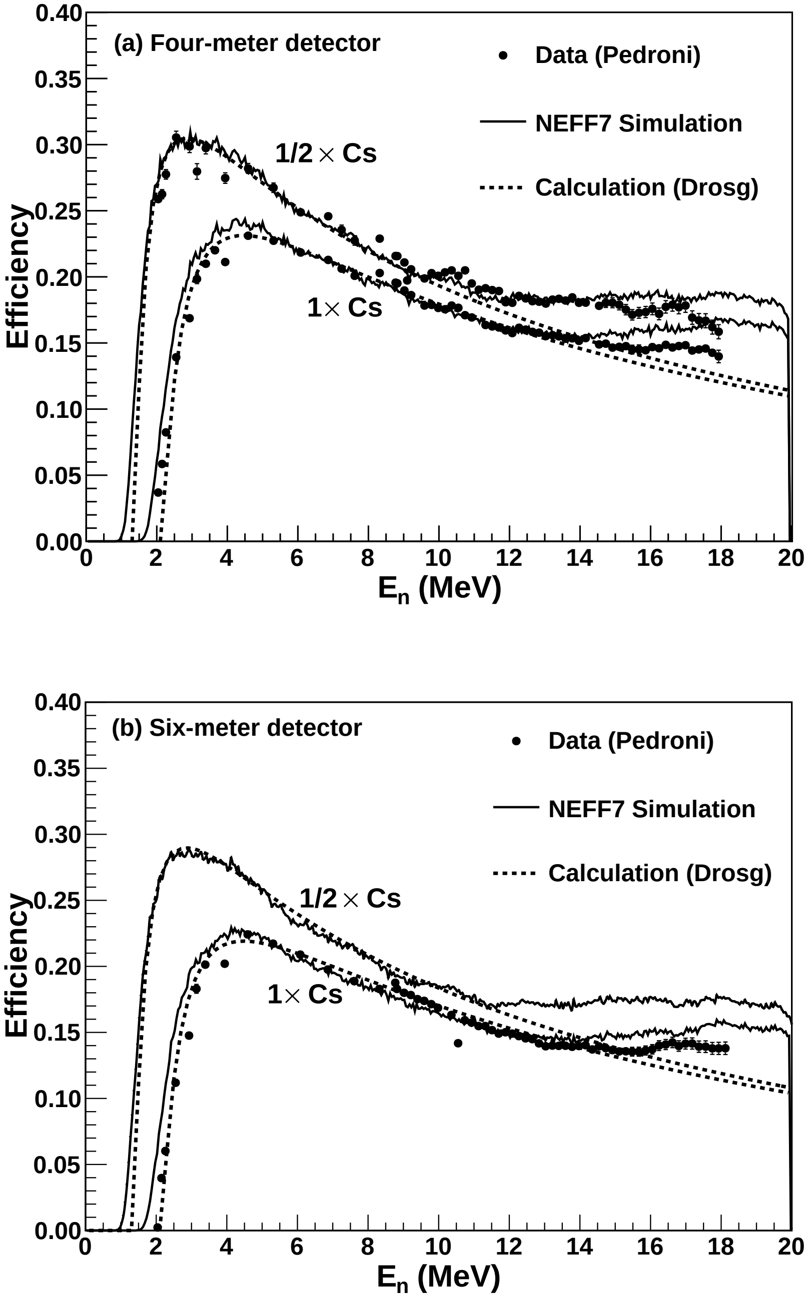

Figure 4.8: Detector efficiencies for the four-meter and six-meter detectors. The data points are taken from Ref.[Ped86]. The solid curve is the NEFF7 simulation. The calculation was performed using the method outlined in Ref.[Dro72].

could contribute to an increase or decrease in the observed count rate. First, a neutron could scatter from an argon or neon nucleus followed by a second scatter from the steel sphere. This process is referred to as "out scattering". Alternatively, a neutron could scatter from the steel sphere followed by a second scatter from the sample and be detected. This process is referred to as "in scattering". The mean free path for a few-MeV neutron in the argon or neon gas is about 15 cm and 20 cm, respectively, and about 5 cm in stainless steel. We therefore expect only a few percent of the incident neutrons to interact in the target. Of the neutrons that do interact, only a few percent of those will undergo a second scatter.

Because the scattering sample and neutron production cell were placed close together, finite-size effects must also be considered in the analysis. Neutrons were produced in the D_2 gas cell with a radial distribution according to the deuteron beam profile and direction determined by the $^2\mathrm{H}(d,n)^3\mathrm{He}$ differential cross section. These neutrons may interact any point in the scattering sample. For our setup, the most extreme angle between the neutron production cell and scattering sample was about 8.5°. Although the neutron beam and scattering target are symmetric about the beam axis, the neutron scattering angle is determined by the differential cross section. Finite-size effects are therefore most important at steep slopes in the differential cross section and negligible where the differential cross section is flat. Additionally, because of kinematic effects, a neutron not produced at zero degrees will have a slightly lower energy than a forward-scattered neutron. The finite-size corrections for the scattering sample and detector were much smaller because of the large source-to-detector distance.

Disc Approximation

The multiple scattering correction for the polyethylene scattering sample (A_p) was determined using the "disc approximation" from Kinney [Kin70] and is given by

$$A_p(\theta_p) = \exp\left[\left(\frac{\pi}{4}\Sigma(E_0)R + \frac{8}{3\pi}\Sigma(E_1)\right)R\right] \tag{4.6}$$

$$\Sigma \equiv n_H\sigma_H + n_C\sigma_C,$$

where E_0 is the incident neutron energy and E_1 is the neutron energy after a single scatter at θ_p. R is the radius of the polyethylene target. The quantities n_H and n_C are the number of hydrogen and carbon atoms in the polyethylene target, respectively. The quantity σ_H is the total neutron cross section for hydrogen and σ_C is the non-elastic neutron cross section for carbon. The hydrogen cross sections were calculated using Ref. [nn-12] as described above and σ_C were taken from the ENDF/B-VII.0 database [Cha06].

Monte-Carlo Method

The scattering data were corrected for multiple scattering, attenuation and finite geometry effects in the target gas and steel cell with a custom C++-based Monte-Carlo simulation in which single simulated neutrons were tracked as they traversed the simulated target and cell geometry. The simulation included all the relevant materials' elastic differential cross sections, densities and dimensions. The simulation also included a neutron beam profile and angular distribution based the incident deuteron beam profile on the production cell convoluted with the ^{2}H$(d,n)^3$He cross section. It returned a "measured" cross section for given input cross section for the target. By taking the appropriate ratio between the measured and input cross sections, we compute a correction factor. This correction was only performed once using the measured data as input, but for some test cases the corrected cross section was used an the input for a second iteration. These second iterations showed a significantly smaller correction, as expected, and provided an estimate for the residual uncertainty in the multiple scattering and geometry corrections. The corrections to the neon data at 5.0 and 8.0 MeV are shown in Fig. 4.9 for the smallest and largest number of sample nuclei in the gas target cell. The effect on the correction factor A_s due to variation in the number of sample nuclei is negligible. This is not surprising, since the multiple scattering effect is dominated by the steel cell and not the gas inside it. The corrections were less than about 10% at most angles but were as high as 25% at the forward angle minimum of $\sigma(\theta)$ for neon at 8.0 MeV.

4.3.3 Uncertainties in Data

The systematic and statistical uncertainties are summarized in Table 4.2. An uncertainty of 3% was assigned to the detector efficiency based on the agreement of the data with the NEFF7 simulation in the neutron energy range used in this experiment. Similar agreement was found using the same simulation code in Ref. [Tro09]. The number of target nuclei in the gas cell was measured by weighing the filled and unfilled gas cell on a balance with 0.01 mg accuracy, resulting in a systematic uncertainty in the number of argon or neon nuclei of 0.2%. The uncertainty in the number of hydrogen atoms in the polyethylene was 0.7% based on the measured dimensions of the scattering sample. An uncertainty of 3% in the polyethylene correction factor A_p was determined from the uncertainties in the target radius and hydrogen and carbon densities in the polyethylene. The contribution of the uncertainties in the hydrogen and carbon cross sections in Eqn. 4.6 to the total uncertainty in A_p was negligible. An uncertainty of 1% was assigned to A_s based on the statistical fluctuation in the correction factor. An uncertainty of 0.5% was assigned to the $n-p$ normalization cross section based on agreement between several different models and analyses of $N-N$ scattering data

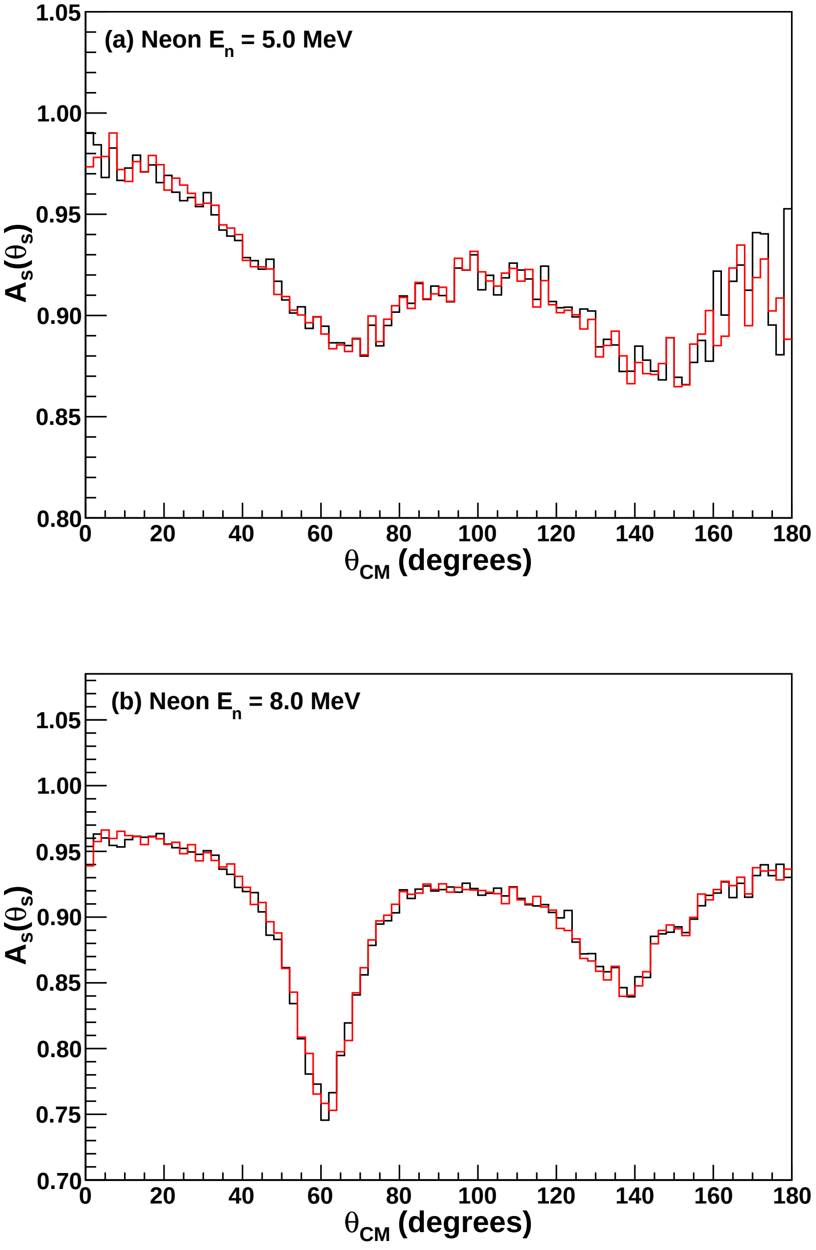

Figure 4.9: Multiple scattering and finite geometry corrections determined from the Monte-Carlo simulation. (a) The correction factor A_s for the 5.0-MeV data for two gas densities. The black line represents 1.09×10^{22} neon nuclei and the red line represents 1.94×10^{22} neon nuclei, corresponding to the smallest and largest number of sample nuclei used in the experiment. (b) The correction factor A_s for the 8.0-MeV data for 1.51×10^{22} neon nuclei (black) and 1.92×10^{22} neon nuclei (red).

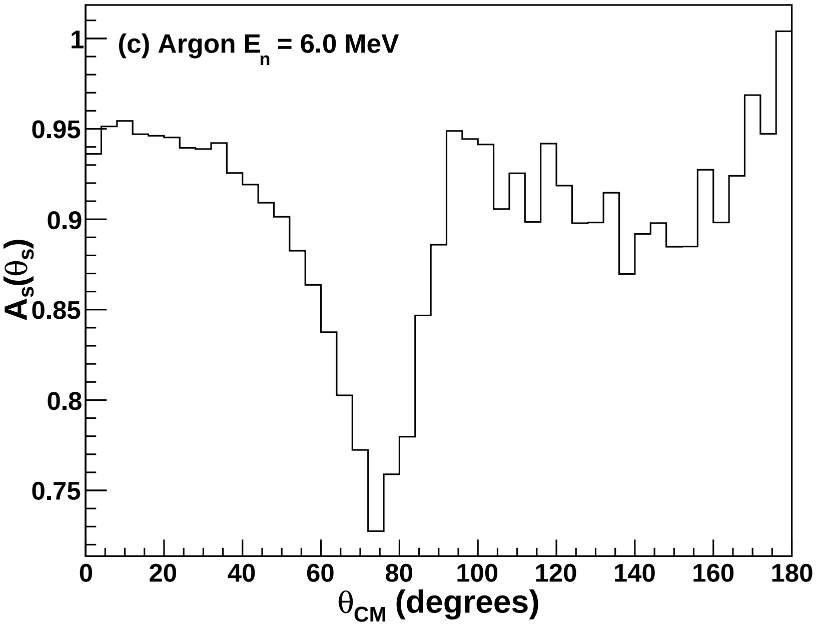

Figure 4.9: Multiple scattering and finite geometry correction for argon determined from the Monte-Carlo simulation for a gas cell filled with 2.4×10^{22} argon nuclei.

available from Nijmegen [nn-12]. To determine the total systematic uncertainty, the individual quantities were added in quadrature.

The statistical uncertainty played the largest role in this experiment. Since there were about four times as many iron nuclei in the gas cell as target nuclei, a large background was subtracted for each angle. We attempted to collect enough scattering events at each angle so that the statistical uncertainty was around 10%. At points where the cross section was small, or where the elastic scattering cross section for ^{56}Fe (from the stainless steel gas cell) was much larger than the ^{20}Ne or ^{40}Ar cross sections, the statistical uncertainty was as high as 20%.

Table 4.2: Systematic and statistical uncertainties for NTOF $\sigma(\theta)$ data. To determine the total systematic uncertainty, the individual quantities were added in quadrature.

Systematic Uncertainties	
multiple scattering correction factor, A_s	1%
polyethylene correction factor, A_p	3%
detector efficiency, ϵ_s/ϵ_p	3%
number of target nuclei, n_p/n_s	0.7%
$n-p$ cross section	0.5%
Total systematic uncertainty	4.4%
Statistical Uncertainties	
Y_s	5–20%
Y_p	1–4%

4.4 Neutron Scattering Cross Sections

4.4.1 Legendre Polynomial Description of the $\sigma(\theta)$ Data

The $\sigma(\theta)$ data were fit with a Legendre polynomial expansion

$$\frac{d\sigma(E_n,\theta_s)}{d\Omega} = \sum_{l=0} A_l(E_n)P_l(\cos\theta_s), \tag{4.7}$$

where $A_l(E_n)$ were free parameters. The maximum value for l was determined for when the χ^2 of the fit for the next order $(l+1)$ was greater than for the current fit (l).

An equivalent form of the Legendre polynomial expansion was also useful:

$$\sigma(E_n,\theta_s) = \frac{\sigma(E_n)}{4\pi}(a_0 + \sum_{l=1}(2l+1)a_l(E_n)P_l(\cos\theta_s)). \tag{4.8}$$

This parameterization is convenient because it relates the a_0 term to the total elastic scattering cross section, $\sigma(E_n)$. The quantities a_l are called the reduced expansion coefficients and are related to the fit parameters by

$$a_0 \equiv 1.00, \tag{4.9}$$
$$a_l = \tfrac{A_l}{A_0(2l+1)}.$$

4.4.2 The Zero-Degree Cross Section and Wick's Limit

It is useful to have a point at zero degrees where the differential cross section is largest. Since a minimum angle of about 20° could be measured using the TUNL time-of-flight spectrometer, Wick's limit [Wic43, Wic49] was used to estimate the zero-degree neutron elastic scattering cross section. Wick's limit is a consequence of the optical theorem, which relates the imaginary part of the zero-degree scattering amplitude ($f(0^\circ)$) to the total cross section σ_T:

$$\sigma(0^\circ) = \Re[f(0^\circ)]^2 + \Im[f(0^\circ)]^2 \geq \Im[f(0^\circ)]^2. \tag{4.10}$$

The zero-degree differential elastic scattering cross section $\sigma(0^\circ)$ must be greater than or equal to Wick's limit, given by

$$\sigma^W(0^\circ) \geq \left(\frac{k}{4\pi}\sigma_T\right)^2, \tag{4.11}$$

where σ_T is the total neutron cross section and k is the wave number. Although Wick's limit is only a lower limit on the zero-degree cross section, the limit is known to be nearly an equality [Coo58, Die03]. The zero-degree cross section was determined based on an extrapolation of the data of Ref. [Vau60], and was included as a data point in each fit.

4.4.3 $^{\text{nat}}$Ne$(n,n)^{\text{nat}}$Ne for E_n = 5.0 and 8.0 MeV

The cross-section data fit with a Legendre polynomial expansion for neutron elastic scattering from $^{\text{nat}}$Ne is shown in Fig. 4.10 and in Tables B.1 and B.2. The total elastic scattering cross section, determined by integrating the Legendre polynomial fits, was found to be 1290 ± 40 mb for E_n = 5.0 MeV and 940 ± 30 mb for E_n = 8.0 MeV. The fit parameters from the Legendre polynomial expansion can be found in Table B.5 and B.6.

4.4.4 $^{\text{nat}}$Ar$(n,n)^{\text{nat}}$Ar for E_n = 6.0 MeV and 14.0 MeV

There was one angular distribution for elastic scattering of neutrons from ^{40}Ar at 14.0 MeV available in the literature measured by Beach et al. [Bea67]. It is included along with the data and fits for the TUNL data taken for ^{40}Ar at 6.0 MeV to help form a complete understanding of the current availability of data and to aid in optical-model predictions, which are presented in the next section. The cross-section data fit with a Legendre polynomial expansion for neutron elastic scattering from $^{\text{nat}}$Ar are shown in Fig. 4.11 and in Tables B.3 and B.4. The 14-MeV data were taken from Ref.[Bea67] and was fit using the same procedure as for the TUNL time-of-flight data. The total elastic scattering cross section, determined by integrating the Legendre polynomial fits, was found to be 2170 ± 60 mb for E_n = 6.0 MeV and 970 ± 20 mb for E_n = 14.0 MeV. The fit parameters from the Legendre polynomial expansion can be found in Table B.7 and B.8.

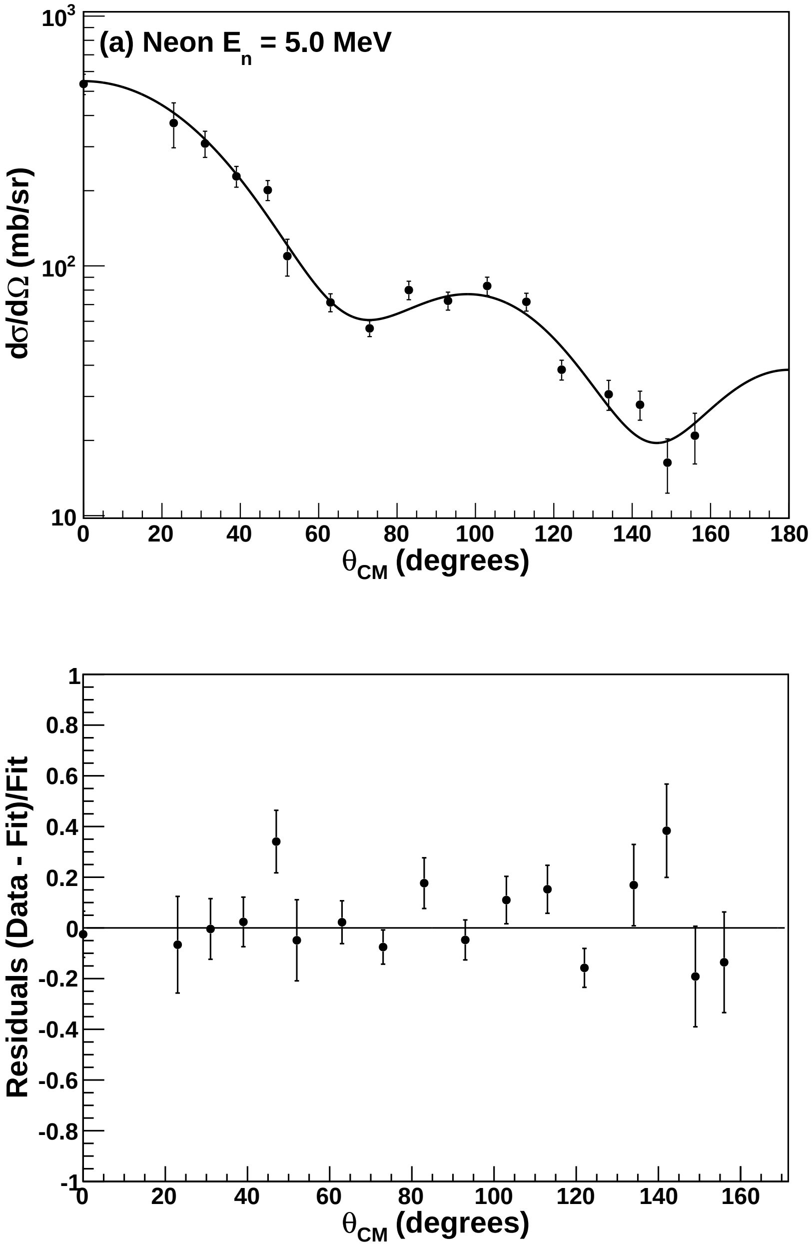

Figure 4.10: The differential elastic scattering cross section of neutrons from $^{\mathrm{nat}}$Ne. The 5.0-MeV data were fit with a fourth-order Legendre polynomial expansion (χ^2/NDF = 2.2). The 8.0-MeV data were fit with a sixth-order Legendre polynomial expansion (χ^2/NDF = 2.0).

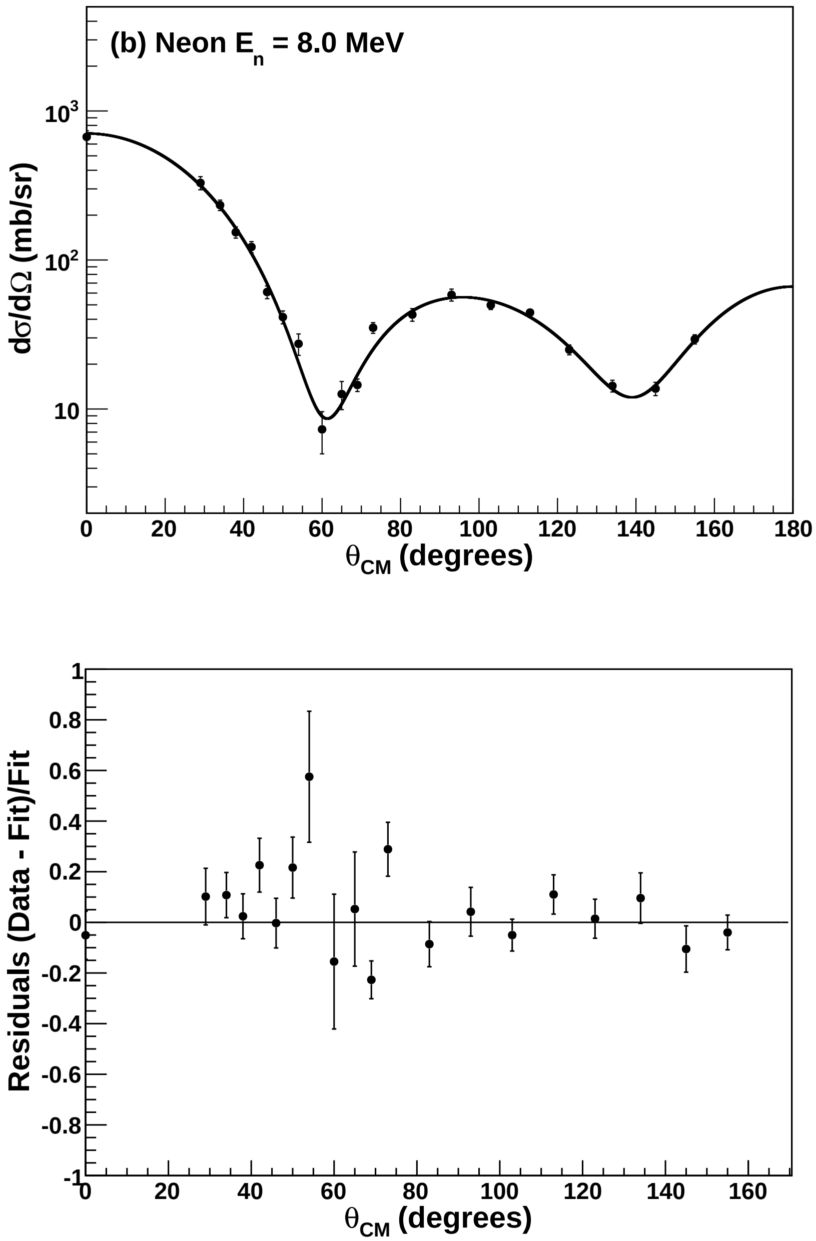

Figure 4.10: (Continued) The differential elastic scattering cross section of neutrons from $^{\mathrm{nat}}$Ne. The 5.0-MeV data were fit with a fourth-order Legendre polynomial expansion (χ^2/NDF = 2.2). The 8.0-MeV data were fit with a sixth-order Legendre polynomial expansion (χ^2/NDF = 2.0).

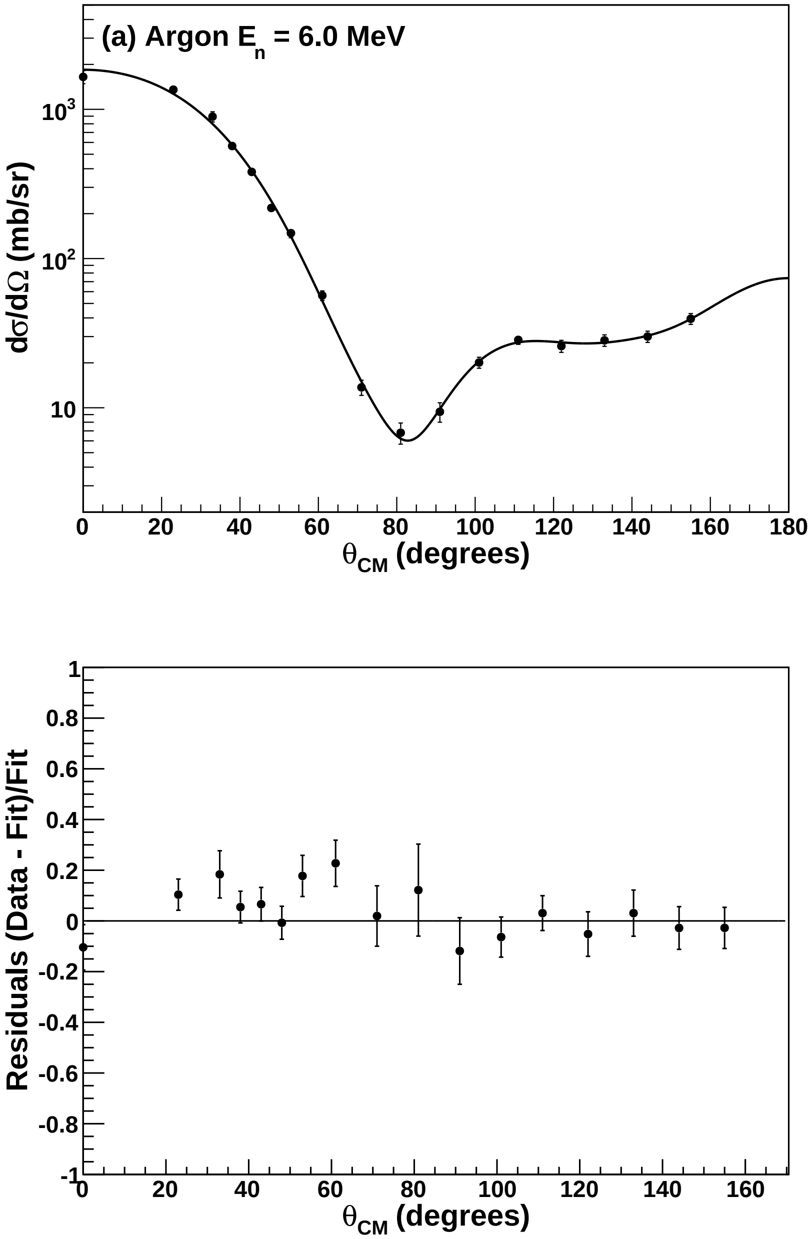

Figure 4.11: The differential elastic scattering cross section of neutrons from $^{\mathrm{nat}}$Ar. The 6-MeV data were fit with a ninth-order Legendre polynomial expansion (χ^2/NDF = 1.6). The 14-MeV data were taken from Ref.[Bea67] and were fit with a tenth-order Legendre polynomial expansion (χ^2/NDF = 6.3).

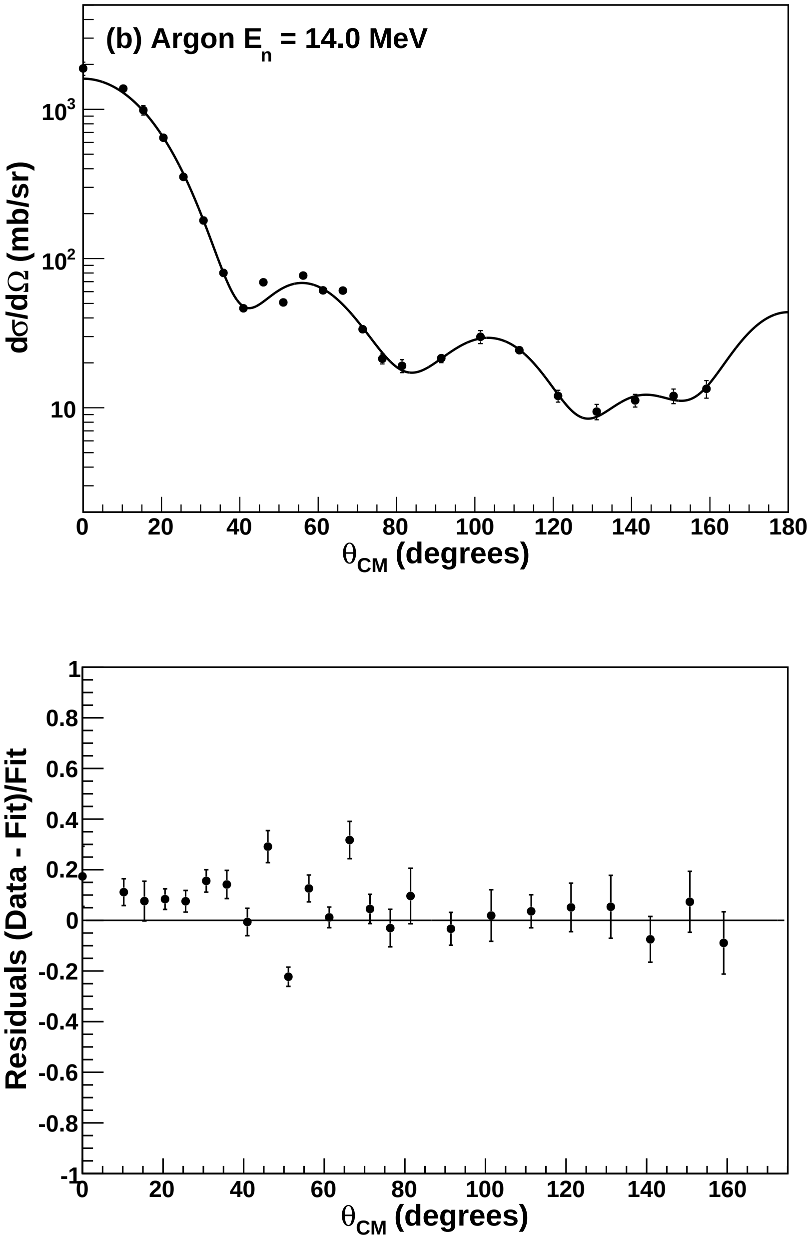

Figure 4.11: The differential elastic scattering cross section of neutrons from $^{\mathrm{nat}}$Ar. The 6-MeV data were fit with a ninth-order Legendre polynomial expansion (χ^2/NDF = 1.6). The 14-MeV data were taken from Ref.[Bea67] and were fit with a tenth-order Legendre polynomial expansion (χ^2/NDF = 6.3).

4.5 Optical-Model Description of Data

4.5.1 Optical-Model Calculations from Existing Parameter Sets

Optical-model calculations were performed for both argon and neon at energies corresponding to those measured in the experiment. The GENOA [Per67] code uses a numerical procedure to solve the time-independent Schrödinger equation, and calculates the differential cross section for a given incident energy, based on a set of optical-model parameters. For argon, calculations were performed using the local optical-model parameters from Koning and Delaroche [Kon03] for ^{40}Ar. The parameterization of this particular model is discussed in Section 2.2. For comparison, a calculation was also done using the ^{40}Ar parameters given in the ENDF/B-VII.0 database [Cha06]. The ENDF parameterization differs from the Koning-Delaroche potential in that the imaginary volume (W_v) and spin-orbit potentials ($W_{s.o}$) are not included.

For neon, calculations were performed using the global optical-model parameters from Koning and Delaroche [Kon03]. A calculation was also done based on Dave and Gould [Dav83], who derived a parameter set, based on experimental data, for light ($A = 6$ to $A = 16$) nuclei from 7 to 15 MeV. This parameterization differs from the Koning-Delaroche potential in that the imaginary volume (W_v) and spin-orbit potentials ($W_{s.o}$) are not included. Although neon lies in a mass range slightly outside the reach of both the Koning-Delaroche and Dave-Gould models, calculations were done with both to compare to data and to provide a starting point for optical model parameter searches.

4.5.2 Compound Nucleus Corrections

Because the optical model only describes the direct reaction, in general, the compound nucleus cross section must be subtracted from the data before optical-model fits are attempted. Compound nucleus cross sections were calculated using the nuclear reaction code TALYS [Kon08], which in turn uses a Hauser-Feshbach statistical calculation with a Moldauer width fluctuation correction factor as described in Section 2.1. In light nuclei, such as neon, analytic expressions for the density of states are not reliable because the level densities are too low and these calculations can only be used to provide an upper limit to the compound nuclear reaction. Below about 10 MeV the compound nucleus contribution to the cross section can be significant, and may be even larger than the direct reaction cross section at some backward angles. At higher energies, where there are many inelastic channels open, the compound nucleus cross section is negligible.

4.5.3 Optical-Model Parameter Searches

The GENOA code, which was used to calculate the differential cross section for a given set of optical-model parameters in Section 4.5.1, was also used to determine a set of parameters that best fit the data. The code performs a searching procedure with up to 10 free parameters to define the potential with numerical fitting based on the generalized least squares method [Gui00].

The best fit to the data was calculated from the optical-model potential (Eqn. 2.4). For neon, the total elastic scattering cross sections found from integrating the optical-model fits were 1160 mb for $E_n = 5.0$ MeV and 990 mb for $E_n = 8.0$ MeV. The cross section was found to differ significantly from the extrapolation of the Dave–Gould potential to the $A = 20$ range. The origin of this discrepancy is largely due to the difference in the real volume term (V_v) in the optical-model potential. Compared to the prediction using the global Koning-Delaroche potential for ^{20}Ne, the total elastic scattering cross section was found to differ by 6% at 5.0 MeV and 13% at 8.0 MeV. The results from the optical-model fits and comparisons to existing datasets can be found in Fig. 4.12.

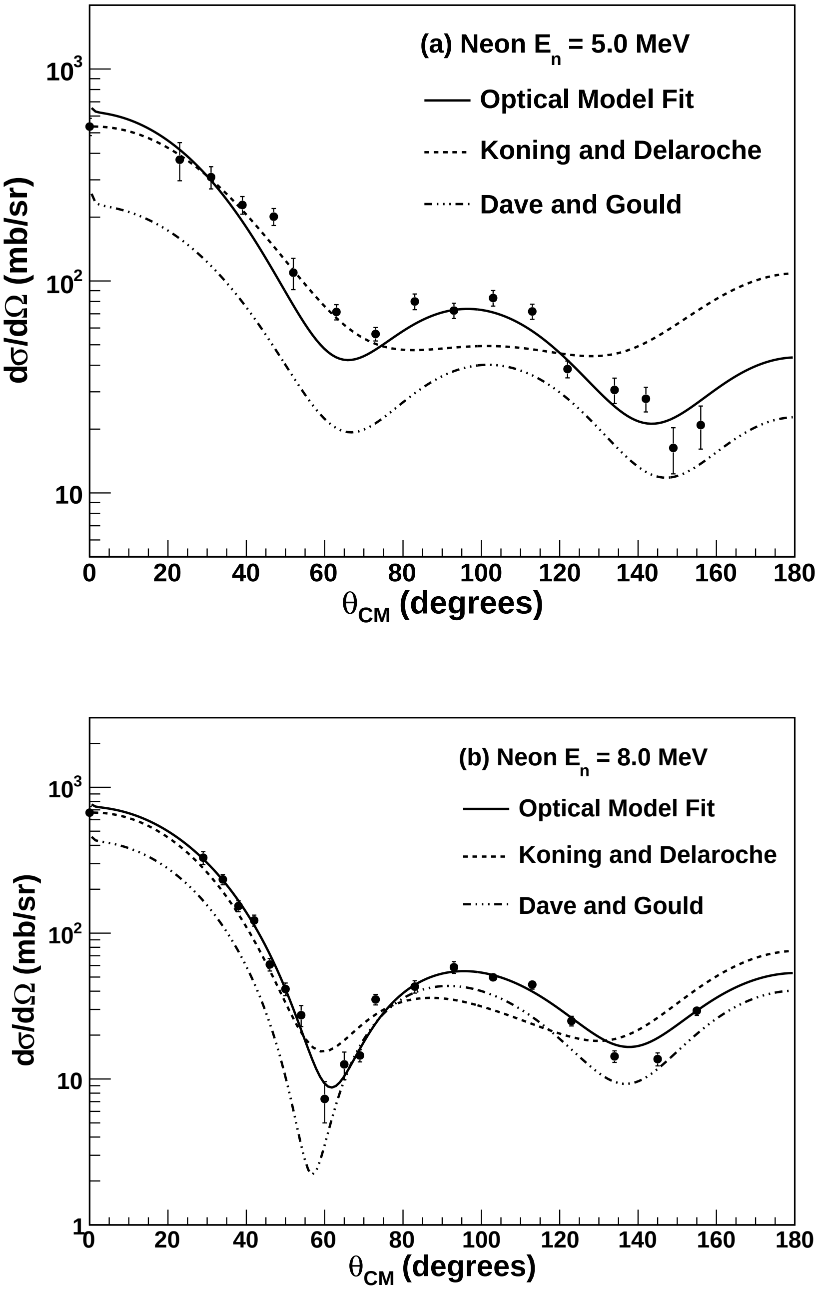

Figure 4.12: The differential elastic scattering cross section of neutrons from $^{\mathrm{nat}}$Ne. The solid curve is based on an optical-model calculation with parameters which best describe the data. The dashed curves are optical-model calculations from existing optical-model parameter sets.

For argon, the total elastic scattering cross section found from integrating the optical-model fits were 2020 mb for $E_n = 6.0$ MeV and 995 mb for $E_n = 14.0$ MeV. The cross section was found to differ significantly from the ENDF/B-VII.0 cross section. This discrepancy is largely due to an over-estimation in the radii (r_v,r_d,$r_{s.o}$) in the ENDF/B-VII.0 parameterization. Compared to the prediction using the local Koning-Delaroche potential for ^{40}Ar, the total elastic scattering cross section was found to differ by 8% at 6.0 MeV and 3% at 14.0 MeV. The results from the optical-model fits and comparisons to existing datasets can be found in Fig. 4.13.

The optical-model parameters for the best fit to data and existing parameters can be found in Tables B.9 – B.14. For argon, only small modifications to Koning and Delaroche [Kon03] for the real volume potential (V_v) and imaginary surface potential (W_d) were needed to describe the data at 6.0 and 14.0 MeV. To calculate the differential cross section at energies that were not measured, the parameters varied in the search were assumed to have a linear energy dependence. The differential elastic scattering cross section for argon from 0.5 to 20 MeV, based on an extrapolation of the the optical-model parameter set that best described our data, is shown in Fig. 4.14. Table 4.3 shows the total elastic and zero-degree cross section from the Legendre polynomial fits and optical-model fits to data, and the calculations based ENDF-VII.0 and Koning and Delaroche [Kon03].

For neon, the data were fit without subtracting the compound nucleus cross section due to its large size relative to the shape elastic cross section and large uncertainty. Although the potential well depths are the only energy-dependent terms in the optical-model potential formulation, good fits to the neon data were not obtained using the radii and surface diffuseness parameters (which should not be energy-dependent) provided by Koning and Delaroche [Kon03] or Dave and Gould [Dav83]. Therefore, we allowed these parameters to vary in the search to obtain good fits to data. Each parameter was

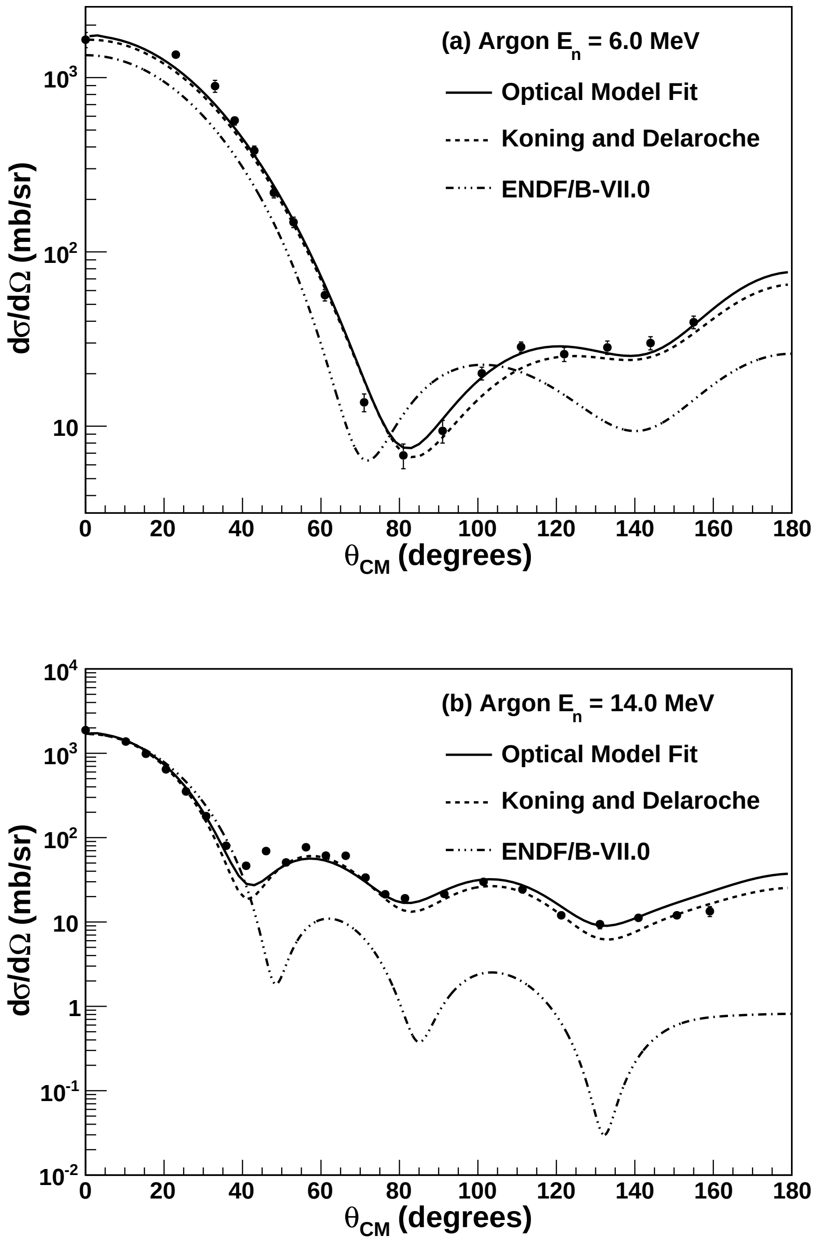

Figure 4.13: The differential elastic scattering cross section of neutrons from $^{\mathrm{nat}}$Ar. The solid curve is based on an optical-model calculation with parameters which best describe the data. The dashed curves are optical-model calculations from existing optical-model parameter sets.

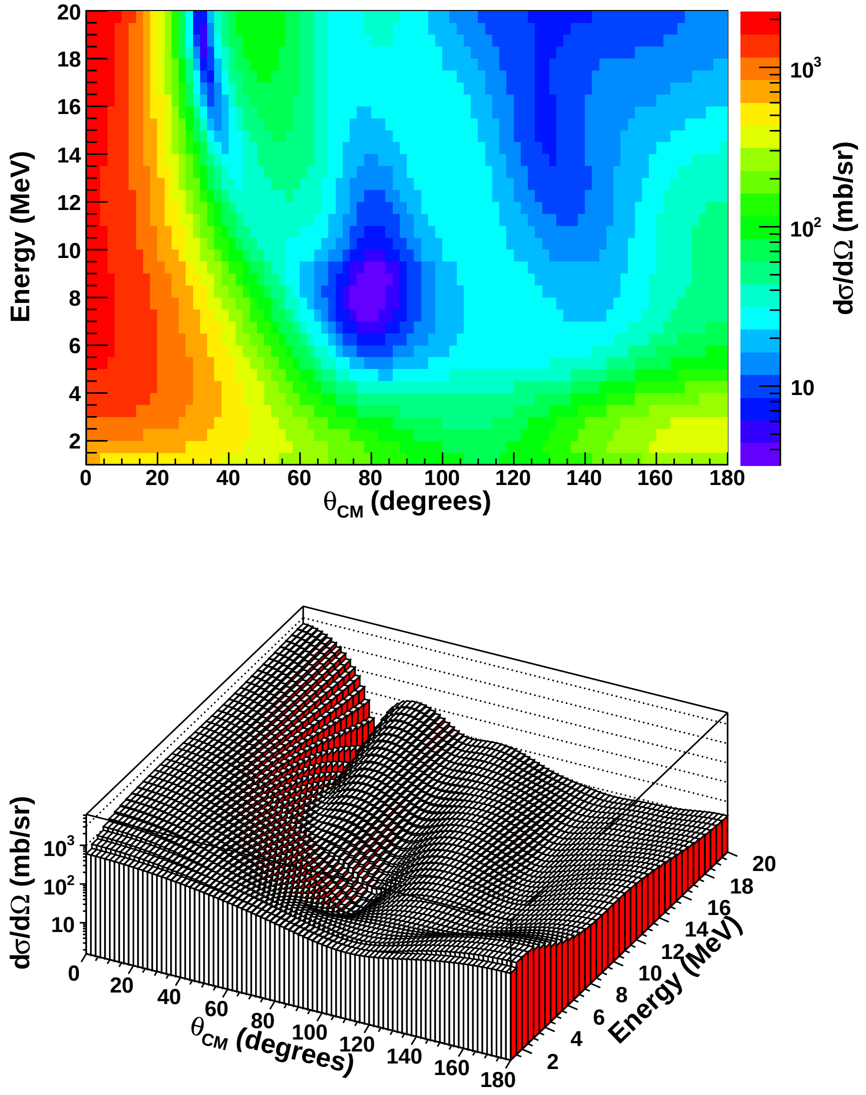

Figure 4.14: The differential elastic scattering cross section of neutrons from $^{\mathrm{nat}}$Ar from 0.5 to 20 MeV, based on an extrapolation of the the optical-model parameter set that best described our data.

Table 4.3: The total elastic and zero-degree cross section for $^{\mathrm{nat}}\mathrm{Ar}(n,n)^{\mathrm{nat}}\mathrm{Ar}$ from optical-model calculations, fits and data.

	E_n (MeV)	σ_{el} (mb)	$\sigma(0^\circ)$ (mb/sr)
ENDF-VII.0	6.0	1417	1343
	14.0	788	1699
Koning and Delaroche	6.0	1903	1649
	14.0	928	1687
Optical model fit to data	6.0	2020	1720
	14.0	995	1720
Legendre polynomial fit to data	6.0	2170 ± 60	1840 ± 130
	14.0	975 ± 20	1600 ± 30

assumed to have a linear energy-dependence. Cross sections were predicted for energies not measured using this global fit to the data. Although the parameters adequately describe the measured data, we do not expect our global fit to apply outside the $A = 20$ mass range and may be limited to the energy-range measured in the current experiment. For these reasons, we restricted our fit to 3–10 MeV. The cross section is shown in Fig. 4.15. Table 4.4 shows the total elastic and zero-degree cross section from the Legendre polynomial fits and optical-model fits to data, and the calculations based Dave and Gould [Dav83] and Koning and Delaroche [Kon03].

Table 4.4: The total elastic and zero-degree cross section for $^{\mathrm{nat}}\mathrm{Ne}(n,n)^{\mathrm{nat}}\mathrm{Ne}$ from optical-model calculations, fits and data.

	E_n (MeV)	σ_{el} (mb)	$\sigma(0^\circ)$ (mb/sr)
Dave and Gould	5.0	525	227
	8.0	561	457
Koning and Delaroche	5.0	1220	535
	8.0	823	670
Optical model fit to data	5.0	1160	650
	8.0	990	760
Legendre polynomial fit to data	5.0	1290 ± 40	550 ± 30
	8.0	940 ± 30	710 ± 40

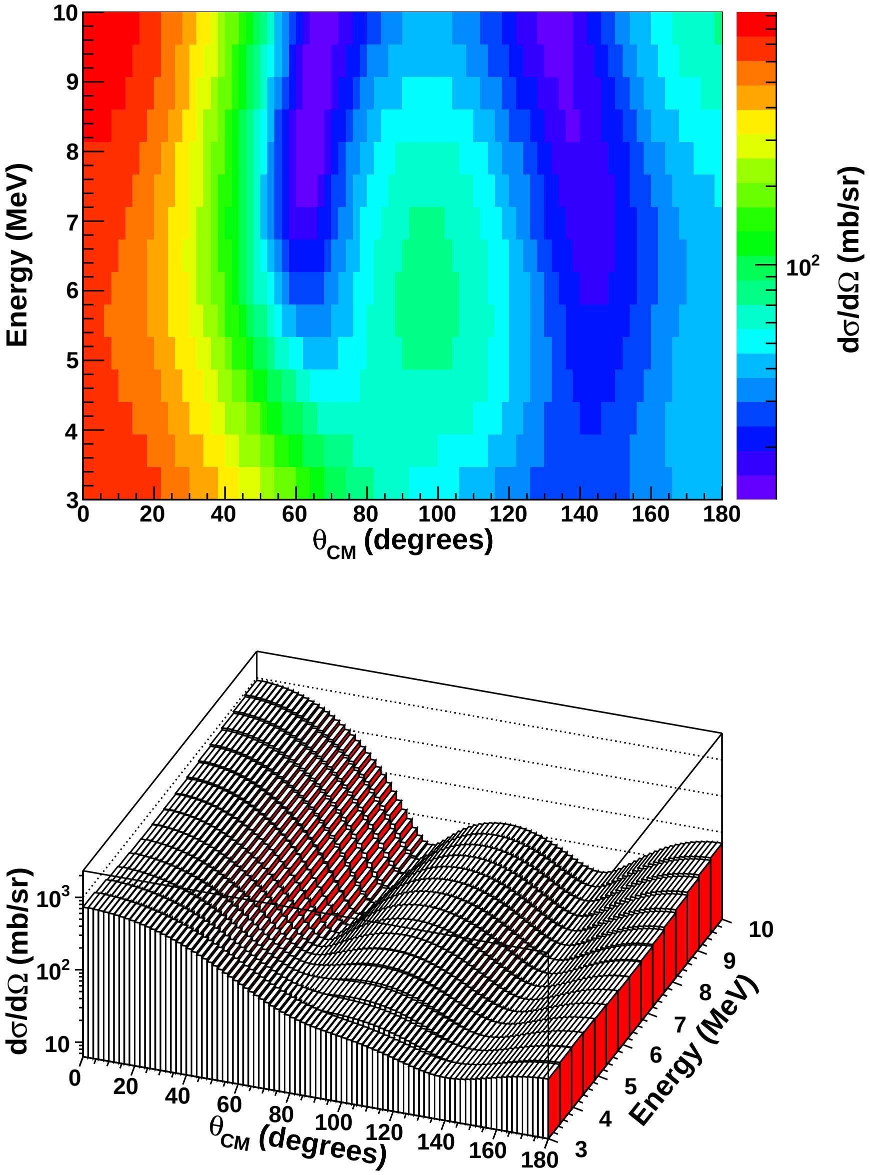

Figure 4.15: The differential elastic scattering cross section of neutrons from $^{\mathrm{nat}}\mathrm{Ne}$ from 3 to 10 MeV, based on an extrapolation of the the optical-model parameter set that best described our data.

4.6 Conclusions

Differential elastic scattering cross-section data for neutrons from $^{\mathrm{nat}}$Ne and $^{\mathrm{nat}}$Ar were obtained at TUNL using the time-of-flight technique. Angular distributions for neon were measured at 5.0 and 8.0 MeV. One full angular distribution was measured for argon at 6.0 MeV. Data from Ref.[Bea67] at 14.0 MeV were also added to the analysis. All data were fit using a Legendre polynomial expansion and the total elastic scattering cross section was at each energy was determined by integrating the fits. The data were also fit using the spherical optical model. The model is known to be capable of describing the differential cross section very well for medium-mass and heavy nuclei. The global optical-model parameter sets are not generally expected to extend to low-mass nuclei, however Dave and Gould [Dav83] were successful in describing measured elastic scattering cross sections for light 1–p shell nuclei from 7 to 15 MeV.

Using the measured cross sections for neon at 5.0 and 8.0 MeV, a parameter set was determined based on the global optical-model parameters from Koning and Delaroche [Kon03] combined with an extrapolation of the global fits from Dave and Gould [Dav83]. Because the neither model's radii and surface diffuseness parameters provided a good description of the data, they were treated as free parameters and the fit was restricted to between 3 and 10 MeV. This is the first available data for nuclear masses from $A = 17$ to $A = 23$.

Using the measured cross sections for argon at 6.0 and 14.0 MeV, a parameter set was determined based on the local optical-model parameters from Koning and Delaroche [Kon03] for ^{40}Ar. Because of the good agreement between the optical-model calculations and experimental data, we conclude that the available data were consistent with each other and also consistent with the trends of the ^{40}Ar local optical-model potential. Significant disagreement was observed between the experimental data and the cross sections in the ENDF/B-VII.0 database. This discrepancy, which can be clearly seen in Fig. 4.13b beyond the first minimum is mostly owing to a significant overestimation of the depth of the absorptive potential, W_d, in the ENDF/B-VII.0 parametrization. Additionally, an overestimation of the real radius, r_0, is largely responsible for the discrepancy in the shape. A calculation using the original ENDF/B-VII.0 parameters with W_d and r_0 modified to be the Koning and Delaroche values recovers a cross section where the shape and magnitude are consistent with both the 6.0- and 14.0-MeV data.

For both argon and neon, the Legendre polynomial fits provided an excellent description of the data. Because it was impractical to measure full angular distributions at many energies, the optical model was used to determine the cross section at unmeasured energies based on the available data. Although the optical model fits were not as good Legendre polynomial fits, owing to fewer free parameters in the optical model, it provided a better description of the data than current global parameterizations.

Chapter 5

Experimental Facilities at the Los Alamos Neutron Science Center

The γ rays produced in $(n, xn\gamma)$ reactions may contribute backgrounds for $\beta\beta(0\nu)$ and direct dark matter detection experiments. The measurement of the partial γ-ray production cross sections combined with Monte-Carlo calculations can quantify the contribution of these backgrounds. Because neutrons from cosmic-ray spallation (up to hundreds of MeV) and (α, n) reactions (few MeV) can induce these reactions, it is necessary to measure these cross-sections for a wide energy range. One method is to use a pulsed "white" spallation source to produce neutrons up to several hundred MeV, where the incident neutron energy may be determined by the time-of-flight. Prompt γ-rays from neutron-induced reactions in a target are then measured using high-resolution γ-ray spectroscopy. This chapter describes the neutron beam facility located at the Los Alamos Neutron Science Center (LANSCE) and the γ-ray detection using the GErmanium Array for Neutron Induced Excitations (GEANIE). The GEANIE beam line is shown schematically in Fig. 5.1.

5.1 Neutron Beam Production

Data were collected at the Weapons Neutron Research (WNR) facility at the Los Alamos Neutron Science Center (LANSCE) [Lis90]. A broad-spectrum (~ 0.2 – 800

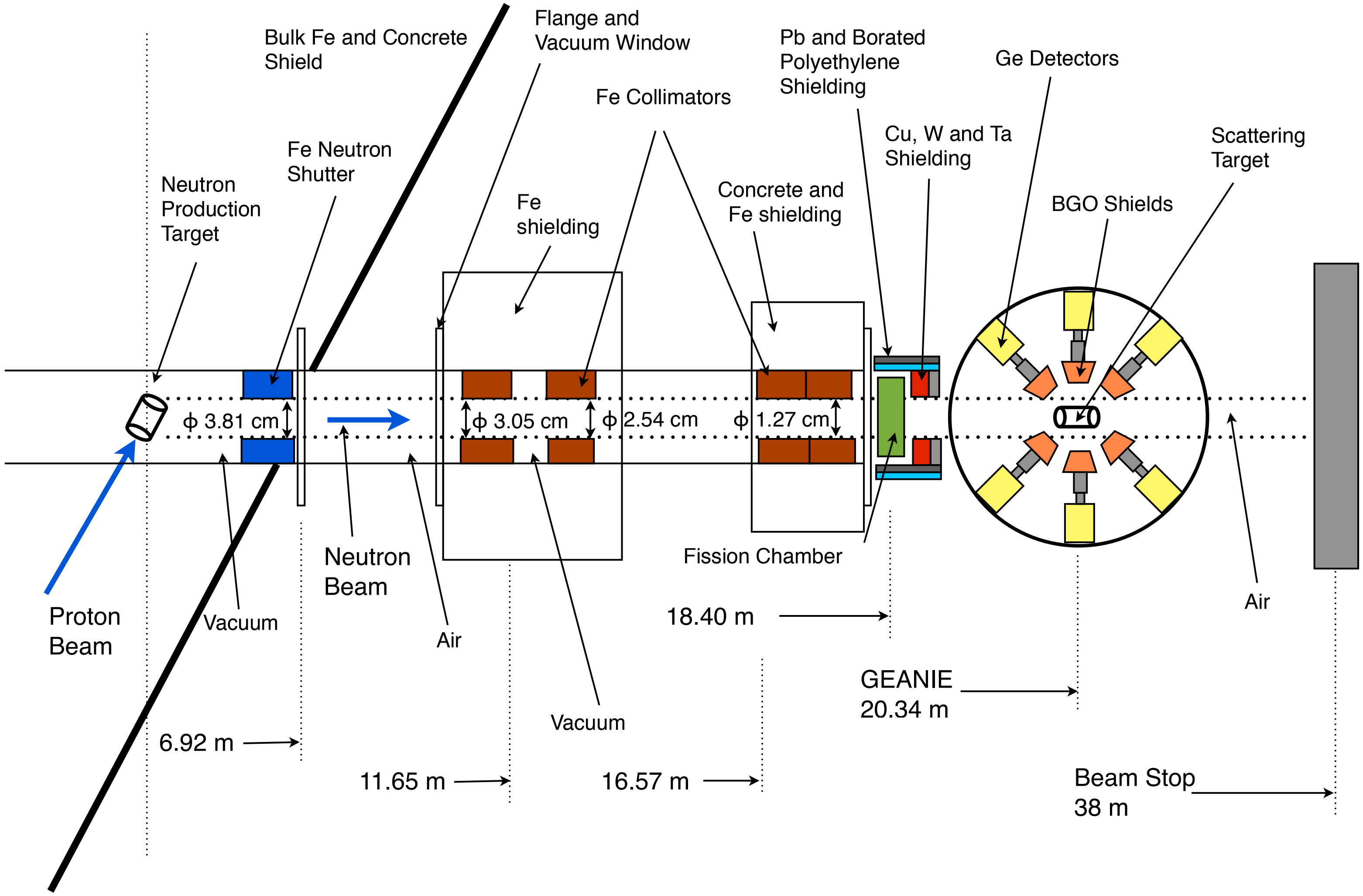

Figure 5.1: Schematic of the GEANIE beam line at LANSCE. The figure is not to scale. Horizontal distances are measured relative to the neutron production target.

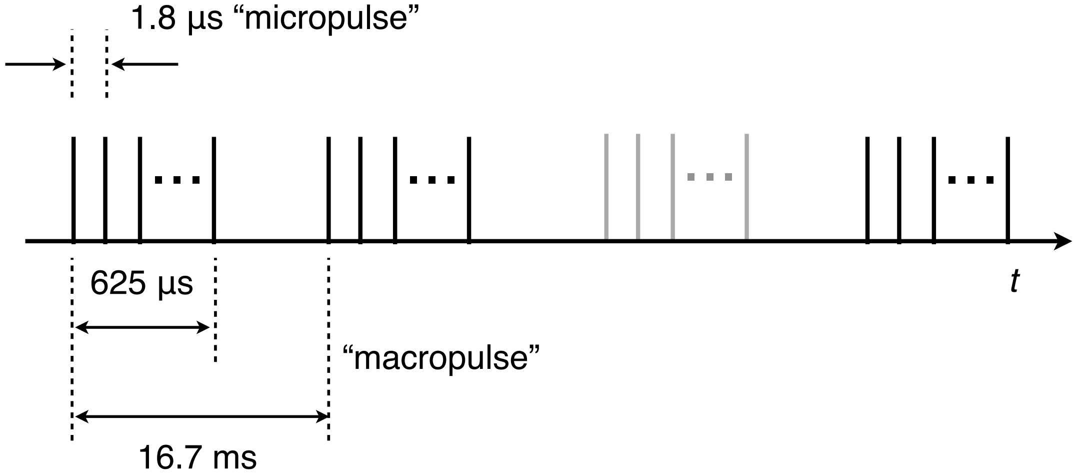

Figure 5.2: The beam pulsing structure of the LANSCE neutron beam (not to scale).

MeV) pulsed neutron beam was produced via spallation on a $^{\mathrm{nat}}$W target by an 800 MeV proton linear accelerator beam. The average proton beam current at the spallation target was about 1 – 2 μA. The proton beam structure contained 625-μs long "macropulses" repeated at 60 Hz, or every 16.7 ms. One in three macropulses was delivered to another facility, resulting in an average rate of 40 s^{-1}. Each macropulse consisted of "micropulses" spaced every 1.8 μs, each less than 1 ns long. The beam-pulsing structure is shown schematically in Fig. 5.2. The pulsed beam allowed incident neutron energies to be determined using the time-of-flight technique.

5.2 Fission Ionization Chambers for Neutron Flux Measurements

In order to make an absolute measurement of the cross section, the incident number of neutrons bombarding the target must be known. In the case of charged-particle beams, this task may be accomplished by determining the integrated beam current with a Faraday cup device. Since neutrons are uncharged, the situation is more complicated. The neutron yield must be determined using a neutron-induced reaction for which the cross section is well known. The neutron flux on target was measured with an in-beam fission ionization chamber, shown schematically in Fig. 5.3 and is fully described in Ref. [Wen93]. It consists of an aluminum chamber with 0.025-cm thick stainless steel end windows. Inside the chamber is a stack of electrodes each individually referred to as a "foil". A negative high-voltage potential was applied to the foils containing deposits of fissionable material. Foils 3, 5 and 7, referred to as the "signal foils", were each connected to a preamplifier. The foil on each end of the stack was connected to ground. Table 5.1 lists the placement of the foils in the fission chamber and their respective functions. The chamber was filled with a 90% argon and 10% methane (P10) gas mixture. Neutron-induced fission fragments from the ^{235}U and ^{238}U foils ionized the gas and the charge was subsequently read out using the signal foils. The analysis of the neutron flux for our cross-section measurements is discussed in Section 6.4.4.

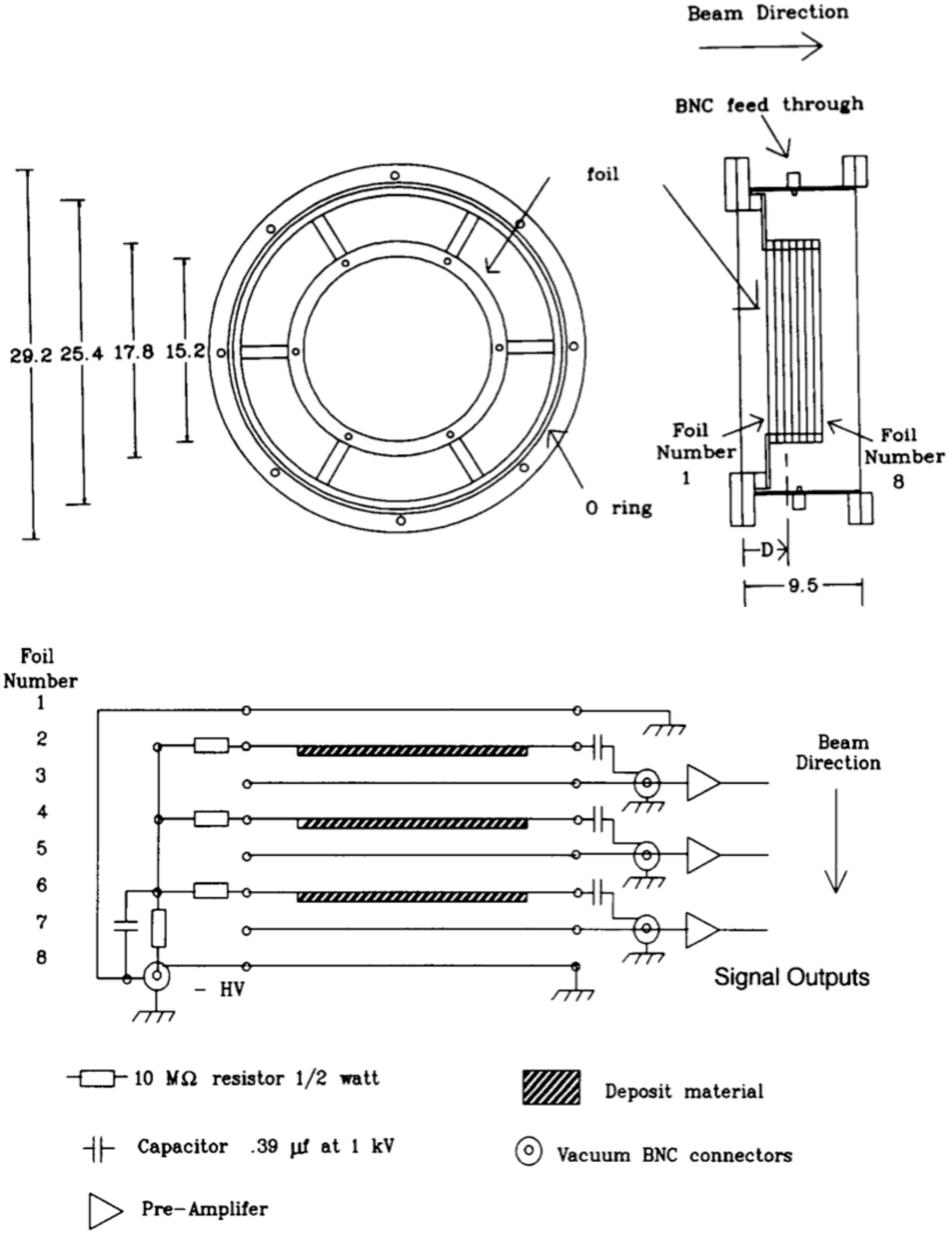

Figure 5.3: The LANSCE in-beam fission ionization chamber. Dimensions are in centimeters. See text for details. Figure from Ref. [Wen93].

Table 5.1: Description of foils in the fission chamber. A diagram of the fission chamber is shown in Fig. 5.3. From Ref. [Wen93].

Foil number	Distance from front window D (cm)	Description
1	2.15	Ground plane
2	2.72	400 μg/cm ^{235}U deposit
3	2.26	Signal foil
4	3.99	400 μg/cm ^{238}U deposit
5	4.63	Signal foil
6	5.26	Blank deposit foil
7	5.90	Signal foil
8	6.53	Ground plane

The fission chamber is located 18.40 m from the spallation target at the WNR 60R flight path. Because the beam line is sufficiently long, the lowest energy neutrons arrive at the target after the highest energy neutrons from the from the next beam pulse. These "wrap-around" neutrons contribute up to about 650 keV. Lighter elements, such as argon and neon, tend to have higher-energy excited states than heavy elements, which makes the wrap-around neutrons irrelevant, because 650 keV is well below the reaction thresholds. The ^{235}U foil is usually used to measure the neutron flux at energies less than a few MeV where the $^{238}\mathrm{U}(n, f)$ cross section is very small. Because the ^{238}U spectra were cleaner due to the fission threshold, it was used exclusively for this experiment.

5.3 The GEANIE Spectrometer

The GErmanium Array for Neutron Induced Excitations (GEANIE) [Fot04] is located 20.34 m from the spallation target at the WNR 60R flight path. GEANIE is designed to measure absolute partial cross sections for $(n, xn\gamma)$ reactions by detecting γ rays from neutron–induced reactions on a target in the center of the array. It comprises 20 HPGe detectors with bismuth germanate (BGO) escape suppression shields. Half of the detectors are a planar and half are a coaxial geometry. The planar and coaxial detectors are typically operated with maximum γ-ray energy ranges of 1 MeV and 4 MeV, respectively. Fig. 5.4 and Table 5.2 illustrate the individual detector positions within the GEANIE array.

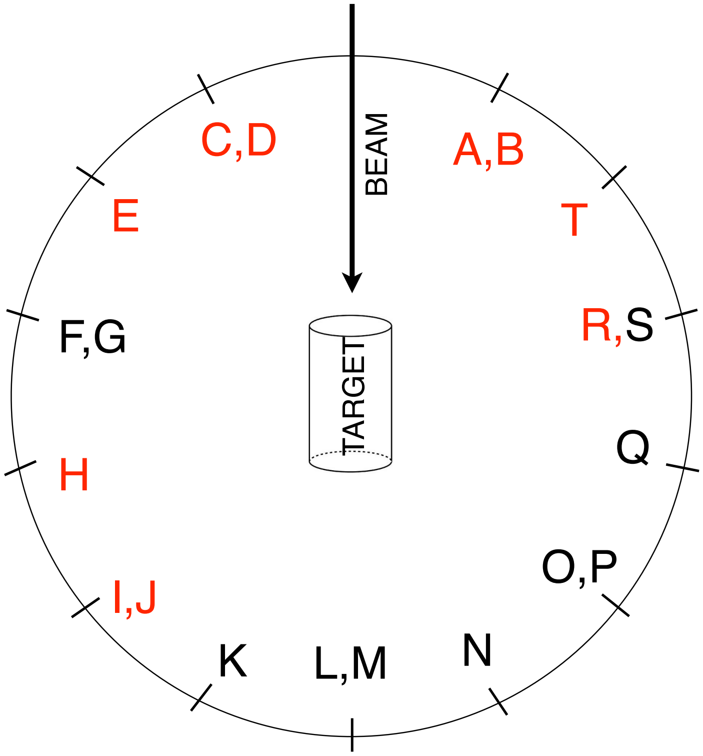

Figure 5.4: Detector placements within the GEANIE array. Each letter corresponds to a single HPGe detector in the array. The detectors labeled with red have a planar geometry and the detectors labeled in black have a coaxial geometry. Details on the placement of the detectors can be found in Table 5.2.

Table 5.2: Detector placements within the GEANIE array for experimental runs. Each detector is marked if it was used in the final cross-section analysis for the argon or neon data. The planar detectors were not considered for either the argon or neon measurements. The quantity θ is the angle relative to the beam axis. A positive value of ϕ indicates a placement above the horizontal plane.

Detector	Type	ϕ (degrees)	θ (degrees)	Diameter (mm)	Thickness (mm)	Distance to front of Ge (cm)
A	planar	29.0	-152.8	51	17	14.415
B	planar	-29.0	-154.0	51	20.4	14.442
C	planar	29.0	157.0	51	18.4	14.379
D	planar	-29.0	157.9	51	18.4	14.318
E	planar	0.0	129.5	51	17	14.237
F (Ne)	coaxial	29.0	102.0	48.8	51	14.288
G	coaxial	-29.0	102.5	50.9	54.9	14.392
H	planar	0.0	78.5	51	17	14.917
I	planar	29.0	53.0	51	19	14.455
J	planar	-29.0	53.5	51	17	14.435
K	coaxial	0.0	26.5	50.5	55.7	14.308
L (Ne)	coaxial	29.0	1.0	49.8	52.9	14.379
M (Ne)	coaxial	-29.0	1.2	49.7	53	14.773
N	coaxial	-29.0	-25.2	52	48.9	14.392
O	coaxial	29.0	-51.0	49.9	54.2	14.392
P (Ne)	coaxial	-29.0	-51.0	48.7	59	13.846
Q (Ar)	coaxial	0.0	-76.9	51	52.9	14.442
R	planar	29.0	-101.7	51	17	14.176
S (Ne)	coaxial	-29.0	-102.0	49.6	53.4	14.308
T	planar	0.0	-128.0	51	20	14.161

Timing and energy resolution are equally important in our experiments. The bremsstrahlung from the proton pulse arrives first at the GEANIE array as a flash of γ rays in the detectors. This early signal serves as a start time of the time-of-flight measurement that also determines the neutron energy. The stop signal is provided by the γ-ray interaction in the HPGe detectors, hence the timing resolution in the HPGe detectors is very important. The typical timing resolutions for a 1-MeV γ ray in the planar and coaxial detectors are about 15 and 10 ns (FWHM), respectively. Typical energy resolutions obtainable with the coaxial detectors are 2.2 keV (FWHM) at $E_\gamma =$ 1332 keV. Typical resolutions from the planar detectors are 0.9 and 1.2 keV (FWHM) at 122 and 661 keV, respectively.

5.3.1 Gas Target Cell

The gas target cell was a 3.81-cm diameter, 6.35-cm length and 0.10-cm thick aluminum cylinder with 0.127-mm thick Kapton windows at either end. The gas cell was placed at the center of the GEANIE array, with the neutron beam passing through the Kapton foils. For the argon experiment, 99.99% $^{\text{nat}}$Ar gas was introduced from a bottle placed outside of the shielded beam area through a length of plastic tubing. The argon gas pressure was maintained at about 2.75 atm over the course of the experiment. Because of a small leak at an unknown location in the cell or filling system, the argon gas was refilled after about a 10% loss in pressure, about twice per day. For this reason, we did not attempt to evacuate the gas cell before running as any air in the cell would be replaced with argon after a few cycles.

Prior to the neon experiment, the leak was repaired by reinforcing the Kapton seals with silicone and the Swagelok vaccuum/gas port was sealed with a resin. The cell was evacuated using a rouging pump and 99.99% $^{\text{nat}}$Ne gas was introduced from a bottle through copper plumbing. Before operation of the gas cell, this process was repeated three times to ensure the neon in the cell was as pure as possible. The pressure in the gas cell was maintained around 3.96 atm over the course of the experiment, with less than 1% variation throughout the 16-day run cycle.

The diameter of the gas cell was larger than the 1.27-cm beam diameter, yielding an areal density of approximately 0.5 target atoms per millibarn in the neutron beam. The number of atoms in the Kapton foils that the beam passed through was 2×10^{-6} mb^{-1} so scattering from the foils had a negligible effect. Attempts were made to align the gas cell in the beam line to minimize scattering from the aluminum cell. Nevertheless, we observed some background from aluminum scattering, which is discussed further in Section 6.3.3.

5.4 Electronics and Data Acquisition

Data were collected with a data acquisition system (DAQ) built around Ortec AD114 analog-to-digital converters (ADCs) and LeCroy time-to-digital converters (TDCs), with fast readout over a LeCroy fast encoding readout amplification (FERA) bus into a VME memory module. The high voltage was supplied to the PMTs for the Compton suppression shields through a multi-channel high-voltage supply. The HPGe detector high-voltage supplies were individual units, each operated manually. Readout of individual events from the VME memory modules, and subsequent online and offline analyses were performed using code based on the Maximum Integrated Data Acquisition System (MIDAS) software framework [MID01]. A block diagram of the electronics used in GEANIE is shown in Fig. 5.5.

The DAQ processed signals from each HPGe detector, two signals from the fission chamber (^{235}U and ^{238}U), and a pulser. They were sent from a preamplifier to timing-filter amplifiers (TFAs) to produce the timing signals and linear spectroscopy amplifiers to provide the energy signals. The energy signals were digitized using the ADCs, and the

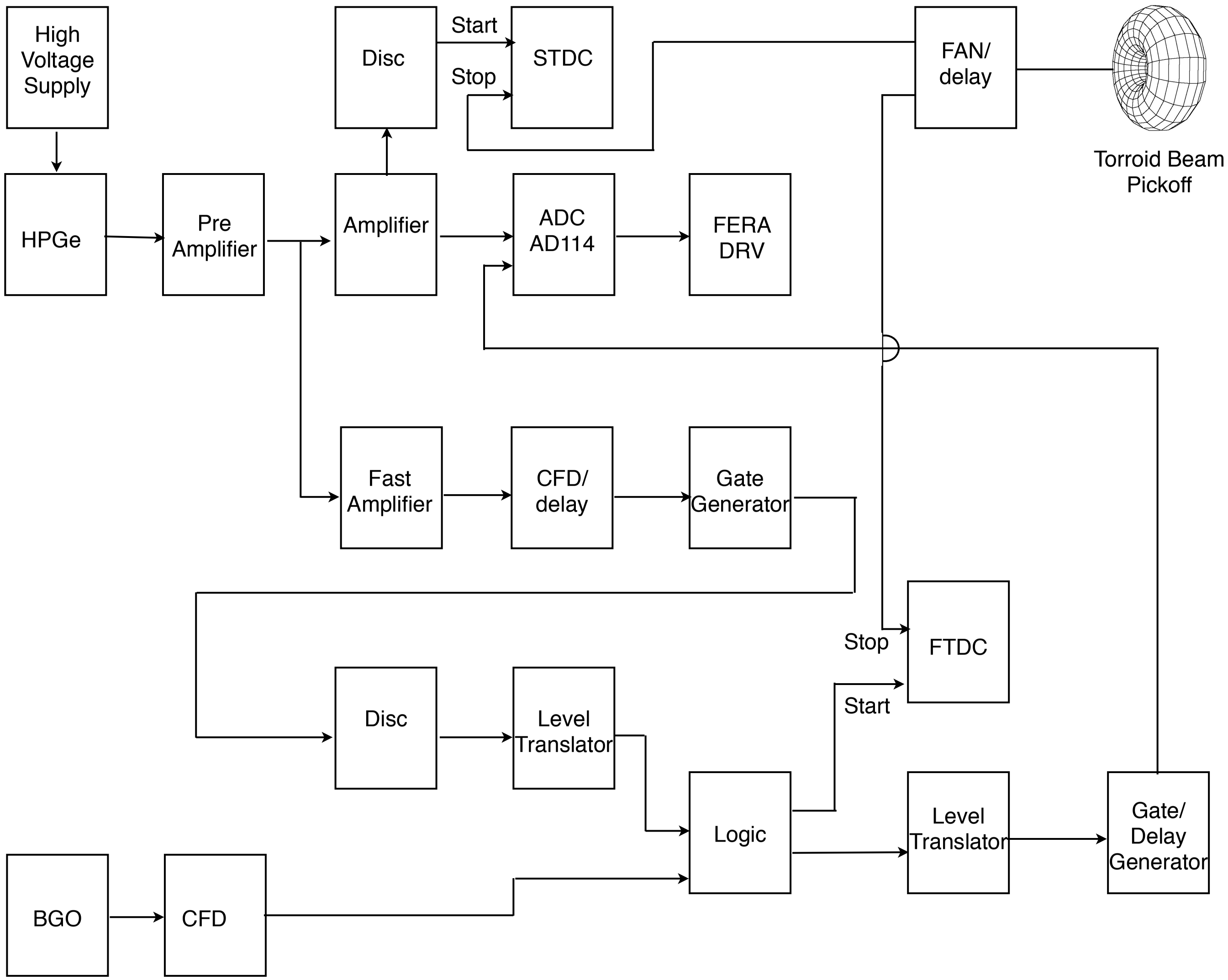

Figure 5.5: A block diagram of the GEANIE detector circuit. Adapted from `geanie.lanl.gov`. Scalers are omitted from the diagram.

TFA signals were processed by constant fraction discriminators (CFDs) which generated logic signals. The HPGe signals were vetoed using an anti-coincidence with the analog signals from the Compton suppression shields.

An unsuppressed pulse from a Ge detector, fission chamber, or pulser triggered the GEANIE array and opened a 20 μs long master gate during which all signals were processed. For the purposes of this discussion, a “GEANIE event” refers to the data read out from all detectors following a single trigger. For each GEANIE event, the ADC value and detector ID for each signal processed within the master gate was recorded. The timing signal from the TDC, called the “fast TDC” (FTDC), and detector ID were also recorded. The TDCs were operated in common stop mode, so that the start signal was produced by any detector, pulser or fission chamber signal and the stop signal was provided using a delayed pickoff signal from the start of the proton macropulse. The resulting TDC spectra were used for determining the neutron time of flight, hence energy. This is discussed in detail in Section 6.3. Although up to only one ADC conversion was allowed per detector in a given trigger, the TDC could be triggered multiple times per GEANIE event. Because of this, a second TDC, called the “slow TDC” (STDC), was used to recover events with multiple FTDC hits. The STDC signal was generated from the spectroscopy amplifier that processed the Ge signal. Although the time resolution was too poor to be used for the time-of-flight measurement, it was correlated with the ADC signal, and thus, the “correct” FTDC signal. Both the FTDC and STDC had a gain of 0.5 ns/channel. Lastly, a clock measured the time, in 100 ns intervals, from the start of the macropulse. From this information, a universal logic module (ULM) provided a bit determining whether the event occurred inside or outside a macropulse, referred to as “beam on” and “beam off”, respectively. This provided a useful veto for non beam-induced data. The data stream is illustrated through an example simplified GEANIE event:

```
eventId = 1

timeStamp = 479341680

ADC[30] = [2050,3295,65535,...,65535]

STDC[30] = [15000,1100,65535,...,65535]

nFTDC = 3

FTDC[nFTDC] = [14250,1000,7710]

FHIT[30] = [1,2,0,...,0]

nFDET = 3

FDET[nFDET] = [1,2,2]

ULM = 1
```

Because the ADC and STDC can only be trigged once per channel in an event, they are read out as a fixed-length array, each element corresponding to a given HPGe detector, fission chamber, or pulser. It is possible that not all channels are used. In this example, only detector 1 and 2 recorded an event. If there was no data for a given channel, a value of 65535 was recorded. The FTDC was read out as a variable-length array, with nFTDC elements, where nFTDC is the number of hits recorded in the event. Similar to FTDC, FDET represents the detector IDs that recorded the FTDC hits. The FHIT array represents the FTDC multiplicity. In this example, detector 1 recorded one hit and detector 2 recorded two hits. It now becomes important to select the "correct" FTDC value for detector 2, which determines the neutron energy correlated with the ADC signal for detector 2. As described above, although the timing information from the STDC is too poor to make a precise time-of-flight measurement, it corresponds directly the the ADC signal, and can be used to select the "correct" FTDC signal for channels with multiple hits. Alternatively, channels that registered multiple hits in an event could be cut from the analysis; of course, there would be a loss of both good data and live time. The ULM registered a value of 1 or 0 depending on whether the event occurred inside or outside of a macropulse.

5.4.1 Data Processing

As described in above, data were collected using both CAMAC and VME modules. The MIDAS data acquisition system was used to read the event-by-event data from these modules and perform the first level of data analysis. The "frontend" nodes are computers which are programmed to read data from the hardware modules. The "backend" is concerned with the storage and analysis of the data. For GEANIE, the backend is a PC running Linux, which processed the data files and transferred them over the network.

MIDAS contains a set of standard applications providing frontend acquisition, run control, slow control, data storage and backend analysis. MIDAS also includes a central database of experimental parameters, calibrations, slow-control values, status and performance data, and any other information defined by the user. A built-in "web-based" electronic logbook provides a method of logging experimental information.

For the data analysis, a standalone C++-based analyzer program was used to perform MIDAS calls to retrieve the necessary data. The analyzer program performs all data cuts and writes files containing ROOT histograms for all detector and scaler data, as well as storing the event-by-event data in ROOT tree format. A graphical viewer called ROODY [ROO12] was used to view histograms built from the MIDAS analyzer and view them as the experiment was running. Once the ROOT histogram and event-by-event files were written, they were transferred from the backend computer for further analysis.

Chapter 6

GEANIE Experimental Data, Analysis and Results

This chapter describes the experimental data, analysis and results for partial γ-ray production cross-section measurements for neutrons incident on $^{\mathrm{nat}}$Ar and $^{\mathrm{nat}}$Ne. The argon data represents beam time taken over 17 days in September 2010 and 9 days in December 2010. The neon data were taken over 16 days in February 2012. During the argon experiment, 6.0×10^{9} micropulses produced about 1.9×10^{11} neutrons of energies from 1 to 100 MeV on target. For the September run, a piece of lead was mistakenly left in the beam line from a previous experiment upstream of the GEANIE array. Although this had no effect on the data analysis, it scattered many neutrons out of the beam. During the neon experiment, 1.2×10^{10} micropulses produced about 1.2×10^{12} neutrons of energies from 1 to 100 MeV on target.

6.1 Detector Selection

Gamma-ray spectroscopy using arrays of HPGe detectors presents a variety of experimental challenges. The detectors in the GEANIE array are subject to continuous neutron exposure from the beam and may be subsequently damaged. Damaged detectors may present tails on the full energy peak or poor energy resolution. For this reason, individual detectors are tested and rehabilitated as necessary about once per year when the LANSCE beam is not running.

For light nuclei the excitation energy of the first excited state is usually high (1.46 MeV for ^{40}Ar and 1.62 MeV for ^{20}Ne). Because the level densities are also low in these nuclei, the γ-ray energies from nuclear de-excitations are typically outside the dynamic range of the planar detectors.

For the argon experiment, all of the detectors were included in the GEANIE trigger and were available for diagnostics. Due to poor energy resolution because of neutron damage or other issues which affected the timing, only one coaxial detector (GeQ: $\theta = 76.9°$ relative to the beam axis, $\phi = 0°$) with the best energy resolution, peak-to-background ratio and timing information was used in the cross-section analysis.

For the neon experiment, the planar detectors were removed from the GEANIE trigger to reduce dead time. Each of the coaxial detector's energy resolutions were measured using γ-ray sources before the beam-on data were taken. The timing resolution was measured by determining the full width at half maximum (FWHM) of the γ-flash from each detector's TDC spectrum during the first day of beam-on data and ranged from 17 to 34 ns. Detectors that could not be used in the cross-section analysis because of energy or timing issues were then removed from the GEANIE trigger, leaving seven detectors available for taking beam-on γ-ray data. Of these, two additional detectors were excluded from the final analysis because of significant ADC gain instability during the experimental runs. Detectors GeF, GeL, GeM, GeP and GeS were used for the final cross section analysis. See Fig. 5.4 and Table 5.2 for details on the detectors.

6.2 Neutron Time-of-Flight

Neutron energies were determined using the time-of-flight (TOF) technique. The neutron TOF was determined relative to the "γ flash" created by Bremsstrahlung and proton-induced excitations in the ${}^{\mathrm{nat}}$W spallation target. The γ-ray TOF is simply d/c where $c \approx 0.299$ m/ns and d is the distance from the source to the target. The neutron TOF is calculated relativistically by

$$t = \frac{d}{\beta c}, \tag{6.1}$$

where

$$\beta = \frac{p}{E_n + m_n} \tag{6.2}$$

and

$$p = \sqrt{(E_n + m_n)^2 - m_n^2}. \tag{6.3}$$

The classical limit, where $E_n << m_n$ ($m_n = 939.565$ MeV), is adequate for all of the neutron energies for which a cross section was measured in this experiment. In this case the difference between the neutron and γ-ray TOF is given by

$$\delta t = \frac{d}{v} - \frac{d}{c} = \frac{d}{c}\left(\sqrt{\frac{m_n}{2E_n}} - 1\right) \tag{6.4}$$

Using the distance to the focal point of the γ-ray spectrometer (20.34 m), one obtains,

$$\begin{aligned} E_n &= 1.0 \text{ MeV} \rightarrow \delta t = 1406 \text{ ns} \\ E_n &= 20.0 \text{ MeV} \rightarrow \delta t = 262 \text{ ns} \\ E_n &= 100.0 \text{ MeV} \rightarrow \delta t = 79 \text{ ns}. \end{aligned} \tag{6.5}$$

6.3 Analysis of γ-ray Data

The digitized energy signals from each of the HPGe detectors were correlated with a time signal from the fast TDC (FTDC) as described in Chapter 5. Only single-multiplicity events were considered for this analysis. Using the time-of-flight technique described in Section 6.2, each γ-ray energy was associated with a neutron time of flight, and therefore a neutron energy using the γ flash from the proton micropulse as a $t = 0$ reference time. Fig. 6.1 shows the fast FTDC spectrum for a single HPGe detector for all γ-ray energies. The micropulse structure is clearly visible and the first few γ flashes are indicated by the arrows in the figure. Each γ flash is followed by HPGe signals corresponding to a particular neutron energy. The FTDC spectra include up to 17 micropulses from a macropulse, determined from the delay in the beam pickoff and gain of the FTDC (0.5 ns/channel). The background in channels above the γ-flash are from time-random γ-ray events and wrap-around neutrons. A TOF spectrum, shown in Fig. 6.2 was obtained by aligning the γ-flashes of consecutive micropulses in a TDC spectrum. The resulting time-of-flight spectrum was then converted to neutron energy and re-binned into 40 equal logarithmic neutron energy bins from 1 to 100 MeV. Although the binning was significantly coarser than the time resolution of the detectors, it proved to be the best choice to generate enough statistics over the measured neutron energy range.

The timing signals from the fission chambers were processed identically to those from the HPGe detectors. Fig. 6.3 shows the self-triggered TDC range for the ^{238}U fission chamber data summed over all 17 days of neon data. The γ flash is indicated in the figure. Because the fission chambers are much less sensitive to γ rays it may be difficult to determine the location of the γ flash. Sometimes it may be necessary to examine additional datasets from previous experimental runs to provide enough statistics to determine the $t = 0$ reference time for the fission chamber data.

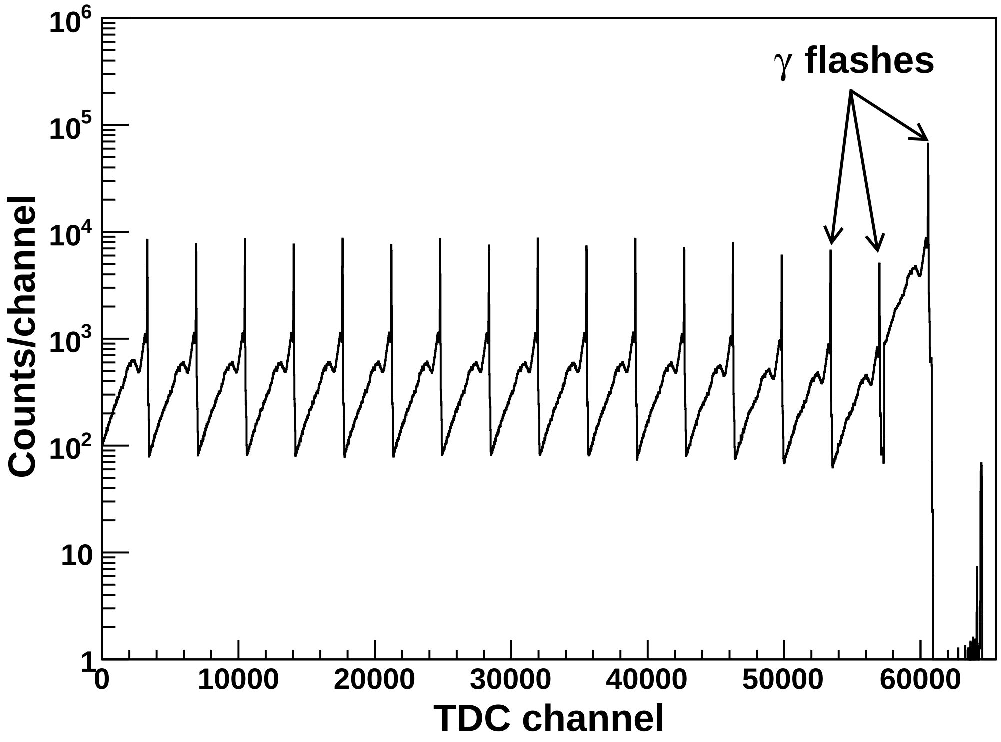

Figure 6.1: A sample TDC spectrum for a GEANIE HPGe detector (GeF) summed over the neon sample data for all HPGe signals. The first few γ-flashes are indicated by the arrows. Time increases with decreasing channel number. The TDC has a gain of 0.5 ns/channel. See text for further description.

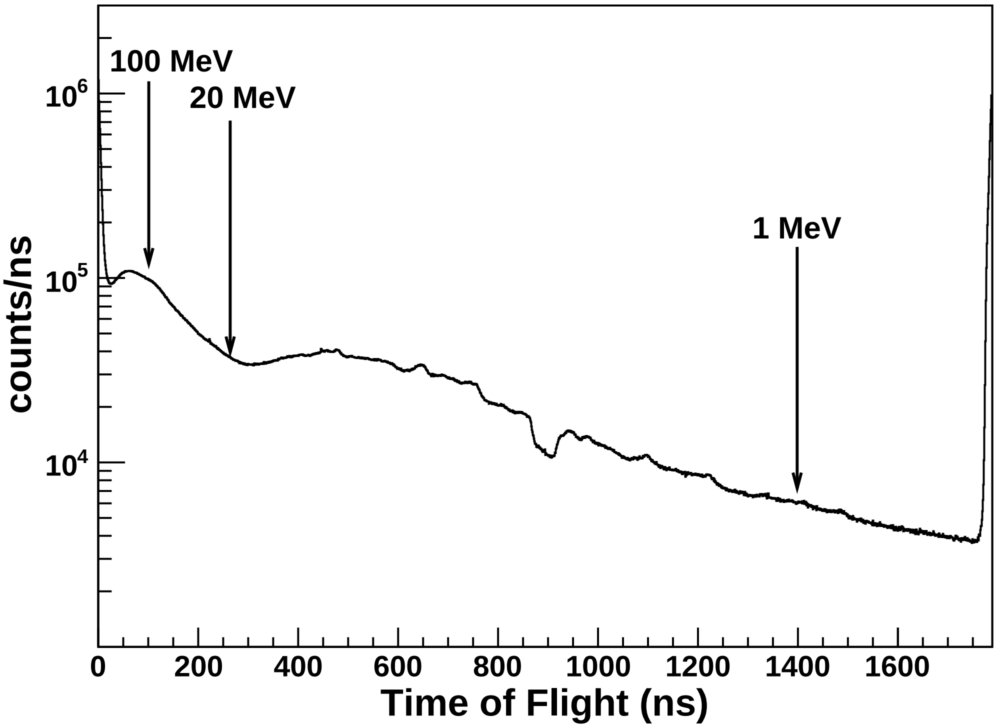

Figure 6.2: A sample TOF spectrum for a GEANIE HPGe detector (GeF) summed over the neon sample data for all HPGe signals. The time-of-flight spectrum was created by aligning the consecutive micropulses in the TDC spectrum. The time $t = 0$ corresponds to the centroid of the summed γ flashes. The time-of-flight for several different incident neutron energies are labeled.

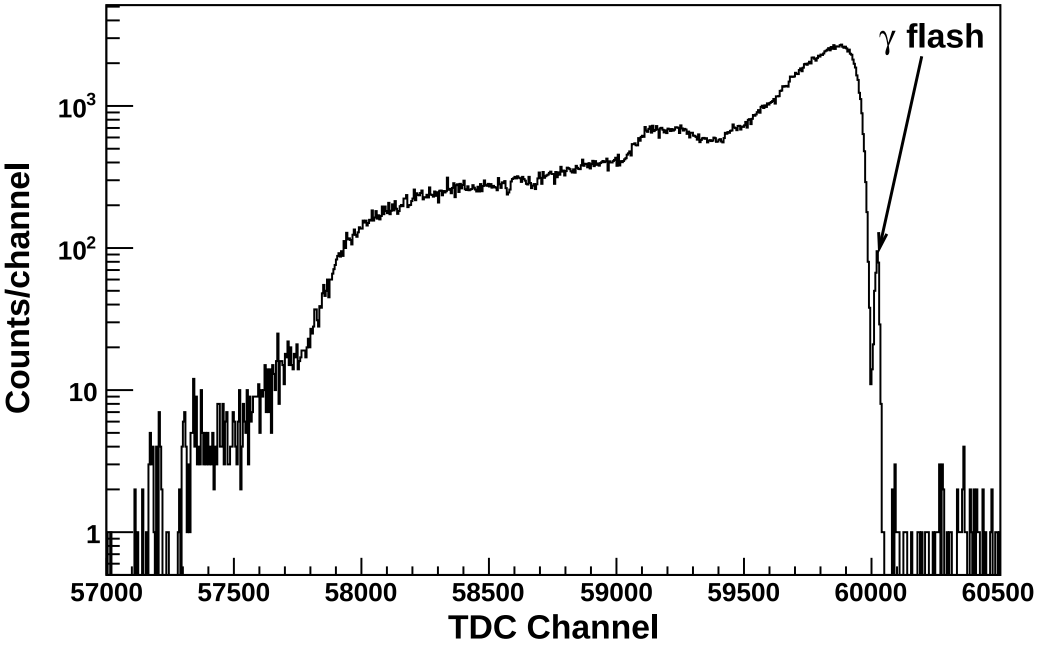

Figure 6.3: Self-triggered TDC range for the ^{238}U fission chamber data summed over all 17 days of neon data. The γ flash is indicated in the figure.

6.3.1 Detector Energy Calibration

The ADC energy spectra from the coaxial HPGe detectors were calibrated using 13 γ rays from ^{152}Eu, ^{60}Co and ^{54}Mn point sources. The ADC channel corresponding to the centroid of each peak was determined by fitting to a Gaussian function. The γ-ray energy was plotted versus the ADC channel number and was fit with a quadratic function. The quadratic terms were small for all of the detectors so a linear calibration was assumed for the entire energy range. An example calibration curve is shown in Fig. 6.4.

6.3.2 E_n vs E_γ Histograms

The neutron energy from the TDC and the γ-ray energy were plot on 2D histograms, shown for the argon and neon sample data in Fig. 6.5. The neutron energy bins were

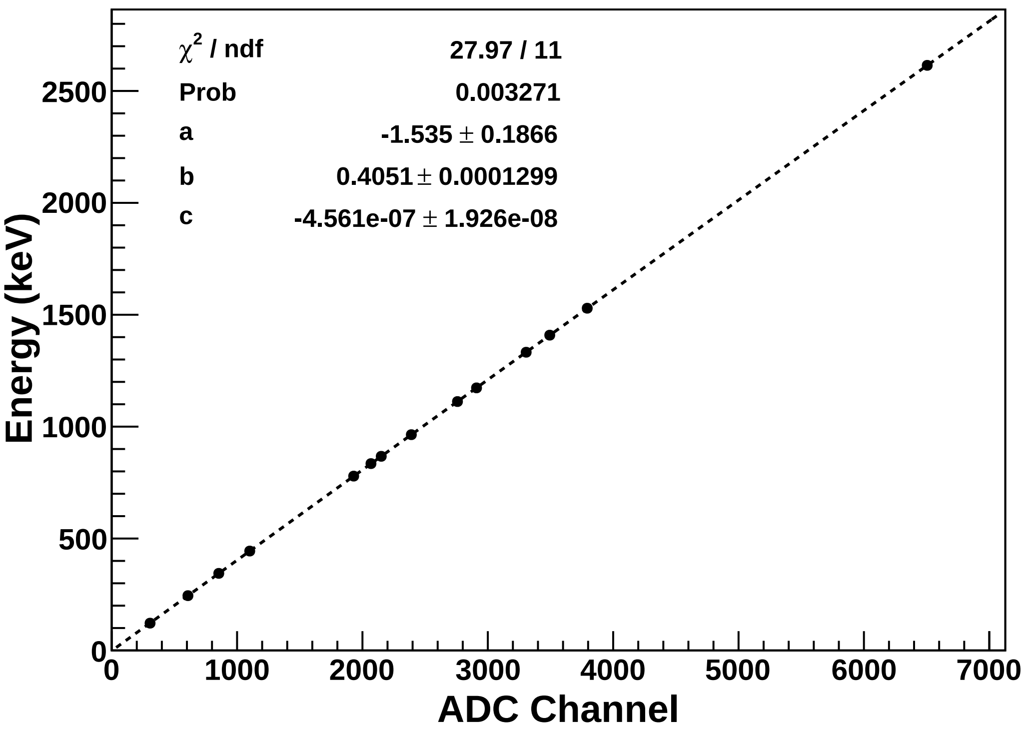

Figure 6.4: An example energy calibration for a GEANIE coaxial HPGe detector (detector GeR). The fit parameters, a, b and c were determined by fitting the data with a quadratic function $E_\gamma = a \cdot channel^2 + b \cdot channel + c$. Although the fit was poor, likely owing to ADC nonlinearity, the calibration did not affect the identification of specific γ-ray lines.

then projected onto the E_γ axis to produce γ-ray spectra for a specific neutron energy range. Typically, data from the planar detectors are analyzed separately from the coaxial data. For the argon data, only one coaxial detector was used in the final analysis. For the neon data, five detectors were used in the cross-section analysis. Since the peak-to-background ratio is worse for detectors at forward angles because there were more beam-induced backgrounds, there was little statistical advantage to summing the detectors. Each detector was analyzed separately which also permitted a measurement of the angular distribution.

6.3.3 Gamma-ray Spectra

Gamma-ray spectra for the argon and neon samples gated on different neutron energies for a single coaxial HPGe detector are shown in Figs. 6.6 and 6.7. Data were also taken with an evacuated gas cell so that argon or neon transitions could be easily distinguished from backgrounds. Because the argon and neon peaks were all well-separated from backgrounds, it was not necessary to subtract backgrounds due to scattering in the target cell or detectors. Because of the beam pulsing structure, the "beam on" data was short compared to the "beam off" data and backgrounds due to naturally occurring radioactive isotopes such as ^{232}Th, ^{222}Rn and ^{40}K were negligible. A 1460.9-keV γ ray from a first excited-state transition in ^{40}Ar due to a neutron-induced excitation is equivalent to a β decay of ^{40}K which has a 10.66% branching ratio for a 1460.9-keV γ ray. For the argon data, the background from ^{40}K was $< 2\%$ compared to the argon-sample data. All γ-ray lines present only in the sample data have been identified. Most other γ-ray lines have been identified as backgrounds from the sample cell (^{27}Al) or neutron inelastic scattering in the germanium crystals or bismuth from the BGO shields. Prominent γ-ray lines for both samples are listed in Table 6.1 and 6.2.

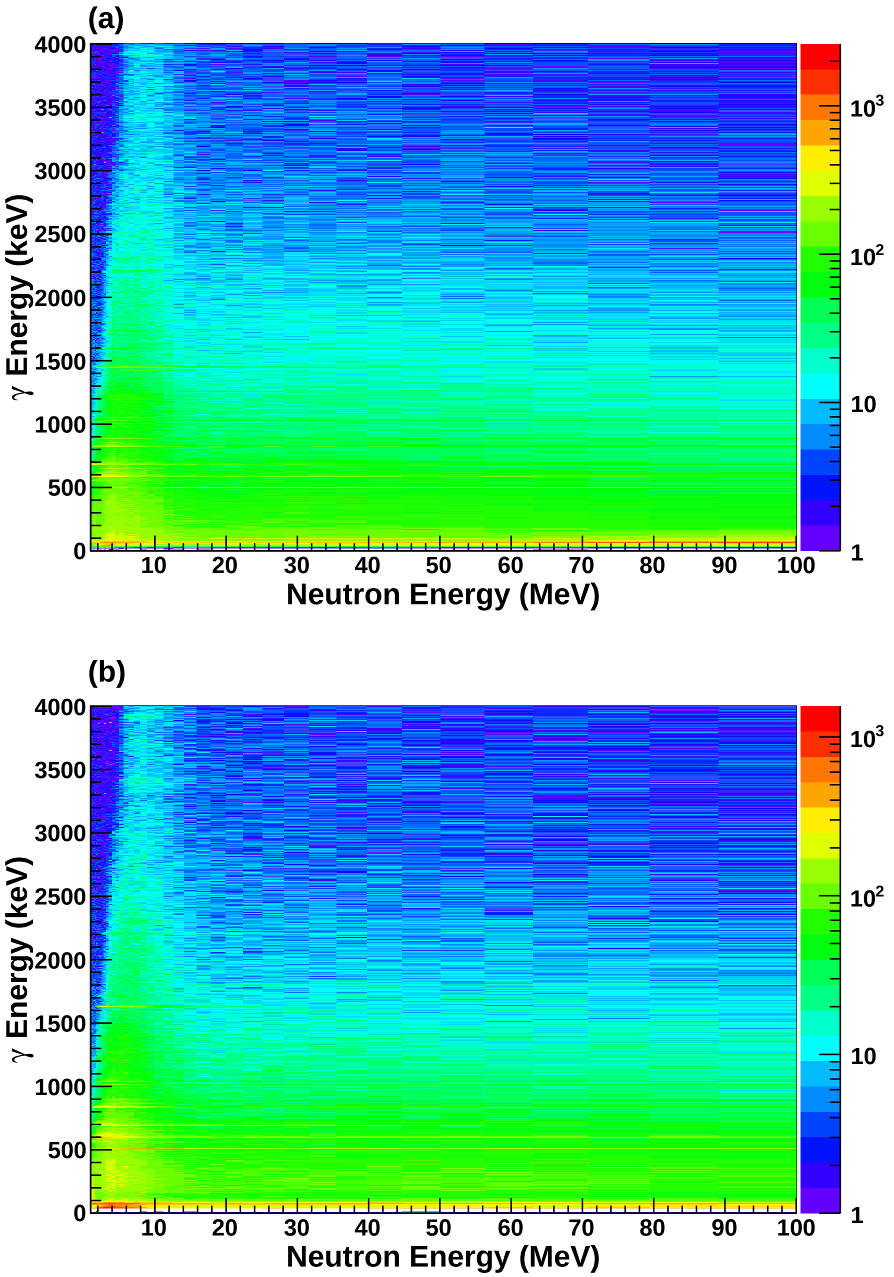

Figure 6.5: E_n vs E_γ histograms for (a) argon and (b) neon sample data.

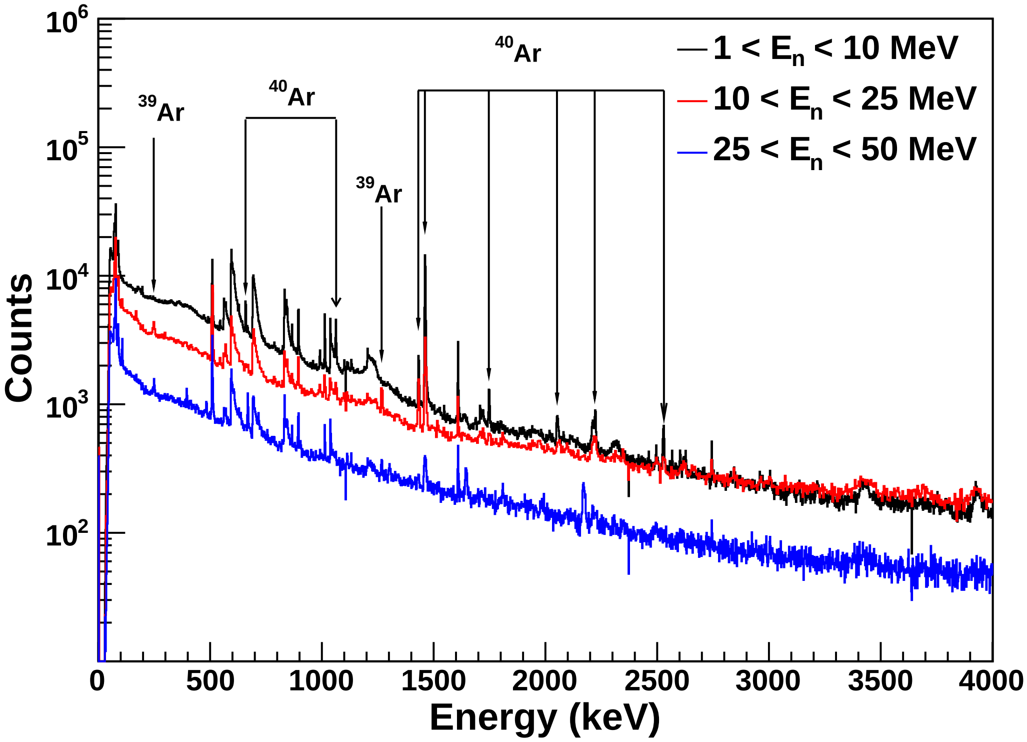

Figure 6.6: Argon-sample γ-ray spectra (detector GeQ) selected for different neutron energy windows. The spectrum shown in black (top) corresponds to $1 < E_n < 10$ MeV. The spectrum shown in red (middle) corresponds to $10 < E_n < 25$ MeV. The spectrum shown in blue (bottom) corresponds to $25 < E_n < 50$ MeV. Transitions in argon are labeled. The prominent γ-ray lines are listed in Table 6.1 and 6.2.

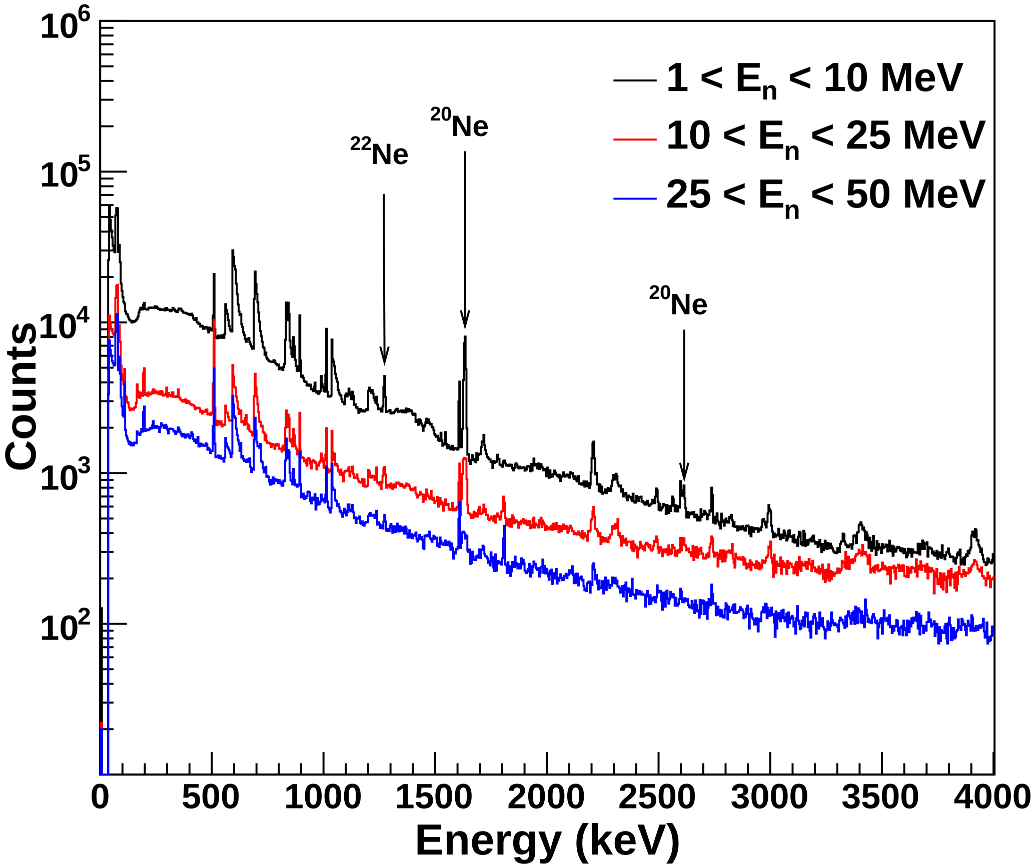

Figure 6.7: Neon-sample γ-ray spectra (detector GeF) selected for different neutron energy windows. The spectrum shown in black (top) corresponds to $1 < E_n < 10$ MeV. The spectrum shown in red (middle) corresponds to $10 < E_n < 25$ MeV. The spectrum shown in blue (bottom) corresponds to $25 < E_n < 50$ MeV. Transitions in argon are labeled. The prominent γ-ray lines are listed in Table 6.1 and 6.2.

Table 6.1: Prominent γ-ray lines in argon and neon sample data. Additional information on the ^{40}Ar and ^{20}Ne transitions can be found in [Cam04] and [Til98].

E (keV)	Source	Transition
Argon sample data		
250.3	^{39}Ar	$3/2^+ \rightarrow 3/2^-$
545	^{40}Ar	$4^- \rightarrow 3^-$
571.9	^{40}Ar	$6^+ \rightarrow 4^+$
660.1	^{40}Ar	$0^+ \rightarrow 2^+$
1063.4	^{40}Ar	$2^+ \rightarrow 2^+$
1267.2	^{39}Ar	$3/2^- \rightarrow 7/2^-$
1431.8	^{40}Ar	$4^+ \rightarrow 2^+$
1460.9	^{40}Ar	$2^+ \rightarrow 0^+$
1746.5	^{40}Ar	$2^+ \rightarrow 2^+$
2050.5	^{40}Ar	$2^+ \rightarrow 2^+$
2054	^{40}Ar	$4^+ \rightarrow 2^+$
2220.0	^{40}Ar	$3^- \rightarrow 2^+$
2524.1	^{40}Ar	$2^+ \rightarrow 0^+$
Neon sample data		
1633.7	^{20}Ne	$2^+ \rightarrow 0^+$
1274.6	^{22}Ne	$2^+ \rightarrow 0^+$

Table 6.2: Prominent backgrounds GEANIE spectra. Additional information on the other transitions may be found in Ref. [Cha06].

E (keV)	Source	Transition
Backgrounds		
511	e^+e^- annihilation	
595.9	^{74}Ge	$2^+ \rightarrow 0^+$
691.5	^{72}Ge	$0^+ \rightarrow 0^+$
834.0	^{72}Ge	$2^+ \rightarrow 0^+$
843.8	^{27}Al	$1/2^+ \rightarrow 5/2^+$
896.3	^{209}Bi	$7/2^- \rightarrow 9/2^-$
1014.5	^{27}Al	$3/2^+ \rightarrow 1/2^+$
1039.2	^{70}Ge	$2^+ \rightarrow 0^+$
1608.5	^{209}Bi	$13/2^+ \rightarrow 9/2^-$

Neutron Scattering in Germanium

The largest source of background in these experiments was due to neutron scattering in the germanium crystals. An incoming neutron may elastically scatter from a germanium atom, knocking it off its lattice site. The lattice site binding energy is less than 100 eV. The recoiling germanium nucleus loses its energy in the crystal by colliding with electrons and nuclei in the detector. If the incident neutron has enough energy, the germanium atom may be knocked from its lattice site and lifted into an excited state. This results in the triangle-shaped peaks where the lower edge is the energy of the nuclear de-excitation and the high-energy tail is due to the recoil nucleus adding to the de-excitation energy [Bam91]. A list of commonly observed γ rays in HPGe detectors from neutron-induced reactions may be found in Ref.[Geh05].

Doppler Broadening

When considering inelastic neutron scattering from light nuclei, enough kinetic energy may be transferred to the recoil nucleus that Doppler shifts in the γ-ray energy from the nuclear de-excitation may be observable in HPGe spectra. The magnitude of the energy shift ΔE is related to the unshifted energy of the γ ray E_0 by

$$\Delta E = E_0(v/c)\cos(\theta) \tag{6.6}$$

where v is the velocity of the recoil nucleus, c is the speed of light and θ is the angle between the direction of motion of the recoil nucleus and emitted the γ ray. The effect of these energy shifts is to broaden the original peak in the HPGe spectrum.

6.4 Calculation of γ-ray Production Cross Sections

The γ-ray cross section for a specific neutron energy bin was calculated using

$$\sigma_\gamma(E_n) = \frac{I_\gamma(E_n)}{I_\Phi(E_n)} \frac{T_\Phi}{T_\gamma} \frac{(1+\alpha)}{t \cdot \epsilon_\gamma} \cdot C_\gamma(E_n) \tag{6.7}$$

where $I_\gamma(E_n)$ is the γ-ray yield (counts/MeV) in the HPGe detectors, $I_\Phi(E_n)$ is the neutron flux (neutrons/MeV). The quantity α is the internal conversion coefficient. For the transitions observed in this experiment, $\alpha < 10^{-4}$ [Hag68]. $C_\gamma(E_n)$ is the angular distribution correction factor, t is the target areal density (atoms/barn), ϵ_γ is the γ-ray detection efficiency, and T_γ and T_Φ are the detector and fission chamber fractional live times, respectively.

6.4.1 Gamma-ray Yields

To extract the γ-ray yields, a Gaussian plus a linear background function was fit to each peak used for analysis. The fit was used to obtain the centroid of the peak and define the limits over which to integrate. The peak area was extracted by summing the counts in a $\pm 3\sigma$ width region. Subtraction of the continuum background was done using one of two methods: (1) Integrate the linear part of the fit extrapolated under the peak and subtract, (2) define two regions, one 3σ to the left and the other 3σ to the right of the peak, average the counts in the two regions, and subtract it from the total integrated peak area. If another peak was within 3σ to the left or right, the background region with no peak present was used rather than the average (See Fig. 6.8 for illustration). We prefer method (2) since it does not rely on the goodness-of-fit. The γ-ray yields were consistent with those obtained using the *gf3* component of the RADWARE package [Rad00].

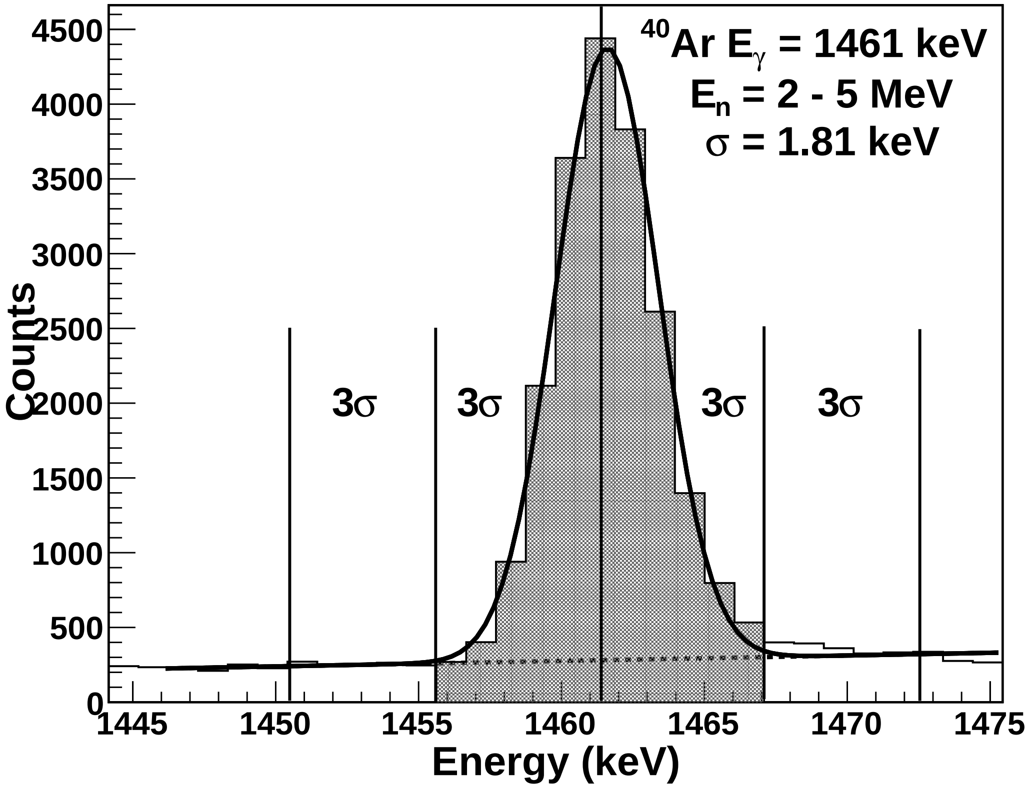

Figure 6.8: First excited-state transition in ^{40}Ar. The peak was fitted with Gaussian function (solid) plus a linear background function (dashed). The peak area (shaded region) was determined by integrating from $+3\sigma$ to -3σ about the centroid of the Gaussian function. The background is subtracted by either integrating the linear background function using the same integration limits or averaging the counts in the 3σ regions to the left and right of the peak.

6.4.2 Determining an Upper Limit

An upper limit for the number of counts R in a counting experiment, assuming a Poission distribution may be calculated using

$$R \leq n\sqrt{B} \tag{6.8}$$

where n is the confidence level at which the result is expressed (n=1 (67%), n=1.64 (90%) , n=2 (99%), etc.) and B is number of counts in a given energy bin.

Peak Window Optimization

Our goal is to choose a region-of-interest (ROI) of optimal width when determining an upper limit. We will focus on the case where the signal is Gaussian and the background is flat. Although we chose this shape since it pertains to γ-ray spectroscopy using HPGe detectors, it may be extended for any signal and background shape.

Varying the width will change two things: (1) B, the amount of background in the ROI will depend on the width, (2) the fraction of the potential Gaussian signal shape contained in the ROI. Following [Ell11], we construct a figure of merit (FoM) based on the parts of the upper limit calculation that will be affected by the width, given as

$$FoM = \frac{\sqrt{B}}{\epsilon_{ROI}}, \tag{6.9}$$

where B is the background in the ROI and ϵ_{ROI} is the efficiency factor due to the fraction of the line shape contained in the peak. For a Gaussian signal (assume the Gaussian is centered at $x = 0$ ie. μ=0) on a flat background, the FoM becomes

$$FoM = \frac{\sqrt{x}}{\int_0^x e^{-x'^2/2\sigma^2} dx'}. \tag{6.10}$$

Integrating the gaussian, this becomes

$$FoM = \frac{\sqrt{x}}{\sqrt{\pi} \cdot \sigma \cdot \mathrm{erf}(\frac{x}{2\sigma})} \tag{6.11}$$

We now attempt to find σ such that our FoM is a minimum.

$$\frac{\partial}{\partial x}\left(\frac{\sqrt{x}}{\sqrt{\pi} \cdot \sigma \cdot \mathrm{erf}(\frac{x}{2\sigma})}\right) = \frac{\sqrt{\pi} \cdot \sigma \cdot \mathrm{erf}(\frac{x}{2\sigma}) - 2xe^{-x^2/4\sigma^2}}{2\pi \cdot \sigma^2 \sqrt{x} \cdot \mathrm{erf}(\frac{x}{2\sigma})^2} \tag{6.12}$$

Setting this equation to zero and solving for x numerically, we find that our FoM has a minimum value at 1.4σ. We therefore conclude that the optimum width for an ROI for a gaussian signal on a flat background is $\pm 1.4\sigma$ about the mean, or a total window width of 2.8σ.

6.4.3 Detector Efficiencies

The full-energy peak (FEP) detection efficiency is defined as the ratio of the number of events detected in the γ-ray peak to the number of events emitted from the source. In general, this depends on many factors, including the crystal, cryostat, shielding and source geometries. There are several methods to determine the FEP detection efficiency: (1) Use analytical calculations [Wan95]. This technique is limited to simple geometries and requires complex calculations. (2) A physical model of the sample can be created using known standards [Smi09]. This process is complicated and time consuming and is of limited accuracy for complex geometries. (3) Perform a point source calibration at several points near the detector. The efficiency curve generated is then corrected for absorption by a sample matrix [Sae04]. (4) Perform a detailed Monte-Carlo simulation for each sample [Fin11]. A distribution of γ rays are tracked from the emission at the source to absorption in the detector active region. By using a pure Monte-Carlo simulation to determine the FEP detection efficiency, self-attenuation in the sample is accounted for and there are no limitations on source or detector configurations. However, Monte-Carlo simulations are limited by the knowledge of the response and geometry of the detector and targets, and the micro-physics models used.

For this experiment, the γ-ray detection efficiency (ϵ_γ) was measured using 17 γ rays from ^{152}Eu, ^{60}Co and ^{137}Cs point sources each placed in the center of the array. For each γ ray, the detection efficiency was calculated using the number of events in the photopeak, known source activity, γ-ray branching ratios and measurement live time. These measured efficiencies were fit to derive an efficiency curve for each detector. A simulation of the efficiency was also done using MaGe [Bos11]; a Monte-Carlo framework developed by the Majorana and GERDA collaborations based on GEANT4 [Ago03, All06]. The detector geometries were adapted from the simulation of the GEANIE detectors done using MCNP by Ref.[McN00a]. Simulated mono-energetic γ rays were tracked from a point source in 10 keV increments from 10 to 4000 keV. The efficiency was calculated for each γ-ray energy using

$$\epsilon_\gamma = \frac{N_{peak}}{N_{sim}} \tag{6.13}$$

where N_{peak} is the number of events in the peak and N_{sim} is the number of events simulated. Enough events were generated for each γ-ray energy so that statistical uncertainties were less than 1%. An example efficiency curve constructed from the simulated data and source data are shown in Fig. 6.9. The data were fit to a power law above 200 keV. At lower energies, the efficiency peaks and then sharply decreases due to absorption in the detector endcap and cryostat. The simulated efficiency curve was consistent with the fit to the experimental data to within 6% from 200 – 3200 keV, which includes all γ rays measured in argon and neon experiments.

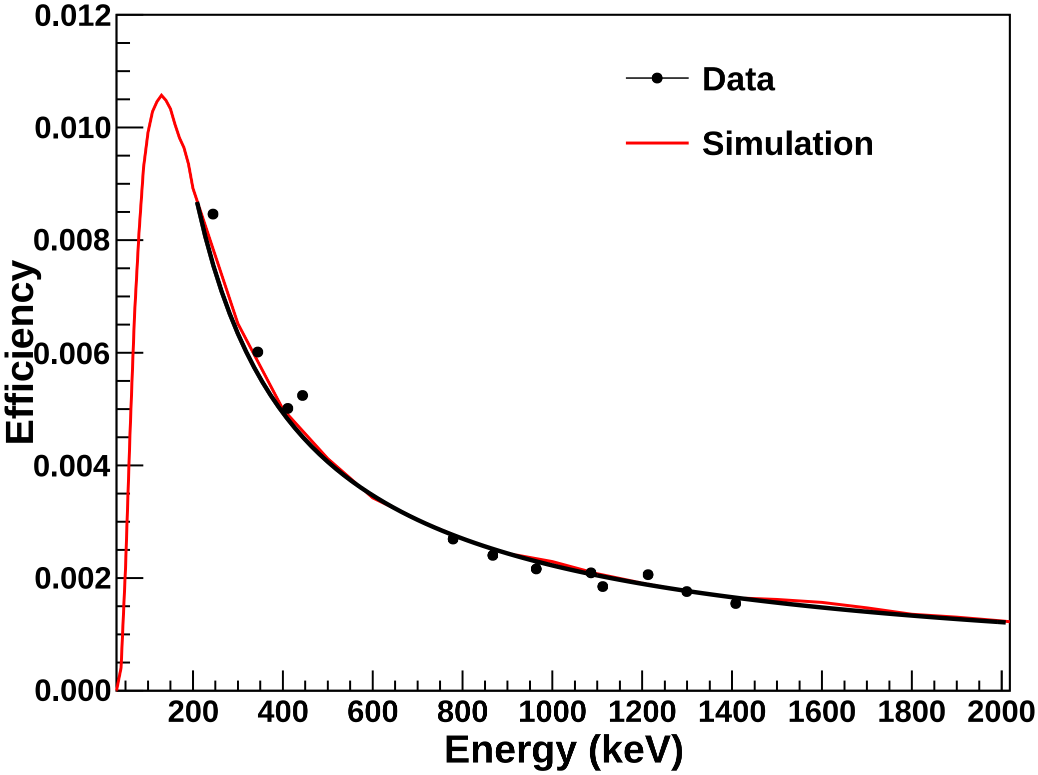

Figure 6.9: An example efficiency curve (detector GeQ). The black circles are data taken with the ^{152}Eu point source. Error bars on the data points are not visible on the scale of this graph. The black curve is a power law fit to the data for energies above 200 keV. The red curve is the simulation.

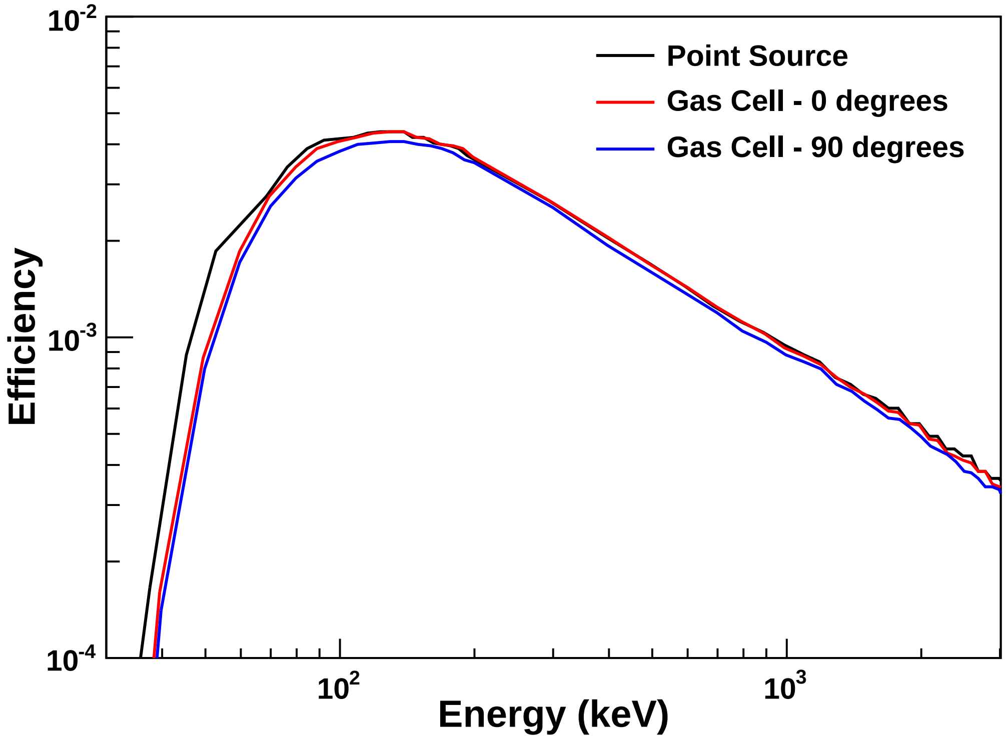

Figure 6.10: Simulated efficiency curves for GeQ using a point source and argon gas cell. The black curve is the efficiency for a point source in the center of the GEANIE array. The red and blue curves are the efficiencies for the gas cell oriented at 0 degrees and 90 degrees with respect to the beam axis, respectively.

The effects of γ-ray attenuation and extended source geometry were investigated using additional Monte-Carlo simulations. Mono-energetic γ rays were generated isotropically in a simulated gas cell in 10 keV increments from 10 to 4000 keV. The gas cell was oriented at 0 degrees and at 90 degrees with respect to the beam axis, representing the most extreme placements of the gas cell relative to any detector in the array. A comparison of the gas cell filled with 2.75 atm argon and point source simulations is shown in Fig. 6.10. While the effect of absorption in the gas cell is significant at γ-ray energies of about $10-50$ keV, the correction due to γ-ray attenuation in the gas target and aluminum cell and extended source geometry was negligible for the measured γ-ray energies at the gas density used in this experiment.

Beam Profile Effects

A measurement of the neutron beam profile and correction for beam profile effects was discussed in [McN00b]. The γ rays emitted from a target are distributed according to the neutron beam profile, which was approximately Gaussian with a 1.27 cm diameter. Since there is more geometric phase space for neutrons further away from the beam center (the area of a ring about the center of width dr is rdr, i.e. is proportional to the distance from the center of the beam profile), the efficiency can be sensitive to the effects of the beam profile. Any part of the neutron beam which passes through the fission chamber is counted, but are not equally likely to result in an observed γ ray.

To determine how the efficiency decreases for detecting γ rays as the source moves away from the center, Ref.[McN00b] performed a series of MCNP calculations for rings of source material 0.1 inches in thickness. For example, the first calculation was for source material evenly distributed from $0 < r < 0.1$ in, the next calculation was for source material evenly distributed from $0.1 < r < 0.2$ in, and so on. It was determined from the flux-weighted beam profile that the majority of the neutrons in the beam were located approximately 5 mm from the center of the beam spot. At this location, the correction factor was determined to be about 10% with a minor dependence on γ-ray energy.

We performed a similar simulation using 1000 keV γ rays for rings of source material 1 mm in thickness using MaGe. The efficiency was calculated relative to a point source. The results of the simulation are shown in Fig. 6.11. The relative efficiency is constant, with less than 2% variation to a ring radius of about 14 mm at which point we expected that γ rays would be significantly attenuated by the lead collimators and BGO shields. We therefore did not include a correction for the beam profile effects.

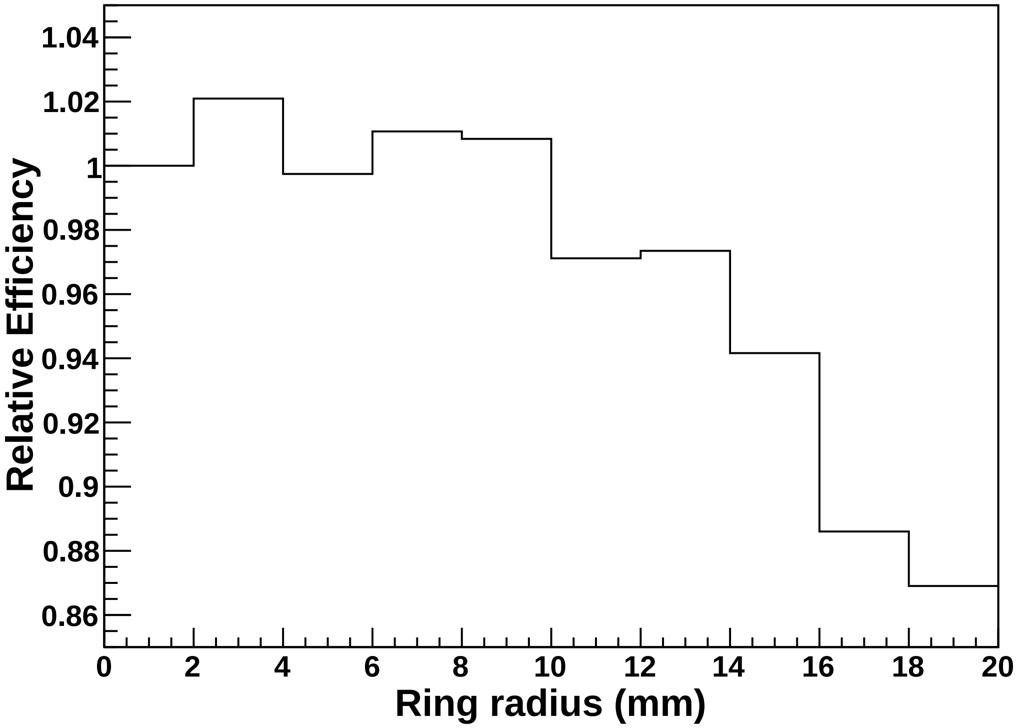

Figure 6.11: The efficiency of GeQ for 1000 keV γ rays distributed in 2-mm thick rings relative to a point source.

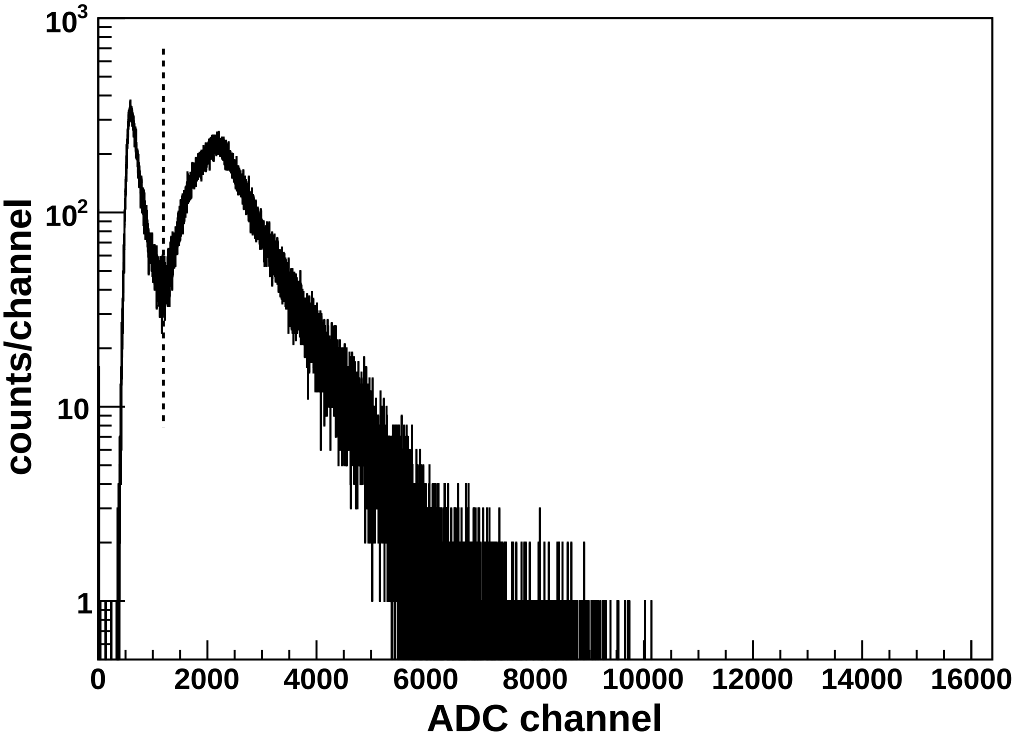

Figure 6.12: A sample ADC spectrum for the ^{238}U fission chamber summed over all neutron energies from 1 to 100 MeV. The peak on the left is from α-particle detection and the peak on the right is from fission fragments. A cut was placed at the dashed line to exclude α-particle events from the neutron flux analysis.

6.4.4 Neutron Flux

The ionization signal from an fission fragment produced in the ^{238}U(n, f) reaction was read out through a fast preamplifier into an ADC as described in Section 5.4. The pulse-height is proportional to the energy loss in the gas. An example pulse-height spectrum, shown in Fig. 6.12 shows two peaks, the lower one originating from α-particle detection and the higher one from fission fragments. A cut was placed on this spectrum during offline analysis to exclude α-particle events. Uncertainty in the placement of the cut had no effect on the determination of the flux.

Following Ref.[Wen93], the neutron flux $I(E_n, \theta)$ is parameterized by defining $I(E_n, \theta)dE_n d\Omega$

to be the number of neutrons per proton micropulse emitted in an energy bin dE_n, centered at a neutron energy E_n, into a solid angle $d\Omega$, centered at an angle θ with respect to the incident proton beam direction. The neutron flux can then be obtained from $N_f(E_n)\Delta E_n$, the number of fission events in a bin of central energy E_n and width ΔE_n by

$$N_f(E_n)\Delta E_n = I(E_n, \theta) \times n_{\mu p} \times \Delta\Omega \times \sigma_f \times \Delta E_n \times \epsilon_f \times \rho_f \tag{6.14}$$

where $n_{\mu p}$ is the number of micropulses and $\Delta\Omega$ is the solid angle of the neutron beam with respect to the neutron source. Because the fission chamber is directly upstream from the detector, the number of micropulses and solid angle are the same as what is seen by the detector during an experiment. It is more convenient to drop these terms from the calculation and to consider the integrated flux over a given energy bin. The ^{235,238}U neutron-induced fission cross sections σ_f are known to better than 5% up to 200 MeV. The areal density of the number of ^{235,238}U deposited on the foil ρ_f was calculated from collimator (beam) size and the deposit thickness of approximately 400 μg/cm^2. The detection efficiency ϵ_f was approximately 98%. The difference from unity is due to some of the fission fragments being emitted close to 90° and either not depositing energy in the fission chamber or having a pulse height below the software cut [Seg46, Car74].

The fission chamber data were processed identically to the HPGe data. The binning on the neutron energy axis was chosen to be the same as for the γ-ray data so that the yields could easily be compared. The time resolution of the fission chambers was better than for the HPGe detectors - 9.5 ns full width at half maximum for the ^{238}U foil. The number of counts in the fission chamber was determined by integrating the ADC spectrum to the right of the threshold cut shown in Fig. 6.12. The integrated neutron flux determined from Equation 6.14 is shown in Fig. 6.13.

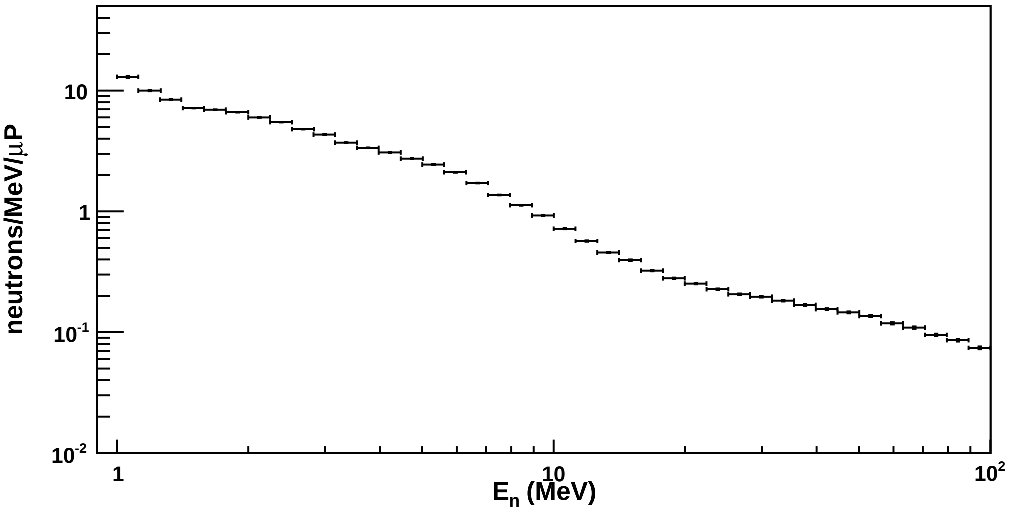

Figure 6.13: The neutron flux per micropulse measured with the fission chamber upstream from the GEANIE array.

6.4.5 Live Time

The fractional live times were determined by dividing the number of converted ADC signals by the number of Compton suppressed ADC scalers. The scalers themselves have essentially no dead time; they can sustain rates up to 30 kHz with a dead time less than 0.1%. The dead time in the pulser channel was 18% due to ADC conversion and other losses in the electronics. The dead time in the fission chambers was about 45%. Although the dead time for the HPGe detectors was more significant (> 50 %) due to backgrounds from scattered neutrons and the γ flash, the beam-induced detector rates were low enough that the energy-dependent dead time effects were negligible. The total detector dead time was determined from the unweighted average of the individual detector dead times.

6.4.6 Angular Distribution

The angle-integrated cross section may be calculated from the angular distribution if it is known, however a measurement of the angular distribution of γ rays is not optimal with GEANIE since there are only six unique detector angles in the array. The angular distributions were measured at GEANIE for ^{238}U$(n, xn\gamma)$ and deviations from an isotropic assumption were mostly less than 5% [Fot01]. Because few angles were measured, we relied on other measurements and modeling to correct for angular distribution effects.

The AVALANCHE code was used to calculate the angular distribution for all of the measured transitions. The routines in AVALANCHE were developed to calculate side-feeding intensities and spin-state orientation parameters corresponding to the side-feeding part of the m-substate population in compound nucleus reactions [Cej93, Cej96], i.e. the quantity σ in Eqn. 2.38. The angular distribution, $W(\theta)$, of emitted photons from a nuclear de-excitation may be expanded in terms of Legendre polynomials:

$$W(\theta) = \sum_{k=even} A_k P_k(\cos(\theta)) \tag{6.15}$$

where the k can only be even due to parity conservation and $k_{max} < 2j_i$ where j_i is the spin of the excited state [Mor76]. The coefficients A_k were calculated according to Section 2.4.2 using the σ value calculated from AVALANCHE. An angular distribution correction factor (C_γ) was determined by comparing the value of the angular distribution function at a particular angle, θ, to an isotropic assumption [W$(\theta) \equiv 1$]. The angular distribution correction at a particular incident neutron energy must be weighted by each detector's efficiency, ϵ_γ and live time, T_γ. The angular distribution correction factor is then given by

$$C_\gamma(E_n) = \frac{\sum_i \epsilon_\gamma^i T_\gamma^i}{\sum_i \epsilon_\gamma^i T_\gamma^i W(\theta_i, E_n)} \tag{6.16}$$

where i runs over all detectors used in the analysis.

The angular distributions computed with AVALANCHE for the $E2$ $2^+ \rightarrow 0^+$

first excited states in ^{40}Ar and ^{20}Ne are shown in Fig. 6.14. As a validation of the AVALANCHE code, the angular distributions were compared with the the available data for several excited at states at $E_n = 3.5$ MeV [Mat65]. Because there were no previous data for $^{20}\mathrm{Ne}(n, n'\gamma)^{20}\mathrm{Ne}$, we attempted to measure the angular distributions by fitting the data for each individual detector using Eqn. 6.15. The angular distribution determined from the data was compared with the angular distribution calculated using the AVALANCHE code. Because there was only a single energy measurement for argon and the statistical uncertainty was large for neon, the AVALANCHE calculations were used to determine $C_\gamma(E_n)$ in all cases. In general, the anisotropy diminished as E_n increased and the angular distribution correction was less than 10%.

6.4.7 Measurement Uncertainties

An uncertainty of 6%, assigned to γ-ray detection efficiency, was derived from the uncertainty in the fit to experimental data over the measured γ-ray energy range. This is consistent with the results from the Monte-Carlo simulation. The uncertainty in the number of target nuclei was 4% for argon and 1% for neon. The uncertainty was mainly due to pressure changes in the gas cell over the course of the experiment. An uncertainty of 2 – 4% was assigned to the neutron flux due to the uncertainty in the measured $^{238}\mathrm{U}(n, f)$ cross section. The cross section is known to about 2% up to 15 MeV and to about 4% up to several hundred MeV. The uncertainty in the neutron energy was based on the time-of-flight cut on the fission chamber data. Based on the maximum deviation from the AVALANCHE calculation and data, a systematic uncertainty in the angular distribution correction of 4% was adopted. An angular distribution correction was not applied to the cross section for the $E_\gamma = 660$ keV $0^+ \rightarrow 2^+$ transition in ^{40}Ar because the γ-ray distribution from an $(n, n'\gamma)$ process is isotropic when $J_i = 0$.

The statistical uncertainty in the fission chamber data was 3 – 4% over the measured

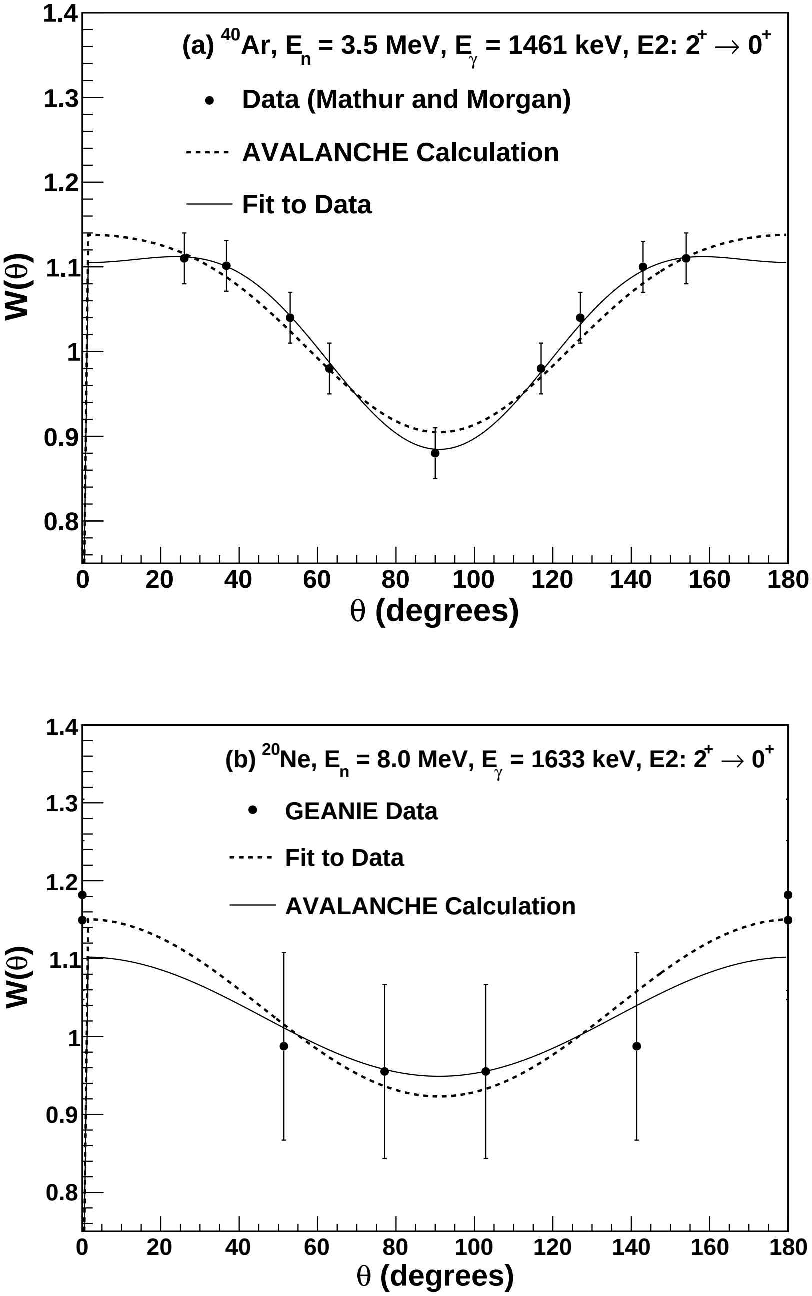

Figure 6.14: The angular distribution of γ rays for the $E2$ $2^+ \rightarrow 0^+$ first excited states in ^{40}Ar and ^{20}Ne.

neutron energy range. The statistical uncertainties in the γ-ray yields were as low as 2% and mainly less than 10%. The statistical uncertainty became more significant as neutron energy increased, and for weakly excited transitions became as high as 23%. The systematic and statistical uncertainties are summarized in Table 6.3.

Table 6.3: GEANIE systematic and statistical uncertainties.

Systematic Uncertainties		
Gamma-ray detection efficiency		6%
Target nuclei		
	Argon	4%
	Neon	1%
Neutron flux		2–4%
Angular distribution		4%
Statistical Uncertainties		
Neutron flux		3 – 4%
γ-ray yield		2 – 23%

6.5 Partial γ-ray Cross Sections

6.5.1 ^{56}Fe Analysis

As a validation of the experiment and analysis techniques, part of each dataset was taken with a 0.127-mm $^{\mathrm{nat}}$Fe foil fixed to each end window of the gas target and the partial γ-ray cross section for the 846.8-keV $2^+ \rightarrow 0^+$ transition in ^{56}Fe was determined. The measured cross section is shown in Fig. 6.15. Our measured cross section was 740 ± 80 mb at $E_n = 15.0 \pm 0.9$ MeV. This value is in good agreement with the cross section of 681 ± 57 mb at $E_n = 14.5$ MeV, measured by Nelson et al. [Nel05].

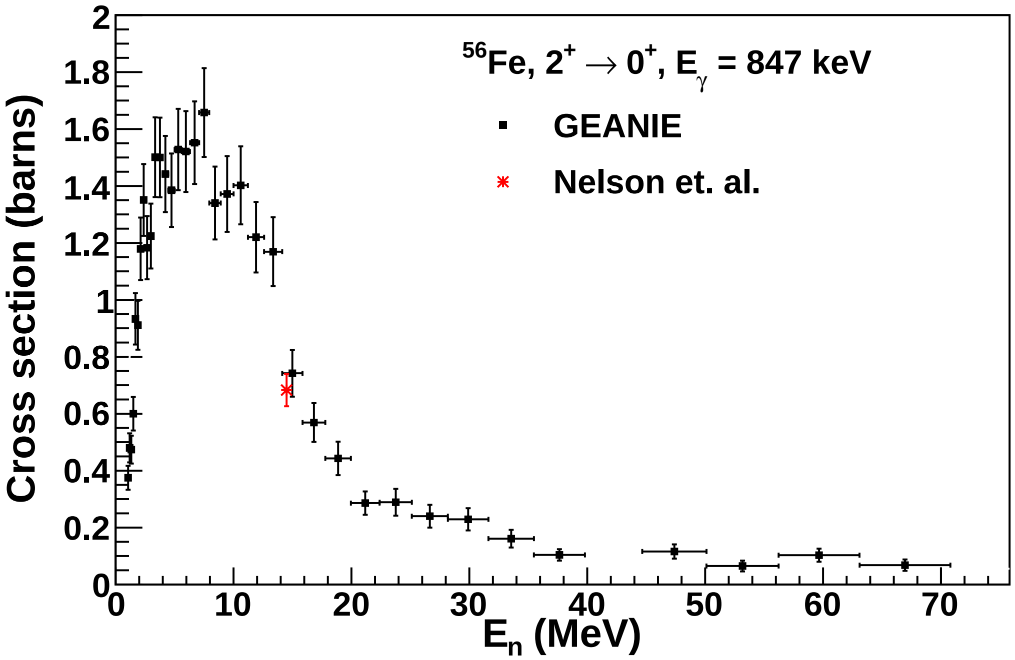

Figure 6.15: Partial γ-ray production cross section for the 846.8-keV $2^+ \rightarrow 0^+$ transition in ^{56}Fe.

6.5.2 Partial γ-ray Cross Sections for $^{\mathrm{nat}}$Ar for $E_n = 1 - 30$ MeV

Partial γ-ray cross sections for six transitions in ^{40}Ar and two transitions in ^{39}Ar were measured from threshold to a neutron energy where the γ-ray yield dropped below the detection sensitivity. The results are shown in Figs. 6.16–6.17 and Tables C.1–C.8. The results were compared to a calculated cross section using the TALYS and CoH$_3$ nuclear reaction codes [Kon08, Kaw03, Kaw10].

Because $^{\mathrm{nat}}$Ar is 99.6 % ^{40}Ar (the balance being ^{38}Ar 0.34% and ^{36}Ar 0.07%), we assumed that only the ^{40}Ar$(n, n'\gamma)^{40}$Ar reaction produced a detectable γ ray from an excited state transition in ^{40}Ar. Similarly, the 250-keV and 1267-keV transitions observed from ^{39}Ar were assumed to have been produced by the ^{40}Ar$(n, 2n\gamma)^{39}$Ar reaction and not a competing reaction channel. A summary of the measured cross sections for argon is shown in Table 6.4.

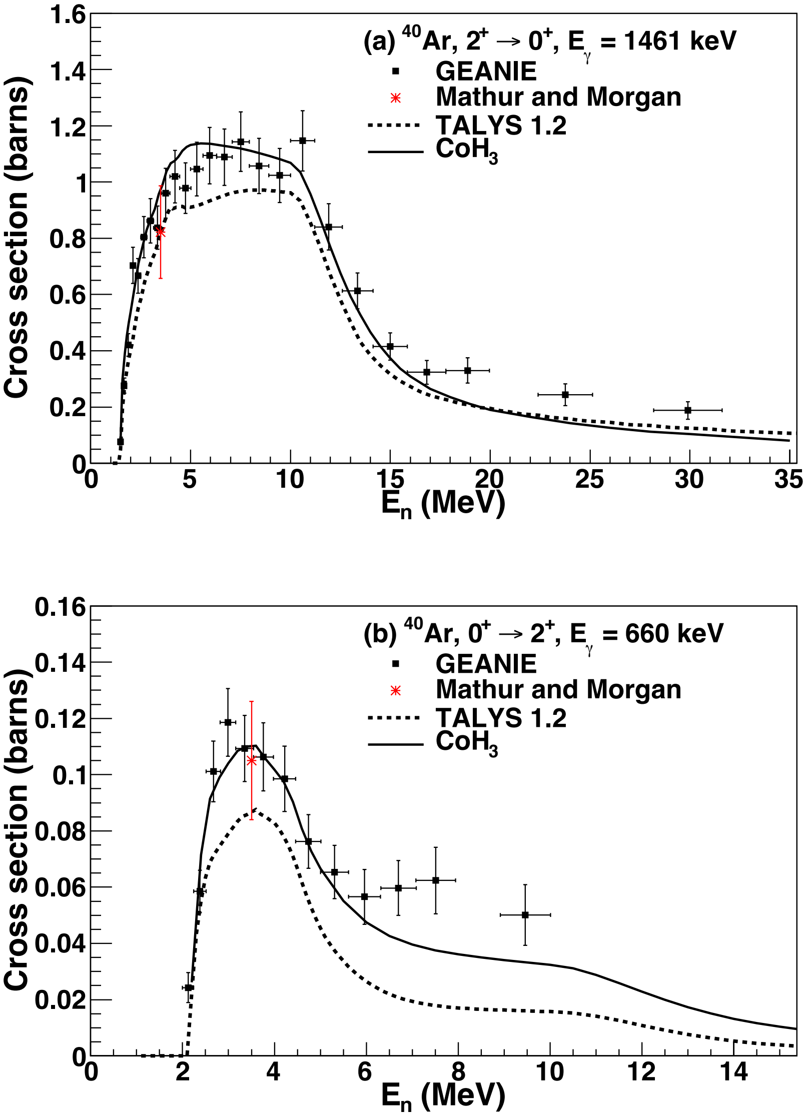

Figure 6.16: Partial γ-ray cross sections for $^{40}\mathrm{Ar}(n, n'\gamma)^{40}\mathrm{Ar}$. The dashed curve is the cross section calculated using the TALYS nuclear reaction code. The solid curve is the cross section calculated using the CoH$_3$ code.

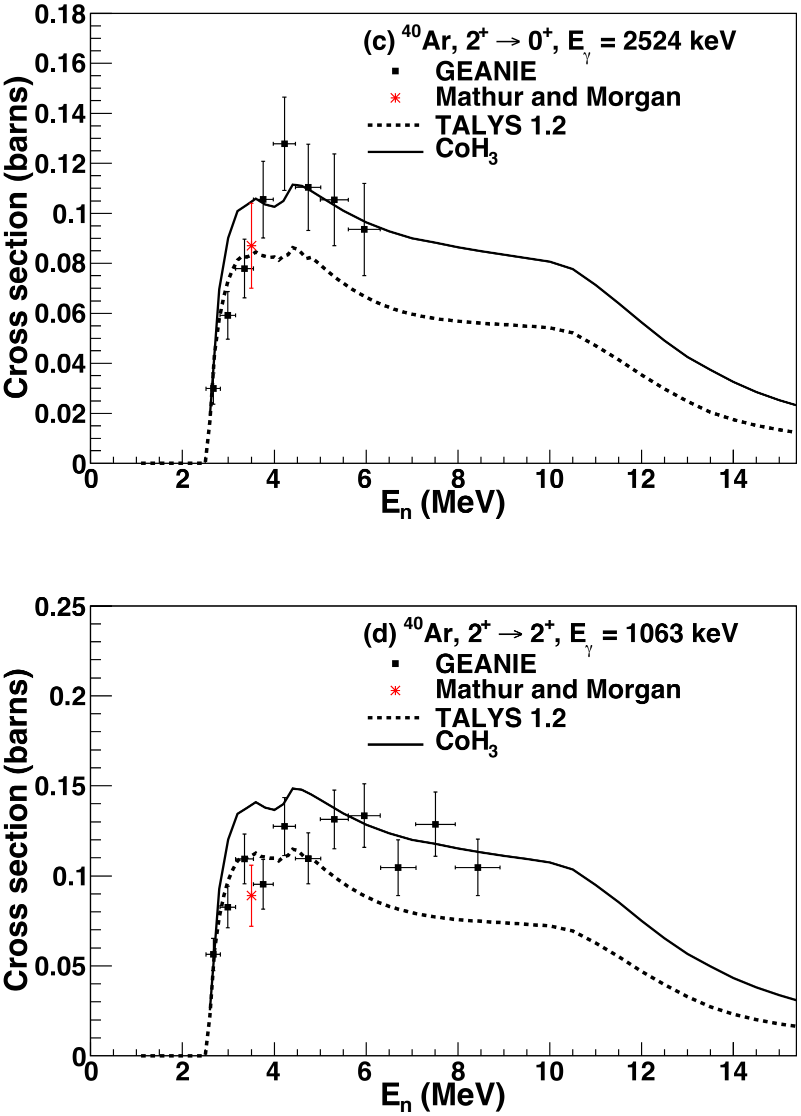

Figure 6.16: (Continued) Partial γ-ray cross sections for $^{40}\mathrm{Ar}(n, n'\gamma)^{40}\mathrm{Ar}$. The dashed curve is the cross section calculated using the TALYS nuclear reaction code. The solid curve is the cross section calculated using the CoH$_3$ code.

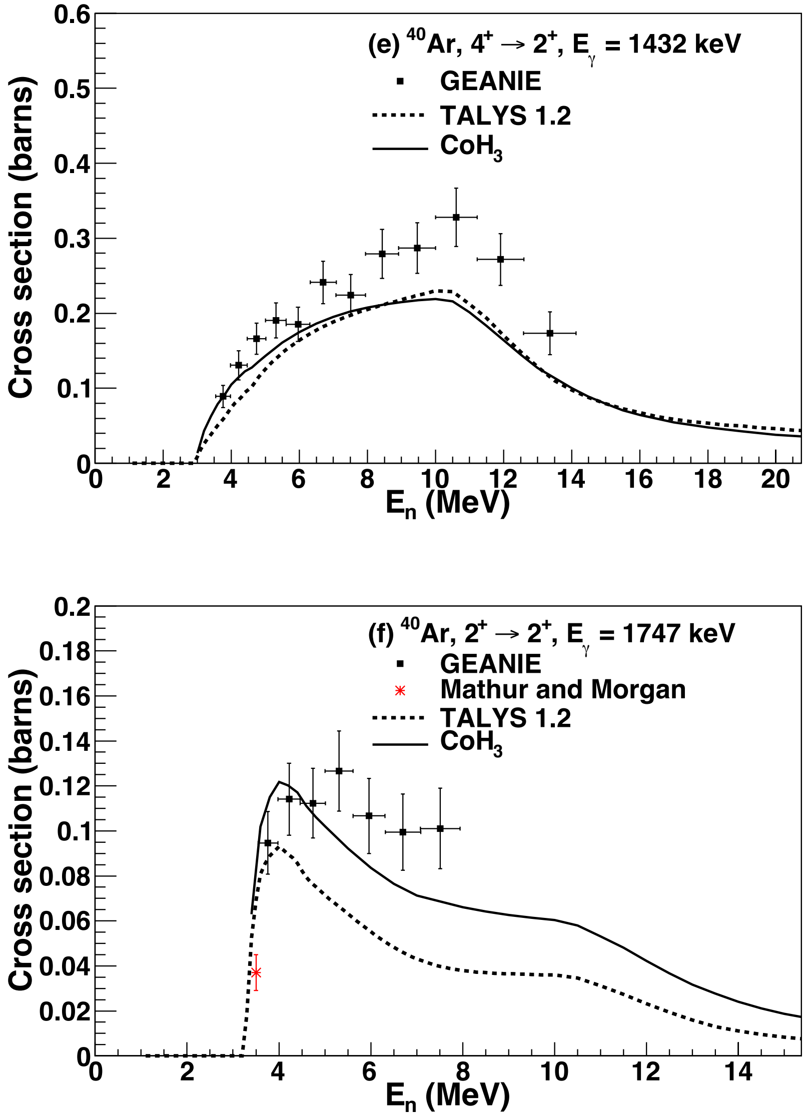

Figure 6.16: (Continued) Partial γ-ray cross sections for $^{40}\text{Ar}(n, n'\gamma)^{40}\text{Ar}$. The dashed curve is the cross section calculated using the TALYS nuclear reaction code. The solid curve is the cross section calculated using the CoH$_3$ code.

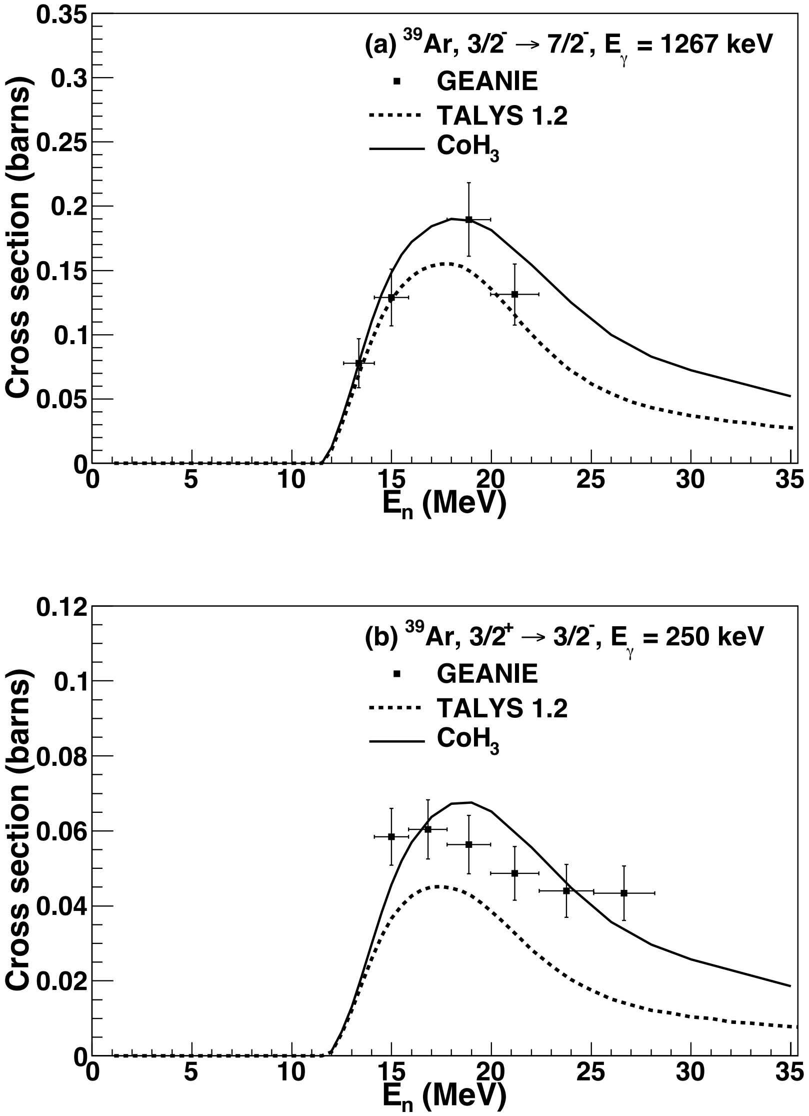

Figure 6.17: Partial γ-ray cross sections for measured transitions in $^{39}\mathrm{Ar}(n, 2n\gamma)^{40}\mathrm{Ar}$. The dashed curve is the cross section calculated using the TALYS nuclear reaction code. The solid curve is the cross section calculated using the CoH$_3$ code.

Table 6.4: Summary of the measured γ-ray production cross sections for argon.

Reaction	Transition	E_γ (keV)	Number of data points	Neutron energy range (MeV)	Cross section range (barn)
$^{40}\mathrm{Ar}(n, n'\gamma)^{40}\mathrm{Ar}$	$2^+ \rightarrow 0^+$	1461	25	1.5 – 29.9	0.08 – 1.1
$^{40}\mathrm{Ar}(n, n'\gamma)^{40}\mathrm{Ar}$	$0^+ \rightarrow 2^+$	660	13	2.1 – 9.5	0.024 – 0.12
$^{40}\mathrm{Ar}(n, n'\gamma)^{40}\mathrm{Ar}$	$2^+ \rightarrow 0^+$	2524	8	2.3 – 6.0	0.030 – 0.13
$^{40}\mathrm{Ar}(n, n'\gamma)^{40}\mathrm{Ar}$	$2^+ \rightarrow 2^+$	1063	11	2.7 – 8.4	0.056 – 0.13
$^{40}\mathrm{Ar}(n, n'\gamma)^{40}\mathrm{Ar}$	$4^+ \rightarrow 2^+$	1432	12	3.8 – 13.4	0.09 – 0.33
$^{40}\mathrm{Ar}(n, n'\gamma)^{40}\mathrm{Ar}$	$2^+ \rightarrow 2^+$	1747	7	3.8 – 7.5	0.10 – 0.13
$^{40}\mathrm{Ar}(n, 2n\gamma)^{39}\mathrm{Ar}$	$3/2^- \rightarrow 7/2^-$	1267	4	13.4 – 21.2	0.08 – 0.19
$^{40}\mathrm{Ar}(n, 2n\gamma)^{39}\mathrm{Ar}$	$3/2^+ \rightarrow 3/2^-$	250	6	15.0 – 26.7	0.043 – 0.060

6.5.3 Partial γ-ray Cross Sections for $^{\mathrm{nat}}$Ne for $E_n = 1 - 16$ MeV

Partial γ-ray cross sections were determined for the $E_\gamma = 1633.7$-keV $2^+ \rightarrow 0^+$ transition in ^{20}Ne and the $E_\gamma = 1274.5$-keV $2^+ \rightarrow 0$ transition in ^{22}Ne. The $E_\gamma = 2613.8$-keV $4^+ \rightarrow 2^+$ transition in ^{20}Ne was visible in the data, but only over a broad energy bin. In the case of ^{20}Ne, most of the levels above the 4966.5-keV 2^- state have a large branching ratio for decay by α-particle emission. TALYS [Kon08] calculations indicate for an 8-MeV neutron, about 35% of the total inelastic cross section will not be seen in γ rays because of competition with the α branch. The results are shown in Figs. 6.18 and 6.19 and Tables C.9 and C.10. The results were compared to a calculated cross section using the TALYS and CoH$_3$ nuclear reaction codes [Kon08, Kaw03, Kaw10].

We assumed that the observed γ ray at 1633 keV was due only to the $^{20}\mathrm{Ne}(n, n'\gamma)^{20}\mathrm{Ne}$ reaction. Considering that neon is 90.48% ^{20}Ne, 9.25% ^{22}Ne and 0.27% ^{21}Ne, the only other reactions that could produce ^{20}Ne are $^{21}\mathrm{Ne}(n, 2n\gamma)^{20}\mathrm{Ne}$ or $^{22}\mathrm{Ne}(n, 3n\gamma)^{20}\mathrm{Ne}$. The low isotopic abundance of ^{21}Ne makes the $^{21}\mathrm{Ne}(n, 2n\gamma)^{20}\mathrm{Ne}$ reaction unlikely to be seen. The $^{22}\mathrm{Ne}(n, 3n\gamma)^{20}\mathrm{Ne}$ does not contribute to the measured cross section because it has a threshold of more than 20 MeV. Similarly, the 1275-keV transition observed from ^{22}Ne was assumed to be from the $^{22}\mathrm{Ne}(n, n'\gamma)^{22}\mathrm{Ne}$ reaction. A summary of the measured cross sections for neon is shown in Table 6.5.

Table 6.5: Summary of the measured γ-ray production cross sections for neon.

Reaction	Transition	E_γ (keV)	Number of data points	Neutron energy range (MeV)	Cross section range (barn)
^{20}Ne$(n, n'\gamma)^{20}$Ne	$2^+ \rightarrow 0^+$	1633	19	1.9 – 15.0	0.19 – 0.65
^{22}Ne$(n, n'\gamma)^{22}$Ne	$0^+ \rightarrow 2^+$	1275	18	1.5 – 10.6	0.08 – 1.21

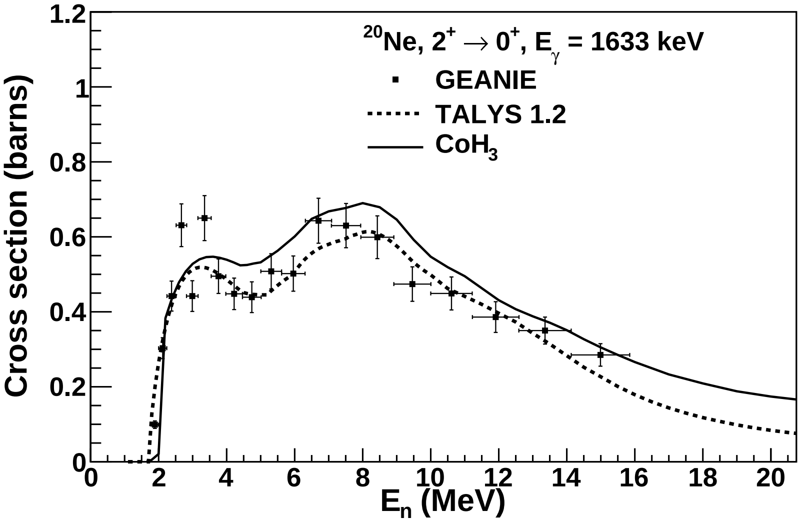

Figure 6.18: Partial γ-ray production cross section for the 1633-keV $2^+ \rightarrow 0^+$ transition in ^{20}Ne. The dashed curve is the cross section calculated using the TALYS nuclear reaction code.

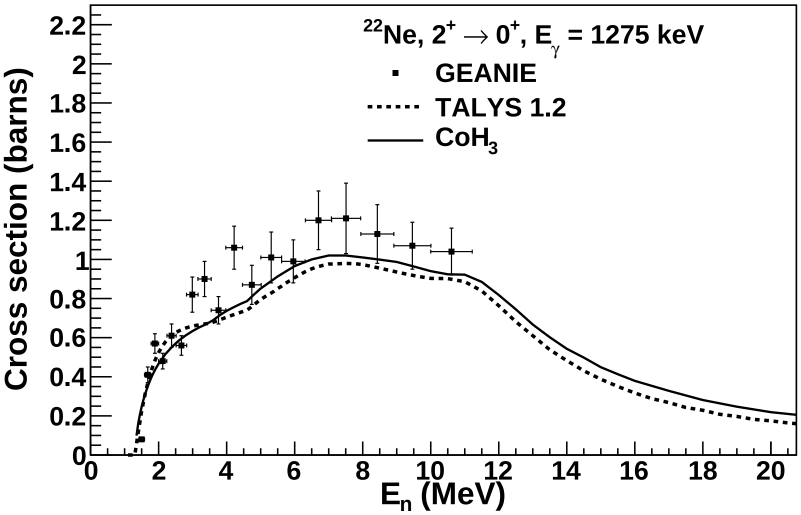

Figure 6.19: Partial γ-ray production cross section for the 1275-keV $2^+ \rightarrow 0^+$ transition in ^{22}Ne. The dashed curve is the cross section calculated using the TALYS nuclear reaction code.

6.6 Conclusions

The TALYS reaction code was used to predict the γ-ray production cross sections for the transitions studied in the present work. The TALYS cross sections were calculated using the default settings, which included a direct reaction model using the optical-model parameterization of Koning and Delaroche [Kon03], a pre-equilibrium model and a compound nucleus reaction model using a Hauser-Feshbach statistical calculation. The TALYS cross sections tend to under-predict the measured cross sections.

In addition to the TALYS calculations, we performed γ-ray production cross section calculations with the CoH$_3$ code [Kaw03, Kaw10], which is similar to TALYS. Both use a Hauser-Feshbach statistical model and a pre-equilibrium model. The statistical model calculations in the relatively light mass region, such as for argon and neon, require careful selection of the discrete levels included, because the nuclear structure and the γ-ray decay scheme significantly impact the calculated γ-ray production cross sections.

For example, in the ^{40}Ar case, the discrete states up to about 4.5 MeV are known in the nuclear structure database including the γ-ray branching ratios from each level. Using these levels directly instead of statistical models would improve the accuracy of the cross-section calculation.

Because the Koning and Delaroche potential is also used in the TALYS default setup calculation, we expect that the two calculations are not so different. The difference in the γ-ray production cross section partly comes from the different modeling of the level density [Kaw06], but largely due to the discrete levels included. TALYS included discrete level information, based on ENSDF for the first 30 levels. The CoH$_3$ code included discrete level information for about 50 levels. In these nuclear reaction codes, when some tentative level assignments exist in the evaluated level scheme, it is often assumed that these levels decay to the ground state directly, which results in underestimation of measured γ-ray production cross sections.

Because neon is a deformed nucleus ($\beta_2 = 0.73$ for ^{20}Ne and $\beta_2 = 0.63$ for ^{22}Ne), the CoH$_3$ code used a Hauser-Feshbach calculation, including transmission coefficients obtained from a coupled-channels calculation [Kaw09]. Although CoH$_3$ reproduced the data more accurately than TALYS, the discrepancy between the CoH$_3$ calculation and data is most likely due to the use of the spherical Koning-Delaroche potential in the coupled-channels calculation. The peaks in the ^{20}Ne cross section around 3 MeV are due to resonances. Neither the TALYS nor the CoH$_3$ calculations reproduce the structure, but rather give the average behavior of the cross section.

Chapter 7

Impact of Cross-Section Measurements on Dark Matter and Double-Beta Decay Experiments

7.1 Cross Sections for ^{76}Ge Double-Beta Decay Experiments

The GEANIE γ-ray data for argon were examined for five neutron energy bins from threshold to 100 MeV for features near the ^{76}Ge $\beta\beta(0\nu)$ region-of-interest at 2039 keV and at 3061 keV, which can produce a double-escape peak at 2039 keV. The γ-ray spectra for neutron energies in the range of 2 to 20 MeV are shown in Fig. 7.1. No features were found in either region. The closest peak to 2039 keV was found around 2052 keV, and is from some combination of the $2^+ \rightarrow 2^+$ $E_\gamma = 2050.5$ keV or $4^+ \rightarrow 2^+$ $E_\gamma = 2054$ keV transitions in ^{40}Ar. Both transitions have a 100% branching ratio for decay to the ground state through the first excited state, and therefore will each produce a coincident 1461-keV γ ray. Because this transition was only observed in the data over a broad energy bin, a cross section could not be measured. TALYS calculations, shown in Fig. 7.2, indicate these cross sections are of a similar size.

Although no peaks were found directly in the regions of interest, upper limits were calculated for the γ-ray production cross section at both 2039 and 3061 keV. The results

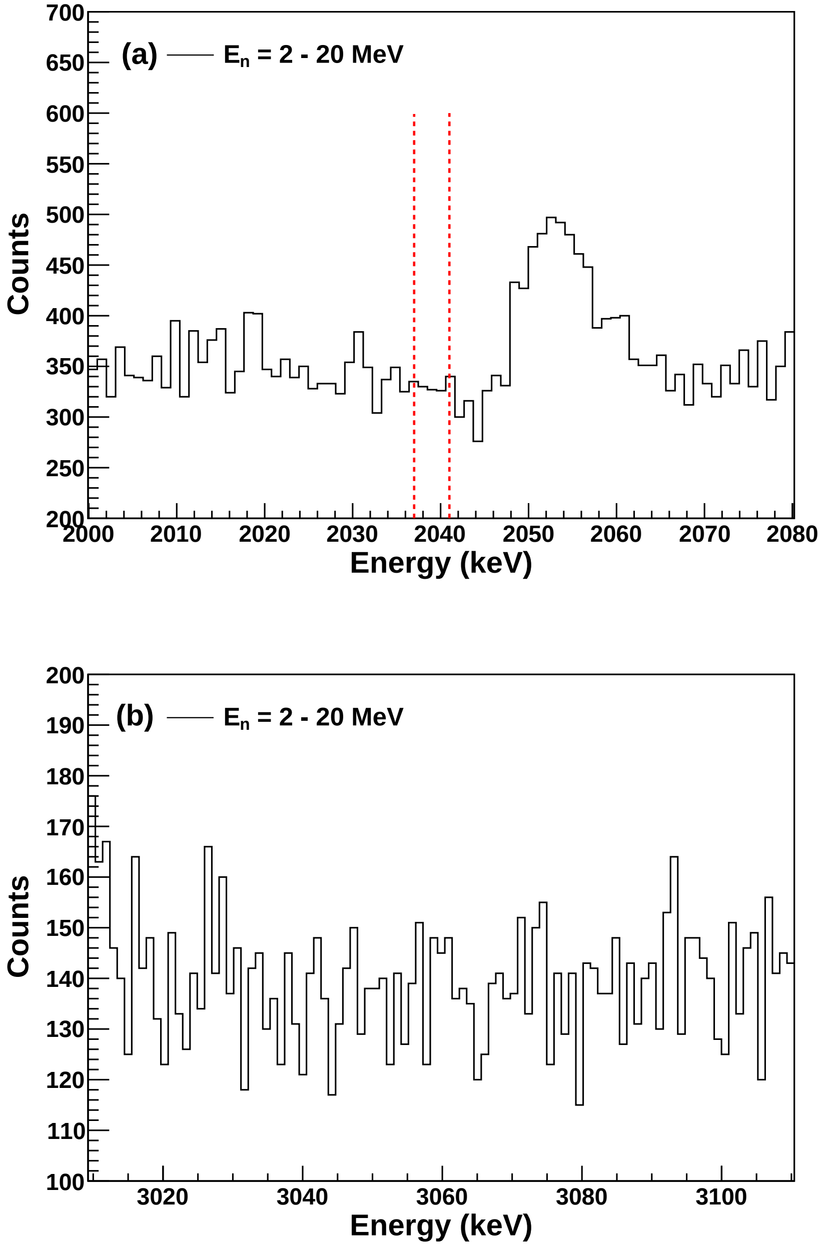

Figure 7.1: Argon γ-ray spectra for neutron energies of 2 to 20 MeV in the ^{76}Ge $0\nu\beta\beta$ regions of interest. (a) The region between the dashed lines indicate a 4-keV window for the ^{76}Ge $\beta\beta(0\nu)$ region-of-interest around 2039 keV. The peak at around 2052 keV is from a combination of the $2^+ \rightarrow 2^+$ $E_\gamma = 2050.5$ keV and $4^+ \rightarrow 2^+$ $E_\gamma = 2054$ keV transitions in ^{40}Ar. (b) The region around 3061 keV, which can produce a double-escape peak at 2039 keV.

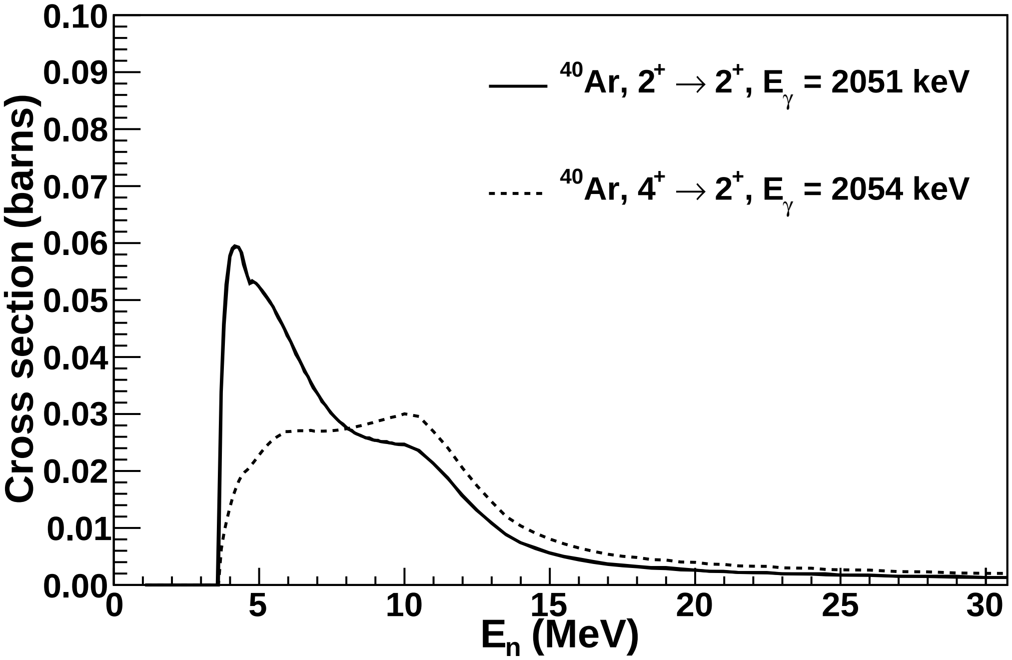

Figure 7.2: TALYS calculations for the $2^+ \rightarrow 2^+$ $E_\gamma = 2050.5$ keV or $4^+ \rightarrow 2^+$ $E_\gamma = 2054$ keV transitions in ^{40}Ar.

are shown in Table 7.1 and Fig. 7.3. These cross sections can be used along with the underground neutron flux to estimate background rates for $\beta\beta(0\nu)$ experiments.

Table 7.1: Upper limits (90% C.L.) for $^{\mathrm{nat}}\mathrm{Ar}(n, xn\gamma)$ reactions. The signal region for the upper limit calculation was chosen to be a window of 2.8σ, where σ was determined from the measured detector energy resolution ($\sigma = 0.77$ keV at $E_\gamma = 1333$ keV).

	Cross section (mb)	
E_n (MeV)	$E_\gamma = 2039$ keV	$E_\gamma = 3061$ keV
1.58 – 3.98	< 50	< 48
3.98 – 10.0	< 76	< 74
10.0 – 25.1	< 64	< 78
25.1 – 50.0	< 50	< 56
50.0 – 100	< 31	< 31

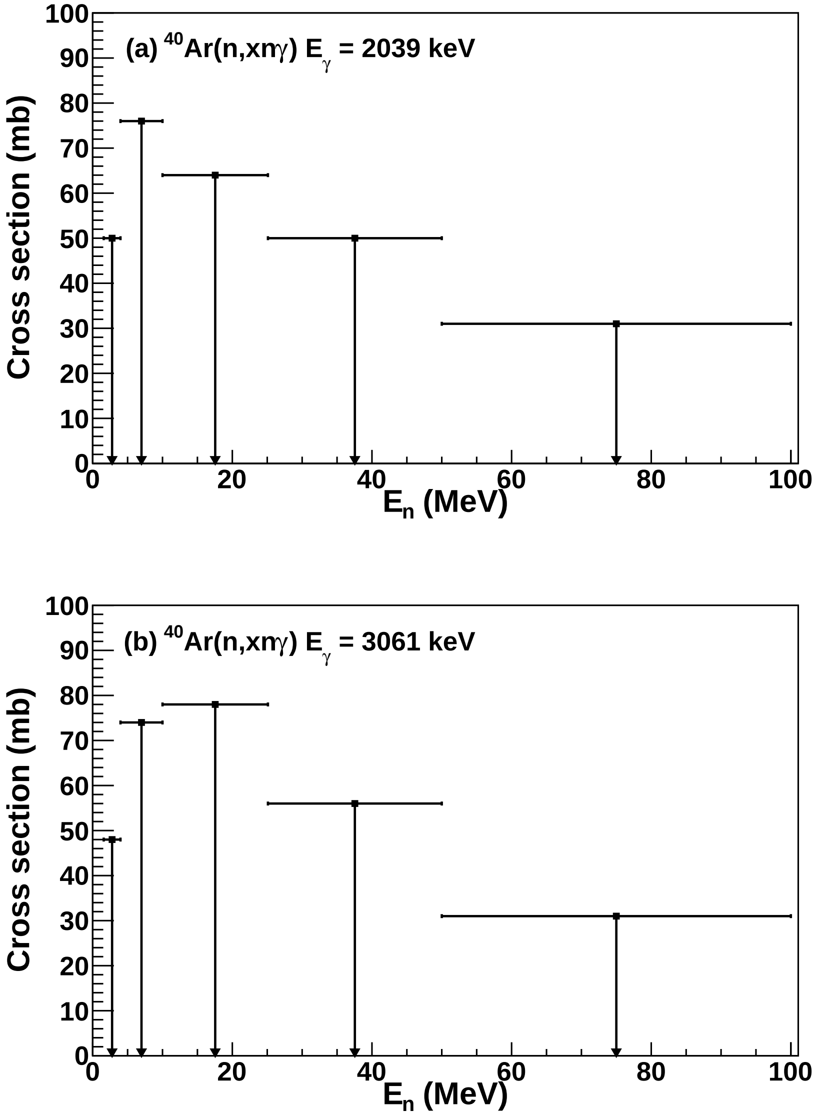

Figure 7.3: Upper limits for $^{\mathrm{nat}}\mathrm{Ar}(n, xn\gamma)$ reactions.

7.2 Evaluation of Neutron Scattering Cross Sections in Geant4 up to 20 MeV

Many direct dark matter searches rely on Monte-Carlo codes such as GEANT4 [Ago03, All06] to simulate experiments and quantify backgrounds. In GEANT4, the `G4NeutronHP` (high precision) class is used to simulate neutron transport below 20 MeV. It relies on G4NDL, a library of data-driven cross sections and angular distributions, mainly from ENDF-6 [Her09] to simulate neutron scattering processes. In the case where no data exist for a given isotope, `G4NeutronHP` will replace it with the cross-section information from the isotope with the nearest Z and A [Men12]. Because cross-section information does not exist for neon in G4NDL library versions up to at least 3.14, `G4NeutronHP` replaces ^{20,22}Ne with ^{22}Na, which has completely different nuclear properties. A linear interpolation between energies is done by `G4NeutronHP` for the data in the G4NDL libraries.

7.2.1 G4NDL Data Files

We have created data files to add to G4NDL for the cross section and angular distributions for elastic scattering of neutrons up to 20.0 MeV from neon and argon. These data files use the cross sections from the optical-model fits to the data presented in Chapter 4. For neon, the optical-model analysis was used from 3.0 to 10.0 MeV. Below 3.0 MeV and from 10.0 to 20.0 MeV, the cross section calculated from the Koning–Delaroche global potential [Kon03] was used, with the exception of from 0.8 to 1.9 MeV. Here, the measurement of Cohn and Fowler [Coh59] was used in order to include the known resonances in ^{20}Ne. The original G4NDL 3.14 cross section and the modified cross section is shown in Fig. 7.4 for the specific neutron energies analyzed in this work. A comparison of the total elastic scattering cross sections is shown in Fig. 7.5. The ^{22}Na cross-section calculation is lower than our cross section for ^{20}Ne by about a factor of two up to about 5 MeV. For energies higher than 5 MeV, these cross sections approach the same value, and agree above about 12 MeV. The agreement between Koning and Delaroche and our modified optical model is good up to about 6 MeV, where our model shows the cross section begins to increase. Because of this, there is a discontinuity at 10.0 MeV, where the cross section transitions back to the calculation from the global potential. We conclude that although the cross-section calculation from the Koning–Delaroche global potential is better than the current ^{22}Na data file used by `G4NeutronHP`, it is not adequate to describe the cross section between 10.0 and 20.0 MeV. Additional measurements would be necessary to constrain our model at energies above 10.0 MeV based on the data. The cross section in this energy range does not affect dark matter background estimates from ^{238}U- and ^{232}Th-induced (α,n) reactions because the neutron spectrum cuts off sharply at about 8 MeV [Mei09a].

For argon, the cross section constructed from the optical-model analysis was used from 0.65 to 20.0 MeV. Below 650 keV, the original cross section, including the resonances, from the G4NDL 3.14 data file for ^{40}Ar was used. This is based on the data of Winters et al. [Win91] and is also included in the ENDF database [Cha06], where most of the G4NDL data is derived from [Men12]. The original G4NDL 3.14 cross section and the modified cross section is shown in Fig. 7.6 for the specific neutron energies analyzed in this work. A comparison of the total elastic scattering cross section are shown in Fig. 7.7.

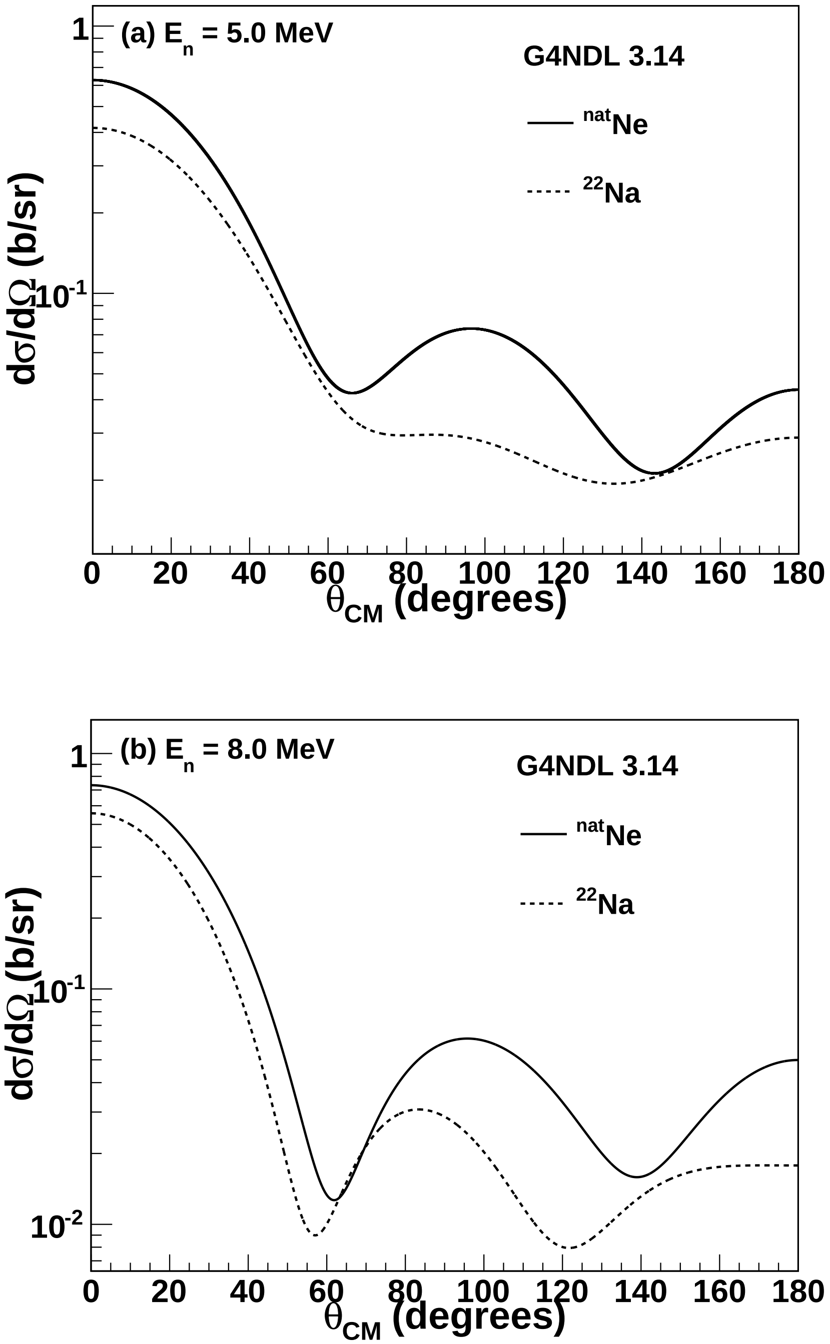

Figure 7.4: The solid curves are the differential elastic scattering cross sections of neutrons from $^{\mathrm{nat}}$Ne at (a) 5.0 and (b) 8.0 MeV added to the G4NDL 3.14 library. The dashed curves are the original G4NDL 3.14 cross sections for ^{22}Na.

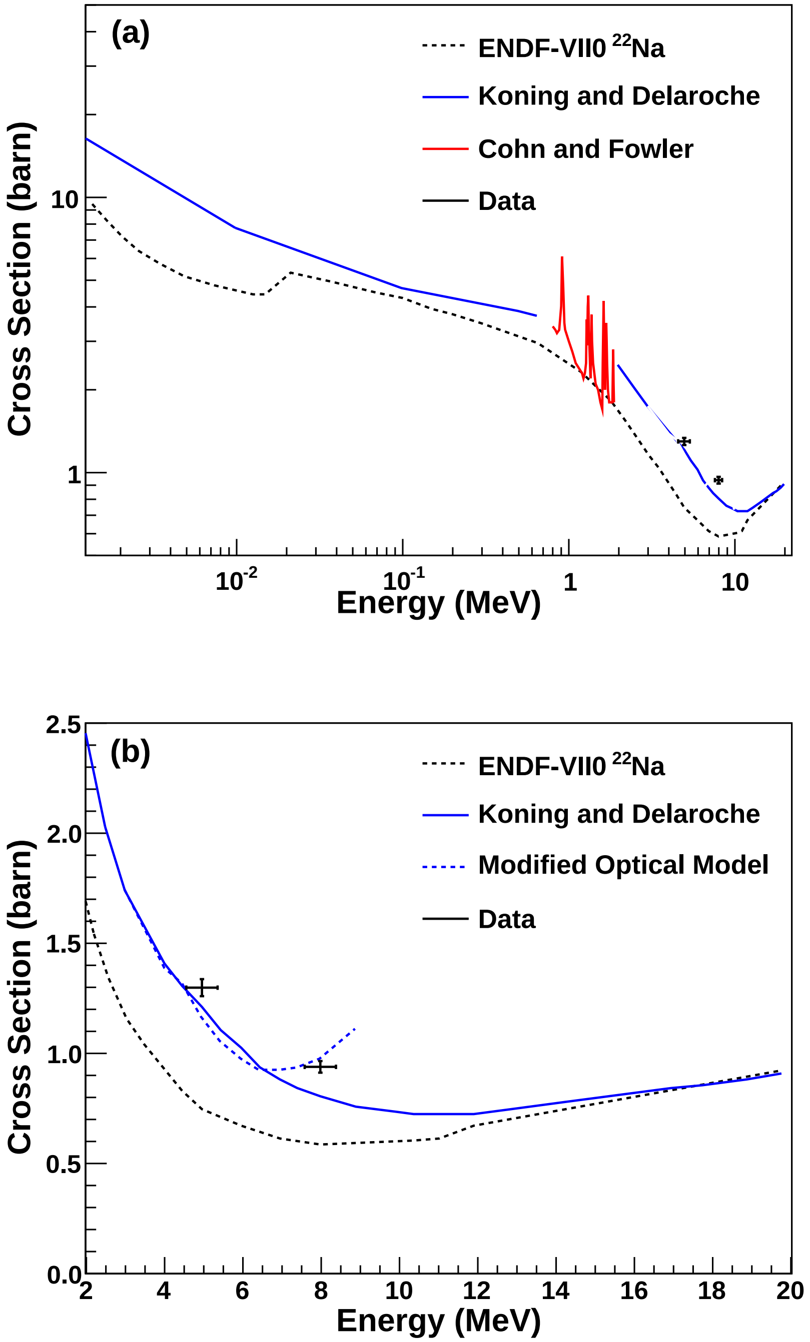

Figure 7.5: A comparison of the original G4NDL 3.14 elastic scattering cross section for ^{22}Na and modified cross section for ^{20}Ne. (a) The dashed black curve is the elastic scattering cross section for ^{22}Na from G4NDL 3.14, which is derived from ENDF [Cha06]. The blue curve is the calculated cross section for ^{20}Ne based on the Koning and Delaroche global optical model [Kon03]. The red curve is the data from Cohn and Fowler [Coh59]. The 5.0- and 8.0-MeV data are also shown. (b) Same as (a) for 3.0 to 20.0 MeV. The dashed blue curve is the cross section calculated from the optical model based on data from this work.

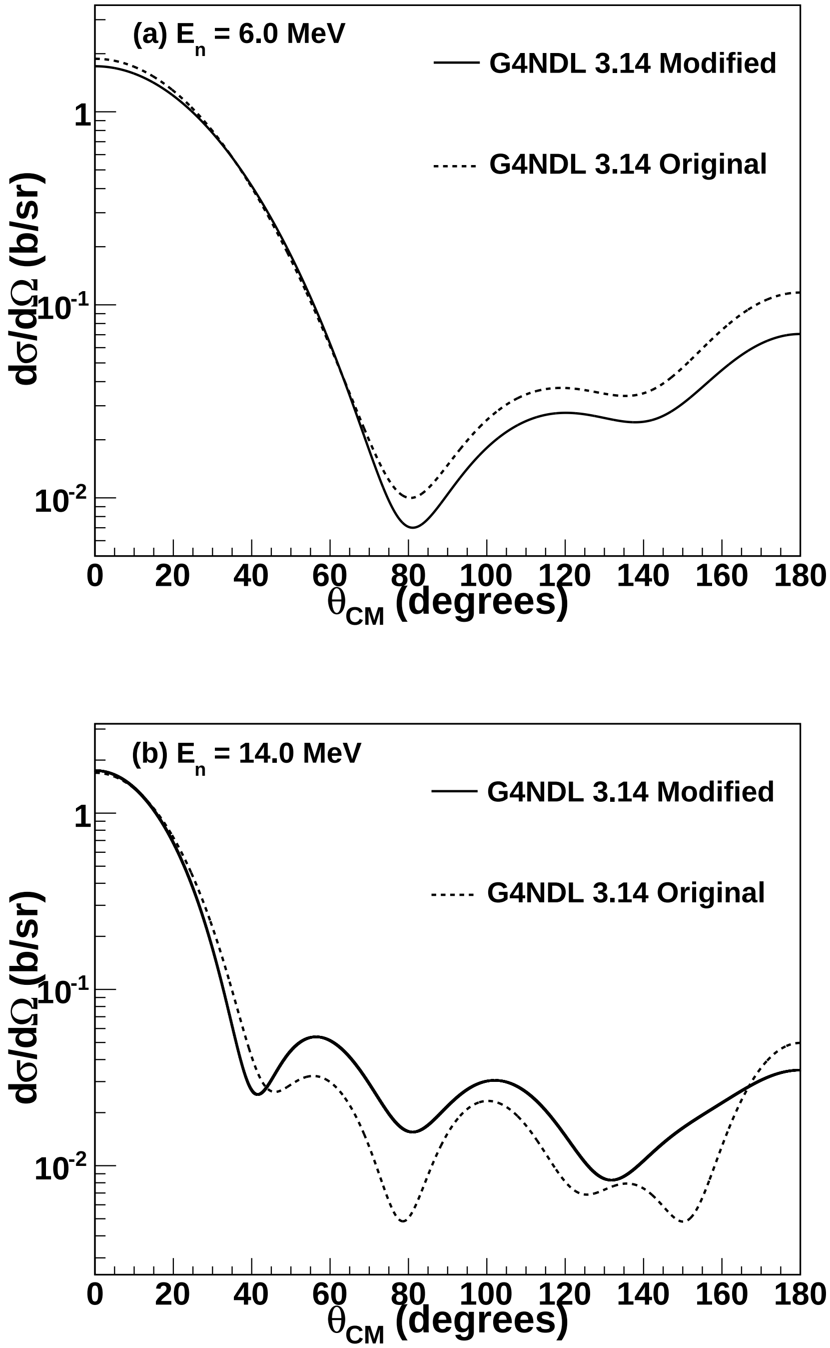

Figure 7.6: The solid curves are the differential elastic scattering cross sections of neutrons from ^{40}Ar at (a) 6.0 and (b) 14.0 MeV added to the G4NDL 3.14 library. The dashed curves are the original G4NDL 3.14 cross sections.

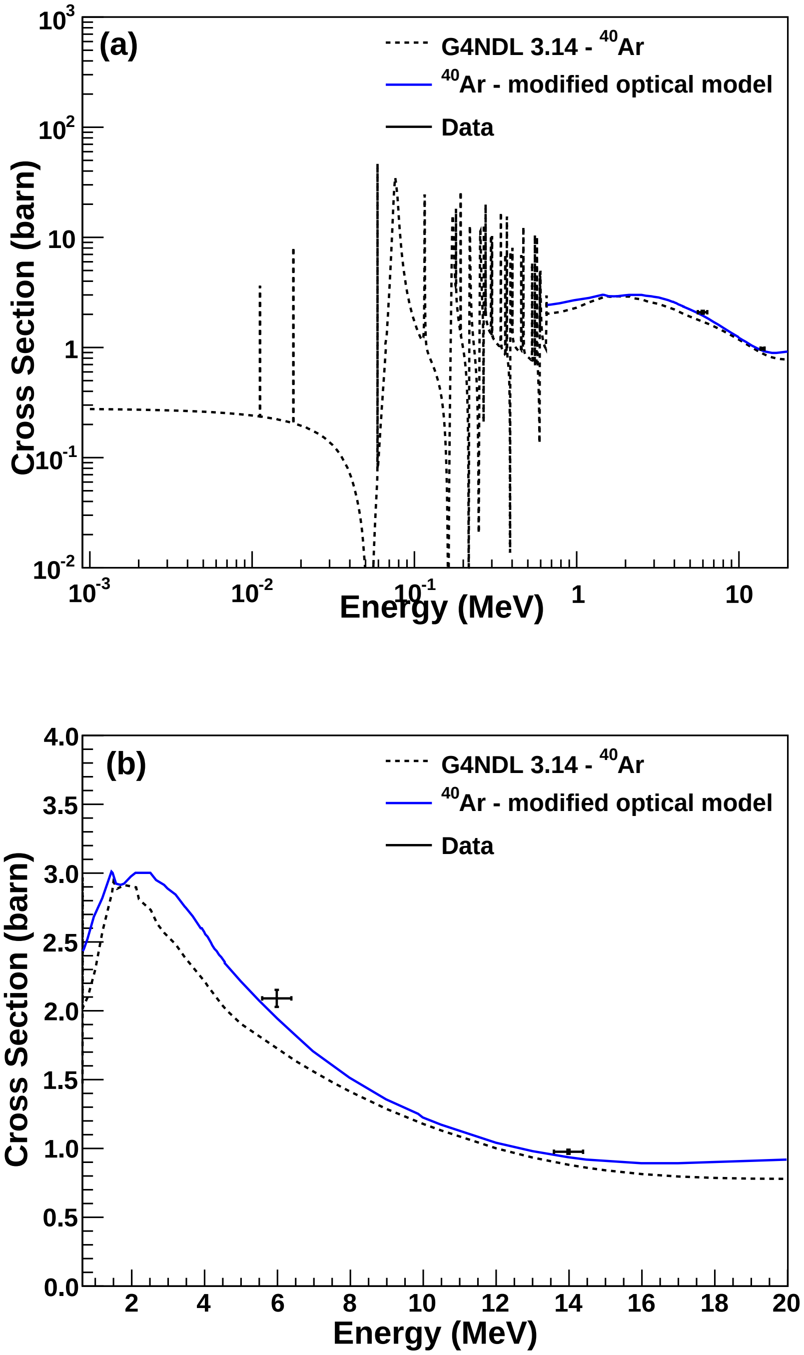

Figure 7.7: A comparison of the original G4NDL 3.14 elastic scattering cross section (dashed black curve) and the modified cross section for ^{40}Ar above 650 keV (blue curve). The 6.0- and 14.0-MeV data are also shown. (a) Below 650 keV, the cross section includes the data from Winters et al [Win91]. (b) Same as (a), for 0.65 to 20 MeV.

7.3 Impacts of Measured Cross Sections on (α, n) Backgrounds in a Liquid Argon or Liquid Neon Dark Matter Experiment

In experiments like DEAP/CLEAN, the most worrisome neutrons come from ^{238}U and ^{232}Th-induced (α, n) reactions in detector and shielding components, specifically in borosilicate PMT glass. The ^{238}U and ^{232}Th-induced (α, n) neutron energy spectrum peaks at about 3–5 MeV and is negligible above about 8 MeV [Mei09a]. A simulation was performed using MaGe [Bos11] and the modified G4NDL files described earlier to investigate the effects of the measured elastic scattering cross section on neutron background estimates in a dark matter detector made from argon or neon.

A simple simulated geometry was created for these background studies to be similar to the MiniCLEAN detector [McK07]. The simulated detector comprised a central sphere made of liquid argon or neon to represent the 45.0-cm radius target volume, see Fig. 7.8. The inner 30.0 cm of the target volume represents the fiducial volume (F.V.). The target volume was surrounded by a 10-cm thick spherical shell of acrylic and a liquid argon or neon buffer volume. Surrounding the buffer volume was the PMT array, which was represented by a 4.5-mm thick spherical shell of borosilicate glass. The thickness of the glass was chosen so the mass was 72 kg, equivalent to the actual MiniCLEAN detector [Him08]. Surrounding the PMT array was a stainless steel inner vessel, a vacuum region and a stainless steel outer vessel.

The neutron production rate in the borosilicate glass was estimated using the known radio-assay values for ^{238}U and ^{232}Th [Fen10] combined with the ^{238}U- and ^{232}Th-induced $^{\mathrm{nat}}$B(α, n) neutron yields [Mei09a]. A summary of the calculation is shown in Table 7.2. It was assumed that borosilicate glass is 10% B_2O_3 by mass. We predict about 48,500 neutrons/year due to $^{\mathrm{nat}}$B(α, n) reactions in the PMT glass using our simple geometry model. This is a reasonable estimate compared to the prediction of

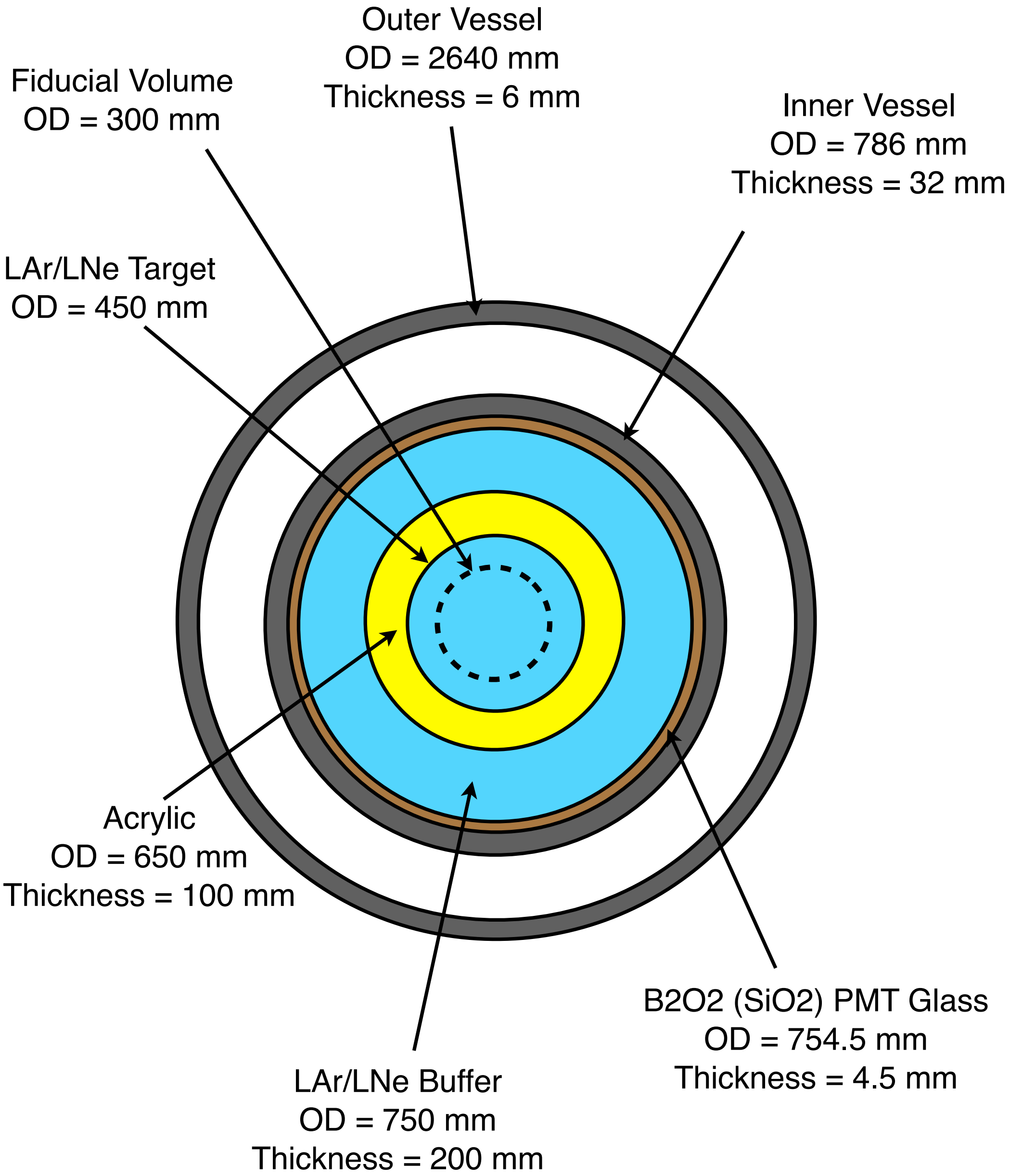

Figure 7.8: A simple model geometry (not to scale) representing the MiniCLEAN detector to be used for neutron background studies. The inner 30.0 cm of the target volume represents the fiducial volume. A drawing of the actual detector is shown in Fig. 1.6.

about 42,000 neutrons per year as stated in Ref. [Him08], which was calculated using a slightly different value for the amount of B_2O_3 in the detector.

Table 7.2: Calculation of the ^{238}U- and ^{232}Th-induced $^{\mathrm{nat}}\mathrm{B}(\alpha, n)$ yields in borosilicate PMT glass using a simple MiniCLEAN geometry model.

	PMT assay results	$^{\mathrm{nat}}\mathrm{B}(\alpha, n)$ yield	neutrons/year
^{238}U	0.1397 ppm	46.5/ppm/g/y	33072
^{232}Th	0.2460 ppm	12.3/ppm/g/y	15431
Total			48503

A primary particle generator was implemented in MaGe to simulate neutrons with the ^{238}U- and ^{232}Th-induced $^{\mathrm{nat}}\mathrm{B}(\alpha, n)$ energy spectrum. We built a cumulative distribution function (CDF) using the evaluation from Ref.[Mei09a]. For the simulations, neutrons were distributed uniformly in the borosilicate glass with the energy distributions shown in Fig. 1.10. Neutrons were emitted from the glass isotropically and were tracked as they propagated through the detector. If a neutron entered the fiducial volume, it's kinetic energy was recorded. The nuclear recoil energy from a neutron that scattered from an argon or neon nucleus was also recorded. These nuclear recoils can mimic a WIMP signal in these types of dark matter experiments. The nuclear recoil energy is dependent on the incident neutron energy and scattering angle. The neutrons also must travel through a buffer volume of liquid argon or neon before entering the fiducial volume. The neutron cross section will therefore affect the energy and direction of the neutrons which enter the fiducial volume. To better understand the direct effects of the elastic scattering cross section, the inelastic processes were turned off for these studies. In a real dark matter experiment, the γ ray a from neutron-induced excitation may be used as a veto provided it does not escape the sensitive volume without interacting.

In each case, 5.0×10^5 neutron events were simulated for both ^{232}Th and ^{238}U-induced $^{\mathrm{nat}}\mathrm{B}(\alpha, n)$ neutrons. The neutron energy spectrum and nuclear recoil spectrum in an argon detector is shown in Fig. 7.9. Simulations using the original G4NDL 3.14 cross section for ^{40}Ar were compared to those based on the cross section constructed from the optical model in this work from 650 keV to 20 MeV. In both cases, below 650 keV, the original G4NDL 3.14 data, based on Winters et al. [Win91], was used. The neutron energy spectrum and nuclear recoil spectrum in a neon detector is shown in Fig. 7.10. Simulations using the original G4NDL 3.14 cross section for ^{22}Na are compared to those based on cross sections for ^{20}Ne shown in Fig. 7.5 for both the global optical model and the modified optical model based on our data.

For neutron-nucleus scattering, the recoil energy, E_r, is related to the neutron energy, E_n, by

$$E_r = \frac{4A}{(1+A)^2}(\cos^2(\theta))E_n, \tag{7.1}$$

where A is the mass number and θ is the scattering angle in the laboratory frame. Table 7.3 shows the numerical results from the simulations. The neutron background was determined using an energy region of interest of 50-100 keV$_r$. The minimum incident neutron energy required to induce a 50-keV nuclear recoil is 275 keV for $A = 20$ and 525 keV for $A = 40$. The first column in the table shows the number of neutrons that enter the fiducial volume per year above the threshold required to induce a 50-keV nuclear recoil. This may be somewhat different than a direct estimate of this quantity for a real experiment because inelastic scattering in the non-active volumes can contribute, although scattering in the acrylic dominates over elastic or inelastic scattering the non-active volumes. The second column shows the rate of nuclear recoils in the F.V. in the 50-100 keV$_r$ region of interest. The simulation did not include a correction for quenching, which accounts for a lower scintillation light yield for a nuclear recoil compared to an electron recoil of the same energy. The quenching factor for both argon and neon is between 25 and 35% for nuclear recoil energies between 50

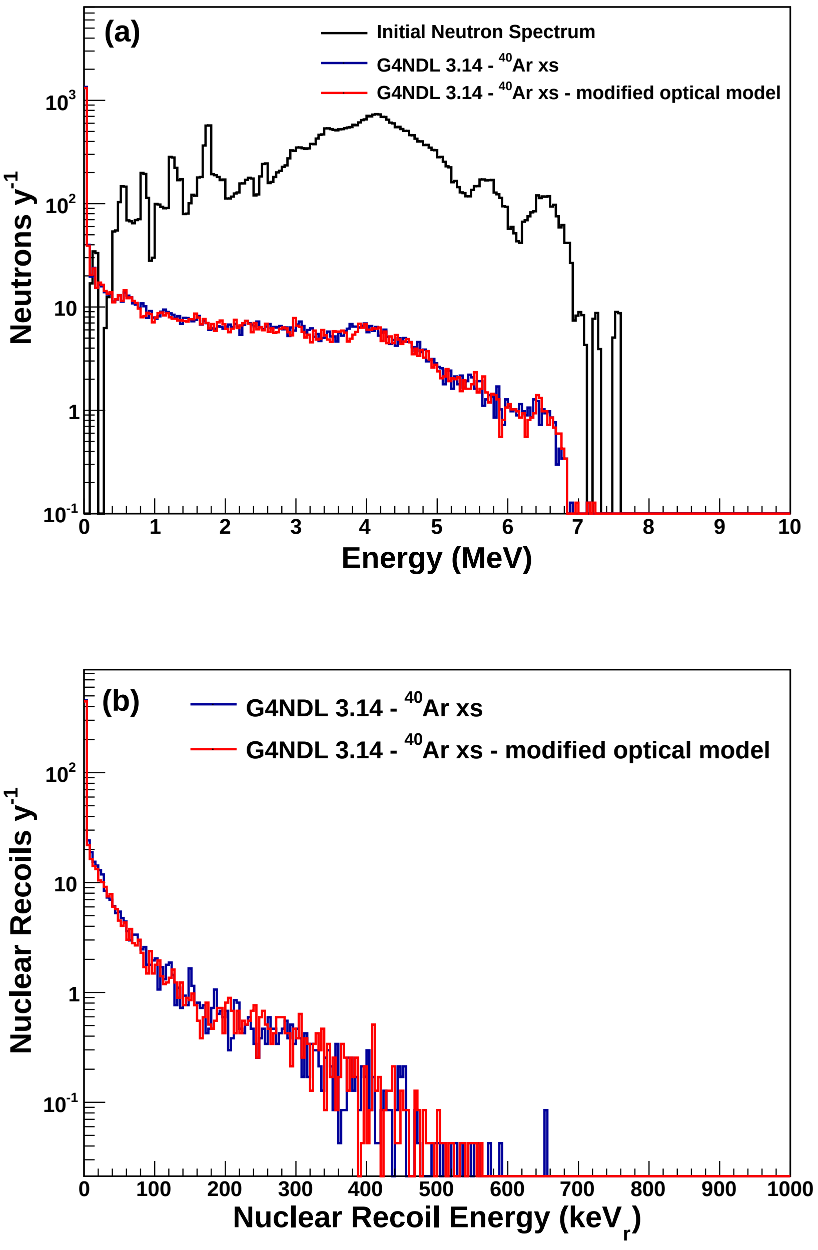

Figure 7.9: (a) Simulated neutron energy spectra for 10^6 ^{238}U- and ^{232}Th-induced $^{\mathrm{nat}}\mathrm{B}(\alpha, n)$ neutrons in the MiniCLEAN fiducial volume made from liquid argon. The initial neutron energy spectrum is shown for comparison. Neutron moderation is dominated by the acrylic. Simulations using the original G4NDL 3.14 cross section are compared to those based on our experimental data. (b) Simulated nuclear recoil energy spectra. Because the differences between the ^{40}Ar cross sections used in the simulations was small, the results appear similar.

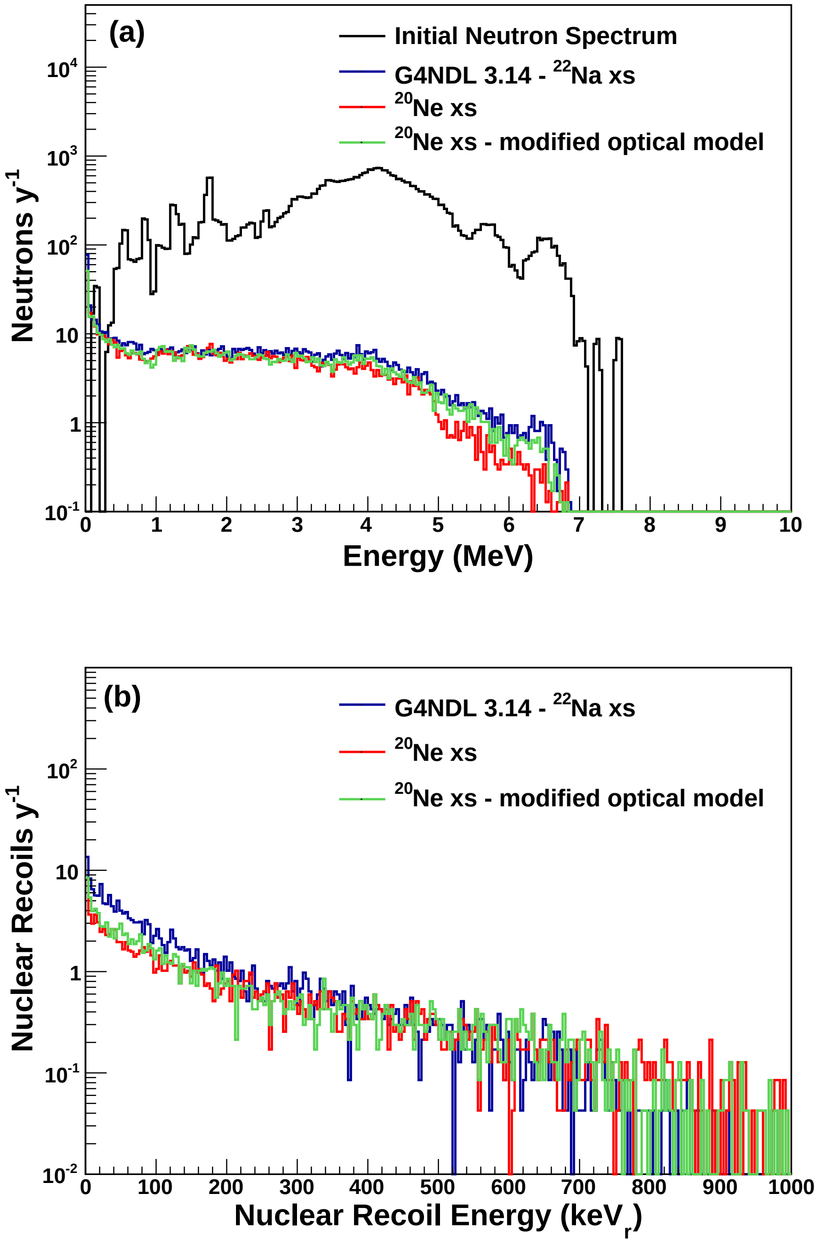

Figure 7.10: (a) Simulated neutron energy spectra for 10^6 ^{238}U- and ^{232}Th-induced $^{\text{nat}}$B(α, n) neutrons in the MiniCLEAN fiducial volume made from liquid neon. The initial neutron energy spectrum is shown for comparison. Neutron moderation is dominated by the acrylic. Simulations using the original G4NDL 3.14 cross section for ^{22}Na are compared to those based on the global optical model for ^{20}Ne and the modified optical model based on our experimental data. (b) Simulated nuclear recoil energy spectra.

and 100 keV [Mei08]. Additional cuts based on neutron capture or multiple scattering may be possible in a real dark matter experiment but were also not included here. Rates were calculated assuming the values from Table 7.2. Quoted uncertainties are based on the statistics of the simulation only.

Table 7.3: Results for 1.0×10^6 ^{238}U- and ^{232}Th-induced $^{\mathrm{nat}}\mathrm{B}(\alpha, n)$ neutrons generated in PMT glass using the simple MiniCLEAN geometry shown in Fig. 7.8. See text for details.

	Neutrons > 525 keV in F.V. (y^{-1})	Nuclear Recoils 50-100 keV$_r$ in in F.V. (y^{-1})
Argon		
G4NDL 3.14	895 ± 13	62 ± 4
G4NDL 3.14 - modified optical model	877 ± 13	57 ± 4
	Neutrons > 275 keV in F.V. (y^{-1})	Nuclear Recoils 50-100 keV$_r$ in in F.V. (y^{-1})
Neon		
G4NDL 3.14 ^{22}Na	848 ± 13	43 ± 3
^{20}Ne	680 ± 11	23 ± 2
^{20}Ne - modified optical model	727 ± 12	28 ± 2

For argon, estimates using both the original G4NDL 3.14 cross section for ^{40}Ar and the values for the modified optical model are in good agreement. For neon, there is a significant disagreement between the estimates using the original G4NDL 3.14 cross section for ^{22}Na and the ^{20}Ne cross section using Koning and Delaroche [Kon03] combined with the resonance data of Cohn and Fowler [Coh59]. Given the differences between the models for the ^{22}Na and ^{20}Ne cross sections, this was not unexpected. Modifying the ^{20}Ne cross section from 3 to 10 MeV, based on the optical-model parameters that best described our data, also affected the background estimate, although the significance is small.

7.4 Inelastic Scattering as a Neutron Veto

Although neutron elastic scattering can mimic a WIMP signal, experiments may be able to use various techniques to discriminate against them. In an experiment like DEAP/CLEAN, the PMT neutron background can be reduced further using event position reconstruction techniques to identify events that multiple scatter. Some of the neutrons may also be tagged using a the prompt γ rays produced from inelastic scattering or a delayed coincidence between the prompt neutron recoil signal and subsequent capture γ rays. For neon, because of the large α-particle decay branch, levels higher than the 4966.5-keV 2^- state in ^{20}Ne are unlikely to be seen through γ-ray emission. However, because the α particle will produce a large amount of scintillation light and will not escape the detector, it may provide a very clean tag for these neutrons.

In addition to using γ rays or α particles from neutron inelastic scattering as a veto, if the rate of inelastic scattering in the detector's sensitive volume is measured via γ-ray detection, the background from neutron elastic scattering may be estimated if both the elastic and inelastic cross sections are known. The ratio of the elastic to inelastic neutron scattering cross sections for ^{40}Ar from 1.5 to 10 MeV are shown in Fig. 7.11, based on this work. The data points are the measured γ-ray production cross section summed over all levels observed in the current experiment. A 15% uncertainty was assigned to the elastic scattering cross section based on the agreement between the model and the ENDF database [Cha06].

The ratio of the elastic scattering to γ-ray production cross sections for ^{20}Ne and ^{22}Ne are shown in Fig. 7.12. In the elastic scattering data, because we were not able to evaluate the contributions to the cross section from ^{20}Ne and ^{22}Ne separately, the cross section was calculated using the Koning-Delaroche global optical model. The γ-ray production cross section corresponds to the experimental data and the error bars represent

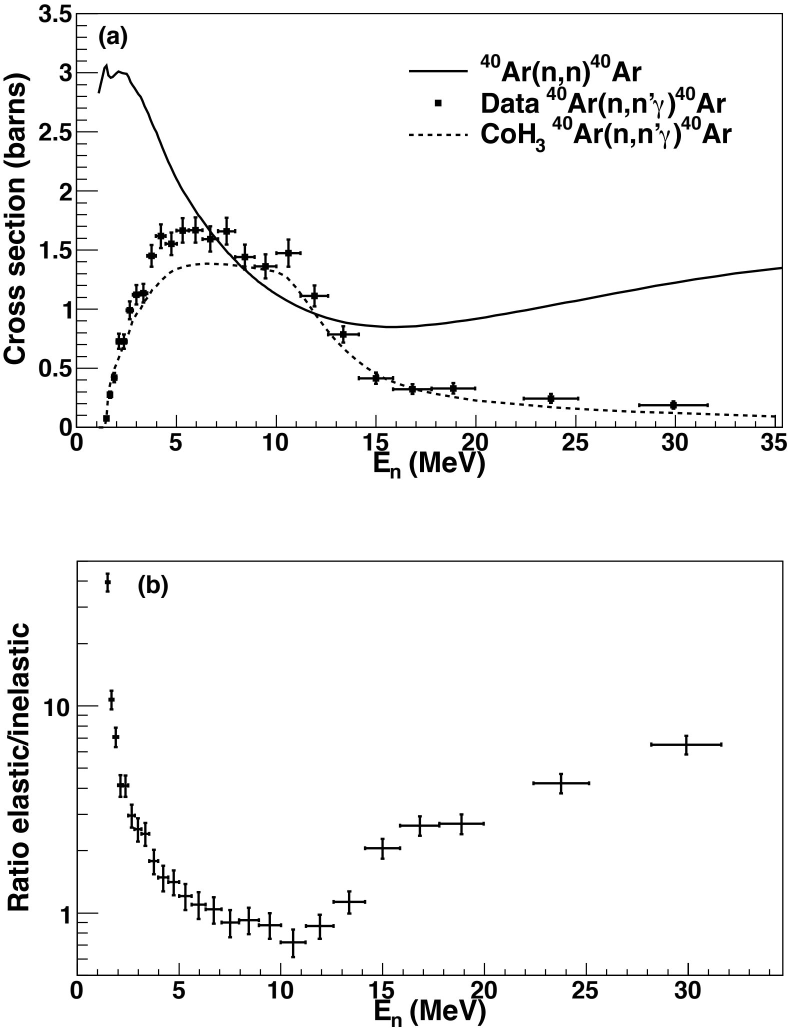

Figure 7.11: (a) The solid curve is the elastic scattering cross section for neutrons incident on ^{40}Ar, calculated from the optical-model analysis presented in Chapter 4. The data points are the measured γ-ray production cross section summed over all levels observed in the current experiment. The dashed curve is the inelastic cross section calculated using CoH$_3$. (b) The ratio of the elastic scattering cross section to the γ-ray production (inelastic) cross section. A 15% uncertainty was assigned to the elastic scattering cross section based on the agreement between the model and the ENDF [Cha06].

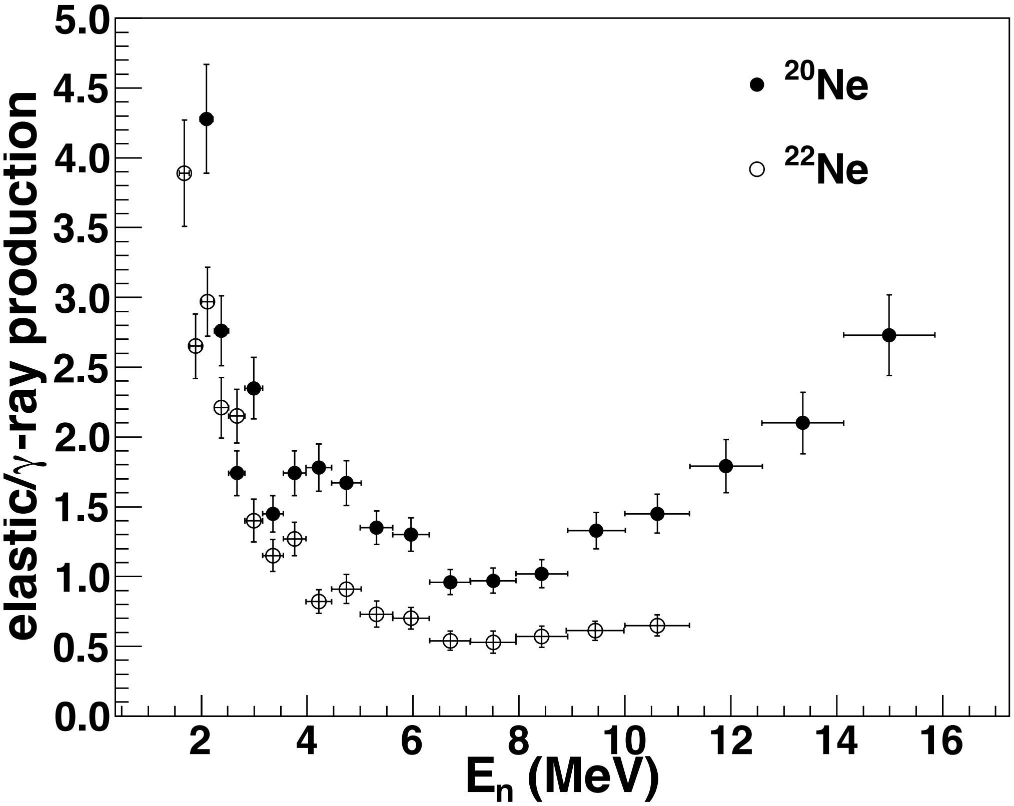

Figure 7.12: The ratio of the elastic scattering cross section to the γ-ray production cross section. The solid circles correspond to ^{20}Ne and the open circles correspond to ^{22}Ne.

only the experiment. Although the ratio of the cross sections becomes large as the neutron energy approaches threshold, only about 15% of the total neutrons produced from ^{238}U and ^{232}Th-induced (α, n) reactions have energies below 2 MeV [Mei09a].

Chapter 8

Conclusion

8.1 Elastic Scattering Measurements

The differential elastic scattering cross section was measured for 5.0- and 8.0-MeV neutrons incident on neon and for 6.0-MeV neutrons incident on argon. These data, along with the 14.0-MeV data for argon from Beach et al. [Bea67], were fit using the spherical optical model and compared to global optical-model predictions. Precise neutron scattering cross sections are required to estimate neutron backgrounds from (α,n) reactions in direct dark matter searches. These cross sections, which were previously unmeasured, are an important component in background estimates of these experiments because simulations rely on available data in the energy range below 20 MeV.

A summary of the elastic cross section for argon and neon is shown in Table 8.1. Optical-model fits to the data at the measured energies are compared to the Koning and Delaroche optical model [Kon03] and the existing G4NDL cross sections. Although argon ($A = 40$) lies at the low end of the reach of the existing optical model, it describes the data fairly well given the agreement with the previous 14.0-MeV measurement for argon from Beach et al. [Bea67]. Our fit to the data agreed with the G4NDL cross-section data to better than 10% from 1 to 20 MeV. Modifying the cross section in

G4NDL based on our data did not produce a statically significant change on neutron background estimates from ${}^{\mathrm{nat}}\mathrm{B}(\alpha, n)$-derived neutrons in a simulated dark matter experiment.

For neon, it was not clear what to expect before performing our measurements. The G4NDL cross-section data for ${}^{22}\mathrm{Na}$ disagrees with the Koning and Delaroche global optical model by almost a factor of two. Our measurement allowed for a determination of a set of optical-model parameters based on experimental data, giving agreement with the Koning and Delaroche global optical model to better than 20% up to 9 MeV. Using the cross section based on our data lowers the expected ${}^{\mathrm{nat}}\mathrm{B}(\alpha, n)$ background in a simulated dark matter experiment by about 35%. Our data significantly improves the current cross-section libraries in the GEANT4 simulation code, adds to the nuclear databases, and provides accurate data for benchmarking global optical models.

Table 8.1: Summary of the elastic scattering cross sections for argon and neon.

	Fit to Data (mb)	Koning and Delaroche (mb)	G4NDL 3.14 (mb)
Argon			
6 MeV	1903	2020	1731
14 MeV	928	995	881
Neon			
5 MeV	1220	1160	745
8 MeV	823	990	584

8.1.1 Future Work

Future measurements are necessary to constrain optical-model parameters for ${}^{20}\mathrm{Ne}$ above 9 MeV. This is not surprising, given that our extrapolation was done based on only two data points. Measurements at 11 MeV and 14 MeV would likely be adequate to derive a set of optical-model parameters that would be applicable over a wider energy range.

Because of the relevance to xenon-based dark matter experiments, elastic scattering of natural xenon should be investigated in the same manner that was described in this work. Because xenon is in a mass range ($Z = 54$) where we expect the optical model to provide a valid prediction for the cross section, the measurement was lower priority than for neon and argon. Nevertheless, as for neon, we are not aware of any existing elastic scattering measurements for fast neutrons.

8.2 Gamma-ray Production Measurements

We have measured neutron-induced γ-ray production cross sections in $^{\mathrm{nat}}$Ar from threshold to as high as 30 MeV, where they fall below our detection sensitivity. Cross sections for six excited states of ^{40}Ar, assumed to be from the $^{40}\mathrm{Ar}(n, n'\gamma)^{40}\mathrm{Ar}$ reaction, were measured. Two cross sections from excited states of ^{39}Ar, assumed to be from the $^{40}\mathrm{Ar}(n, 2n\gamma)^{39}\mathrm{Ar}$ reaction, were also measured. In all cases where a comparison could be made, these data were in agreement with the 3.5-MeV measurement of Mathur and Morgan [Mat65].

Although there was no statistically significant signal in the regions relevant to $\beta\beta(0\nu)$ in ^{76}Ge, upper limits were placed on $^{40}\mathrm{Ar}(n, xn\gamma)$ cross sections for $1 < E_n < 100$ MeV. The measured cross sections and upper limits can be included in Monte-Carlo simulations combined with the expected neutron spectrum to yield background rates for future low-background experiments that will use argon as a detector or shield material. The measured cross sections will also aid in the discrimination of neutron backgrounds in WIMP detection experiments which use argon as a detector, where neutrons are the most dangerous source of background.

We have also measured neutron-induced γ-ray production cross sections for the first excited-state transitions in ^{20}Ne and ^{22}Ne from threshold to as high as 16 MeV, where they fall below our detection sensitivity. The measured cross sections will aid in the identification and discrimination of neutrons in underground experiments that will use neon as a detection material. Because these are the first experimental data for (n, n') reactions in neon, they will enrich the nuclear databases and provide a useful benchmark in a mass region where the optical model is not well constrained.

8.2.1 Future Work

As a follow-up to the neon experiment, it would be good to better understand the relative probability for γ-ray to α-particle emission for neutron-induced excitation of ^{20}Ne because of the relevance to neutron tagging in a dark matter experiment. Cross sections for $(n, n'\alpha)$ reactions are typically measured using the activation technique [Pu03], however, this is not possible in our case because of the stability of the residual ^{16}O nucleus. The cross sections for excited states may be measured with a time-of-flight spectrometer such as the one described in this work, however, it may be challenging to separate levels close in energy owing to the limited time resolution of the spectrometer. A higher target density would also be necessary to separate the inelastic peaks from background.

As an alternative, if the partial γ-ray production cross sections were known well for the first three excited states in ^{20}Ne, the $(n, n'\alpha)$ component to the inelastic cross section may be estimated using the elastic and total neutron cross sections. If more precise cross-section data are warranted, γ-ray production measurements may also be performed at TUNL, see for example, Ref. [Hut08]. The advantages of such a measurement over GEANIE are smaller statistical uncertainties and a slightly better overall sensitivity. However, a large amount of beam time at TUNL would be required owing to the fact that only a single neutron energy can be measured during an experimental run. Additionally, with the ^{2}H$(d, n)^{3}$He source reaction used at TUNL, incident neutron energies lower than about 4 MeV are not accessible. A study to determine the feasibility for such an experiment at TUNL for ^{136}Xe was performed in 2012 using 8-MeV neutrons [Tor12].

Additional isotopes should also be studied as a part of an ongoing campaign to measure γ-ray production cross sections in target and shielding materials relevant to the low-background physics community. Analyses are planned for data taken for Cadmium Zinc Telluride (CdZnTe) [Sch11b] and ^{76}Ge using GEANIE in 2008 and 2009. Future measurements of $^{136}\mathrm{Xe}(n, xn\gamma)$ and $^{130}\mathrm{Te}(n, xn\gamma)$ may also be of interest to the EXO [Aug12] and CUORE [Bel10] collaborations.

8.3 Looking Ahead

There are a number of additional experiments that may be done to further understand the neutron-induced background in dark matter and neutrinoless double-beta decay experiments. A natural extension to the measurement of cross sections for γ-ray production from excited-state decays using fast neutrons is to measure the thermal neutron capture cross sections. Neutrons that thermalize within a detector may produce specific γ rays at energies dangerous to $\beta\beta(0\nu)$ experiments. These capture signals may also provide an additional veto for neutrons in dark matter experiments. The Detector for Advanced Neutron Capture Experiments (DANCE) [Hei01] at LANSCE is a 162-crystal 4π $\mathrm{BaF_2}$ detector for calorimetrically detecting γ-rays following a neutron capture. A proposal is currently submitted to perform such a measurement with a ^{136}Xe target [Kau12].

Additional reactions relevant to cosmogenic isotopes may also be of interest. For example $^{40}\mathrm{Ar}(n,p)^{40}\mathrm{Cl}$ produces radioactive ^{40}Cl. This particular reaction cross section was recently measured by Ref. [Bha12] for estimating backgrounds in argon-based $\beta\beta(0\nu)$ and dark matter experiments.

Appendix A

The ^{232}U and ^{238}U Decay Chains

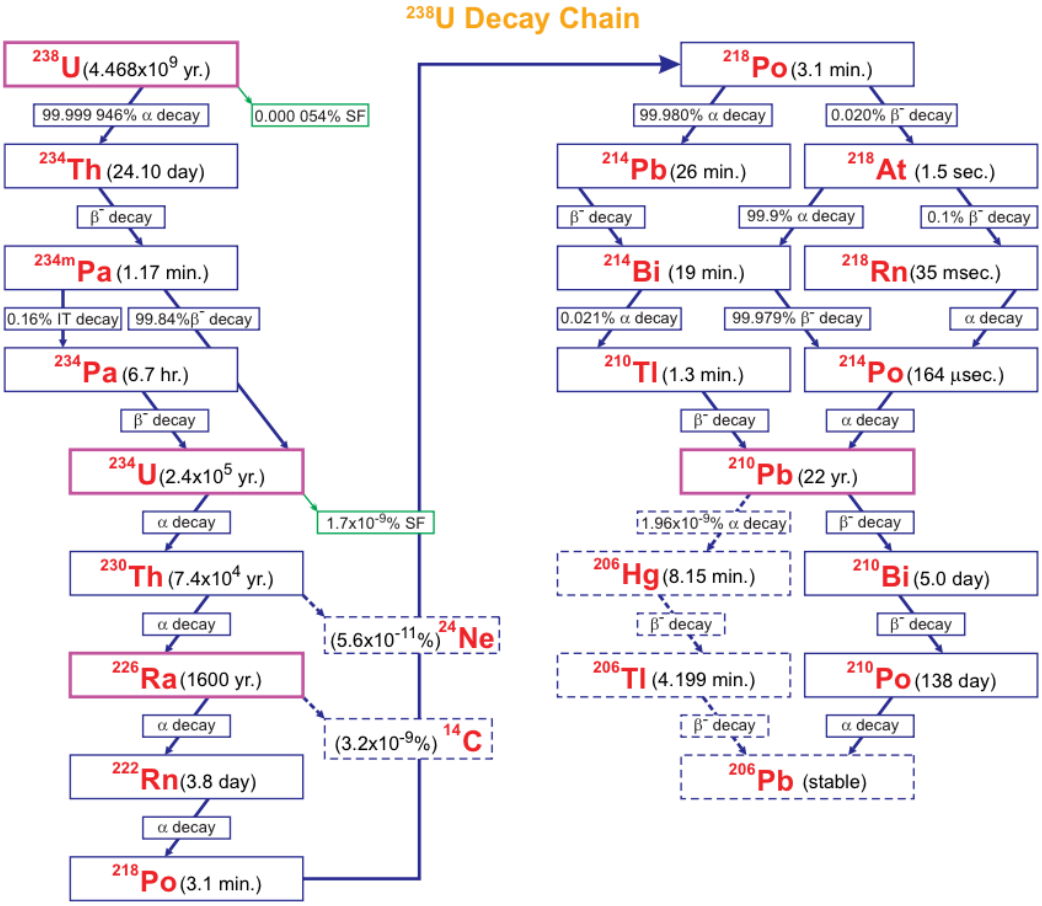

Figure A.1: The ^{238}U decay chain. Figure from `radiochemistry.org`.

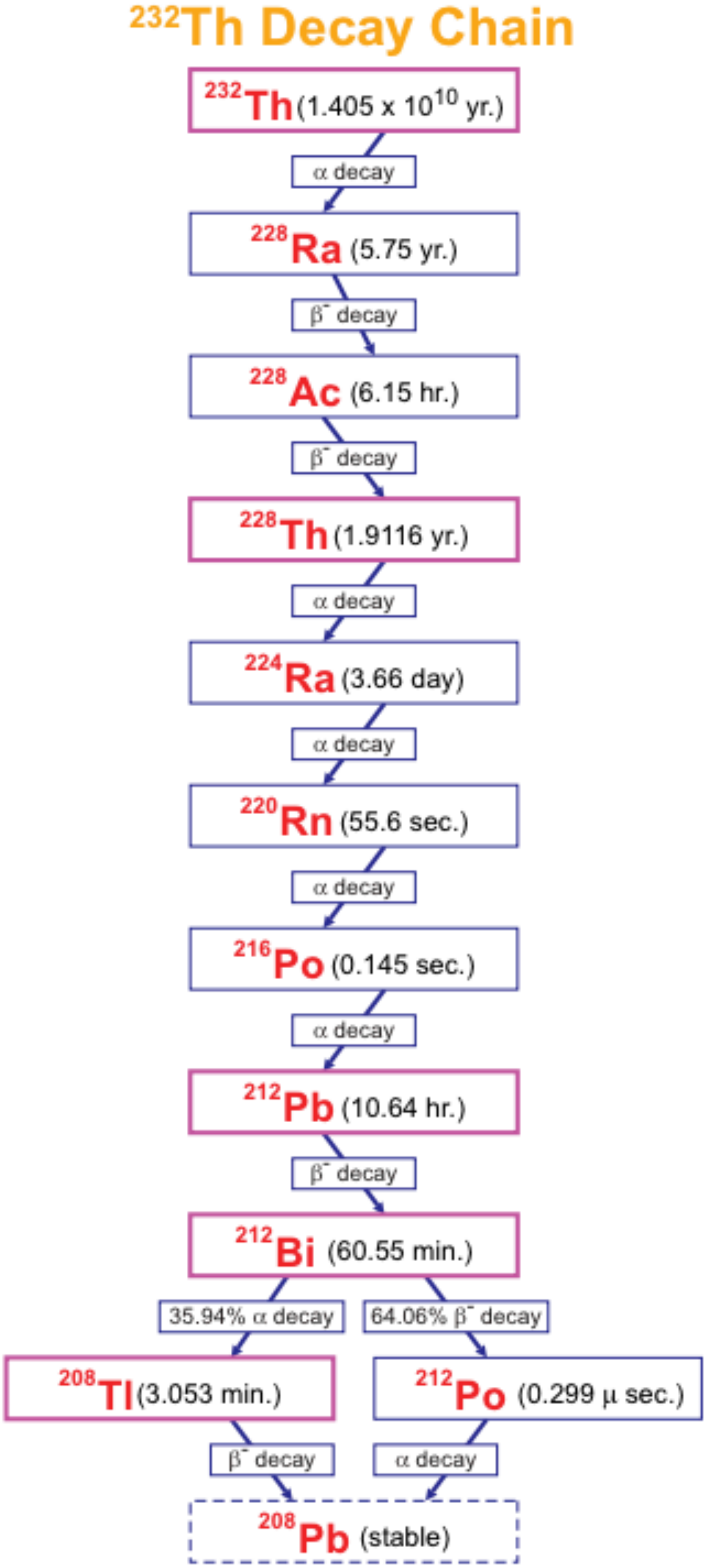

Figure A.2: The ^{232}Th decay chain. Figure from `radiochemistry.org`.

Appendix B

Data Tables, Fits, Legendre Coefficients and Optical-Model Parameters for Elastic Scattering

B.1 Data Tables and Fits for Elastic Scattering

Table B.1: Measured differential cross sections for the scattering of 5.0-MeV neutrons from $^{\mathrm{nat}}$Ne.

$E_n = 5.0 \pm 0.4$ MeV
$\sigma_{el} = 1290 \pm 40$ mb
$\sigma(0°) = 550 \pm 30$ mb/sr

θ_{CM} (degrees)	$\sigma(\theta)_{\mathrm{data}}$ (mb/sr)	$\Delta\sigma(\theta)_{\mathrm{data}}$ (mb/sr)	$\sigma(\theta)_{\mathrm{fit}}$ (mb/sr)	χ^2_{fit}/datapoint
0	535	50	549	0.08
23	373	76	409	0.2
31	308	37	320	0.09
39	228	21	232	0.03
47	201	18	157	5.7
52	109	18	120	0.3
63	71	5	71	0.005
73	56	4	60	0.9
83	80	6	67	3.7
93	72	6	75	0.2
103	83	7	75	1.3
113	71	5	63	2.2
122	38	3	47	6.0
134	30	4	27	0.7
142	27	3	20	4.4
149	16	4	19	0.5
156	20	4	23	0.2

Table B.2: Measured differential cross sections for the scattering of 8.0-MeV neutrons from $^{\text{nat}}$Ne.

$E_n = 8.0 \pm 0.4$ MeV
$\sigma_{el} = 940 \pm 30$ mb
$\sigma(0°) = 710 \pm 40$ mb/sr

θ_{CM} (degrees)	$\sigma(\theta)_{\text{data}}$ (mb/sr)	$\Delta\sigma(\theta)_{\text{data}}$ (mb/sr)	$\sigma(\theta)_{\text{fit}}$ (mb/sr)	χ^2_{fit}/datapoint
0	670	70	706	0.3
29	329	33	315	0.2
34	233	18	225	0.2
38	153	13	162	0.4
42	122	10	110	1.3
46	61	6	68	1.4
50	41	4	39	0.3
54	27	4	20	2.7
60	7	2	8	0.1
65	12	2	10	0.9
69	14	1	17	3.2
73	35	2	25	12.1
83	43	4	45	0.2
93	58	5	55	0.4
103	49	3	53	0.9
113	44	3	41	1.2
123	25	1	25	0.01
134	14	1	13	1.0
145	13	1	14	0.04
155	29	2	28	0.4

Table B.3: Measured differential cross sections for the scattering of 6.0-MeV neutrons from ${}^{\text{nat}}$Ar.

$E_n = 6.0 \pm 0.4$ MeV
$\sigma_{el} = 2170 \pm 60$ mb
$\sigma(0^\circ) = 1840 \pm 130$ mb/sr

θ_{CM} (degrees)	$\sigma(\theta)_{\text{data}}$ (mb/sr)	$\Delta\sigma(\theta)_{\text{data}}$ (mb/sr)	$\sigma(\theta)_{\text{fit}}$ (mb/sr)	χ^2_{fit}/datapoint
0	1650	165	1842	1.4
23	1354	75	1268	1.3
33	893	70	796	1.9
38	567	33	575	0.05
43	380	23	386	0.05
48	218	14	241	2.5
53	148	10	139	0.8
61	56	4	51	1.7
71	13	1	14	0.04
81	6	1	6	0.5
91	9	1	9	0.08
101	20	1	20	0.003
111	28	1	27	0.6
122	25	2	27	0.2
133	28	2	27	0.3
144	30	2	30	0.001
155	39	3	39	0.02

Table B.4: Measured differential cross sections for the scattering of 14.0-MeV neutrons from $^{\mathrm{nat}}$Ar. The data were taken from Ref.[Bea67] at fit using the same procedure as the TUNL data.

E_n = 14.0 ± 0.4 MeV
σ_{el} = 975 ± 20 mb
$\sigma(0°)$= 1600 ± 30 mb/sr

θ_{CM} (degrees)	$\sigma(\theta)_{\mathrm{data}}$ (mb/sr)	$\Delta\sigma(\theta)_{\mathrm{data}}$ (mb/sr)	$\sigma(\theta)_{\mathrm{fit}}$ (mb/sr)	χ^2_{fit}/datapoint
0	1880	190	1604	2.1
10	1378	66	1290	1.8
15	987	72	976	0.02
20	645	24	648	0.02
26	353	14	367	1.07
31	180	7	179	0.02
36	80	4	79	0.08
41	46	3	47	0.06
46	69	3	51	29.0
51	51	3	63	24.0
56	77	4	68	6.0
61	61	3	62	0.1
66	61	3	48	14.5
71	34	2	34	0.05
76	21	2	23	1.09
81	19	2	17	1.2
91	22	1	21	0.1
101	30	3	29	0.1
111	24	2	24	0.04
121	12	1	12	0.001
131	9.4	1.1	8	1.6
141	11	1	11	0.03
151	12	1	11	0.6
159	13	2	13	0.05

B.2 Legendre Coefficients for Elastic Scattering

Table B.5: Fit parameters for ${}^{\mathrm{nat}}$Ne 5.0-MeV scattering data.

l	A_l	a_l
0	103 ± 3	1.00
1	135 ± 7	0.44 ± 0.03
2	115 ± 9	0.22 ± 0.02
3	120 ± 8	0.17 ± 0.01
4	76 ± 7	0.082 ± 0.008

Table B.6: Fit parameters for ${}^{\mathrm{nat}}$Ne 8.0-MeV scattering data.

l	A_l	a_l
0	75 ± 2	1.00
1	112 ± 5	0.50 ± 0.03
2	141 ± 8	0.38 ± 0.02
3	162 ± 8	0.31 ± 0.02
4	151 ± 8	0.22 ± 0.01
5	47 ± 6	0.057 ± 0.007
6	20 ± 5	0.021 ± 0.005

Table B.7: Fit parameters for $^{\mathrm{nat}}$Ar 6.0-MeV scattering data.

l	A_l	a_l
0	173 ± 5	1.00
1	382 ± 14	0.74 ± 0.03
2	501 ± 19	0.58 ± 0.03
3	423 ± 22	0.35 ± 0.02
4	273 ± 22	0.18 ± 0.02
5	109 ± 23	0.06 ± 0.01
6	32 ± 19	0.014 ± 0.008
7	-16 ± 18	-0.006 ± 0.007
8	-21 ± 10	-0.007 ± 0.003
9	-14 ± 9	-0.004 ± 0.003

Table B.8: Fit parameters for $^{\mathrm{nat}}$Ar 14.0-MeV scattering data.

l	A_l	a_l
0	77 ± 1	1.00
1	158 ± 3	0.68 ± 0.02
2	205 ± 5	0.53 ± 0.02
3	227 ± 6	0.42 ± 0.01
4	237 ± 7	0.34 ± 0.01
5	213 ± 7	0.250 ± 0.009
6	202 ± 7	0.201 ± 0.007
7	154 ± 6	0.132 ± 0.005
8	86 ± 6	0.065 ± 0.004
9	29 ± 4	0.020 ± 0.003
10	16 ± 3	0.010 ± 0.002

B.3 Optical Model Parameters for Elastic Scattering

Table B.9: Neutron volume optical model parameters for $^{\text{nat}}$Ne.

	E_n (MeV)	V_v (MeV)	W_v (MeV)	r_v (fm)	a_v (fm)
Dave and Gould	5.0	45.0735		1.242	0.5
	8.0	45.0336		1.242	0.5
	Global	$45.14 - 0.020E$ $-23.48\frac{N-Z}{A}$		$1.508 - 0.0133A$	0.5
Koning and Delaroche	5.0	52.43	0.53	1.155	0.675
	8.0	51.28	0.73	1.155	0.675
Best fit to data (3–10 MeV)	5.0	52.340		1.092	0.518
	8.0	45.057		1.126	0.306
	Global	$64.478 - 2.428E$		$1.035 + 0.011E$	$0.871 - 0.071E$

Table B.10: Neutron surface optical model parameters for $^{\text{nat}}$Ne.

	E_n (MeV)	W_d (MeV)	r_d (fm)	a_d (fm)
Dave and Gould	5.0	12.505	1.353	0.200
	8.0	13.216	1.353	0.200
	Global	$11.32 + 0.237E$ $-16.08\frac{N-Z}{A}$	1.353	0.200
Koning and Delaroche	5.0	7.40	1.299	0.541
	8.0	7.73	1.299	0.541
Best fit to data (3–10 MeV)	5.0	7.840	2.014	0.179
	8.0	7.759	1.954	0.145
	Global	$7.975 - 0.027E$	$2.114 - 0.020E$	$0.236 - 0.011E$

Table B.11: Neutron spin-orbit optical model parameters for $^{\mathrm{nat}}$Ne.

	E_n (MeV)	$V_{s.o}$ (MeV)	$W_{s.o}$ (MeV)	$r_{s.o.}$ (fm)	$a_{s.o}$ (fm)
Dave and Gould	5.0	5.550		1.150	0.500
	8.0	5.550		1.150	0.500
	Global	5.550		1.150	0.500
Koning and Delaroche	5.0	5.62	-0.03	0.947	0.590
	8.0	5.55	-0.04	0.947	0.590
Best fit to data (3–10 MeV)	5.0	5.550	-0.03	1.150	0.500
	8.0	5.550	-0.04	1.150	0.500
	Global	5.550		1.150	0.500

Table B.12: Neutron volume optical model parameters for $^{\mathrm{nat}}$Ar.

	E_n (MeV)	V_v (MeV)	W_v (MeV)	r_v (fm)	a_v (fm)
ENDF-VII.0	6.0	52.050		1.301	0.536
	14.0	45.0336		1.301	0.536
	Global	$53.39 - 0.2233E$		1.301	0.536
Koning and Delaroche	6.0	50.93	0.41	1.188	0.670
	14.0	47.99	0.96	1.188	0.670
Best fit to data	6.0	51.814		1.188	0.670
	14.0	49.827		1.188	0.670
	Global	$53.304 - 0.248E$		1.188	0.670

Table B.13: Neutron surface optical model parameters for $^{\mathrm{nat}}$Ar.

	E_n (MeV)	W_d (MeV)	r_d (fm)	a_d (fm)
ENDF-VII.0	6.0	18.035	1.095	0.419
	14.0	37.595	1.095	0.419
	Global	$3.365 + 2.445E$	1.095	0.419
Koning and Delaroche	6.0	5.07	1.290	0.543
	14.0	5.78	1.290	0.543
Best fit to data	6.0	4.579	1.290	0.543
	14.0	5.180	1.290	0.543
	Global	$4.055 + 0.080E$	1.290	0.543

Table B.14: Neutron spin-orbit optical model parameters for $^{\mathrm{nat}}$Ar.

	E_n (MeV)	$V_{s.o}$ (MeV)	$W_{s.o}$ (MeV)	$r_{s.o.}$ (fm)	$a_{s.o}$ (fm)
ENDF-VII.0	6.0	4.705		1.406	0.600
	14.0	4.705		1.406	0.600
	Global	4.705		1.406	0.600
Koning and Delaroche	6.0	5.77	-0.02	1.010	0.580
	14.0	5.59	-0.06	1.010	0.580
Best fit to data	6.0	5.77	-0.02	1.010	0.580
	14.0	5.59	-0.06	1.010	0.580
	Global	5.59		1.010	0.580

Appendix C

Partial γ-Ray Production Cross Sections

C.1 Data Tables for Argon Cross Sections

Table C.1: ^{40}Ar$(n, n'\gamma)^{40}$Ar $2^+ \rightarrow 0^+$ $E_\gamma = 1461$ keV

E_n (MeV)	σ_{data} (barn)	σ_{TALYS} (barn)	σ_{CoH_3} (barn)
1.5 ± 0.1	0.08 ± 0.01	0.05	0.07
1.7 ± 0.1	0.28 ± 0.03	0.28	0.39
1.9 ± 0.1	0.42 ± 0.04	0.37	0.50
2.1 ± 0.1	0.70 ± 0.07	0.43	0.62
2.4 ± 0.1	0.67 ± 0.06	0.55	0.71
2.7 ± 0.2	0.80 ± 0.07	0.64	0.83
3.0 ± 0.2	0.86 ± 0.08	0.71	0.87
3.4 ± 0.2	0.84 ± 0.08	0.77	0.96
3.8 ± 0.2	0.96 ± 0.09	0.88	1.04
4.2 ± 0.2	1.02 ± 0.09	0.91	1.07
4.7 ± 0.3	0.98 ± 0.09	0.91	1.13
5.3 ± 0.3	1.1 ± 0.1	0.9	1.1
6.0 ± 0.3	1.1 ± 0.1	0.9	1.1
6.7 ± 0.4	1.1 ± 0.1	1.0	1.1
7.5 ± 0.4	1.1 ± 0.1	1.0	1.1
8.4 ± 0.5	1.1 ± 0.1	1.0	1.1
9.5 ± 0.6	1.0 ± 0.1	1.0	1.1
10.6 ± 0.6	1.1 ± 0.1	0.9	1.0
11.9 ± 0.7	0.84 ± 0.08	0.67	0.77
13.4 ± 0.8	0.61 ± 0.06	0.43	0.53
15.0 ± 0.9	0.42 ± 0.05	0.32	0.37
16.8 ± 1.0	0.32 ± 0.04	0.24	0.26
18.9 ± 1.0	0.33 ± 0.05	0.21	0.21
23.8 ± 1.3	0.24 ± 0.04	0.16	0.14
29.9 ± 1.7	0.19 ± 0.03	0.12	0.10

Table C.2: ^{40}Ar$(n, n'\gamma)^{40}$Ar $0^+ \rightarrow 2^+$ $E_\gamma = 660$ keV

E_n (MeV)	σ_{data} (barn)	σ_{TALYS} (barn)	σ_{CoH_3} (barn)
2.1 ± 0.1	0.024 ± 0.005	0.023	0.026
2.4 ± 0.1	0.058 ± 0.008	0.055	0.072
2.7 ± 0.2	0.10 ± 0.01	0.07	0.09
3.0 ± 0.2	0.12 ± 0.01	0.08	0.10
3.4 ± 0.2	0.11 ± 0.01	0.09	0.11
3.8 ± 0.2	0.11 ± 0.01	0.09	0.11
4.2 ± 0.2	0.10 ± 0.01	0.08	0.10
4.7 ± 0.2	0.08 ± 0.01	0.06	0.08
5.3 ± 0.3	0.07 ± 0.01	0.04	0.06
6.0 ± 0.3	0.06 ± 0.01	0.03	0.05
6.7 ± 0.4	0.06 ± 0.01	0.03	0.04
7.5 ± 0.4	0.06 ± 0.01	0.02	0.04
9.5 ± 0.6	0.05 ± 0.01	0.02	0.03

Table C.3: ^{40}Ar$(n, n'\gamma)^{40}$Ar $2^+ \rightarrow 0^+$ $E_\gamma = 2524$ keV

E_n (MeV)	σ_{data} (barn)	σ_{TALYS} (barn)	σ_{CoH_3} (barn)
2.3 ± 0.2	0.030 ± 0.006	0.044	0.019
3.0 ± 0.2	0.059 ± 0.009	0.073	0.090
3.4 ± 0.2	0.08 ± 0.01	0.08	0.10
3.8 ± 0.2	0.11 ± 0.02	0.08	0.10
4.2 ± 0.2	0.13 ± 0.02	0.08	0.10
4.7 ± 0.3	0.11 ± 0.02	0.08	0.11
5.3 ± 0.3	0.11 ± 0.02	0.07	0.10
6.0 ± 0.3	0.10 ± 0.02	0.07	0.10

Table C.4: ^{40}Ar$(n, n'\gamma)^{40}$Ar $2^+ \rightarrow 2^+$ $E_\gamma = 1063$ keV

E_n (MeV)	σ_{data} (barn)	σ_{TALYS} (barn)	σ_{CoH_3} (barn)
2.7 ± 0.2	0.056 ± 0.009	0.059	0.059
3.0 ± 0.2	0.08 ± 0.01	0.10	0.12
3.4 ± 0.2	0.11 ± 0.01	0.11	0.14
3.8 ± 0.2	0.09 ± 0.01	0.11	0.14
4.2 ± 0.2	0.13 ± 0.02	0.11	0.14
4.7 ± 0.3	0.11 ± 0.01	0.11	0.15
5.3 ± 0.3	0.13 ± 0.02	0.10	0.14
6.0 ± 0.3	0.13 ± 0.02	0.09	0.13
7.0 ± 0.4	0.10 ± 0.02	0.08	0.12
7.5 ± 0.4	0.13 ± 0.02	0.08	0.12
8.4 ± 0.5	0.10 ± 0.02	0.07	0.11

Table C.5: $^{40}\mathrm{Ar}(n,n'\gamma)^{40}\mathrm{Ar}$ $4^+ \rightarrow 2^+$ $E_\gamma = 1432$ keV

E_n (MeV)	σ_{data} (barn)	σ_{TALYS} (barn)	σ_{CoH_3} (barn)
3.8 ± 0.2	0.09 ± 0.02	0.06	0.09
4.2 ± 0.2	0.13 ± 0.02	0.08	0.11
4.7 ± 0.3	0.17 ± 0.02	0.11	0.14
5.3 ± 0.3	0.19 ± 0.02	0.14	0.16
6.0 ± 0.3	0.19 ± 0.02	0.16	0.17
6.7 ± 0.4	0.24 ± 0.03	0.18	0.19
7.5 ± 0.4	0.22 ± 0.02	0.20	0.20
8.4 ± 0.5	0.28 ± 0.03	0.21	0.21
9.5 ± 0.6	0.29 ± 0.03	0.22	0.22
10.6 ± 0.6	0.33 ± 0.04	0.23	0.22
11.9 ± 0.7	0.27 ± 0.04	0.17	0.16
13.4 ± 0.8	0.17 ± 0.03	0.11	0.11

Table C.6: $^{40}\mathrm{Ar}(n,n'\gamma)^{40}\mathrm{Ar}$ $2^+ \rightarrow 2^+$ $E_\gamma = 1747$ keV

E_n (MeV)	σ_{data} (barn)	σ_{TALYS} (barn)	σ_{CoH_3} (barn)
3.8 ± 0.2	0.10 ± 0.01	0.09	0.12
4.2 ± 0.2	0.11 ± 0.02	0.09	0.12
4.7 ± 0.3	0.11 ± 0.02	0.08	0.11
5.3 ± 0.3	0.13 ± 0.02	0.06	0.09
6.0 ± 0.3	0.11 ± 0.02	0.06	0.08
6.7 ± 0.4	0.10 ± 0.02	0.05	0.08
7.5 ± 0.4	0.10 ± 0.02	0.04	0.07

Table C.7: $^{40}\mathrm{Ar}(n,2n\gamma)^{39}\mathrm{Ar}$ $3/2^- \rightarrow 7/2^-$ $E_\gamma = 1267$ keV

E_n (MeV)	σ_{data} (barn)	σ_{TALYS} (barn)	σ_{CoH_3} (barn)
13.4 ± 0.8	0.08 ± 0.02	0.08	0.09
15.0 ± 0.9	0.13 ± 0.02	0.13	0.15
18.9 ± 1.0	0.19 ± 0.03	0.15	0.19
21.2 ± 1.2	0.13 ± 0.02	0.12	0.15

Table C.8: $^{40}\mathrm{Ar}(n,2n\gamma)^{39}\mathrm{Ar}$ $3/2^+ \rightarrow 3/2^-$ $E_\gamma = 250$ keV

E_n (MeV)	σ_{data} (barn)	σ_{TALYS} (barn)	σ_{CoH_3} (barn)
15.0 ± 0.9	0.058 ± 0.008	0.037	0.046
16.8 ± 1.0	0.060 ± 0.008	0.050	0.064
18.9 ± 1.0	0.056 ± 0.008	0.043	0.068
21.2 ± 1.2	0.049 ± 0.007	0.034	0.056
23.8 ± 1.4	0.044 ± 0.007	0.020	0.045
26.7 ± 1.5	0.043 ± 0.007	0.024	0.036

C.2 Data Tables for Neon Cross Sections

Table C.9: $^{20}\mathrm{Ne}(n, n'\gamma)^{20}\mathrm{Ne}$ $2^+ \rightarrow 0^+$ $E_\gamma = 1633$ keV

E_n (MeV)	σ_{data} (barn)	σ_{TALYS} (barn)	σ_{CoH_3} (barn)
1.9 ± 0.1	0.10 ± 0.01	0.19	0.13
2.1 ± 0.1	0.30 ± 0.03	0.31	0.30
2.4 ± 0.1	0.44 ± 0.04	0.39	0.44
2.7 ± 0.2	0.63 ± 0.06	0.45	0.49
3.0 ± 0.2	0.44 ± 0.04	0.48	0.53
3.4 ± 0.2	0.65 ± 0.06	0.49	0.55
3.8 ± 0.2	0.50 ± 0.05	0.47	0.54
4.2 ± 0.2	0.45 ± 0.04	0.44	0.53
4.7 ± 0.3	0.44 ± 0.04	0.42	0.53
5.3 ± 0.3	0.51 ± 0.05	0.43	0.56
6.0 ± 0.3	0.50 ± 0.05	0.48	0.60
6.7 ± 0.4	0.64 ± 0.06	0.53	0.66
7.5 ± 0.4	0.63 ± 0.06	0.56	0.68
8.4 ± 0.5	0.60 ± 0.06	0.57	0.68
9.5 ± 0.5	0.47 ± 0.05	0.50	0.59
10.6 ± 0.6	0.45 ± 0.04	0.43	0.52
11.9 ± 0.7	0.39 ± 0.04	0.38	0.43
13.4 ± 0.7	0.35 ± 0.04	0.31	0.37
15.0 ± 0.8	0.29 ± 0.03	0.22	0.31

Table C.10: ^{22}Ne$(n, n'\gamma)^{22}$Ne $2^+ \rightarrow 0^+$ $E_\gamma = 1275$ keV

E_n (MeV)	σ_{data} (barn)	σ_{TALYS} (barn)	σ_{CoH_3} (barn)
1.5 ± 0.1	0.08 ± 0.01	0.00	0.25
1.7 ± 0.1	0.41 ± 0.04	0.34	0.36
1.9 ± 0.1	0.57 ± 0.05	0.46	0.44
2.1 ± 0.1	0.48 ± 0.04	0.53	0.49
2.4 ± 0.1	0.61 ± 0.06	0.58	0.55
2.7 ± 0.2	0.56 ± 0.05	0.61	0.60
3.0 ± 0.2	0.82 ± 0.09	0.63	0.63
3.4 ± 0.2	0.90 ± 0.09	0.63	0.67
3.8 ± 0.2	0.74 ± 0.07	0.65	0.72
4.2 ± 0.2	1.06 ± 0.11	0.65	0.78
4.7 ± 0.3	0.87 ± 0.10	0.71	0.80
5.3 ± 0.3	1.01 ± 0.13	0.78	0.90
6.0 ± 0.3	0.99 ± 0.11	0.85	0.97
6.7 ± 0.4	1.20 ± 0.15	0.91	1.02
7.5 ± 0.4	1.21 ± 0.18	0.92	1.02
8.4 ± 0.5	1.13 ± 0.15	0.90	1.00
9.5 ± 0.5	1.07 ± 0.12	0.86	0.96
10.6 ± 0.6	1.04 ± 0.12	0.84	0.92

Bibliography

[Aad08] G. Aad et al., "The ATLAS experiment at the CERN Large Hadron Collider", JINST **3**, S08003 (2008).

[Aal02] C. Aalseth et al., "IGEX ^{76}Ge neutrinoless double-beta decay experiment: Prospects for next generation experiments", Phys. Rev. D , 092007 (2002).

[Aal11] C. E. Aalseth et al., "Results from a Search for Light-Mass Dark Matter with a p-Type Point Contact Germanium Detector", Phys. Rev. Lett. **106**, 131301 (2011).

[Abd09] A. Abdo et al., "Measurement of the Cosmic Ray $e^+ + e^-$ Spectrum from 20 GeV to 1 TeV with the Fermi Large Area Telescope", Phys. Rev. Lett. **102**, 181101 (2009).

[Abe08] S. Abe et al., Phys. Rev. Lett. **100**, 221803 (2008).

[Ada12] P. Adamson et al., "Improved Measurement of Muon Antineutrino Disappearance in MINOS", Phys. Rev. Lett. **108**, 191801 (2012).

[Ado08] R. Adolphi et al., "The CMS experiment at the CERN LHC", JINST **3**, S08004 (2008).

[Adr09] O. Adriani et al., "An anomalous positron abundance in cosmic rays with energies 1.5-100 GeV", Nature **458**, 607 (2009).

[Ago03] S. Agostinelli et al., Nucl. Instr. and Meth. A **506**, 250 (2003), http://geant4.web.cern.ch/geant4/.

[Agu11a] E. Aguayo et al., "Depth Requirements for a Tonne-scale 76-Ge Neutrinoless Double-beta Decay Experiment", Arxiv preprint, arXiv:1109.4154 (2011).

[Agu11b] E. Aguayo et al., "The MAJORANA Experiment", AIP Conf. Proc. **1417**, 95 (2011).

[Aha08] B. Aharmim et al., "Independent Measurement of the Total Active ^{8}B Solar Neutrino Flux Using an Array of ^{3}He Proportional Counters at the Sudbury Neutrino Observatory", Phys. Rev. Lett. **101**, 111301 (2008).

[Ahm01] Q. Ahmad et al., "Measurement of the Rate of $\nu_e + d \rightarrow p + p + e^-$ Interactions Produced by ^{8}B Solar Neutrinos at the Sudbury Neutrino Observatory", Phys. Rev. Lett. **87**, 071301 (2001).

[Ahn06] M. Ahn et al., "Measurement of neutrino oscillation by the K2K experiment", Phys. Rev. D **74**, 072003 (2006).

[Ahn12] J. Ahn et al., "Observation of Reactor Electron Antineutrinos Disappearance in the RENO Experiment", Phys. Rev. Lett. **108**, 191802 (2012).

[All06] J. Allison et al., "Geant4 developments and applications", IEEE Trans. Nucl. Sci. **53**, 270 (2006).

[An12] F. An et al., "Observation of Electron-Antineutrino Disappearance at Daya Bay", Phys. Rev. Lett. **108**, 171803 (2012).

[Ang79] M. Anghinolfi et al., "The response function of organic scintillators to fast neutrons", Nucl. Instrum. Methods **165**, 217 (1979).

[Ang11] G. Angloher et al., "Results from 730 kg days of the CRESST-II Dark Matter Search", Arxiv preprint: arXiv:1109.0702v1 (2011).

[Apr05] E. Aprile, "Scintillation response of liquid xenon to low energy nuclear recoils", Phys. Rev. D **72** (2005).

[Apr11] E. Aprile et al., "Dark Matter Results from 100 Live Days of XENON100 Data", Phys. Rev. Lett. **107**, 131302 (2011).

[Ato95] A. Atoian, F. Aharoian, and H. Falk, "Electrons and positrons in the galactic cosmic rays", Phys. Rev. D **52**, 3265 (1995).

[Aug12] M. Auger et al., "Search for Neutrinoless Double-Beta Decay in ^{136}Xe with EXO-200", Phys. Rev. Lett. **109**, 032505 (2012).

[Avi08] F. Avignone, S. Elliott, and J. Engel, "Double beta decay, Majorana neutrinos, and neutrino mass", Rev. Mod. Phys. **80**, 481 (2008).

[Axe62] P. Axel, "Electric Dipole Ground-State Transition Width Strength Function and 7-MeV Photon Interactions", Phys. Rev. **126**, 671 (1962).

[Bah64] J. Bahcall, "Solar Neutrinos I. Theoretical", Phys. Rev. Lett. **12**, 300 (1964).

[Bah99] N. Bahcall, J. Ostriker, S. Perlmutter, and P. Steinhard, "The Cosmic Triangle: Revealing the State of the Universe", Science **284**, 1481 (1999).

[Bam91] G. Bamford et al., "Neutron, proton and gamma-ray event identification with a HPGe detector through pulse shape analysis", IEEE Trans. Nucl. Sci. **38**, 200 (1991).

[Bau99] L. Baudis et al., "Limits on the Majorana mass in the 0.1 eV range", Phys. Rev. Lett. **83**, 41 (1999).

[Bea67] P. Beach et al., "Elastic Scattering of Neutrons from O and Ar at 14.0 MeV", Phys. Rev. **156**, 1201 (1967).

[Bel10] F. Bellini et al., "Monte Carlo evaluation of the external gamma, neutron and muon induced background sources in the CUORE experiment", Astropart. Phys. **33**, 169 (2010).

[Ben03] C. Bennett et al., "First-Year Wilkinson Microwave Anisotropy Probe (WMAP) Observations: Preliminary Maps and Basic Results", Astrophys. J. Supp. **148**, 1 (2003).

[Ber00] L. Bergstrom, "Non-baryonic dark matter: observational evidence and detection methods", Rep. Prog. Phys. **63**, 793 (2000).

[Ber05] G. Bertone, D. Hooper, and J. Silk, "Particle dark matter: evidence, candidates and constraints", Phys. Rep. **405**, 279 (2005).

[Ber07] R. Bernabei et al., "Possible implications of the channeling effect in NaI(Tl) crystals", Arxiv preprint: arXiv:0710.0288v1 (2007).

[Ber10] G. Bertone, *Particle Dark Matter*, Cambridge University Press, 2010.

[Ber12] J. Beringer et al., Phys. Rev. D **86**, 010001 (2012).

[Bha12] C. Bhatia, S. Finch, M. Gooden, and W. Tornow, "$^{40}\mathrm{Ar}(n,p)^{40}\mathrm{Cl}$ cross section between 9 and 15 MeV", Phys. Rev. C **86**, 041602(R) (2012).

[Bie52] L. Biedenharn, J. Blatt, and M. Rose, "Some Properties of the Racah and Associated Coefficients", Rev. Mod. Phys. **24**, 249 (1952).

[Bil78] S. Bilenky and B. Pontecorvo, "Lepton mixing and neutrino oscillations", Phys. Reports **41**, 225 (1978).

[Boe92] F. Boehm and P. Vogel, *Physics of Massive Neutrinos*, Cambridge University Press, 1992.

[Boh36] N. Bohr, "Neutron capture and nuclear constitution", Nature **137**, 344 (1936).

[Bol99] A. Bolozdynya, "Two-phase emission detectors and their applications", Nucl. Instrum. Methods A **422**, 314 (1999).

[Bol06] A. Bolozdynya, "Two-phase Emission Detectors: Foundations and Applications", IEEE Trans. Nucl. Sci. **13**, 616 (2006).

[Bos10] M. Boswell et al., 2010 Fall Meeting of the APS Division of Nuclear Physics, Santa Fe, NM, 2010, http://meetings.aps.org/link/BAPS.2010.DNP.GD.4.

[Bos11] M. Boswell et al., "MaGe-a Geant4-Based Monte Carlo Application", IEEE Trans. Nucl. Sci **58**, 1212 (2011).

[Bot02] R. Bottema et al., "MOND rotation curves for spiral galaxies wiht Cepheid-based distances", Astronomy & Astrophysics **393**, 453 (2002).

[Bou04] M. Boulay, A. Hime, and J. Lidgard, "Design Constraints for a WIMP Dark Matter and *pp* Solar Neutrino Liquid Neon Scintillation Detector", Arxiv preprint arXiv:nucl-ex/0410025 (2004).

[Bou08] M. Boulay and B. Cai, "Dark Matter Search at SNOLAB with DEAP-1 and DEAP/CLEAN-3600", J. Phys. Conf. Ser. **136**, 042081 (2008).

[Bri57] D. Brink, "Individual particle and collective aspects of the nuclear photoeffect", Nucl. Phys. **4**, 215 (1957).

[Bro81] G. Brown and M. Rho, "The Giant Gamow-Teller Resonance", Nucl. Phys. A **372**, 397 (1981).

[Bru97] R. Brun and F. Rademakers, "ROOT - an object-oriented data analysis framework", Nucl. Instrum. Methods A **389**, 81 (1997), http://root.cern.ch.

[Cam04] J. Cameron and B. Singh, "Adopted Levels, Gammas for ^{40}Ar", Nuclear Data Sheets **102**, 293 (2004).

[Cam08] L. Camilleri, E. Lisi, and J. Wilkerson, "Neutrino Masses and Mixings: Status and Prospects", Annu. Rev. Nucl. Part. Sci. **58**, 343 (2008).

[Cap09] R. Capote et al., "Reference Input Parameter Library (RIPL-3)", Nuclear Data Sheets **110**, 3107 (2009).

[Car74] G. Carlson, "The effect of fragment anisotropy on fission-chamber efficiency", Nucl. Instrum. Methods **119**, 97 (1974).

[Car12] E. Cartlidge, "Beta Test", Nature: News Feature **487**, 160 (2012).

[Cec79] R. Cecil, B. Anderson, and R. Madey, "Improved predictions of neutron detection efficiency for hydrocarbon scintillators from 1 MeV to about 300 MeV", Nucl. Instrum. Methods **161**, 439 (1979).

[Cej93] P. Cejnar and J. Kern, "Monte Carlo analysis of $(\alpha, xn\gamma)$-feeding intensities in Cd nuclei", Nucl. Phys. **A561**, 317 (1993).

[Cej96] P. Cejnar, S. Drissi, and J. Kern, "Calculation of the spin deorientation in $(\alpha, 2n\gamma)$ reactions", Nucl. Phys. **A602**, 225 (1996).

[Cen99] R. Cen and J. Ostriker, "Where are the baryons?", Astrophys. J. **514**, 1 (1999).

[CER12] CERN European Organization for Nuclear Research, "The Large Hadron Collider: Our understanding of the Universe is about to change...", 2012, http://public.web.cern.ch/public/en/lhc/lhc-en.html, accessed December 17, 2012.

[Cha06] M. B. Chadwick et al., "ENDF/B-VII.0: Next Generation Evaluated Nuclear Data Library for Nuclear Science and Technology", Nucl. Data Sheets **107**, 2931 (2006), `http://www-nds.iaea.org/exfor/endf.htm`.

[Cle98] B. Cleveland et al., "Measurement of the solar electron neutrino flux with the Homestake chlorine detector", Astrophys. J **496**, 505 (1998).

[Clo06] D. Clowe et al., "A Direct Empirical Proof of the Existence of Dark Matter", Astrophys. J. **648**, L109 (2006).

[Coh59] H. Cohn and J. Fowler, "Differential Elastic Scattering of Neutrons from Neon", Phys. Rev. **114**, 194 (1959).

[Coo58] J. Coon et al., "Scattering of 14.5-MeV Neutrons by Complex Nuclei", Phys. Rev. **111**, 250 (1958).

[Coo10] J. Cooley et al., "Dark Matter Search Results from the CDMS II Experiment", Science **327**, 1619 (2010).

[Cow56] C. Cowan et al., "Detection of the Free Neutrino: a Confirmation", Science **3212**, 103 (1956).

[dA06] R. de Austri, R. Trotta, and L. Roszkowski, "A Markov chain Monte Carlo analysis of the CMSSM", Journal of High Energy Physics **2006**, 002 (2006).

[Dan62] G. Danby et al., "Observation of High-Energy Neutrino Reactions and the Existence of Two Kinds of Neutrinos", Phys. Rev. Lett. **9**, 36 (1962).

[Dav64] R. Davis, "Solar Neutrinos II. Experimental", Phys. Rev. Lett. **12**, 303 (1964).

[Dav83] J. Dave and C. Gould, "Optical model analysis of scattering of 7- to 15-MeV neutrons from 1-p shell nuclei", Phys. Rev. C **28**, 2212 (1983).

[DeC89] D. DeCamp et al., "Determination of the Number of Light Neutrino Species", Phys. Lett. B **16** (1989).

[Del89] J. Delaroche, Y. Wang, and J. Rapaport, "Neutron-^{90}Zr mean field from a dispersive optical model analysis", Phys. Rev. C **39**, 391 (1989).

[DeP95] F. DePaolis, C. Ingrosso, P. Jetzer, and M. Roncadelli, "A Case for a Baryonic Dark Halo", Phys. Rev. Lett. **74**, 14 (1995).

[Die82] G. Dietze and H. Klein, Technical Report PTB-ND-22 (1982).

[Die03] F. S. Dietrich et al., "Wick's limit and a new method for estimating neutron reaction cross sections", Phys. Rev. C **68**, 064608 (2003).

[Dim81] S. Dimopoulos and H. Georgi, "Softly Broken Supersymmetry and SU(5)", Nucl. Phys. B **193**, 150 (1981).

[Dol70] B. Dolgoshein, V. Lebedenko, and B. Rodionov, "New method of registration of ionizing-particle tracks in condensed matter", JETP Lett. **11**, 351 (1970).

[Dro72] M. Drosg, "Accurate measurement of the counting efficiency of a NE-213 neutron detector between 2 and 26 MeV", Nucl. Instrum. and Methods **105**, 573 (1972).

[Dro78] M. Drosg, "Unified Absolute Differential Cross Sections for Neutron Production by the Hydrogen Isotopes for Charged-Particle Energies between 6 and 17 MeV", Nucl. Sci. Eng. **67**, 190 (1978).

[Ein16] A. Einstein, "The Foundation of the General Theory of Relativity", Annalen der Physik **354**, 769 (1916), Title translated from German.

[Eis05] D. Eisenstein, "Dark energy and cosmic sound", New Astronomy Reviews **49**, 360 (2005).

[Ell87] S. Elliott, A. Hahn, and M. Moe, "Direct Evidence for Two-Neutrino Double-Beta Decay in ^{82}Se", Phys. Rev. Lett. **59**, 2020 (1987).

[Ell02] S. Elliott and P. Vogel, "Double Beta Decay", Annu. Rev. Nucl. Part. Sci. **52**, 65 (2002).

[Ell11] S. Elliott et al., "An Improved Limit on Pauli-Exclusion-Principle Forbidden Atomic Transitions", arXiv:1107.3118v1 (2011).

[Eri60] T. Ericson, "The statistical model and nuclear level densities", Adv. Phys. **9**, 425 (1960).

[ETH] ETH Zurich, "The Neutrino", `http://www.library.ethz.ch/exhibit/pauli/neutrino_e.html`, accessed December 17, 2012.

[Fen10] L. Feng, "PMT (α, n) spectrum", MiniCLEAN Neutron Verification Meeting, unpublished, 2010.

[Fer34] E. Fermi, "Attempt at a theory of β-rays", Z. Phys. **88**, 161 (1934), Article in German.

[Fer55] M. Ferentz and N. Rosenzweig, "Table of F Coefficients", Argonne National Laboratory Report ANL-5324 (1955).

[Fin11] P. Finnerty et al., “Low-background gamma counting at the Kimballton Underground Research Facility”, Nucl. Instrum. Methods A **642**, 65 (2011).

[For04] J. Formaggio and C. Martoff, “Backgrounds to Sensitive Experiments Underground”, Annu. Rev. Nucl. Part. Sci. **54**, 361 (2004).

[Fot01] N. Fotiades et al., “Measurement of 238U(n,xngamma) partial gamma-ray cross sections with GEANIE at LANSCE/WNR”, Los Alamos National Lab. Report No. LA-UR-01-4281 (2001).

[Fot04] N. Fotiades et al., “Measurements and calculations of ^{238}U$(n, xn\gamma)$ partial gamma-ray cross sections”, Phys. Rev. C **69**, 024601 (2004).

[Fow10] A. Fowler et al., “The Atacama Cosmology Telescope: A Measurement of the $600 < l < 8000$ Cosmic Microwave Background Power Spectrum at 148 GHz”, Astrophys. J. **722**, 1148 (2010).

[Fuk98] Y. Fukuda et al., “Evidence for Oscillation of Atmospheric Neutrinos”, Phys. Rev. Lett. **81**, 1562 (1998).

[Fuk04] M. Fukugita and P. Peebles, “The Cosmic Energy Inventory”, Astrophys. J. **616**, 643 (2004).

[Geh05] R. Gehrke and J. Davidson, “Acquisition of quality γ-ray spectra with HPGe detectors”, App. Rad. Isotopes **62**, 479 (2005).

[Gil65] A. Gilbert and A. G. W. Cameron, “A composite nuclear-level density formula with shell corrections”, Can. J. Phys. **43**, 1446 (1965).

[Gla74] D. Glasgow et al., “A high-precision neutron time-of-flight facility”, Nucl. Instrum. Methods **114**, 541 (1974).

[Gle80] S. Glendinning, “Elastic and inelastic neutron scattering cross sections for ^{10}B, ^{11}B and ^{16}O”, Ph.D. Thesis, Duke University, 1980.

[GM35] M. Goeppert-Mayer, “Double Beta-Disintigration”, Phys. Rev. **48**, 512 (1935).

[Gri91] K. Griest, “Galactic Microlensing as a Method of Detecting Massive Compact Halo Objects”, Astrophys. J. **366**, 412 (1991).

[Gui00] F. Guimares and C. Fu, “TNG-GENOA User’s Manual”, ORNL/TM-2000/252, 2000.

[Gui09] V. Guiseppe et al., “Neutron inelastic scattering and reactions in natural Pb as a background in neutrinoless double-β-decay experiments”, Phys. Rev. C **79**, 054604 (2009).

[Gut81] A. Guth, “Inflationary universe: A possible solution to the horizon and flatness problems”, Phys. Rev. D **23**, 347 (1981).

[Hab85] H. Haber and G. Kane, “The Search for Supersymmetry: Probing Physics Beyond the Standard Model”, Phys. Reports **117**, 75 (1985).

[Hag68] R. Hager and E. Selzer, Nucl. Data Tables **A4**, 1 (1968).

[Han06] S. Hannestad, “Primordial Neutrinos”, Ann. Rev. Nucl. Part. Sci. **56**, 137 (2006).

[Hau52] W. Hauser and H. Feshbach, “The Inelastic Scattering of Neutrons”, Phys. Rev. **87**, 366 (1952).

[Hav] Havar® - High-Strength Non-Magnetic Alloy, `http://www.goodfellow.com/E/Havar-High-Strength-Non-Magnetic-Alloy.html`, accessed January 22, 2013.

[Hei01] M. Heil et al., “A 4π BaF$_2$ detector for (n,γ) cross-section measurements at a spallation neutron source”, Nucl. Instrum. Methods A **459**, 229 (2001), `http://wnr.lanl.gov/newwnr/1FP14/About.shtml`.

[Her09] M. Herman and A. Trkov, “”ENDF-6 Formats Manual””, Brookhaven National Lab Report BNL-90365-2009 (2009).

[Heu95] G. Heusser, “Low-radioactivity background techniques”, Ann. Rev. Nucl. Part. Sci. **45**, 543 (1995).

[Hil03] S. Hilaire, C. Lagrange, and A. Koning, “Comparisons between various width fluctuation correction factors for compound nucleus reactions”, Ann. Phys. **306**, 209 (2003).

[Him08] A. Hime, “Backgrounds Document for the MiniCLEAN DOR Proposal”, Unpublished, 2008.

[Hin09] G. Hinshaw, “Five-Year Wilkinson Anisotropy Probe Observations: Data Processing, Sky Maps, and Basic Results”, Astrophys. J. **180**, 225 (2009).

[Hit83] A. Hitachi and T. Takahashi, “Effect of ionization density on the time dependence of luminescence from liquid argon and xenon”, Phys. Rev. B **27**, 5279 (1983).

[Hod63] P. E. Hodgson, *The Optical Model of Elastic Scattering*, Oxford at the Clarendon Press, 1963.

[Hod71] P. Hodgson, *Nuclear Reactions and Nuclear Structure*, Clarendon Press, Oxford, 1971.

[Hod87] P. E. Hodgson, “Compound nucleus reactions”, Rep. Prog. Phys. **50**, 1171 (1987).

[Hof75] H. Hofmann et al., “Direct reactions and Hauser-Feshbach theory”, Ann. Phys. **90**, 403 (1975).

[Hof80] H. Hofmann et al., “Hauser-Feshbach calculations in the presence of weakly absorbing channels with special reference to elastic enhancement factor and the factorization assumption”, Z. Physik A **297**, 153 (1980).

[Hop08] E. Hoppe et al., “A method for removing surface contamination on ultra-pure copper spectrometer components”, J. Radioanal. Nucl. Chem. **276**, 645 (2008).

[Hou12] Z. Hou et al., Astrophys. J. Submitted (2012), arXiv:1212.6267.

[Hu96a] W. Hu and M. White, “Acoustic signatures in the cosmic microwave background”, Astrophys. J. **471**, 30 (1996).

[Hu96b] W. Hu and M. White, “Small-scale cosmological perturbations: an analytic approach”, Astrophys. J. **471**, 542 (1996).

[Hu97] W. Hu, N. Sugiyama, and J. Silk, “The physics of microwave background anisotropies”, Nature **386**, 37 (1997).

[Hu12] W. Hu, “Intermediate Guide to the Acoustic Peaks and Polarization”, 2012, http://background.uchicago.edu/ whu/intermediate/intermediate.html, accessed October 25, 2012.

[Hut77] P. Hut, “Limits on masses and number of neutral weakly interacting particles”, Phys. Lett. B **69**, 85 (1977).

[Hut07] A. Hutcheson et al., “Pulsed monoenergetic beams for neutron cross-section measurements using activation and scattering techniques at Triangle Universities Nuclear Laboratory”, Nucl. Instrum. Methods B **261**, 369 (2007).

[Hut08] A. Hutcheson, “Neutron-Induced Partial Gamma-Ray Cross-Section Measurements on Uranium”, Ph.D. Thesis, Duke University, 2008.

[Ins12] Institute for Structure and Nuclear Astrophysics, University of Notre Dame FN Tandem Van de Graaff Accelerator, `http://isnap.nd.edu/html/researchFN.html`, accessed May 2, 2012, 2012.

[Jun96] G. Jungman, M. Kamionkowski, and K. Griest, “Supersymmetric dark matter”, Phys. Rep. **267**, 195 (1996).

[Kam98] M. Kamionkowski and A. Kinkhabwala, “Galactic halo models and particle dark-matter detection”, Phys. Rev. D **57**, 3256 (1998).

[Kan94] G. Kane, C. Kolda, L. Roszkowski, and J. Wells, "Study of constrained minimal supersymmetry", Phys. Rev. D **49**, 6173 (1994).

[Kau12] L. Kaufman, Private communication, 2012.

[Kaw03] T. Kawano, "CoH: The Hauser-Feshbach-Moldauer statistical model with the coupled-channels theory", Los Alamos National Laboratory, unpublished, 2003.

[Kaw06] T. Kawano, S. Chiba, and H. Koura, "Phenomenological Nuclear Level Densities using the KTUY05 Nuclear Mass Formula for Applications Off-Stability", J. Nucl. Sci. Technol. **43**, 1 (2006), updated parameters based on RIPL-3, (unpublished, 2009).

[Kaw09] T. Kawano et al., "Calculation of nuclear reaction cross sections on excited nuclei with the coupled-channels method", Phys. Rev. C **80**, 024611 (2009).

[Kaw10] T. Kawano et al., "Monte Carlo Simulation for Particle and γ-Ray Emissions in Statistical Hauser-Feshbach Model", J. Nucl. Sci. Technol. **47**, 462 (2010).

[Kin70] W. Kinney, "Finite-sample Corrections to Neutron Scattering Data", Nucl. Instrum. Methods **83**, 15 (1970).

[KK04] H. Klapdor-Kleingrothaus et al., "Search for neutrinoless double beta decay with enriched ^{76}Ge in Gran Sasso 1990-2003", Phys. Lett. B **586**, 198 (2004).

[KK06] H. Klapdor-Kleingrothaus and I. Krivosheina, "The evidence for the observation of $0n\beta\beta$ decay: The identification of $0n\beta\beta$ events from the full spectra", Mod. Phys. Lett. A **21**, 1547 (2006).

[Kno00] G. Knoll, *Radiation Detection and Measurement*, John Wiley & Sons, Inc., 3rd edition, 2000.

[Kod02] K. Kodama et al., "Detection and analysis of tau-neutrino interactions in DONUT emulsion target", Nucl. Instrum. Methods A **493**, 45 (2002).

[Kon03] A. J. Koning and J. P. Delaroche, "Local and global nucleon optical models from 1 keV to 200 MeV", Nucl. Phys. A **713**, 231 (2003).

[Kon08] A. Koning, S. Hilaire, and M. Duijvestijn, "TALYS-1.0", in *Proceedings of the International Conference on Nuclear Data for Science and Technology*, edited by E. R. O.Bersillon, F.Gunsing and S.Leray, pages 211–214, EDP Sciences, 2008.

[Kop90] J. Kopecky and M. Uhl, "Test of gamma-ray strength functions in nuclear reaction model calculations", Phys. Rev. C **41**, 1941 (1990).

[Kra88] K. Krane, *Introductory Nuclear Physics*, John Wiley & Sons, Inc., 1988.

[Kub77] S. Kubota et al., "Recombination luminescence in liquid argon and in liquid xenon", Phys. Rev. B **17**, 2762 (1977).

[Lar11] D. Larson et al., "Seven-Year Wilkinson Microwave Anisotropy Probe (WMAP) Observations: Power Spectra and WMAP-Derived Parameters", Astrophys. J. Suppl. **192**, 16 (2011).

[Lee77] B. Lee and S. Weinberg, "Cosmological lower bound on heavy-neutrino mass", Phys. Rev. Lett. **39**, 165 (1977).

[Lef62] H. Lefevre, R. Borchers, and C. Poppe, "Fast neutron time-of-flight spectrometer", **1962**, 1231 (1962).

[Lem59] R. Lemmer, A. Marsis, and Y. Tang, "On the imaginary optical potential", Nucl. Phys **12**, 619 (1959).

[Lew96] J. Lewin and P. Smith, "Review of mathematics, numerical factors, and corrections for dark matter experiments based on elastic nuclear recoil", Astropart. Phys. **6**, 87 (1996).

[Lid99] A. Liddle, *An Introduction to Modern Cosmology*, John Wiley & Sons, Inc., 1999.

[Lip08] W. H. Lippincott et al., "Scintillation time dependence and pulse shape discrimination in liquid argon", Phys. Rev. C **78**, 035801 (2008).

[Lis90] P. Lisowski et al., "The Los Alamos National Laboratory Spallation Neutron Sources", Nucl. Sci. Eng. **106**, 208 (1990).

[Maj37] E. Majorana, "Symmetric theory of the electron and the positron", Nuovo Cimento **14**, 171 (1937), Title translated from Italian.

[Mak62] Z. Maki, M. Nakagawa, and S. Sakata, "Remarks on the Unified Model of Elementary Particles", Prog. Theor. Phys. **28**, 870 (1962).

[Mar71] P. Marmier and E. Sheldon, *Physics of Nuclei and Particles*, volume 2, Academic Press Inc., 1971.

[Mar05] M. Markevitch, "Chandra Observation of the most Interesting Cluster in the Universe", arxiv preprint arXiv:astro-ph/0511345v1 (2005).

[Mar11] S. Martin, "A Supersymmetry Primer", arxiv preprint: arXiv:hep-ph/9709356v6 (2011).

[Mas70] T. Masterson, "Response of NE 218 to fast neutrons", Nucl. Instrum. Methods **88**, 61 (1970).

[Mat65] S. Mathur and I. Morgan, "Angular distribution of gamma rays produced in the ^{40}Ar(n,n'γ)^{40}Ar reaction", Nucl. Phys. **73**, 579 (1965).

[McK05] D. McKinsey and K. Coakley, ""Neutrino detection with CLEAN"", Astropart. Phys. **22**, 355 (2005).

[McK07] D. N. McKinsey, "The Mini-CLEAN experiment", Nucl. Phys. B Proc. Suppl. **173**, 152 (2007).

[McN00a] D. McNabb et al., "Neutron-induced partial gamma-ray cross-section measurements with GEANIE at LANSCE/WNR", AIP. Conf. Proc. **529**, 384 (2000).

[McN00b] D. McNabb et al., "Uncertainty Budget and Efficiency Analysis for the 239Pu$(n, 2n\gamma)$ Partial Reaction Cross-Section Measurements", LLNL Report UCRL-ID-139906, 2000.

[Mei06] D.-M. Mei and A. Hime, "Muon-induced background study for underground laboratories", Phys. Rev. D **73**, 053004 (2006).

[Mei08] D.-M. Mei, Z.-B. Yin, L. Stonehill, and A. Hime, "A Model of Nuclear Recoil Scintillation Efficiency in Noble Liquids", Astropart. Phys. **30**, 12 (2008).

[Mei09a] D.-M. Mei, C. Zhang, and A. Hime, "Evaluation of $(\alpha$,n) induced neutrons as a background for dark matter experiments", Nucl. Instrum. Methods Phys. Res., Sect. A **606**, 651 (2009).

[Mei09b] D.-M. Mei, Z.-B. Zin, and S. Elliott, "Cosmogenic production asa background in searching for rare physics processes", Astropart. Phys. **31**, 417 (2009).

[Men12] E. Mendoza et al., "New evaluated neutron cross section libraries for the GEANT4 code", IAEA technical report INDC(NDS)-0612 (2012), `http://www-nds.iaea.org/geant4`.

[Mes] Mesytec MPD-4 Datasheets, `http://www.mesytec.com/datasheets/MPD-4.pdf`, accessed November 27, 2012.

[MID01] MIDAS - Maximum Integrated Data Acquisition System, 2001, midas.psi.ch, accessed December 6, 2012.

[Mil76] W. Milner, "Double-drift beam bunching systems", IEEE Trans. Nucl. Sci. **NS-26**, 1445 (1976).

[Moe91] M. Moe, "Experimental Review of Double Beta Decay", Nucl. Phys. B Proc. Suppl. **19**, 158 (1991).

[Mol76] P. A. Moldauer, "Evaluation of the fluctuation enhancement factor", Phys. Rev. C **14**, 764 (1976).

[Mol80] P. A. Moldauer, "Statistics and the average cross section", Nucl. Phys. A **344**, 185 (1980).

[Mor76] H. Morinaga and T. Yamazaki, *In-Beam Gamma-Ray Spectroscopy*, North-Holland Publishing Company, 1976.

[Mos98] I. Moskalenko and A. Strong, "Production and propagation of cosmic-ray positrons and electrons", Astrophys. J. **493**, 694 (1998).

[Nak01] N. Nakao et al., "Absolute measurements of the response function of an NE213 organic liquid scintillator for the neutron energy range up to 206 MeV", Nucl. Instrum. Methods A **463**, 275 (2001).

[NAS06] NASA 1E 0657-56: NASA Finds Direct Proof of Dark Matter, 2006, http://chandra.harvard.edu/photo/2006/1e0657/, accessed October 11, 2012.

[Nat12] National Electrostatics Company Inc., `http://www.pelletron.com/charging.htm`, accessed May 2, 2012, 2012.

[Nel05] R. Nelson et al., "Cross-Section Standards for Neutron-Induced Gamma-Ray Production in the MeV Energy Range", Proceedings of the International Conference on Nuclear Data for Science and Technology **768**, 838 (2005).

[Nik08] J. A. Nikkel, R. Hasty, W. H. Lippincott, and D. N. McKinsey, "Scintillation of liquid neon from electronic and nuclear recoils", Astropart. Phys. **29**, 161 (2008).

[nn-12] nn-online, http://nn-online.org, accessed May 9, 2012, 2012.

[Pac86] B. Paczynski, "Gravitational Microlensing by the Galactic Halo", Astrophys. J. **304**, 1 (1986).

[Pec77a] R. Peccei and H. Quinn, "Constraints imposed by *CP* conservation in the Presence of pseudoparticles", Phys. Rev. D **16**, 1791 (1977).

[Pec77b] R. Peccei and H. Quinn, "*CP* Conservation in the Presence of Pseudoparticles", Phys. Rev. Lett. **38**, 1440 (1977).

[Ped86] R. Pedroni, Ph.D. Thesis, Duke University, 1986.

[Per67] F. Perey, "Computer code GENOA - A searching procedure for global optical model parameters", Oak Ridge National Laboratory, unpublished, 1967.

[Phi12] D. Phillips et al., "The MAJORANA experiment: an ultra-low background search for neutrinoless double-beta decay", J. Phys.: Conf. Ser. **381**, 012044 (2012).

[Pon68] B. Pontecorvo, "Neutrino Experiments and the Problem of Conservation of Leptonic Charge", Soviet Physics JETP **26**, 984 (1968), Title translated from Russian.

[Pri88] J. Primack, D. Seckel, and B. Sadoulet, "Detection of Cosmic Dark Matter", Ann. Rev. Nucl. Part. Sci. **38**, 751 (1988).

[Pu03] Z. Pu, J. Yang, and X. Kong, "Cross-section measurements for $(n, 2n)$, (n, p) and $(n, n'\alpha)$ reactions on gallium isotopes in the neutron energy range of 13.5-14.6 MeV", Appl. Radiat. Isot. **58**, 723 (2003).

[Pyw06] R. Pywell et al., "Light output response of BC-505 liquid scintillator", Nucl. Instrum. Methods A **565**, 725 (2006).

[Rac37] G. Racah, "On the symmetry between particles and antiparticles", Nuovo Cimento **14**, 322 (1937), Article title translated from Italian.

[Rac42] G. Racah, "Theory of Complex Spectra. II", Phys. Rev. **62**, 438 (1942).

[Rad00] D. Radford, "Notes on the program gf3", (2000).

[Rei53] F. Reines and C. Cowan, "Detection of the Free Neutrino", Phys. Rev. **92**, 830 (1953).

[ROO12] ROODY - Viewer for online histograms generated by MIDAS and ROME and for ROOT files., 2012, https://daq-plone.triumf.ca/SR/ROODY, accessed December 6, 2012.

[Rup09] G. Rupp et al., "High pressure gas spheres for neutron and photon experiments", Nucl. Instrum. Methods A **608**, 152 (2009).

[Sae04] J. Saegusa et al., "Determination of detection efficiency curves of HPGe detectors on radioactivity measurement of volume samples", App. Radiat. Isot. **61**, 1383 (2004).

[Sas02] M. Sasaki et al., "Measurements of the response functions of an NE213 organic liquid scintillator to neutrons up to 800 MeV", Nucl. Instrum. Methods A **480**, 440 (2002).

[Sch82] J. Schechter and J. F. Valle, "Neutrinoless double-β decay in SU(2) $\times$ U(1) theories", Phys. Rev. D **25**, 2951 (1982).

[Sch05] S. Schönert et al., "The GERmanium Detector Array (GERDA) for the search for neutrinoless $\beta\beta$ decays of ^{76}Ge at LNGS", Nucl. Phys. B Proc. Suppl. **145**, 242 (2005).

[Sch11a] A. G. Schubert et al., "The MAJORANA DEMONSTRATOR: A Search for Neutrinoless Double-beta Decay of Germanium-76", AIP Conf. Proc. **1441**, 480 (2011).

[Sch11b] M. Schwenke et al., “Exploration of Pixelated detectors for double beta decay searches within the COBRA experiment”, Nucl. Instrum. Methods A **650**, 73 (2011).

[Seg46] E. Segrè and C. Wiegand, “Stopping power of various substances for fission fragments”, Phys. Rev. **70**, 808 (1946).

[Sik57] C. Sikkema, “Scattering of Fast Neutrons by Neon in the Energy Region 1.9 to 3.5 MeV”, Nucl. Phys. **3**, 375 (1957).

[Sik58] C. Sikkema, P. Pasma, and H. V. Barneveld, “Scattering of Fast Neutrons by Neon-22”, Nucl. Phys. **5**, 351 (1958).

[Šim08] F. Šimkovic et al., “Anatomy of the $0\nu\beta\beta$ nuclear matrix elements”, Phys. Rev. C **77**, 045503 (2008).

[Smi09] A. Smith, private communication, 2009.

[Smo92] G. Smoot et al., “Structure in the COBE Differential Microwave Radiometer First-Year Maps”, Astrophys. J. **396**, L1 (1992).

[Sto93] V. G. J. Stoks et al., “Partial-wave analysis of all nucleon-nucleon scattering data below 350 MeV”, Phys. Rev. C **48**, 792 (1993).

[Sus84] L. Susskind, “The Gauge Hierarchy Problem, Technicolor, Supersymmetry, and all that”, Phys. Reports **104**, 181 (1984).

[Tep74] J. Tepel, H. Hofmann, and H. Weidenmüller, “Hauser-Feshbach formulas for medium and strong absorption”, Phys. Lett. B **49**, 1 (1974).

[Til98] D. Tilley et al., “Energy Levels of Light Nuclei, A = 20”, Nucl. Phys. A **636**, 247 (1998).

[Tor12] W. Tornow, Private communication, 2012.

[Tow67] J. Towle and R. Owens, “Absolute level densities from neutron inelastic scattering”, Nucl. Phys. A **100**, 257 (1967).

[Tro09] D. E. Trotter et al., “Neutron detection efficiency determinations for the TUNL neutron-neutron and neutron-proton scattering-length measurements”, Nucl. Instrum. Methods Phys. A **599**, 234 (2009).

[Vau60] F. Vaughn et al., “Total Neutron Cross Sections of Helium, Neon, Argon, Krypton, and Xenon”, Phys. Rev. **118**, 683 (1960).

[Ver85] J. J. M. Verbaarschot, H. Weidenmüller, and M. Zirnbauer, “Grassmann integration in stochastic quantum physics: The case of compound nucleus scattering”, Phys. Reports **129**, 367 (1985).

[Wan95] T.-K. Wang et al., “HPGe Detector Absolute-peak-efficiency Calibration by Using the ESOLAN Program”, Appl. Radiat. Isot. **46**, 933 (1995).

[Wei51] V. Weisskopf, “Radiative transition probabilities in nuclei”, Phys. Rev. **81**, 1073 (1951).

[Wen80] S. Wender et al., “A high efficiency bunching system for polarized beams”, Nucl. Instrum. Methods , 341 (1980).

[Wen93] S. Wender et al., “A fission ionization detector for neutron flux measurements at a spallation source”, Nucl. Instrum. Methods A , 226 (1993).

[Wic43] G. C. Wick, Atti reale. Italia. Mem. classe. Sci. fis. mat. e nat. **13**, 1203 (1943).

[Wic49] G. C. Wick, Phys. Rev. **75**, 1459 (1949).

[Wie07] H. Wiedermann, *Particle Accelerator Physics*, Springer, 3rd edition, 2007.

[Win91] R. Winters et al., “Total cross section and neutron resonance spectroscopy for n + 40Ar”, Phys. Rev. C **43**, 492 (1991).

[Wol78] L. Wolfenstein, “Neutrino oscillations in matter”, Phys. Rev. D **17**, 2369 (1978).

[Wol10] J. Wolf et al., “The KATRIN neutrino mass experiment”, Nucl. Instrum. Methods A **623**, 442 (2010).

[Won98] S. Wong, *Introductory Nuclear Physics*, John Wiley & Sons, Inc., 2nd edition, 1998.

[Woo54] R. Woods and D. Saxon, “Diffuse Surface Optical Model for Nucleon-Nuclei Scattering”, Phys. Rev. **95**, 577 (1954).

[Wu57] C. Wu et al., “Experimental Test of Parity Conservation in Beta Decay”, Phys. Rev. **105**, 1413 (1957).

[Zwi33] F. Zwicky, “The redshift of extragalactic nebulae”, Helvetica Physica Acta **6**, 110 (1933), Article in German.